

MINISTRY OF
EDUCATION AND TRAINING

VIETNAM ACADEMY OF
SCIENCE AND TECHNOLOGY

GRADUATE UNIVERSITY OF SCIENCE AND TECHNOLOGY



Nguyen Thi Ngoc Hoi

**STRUCTURE-ADJUSTABLE SYNTHESIS OF HOLLOW
MESOPOROUS SILICA NANOPARTICLES AND ITS
SURFACE MODIFICATION FOR ANTI-CANCER DRUG
DELIVERY**

DOCTORAL THESIS OF MATERIAL SCIENCE

Ho Chi Minh City – 2022

MINISTRY OF
EDUCATION AND TRAINING

VIETNAM ACADEMY OF
SCIENCE AND TECHNOLOGY

GRADUATE UNIVERSITY OF SCIENCE AND TECHNOLOGY

Nguyen Thi Ngoc Hoi

**STRUCTURE-ADJUSTABLE SYNTHESIS OF HOLLOW
MESOPOROUS SILICA NANOPARTICLES
AND ITS SURFACE MODIFICATION
FOR ANTI-CANCER DRUG DELIVERY**

DOCTORAL THESIS OF MATERIAL SCIENCE

Code: 9440125

Graduate University
of Science and Technology

KT. GIÁM ĐỐC

PHÓ GIÁM ĐỐC



Nguyễn Thị Trung

Scientific supervisor

(Signed and full name)

PGS.TS. Nguyễn Đại Hải

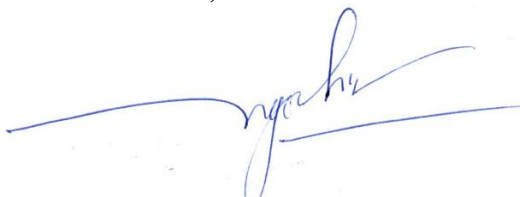
Ho Chi Minh City - 2022

DECLARATION

The work was carried out at the Department of Biomaterials & Bioengineering
- Institute of Applied Materials Science (IAMS) - Vietnam Academy of Science
and Technology (VAST) in Ho Chi Minh City.

I hereby declare that this is my research work under the scientific guidance of
Assoc.Prof.Dr. Nguyen Dai Hai. The research contents and results presented in
this thesis are honest and completely based on my research results. The results
of this study have not been published on any thesis of the same level.

Ho Chi Minh, December 30th 2022



NGUYEN THI NGOC HOI

ACKNOWLEDGEMENTS

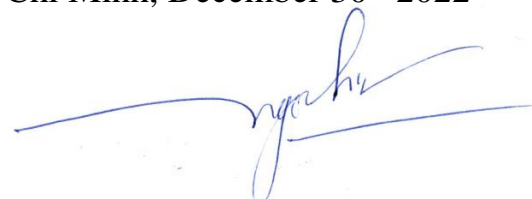
First of all, I would like to express my most profound gratitude to my supervisor Assoc. Prof., PhD. Nguyen Dai Hai - Vice Director of the Institute of Applied Materials Science, and Head of Department of Biomaterials and Bioengineering. He has given me the delightful lessons, inspiration, constant motivation and enthusiasm that have surely encouraged and helped me to overpass the difficulties encountered, and exerted great aids for my accomplishment of this thesis research.

Secondly, my sincere gratitude also goes to the enthusiastic help and favorable supports during my PhD course from Graduate University of Science and Technology (GUST) and the Institute of Applied Materials Science (IAMS) - Vietnam Academy of Science and Technology (VAST).

Furthermore, it is impossible not to mention the valuable support from MSc. Nguyen Dinh Tien Dung and BS. Truong Thi Ngoc Hang. They contributed great help during the experiments at IAMS.

Last but not least, I am grateful to have my family and friends, who always encourage and support all over time that makes my thesis experience more meaningful.

Ho Chi Minh, December 30th 2022



NGUYEN THI NGOC HOI

TABLE OF CONTENTS

	Page
DECLARATION	i
ACKNOWLEDGEMENTS	ii
TABLE OF CONTENTS	iii
LIST OF ABBREVIATIONS	vii
LIST OF FIGURES	ix
LIST OF DIAGRAMS	xiv
LIST OF TABLES	xv
INTRODUCTION	1
CHAPTER 1. LITERATURE REVIEW	4
<i>1.1. Overview of cancer and cancer treatment</i>	4
<i>1.1.1. Overview of cancer</i>	4
<i>1.1.2. Common cancer treatment therapies</i>	5
<i>1.2. Nanomaterials in cancer treatment</i>	8
<i>1.2.1. Nanomaterials in anti-cancer drug delivery applications</i>	8
<i>1.2.2. Silica nanomaterials in anti-cancer drug delivery applications</i>	9
<i>1.3. Recent progress of nano silica particle applications in drug delivery</i>	11
<i>1.3.1. International research</i>	11
<i>1.3.2. National research</i>	13
<i>1.4. Hollow mesoporous silica nanoparticles (HMSN)</i>	14
<i>1.4.1. Structure of HMSN</i>	14
<i>1.4.2. Synthesis methods of HMSN</i>	15
<i>1.4.3. Reaction mechanisms in the synthesis of HMSN by silica based hard-template method</i>	22
<i>1.4.4. Modular factors in HMSN fabrication</i>	27
<i>1.4.5. Modifications of HMSN</i>	36
<i>1.4.6. Multiple-Drug Loading HMSN</i>	41
CHAPTER 2. MATERIALS AND EXPERIMENTAL METHODS	44
<i>2.1. Materials</i>	44

2.1.1. Chemicals.....	44
2.1.2. Equipments.....	45
2.2. Synthesis Methods.....	46
2.2.1. Synthesis of HMSN.....	46
2.2.2. The effect of PEG on the mesoporous shell thickness of HMSN	49
2.2.3. The effect of non-ionic surfactants on the mesopore diameter of HMSN.....	51
2.2.4. Surface Modification Method of HMSNs with Pluronic	53
2.2.5. The effect of Pluronic on dual-drugs delivery characteristics of HMSN-Plu	56
2.3. Physicochemical Analysis Methods.....	57
2.4. Drug loading and in vitro release study	58
2.5. Cell culture and MTT assay.....	59
2.6. Statistical analysis	59
CHAPTER 3. A MODIFIED HARD-TEMPLATE METHOD FOR HOLLOW MESOPOROUS SILICA NANOPARTICLES SYNTHESIS WITH SUITABLE PARTICLE SIZE AND SHORTENED SYNTHETIC TIME	61
3.1. Synthesis of silica hard-template.....	61
3.2. Etching over time of silica hard-template in the synthesis of HMSN.....	62
3.3. Characterizations of synthesized HMSN.....	63
3.4. Cytotoxicity of synthesized HMSN	66
3.5. Summary.....	67
CHAPTER 4. SIMPLY AND EFFECTIVELY CONTROL THE SHELL THICKNESS OF HOLLOW MESOPOROUS SILICA NANOPARTICLES BY POLYETHYLENE GLYCOL FOR DRUG DELIVERY APPLICATIONS.....	69
4.1. Effect of PEG molecular weight on the mesoporous shell thickness of $dSiO_2@MSN$	69
4.2. Effect of PEG weight percentage on the mesoporous shell thickness of $dSiO_2@MSN$	71

4.3. Characterizations of the synthesized HMSNs.....	74
4.3.1. Drug loading and in vitro drug release study of the synthesized HMSN.....	77
4.4. Cytotoxicity of the synthesized HMSN.....	79
4.5. Summary.....	80
CHAPTER 5. NON-IONIC SURFACTANTS AS CO-TEMPLATES TO CONTROL THE MESOPORE DIAMETER OF HOLLOW MESOPOROUS SILICA NANOPARTICLES FOR DRUG DELIVERY APPLICATIONS	81
5.1. Preparation of mixed micelles of non-ionic surfactants with CTAB.....	81
5.2. Effect of non-ionic surfactants on the mesoporous shell thickness of $dSiO_2@MSN$	83
5.3. Effect of non-ionic surfactants on the mesopore diameter of $dSiO_2@MSN$	85
5.4. Characterizations of the synthesized HMSNs.....	87
5.5. Drug loading and in vitro drug release study of the synthesized HMSNs.....	89
5.6. Cytotoxicity of the synthesized HMSNs.....	90
5.7. Summary.....	91
CHAPTER 6. SURFACE MODIFICATION OF HOLLOW MESOPOROUS SILICA NANOPARTICLES WITH PLURONICS FOR DUAL DRUGS DELIVERY.....	93
6.1. Activation Pluronic with NPC.....	93
6.2. Amination of HMSNs' surface.....	94
6.3. Modification of HMSNs' surface with Pluronics via amine intermediate.....	96
6.4. Dual-drug loading capacity and in vitro release behavior of HMSN-Plu.....	99
6.5. In vitro drug release behavior of HMSN-Plu.....	100
6.6. Cytotoxicity of HMSN-Plu.....	103
6.7. Characterizations of HMSN-F127.....	104
6.8. Cancer cell killing ability of $DOX.QUE@HMSN-Plu$	108
6.9. Summary.....	109
CONCLUSIONS AND FUTURE PERSPECTIVES.....	111

<i>Conclusion</i>	111
<i>Novelty of the thesis</i>	112
<i>Future perspective</i>	112
LIST OF PUBLICATIONS	114
REFERENCES	115

LIST OF ABBREVIATIONS

APTES	(3-Aminopropyl)triethoxysilane
BET	Brunauer-Emmett-Teller
BJH	Barret Joyner and Halenda
BTES	Bis (triethoxysilylpropyl) disulfide
C18TMS	n-octadecyltrimethoxysilan
CMC	Critical micelle concentration
CTAB	Cetyltrimethylammonium Bromide
CTAC	Cetyltrimethylammonium Chloride
DI	Deioned water
DLC	Drug loading capacity
DLE	Drug loading efficiency
DLS	Dynamic Light Scattering
DOX	Doxorubicin
dSiO₂	dense Silicone dioxide
EDX	Energy Dispersive X-ray
EPR	Enhanced Permeability and Retention
FDA	Food and Drug Administration
FE-SEM	Field Emission Scanning Electron Microscope
FT-IR	Fourier Transform Infrared
GPC	Gel Permeation Chromatography
HMSN	Hollow Mesoporous Silica Nanoparticles
HPLC	High Performance Liquid Chromatography
MCM-41	Mobil Composition of Matter No. 41
MCM-48	Mobil Composition of Matter No. 48
MCM-50	Mobil Composition of Matter No. 50
MDR	Multidrug Resistance
MON	Mesoporous Organosilica Nanoparticle
MSN	Mesoporous Silica Nanoparticles
PAA	Poly (Acrylic Acid)
PBS	Phosphate Buffered Saline
PEG	Polyethylene Glycol
PEO	Poly(Ethylene Oxide)
PPO	Poly(Propylene Oxide)
PMMA	Polymethylmethacrylate

PS	Polystyrene
PVP	Polyvinylpyrrolidone
QUE	Quercetin
RB	Rose Bengal
SBA-15	Santa Barbara Amorphous-15
SEM	Scanning electron microscope
TGA	Thermogravimetric analysis
TEA	Triethanolamine
TEM	Transmission electron microscopy
TEOS	Tetraethyl orthosilicate
XRD	X-ray Diffraction

LIST OF FIGURES

<i>Figure 1.1.</i> Global cancer data in 2020: a) Female, b) Male [1]	5
<i>Figure 1.2.</i> Common treatments for cancers [2].....	7
<i>Figure 1.3.</i> Popular nanomaterials applied in drug delivery [6].....	9
<i>Figure 1.4.</i> Members of the M41S family [8].....	10
<i>Figure 1.5.</i> Structural classification of Mesoporous Silica Nanoparticles [9].....	10
<i>Figure 1.6.</i> Structure of Hollow Mesoporous Silica Nanoparticle (HMSN): a) 2D radial section; b) 3D model; and c) Mesoporous structure of the shell	14
<i>Figure 1.7.</i> Synthesis methods of HMSN	15
<i>Figure 1.8.</i> Hydrolysis and condensation of TEOS precursors in alcohol-water-ammonia medium.....	23
<i>Figure 1.9.</i> Multistage growth diagram of silica particles by hydrolysis of TEOS in alcohol-water-ammonia medium [62].....	24
<i>Figure 1.10.</i> Illustration of the formation mechanism of the mesoporous shell (MCM-41) [18]	25
<i>Figure 1.11.</i> Etching process of hard template $dSiO_2$ by Na_2CO_3 [64]	25
<i>Figure 1.12.</i> Etching mechanism of hard template $dSiO_2$ to form HMSN by Na_2CO_3 : a) Etching process with the presence of CTAB micelles, and b) Etching process without CTAB micelles [64].....	26
<i>Figure 1.13.</i> Modular factors of the HMSN	27
<i>Figure 1.14.</i> Adjustable shell thickness of microporous hollow core@shell silica nanoparticles for controlled release of doxorubicin [70].....	30
<i>Figure 1.15.</i> The size of biodegradable silica nanoparticles was reduced for efficient curcumin loading [74].....	31
<i>Figure 1.16.</i> The effect of polyethylene glycol on shape and size of $SrTiO_3$ nanoparticles [83].....	32

<i>Figure 1.17.</i> Self-assembly of mixed micelle of CTAB and P123 used as mesoporous templates in MSN particle synthesis [96]	35
<i>Figure 1.18.</i> Aminated HMSN using 3-Aminopropyl)triethoxysilane for better DOX loading capacity and controlled release [40].....	38
<i>Figure 1.19.</i> Molecular structure of Pluronics	40
<i>Figure 1.20.</i> Conjugation of polyamidoamine dendrimer and pluronics for hydrophobic drug delivery [108]	41
<i>Figure 2.1.</i> Molecular formulas of the used non-ionic surfactants versus CTAB ...	51
<i>Figure 3.1.</i> Characterizations of the synthesized hard-template dSiO ₂ : a) Zeta potential; b) DLS particle size distribution; c) SEM image; d) TEM image	61
<i>Figure 3.2.</i> SEM and TEM images of HMSN over etching time	63
<i>Figure 3.3.</i> a) TEM image of dSiO ₂ @MSN; b) TEM image of HMSN, c) N ₂ adsorption-desorption isotherms of HMSN and d) Pore size distributions of HMSN	65
<i>Figure 3.4.</i> Characterizations of the synthesized HMSN: a) FT-IR spectrum; b) EDX pattern; c) Zeta potential; d) DLS particle size distribution; e) XRD pattern; and f) TGA graph	66
<i>Figure 3.5.</i> a) Cell viability assay by MTT assay with variable concentrations of HMSN on MCF-7 cells; b) Morphology of MCF-7 cells treated by HMSN at different concentrations	67
<i>Figure 4.1.</i> Size dispersion by DLS measurement and field-emission scanning electron microscopy (FE-SEM) images of (a, a')dSiO ₂ , (b, b') dSiO ₂ @MSN, (c, c') dSiO ₂ @MSN-P1k, (d, d') dSiO ₂ @MSN-P2k, (e, e') dSiO ₂ @MSN-P4k and (f, f') dSiO ₂ @MSN-P6k	69
<i>Figure 4.2.</i> Size dispersion by DLS measurement and field-emission scanning electron microscopy (FE-SEM) images of (a, a') dSiO ₂ @MSN-P1%, (b, b')	

dSiO₂@MSN-P2%, (c, c') dSiO₂@MSN-P3%, (d, d') dSiO₂@MSN-P4% and (e, e') dSiO₂@MSN-P5% 72

Figure 4.3. The structure of PEG changes from a) zigzag chains to b) ordered net structure in the solution 74

Figure 4.4. Characterizations of the synthesized silica nanoparticles: a) TEM images of dSiO₂@MSN-0 and a') dSiO₂@MSN-P; TEM images of b) HMSN-0 and b') HMSN-P; Size distribution of c) HMSN-0 and c') HMSN-P; Zeta potential of d) HMSN-0 and d') HMSN-P 75

Figure 4.5. The N₂ adsorption-desorption isotherms and pore size distributions of dSiO₂@MSN (a and b) and dSiO₂@MSN-P (a' and b') 76

Figure 4.6. Characterizations of the synthesized HMSN-0 (square dot) and HMSN-P (solid): a) EDX patterns; b) FT-IR spectra. 77

Figure 4.7. DOX loading capacity (DLC - grey) and DOX loading efficiency (DLE - black) of HMSN-0 and HMSN-P (a); *In vitro* release profile of Dox@HMSN-0 (empty circle) and Dox@HMSN-P (solid circle) (b). The marked points correspond to 0, 1, 3, 6, 9, 12, 24, 36 and 48 h, respectively 78

Figure 4.8. Cell viability by MTT assay with variable concentrations of HMSN-0 and HMSN-P on MCF-7 cells (a); MCF-7 cells treated by HMSN-0 and HMSN-P at different concentrations (b) 79

Figure 5.1. a) Viscosity of mixed micelles versus molar ratio of non-ionic surfactants and CTAB. Molar concentration of CTAB remained constantly at 0.02 M. b) Hydrodynamic diameter of mixed micelles versus molar ratio. Molar concentration of CTAB in each mixture was 50 mM in the presence of 1 mM KBr 82

Figure 5.2. Size distribution by DLS measurement of a) dSiO₂@MSN-T20, b) dSiO₂@MSN-T80, and c) dSiO₂@MSN-BS10 83

Figure 5.3. Illustration of the effect of non-ionic surfactants in mixed micelles on the mesoporous shell thickness of dSiO₂@MSN 85

<i>Figure 5.4.</i> The N ₂ adsorption-desorption isotherms and pore size distributions of a) dSiO ₂ @MSN, b) dSiO ₂ @MSN-T20, c) dSiO ₂ @MSN-T80 and d) dSiO ₂ @MSN-BS10.....	86
<i>Figure 5.5.</i> SEM images, TEM images, Size distribution and Zeta potential of HMSN, HMSN-T20, HMSN-T80 and HMSN-BS10.....	87
<i>Figure 5.6.</i> a) XRD patterns and b) FT-IR spectra of HMSN, HMSN-T20, HMSN-T80 and HMSN-BS10.....	88
<i>Figure 5.7.</i> (a) Rose bengal (RB) loading capacity (DLC - grey) and loading efficiency (DLE - black) of HMSN, HMSN-T20, HMSN-T80 and HMSN-BS10; (b) <i>In vitro</i> release profile of RB from HMSN, HMSN-T20, HMSN-T80 and HMSN-BS10. The marked points correspond to 0, 1, 3, 6, 9, 12, 24, 36, 48, 60 and 72 h, respectively	90
<i>Figure 5.8.</i> a) Cell viability by MTT assay on MCF-7 cells; and b) MCF-7 cells treated by HMSN, HMSN-T20, HMSN-T80 and HMSN-BS10 at different concentrations	91
<i>Figure 6.1.</i> FT-IR spectra of NPC-Plu-OH.....	93
<i>Figure 6.2.</i> ¹ H-NMR spectra of NPC-Plu-OH: a) NPC-L64-OH, b) NPC-F68-OH, c) NPC-F127-OH, d) Annotation the molecular structure of NPC-Plu-OH.....	94
<i>Figure 6.3.</i> Characterizations of HMSN and HMSN-NH ₂ : a) Zeta potential; b) Hydrodynamic particle diameter; c) FT-IR spectra; and d) EDX patterns.....	95
<i>Figure 6.4.</i> Characterizations of HMSN-L64, HMSN-F68 and HMSN-F127: a) Zeta potential; b) Hydrodynamic particle diameter; c) FT-IR spectra; and d) TGA graphs	97
<i>Figure 6.5.</i> <i>In vitro</i> release behaviour of free drugs and loaded drugs in different conditions of temperatures and pH values	101
<i>Figure 6.6.</i> Illustration of release behavior of HMSN-Plu in different conditions	103

<i>Figure 6.7.</i> a) Cytotoxicity by MTT assay of HMSN-Plu on Hela cells; b) Morphology of Hela cells treated by HMSN at different concentrations.....	104
<i>Figure 6.8.</i> TEM images and Size distribution of a), a') HMSN and b), b') HMSN-F127.....	105
<i>Figure 6.9.</i> The N ₂ adsorption-desorption isotherms and pore size distributions of HMSN (a, a') and HMSN-F127 (b, b').....	106
<i>Figure 6.10.</i> (a) XRD patterns of HMSN (dash line) and HMSN-F127 (solid line); (b) Fitting XRD peaks of HMSN (XRD pattern – Dash; Cumulative fit peak – Solid line); and (c) Fitting XRD peaks of HMSN-F127 (XRD pattern – Dash; Cumulative fit peak – Solid line).....	107
<i>Figure 6.11.</i> a) Cell viability and b) Morphology of Hela cells treated by Free DOX, Free QUE and DOX.QUE@HMSN-F127.....	108

LIST OF DIAGRAMS

<i>Diagram 1.1.</i> Sol-Gel synthesis of a) hard template dSiO ₂ and b) mesoporous shell MSN	23
<i>Diagram 2.1.</i> The preparation of the hard template dSiO ₂	47
<i>Diagram 2.2.</i> The preparation of core@shell structure dSiO ₂ @MSN	48
<i>Diagram 2.3.</i> The selective etching of dSiO ₂ @MSN to form HMSN	49
<i>Diagram 2.4.</i> Mesoporous silica layer coating step in HMSN synthesis process with the presence of PEG	50
<i>Diagram 2.5.</i> Mesoporous silica layer coating step in HMSN synthesis process with the presence of non-ionic surfactants as co-templates	52
<i>Diagram 2.6.</i> The surface activation of HMSN with APTES	54
<i>Diagram 2.7.</i> The activation of Pluronic with NPC	55
<i>Diagram 2.8.</i> The preparation of HMSN-Plu from HMSN-NH ₂ and NPC-Plu-OH	56

LIST OF TABLES

<i>Table 1.1.</i> Advantages and limitation of different HMSN synthesis methods	21
<i>Table 2.1.</i> List of used chemicals.....	44
<i>Table 2.2.</i> List of used equipments	46
<i>Table 2.3.</i> Characteristics of the used Pluronics	57
<i>Table 4.1.</i> Effect of PEG molecular weight (1000, 2000, 4000 and 6000) at 3% (w/v) on the particle diameter and mesoporous shell thickness of dSiO ₂ @MSN samples (based on FE-SEM images). Means with the same upper letters (a, b, c) are not statistically different based on the least significant difference at $p < 0.05$	70
<i>Table 4.2.</i> Effect of weight percentage of PEG 6000 (1% - 5%) on the particle diameter and mesoporous shell thickness of dSiO ₂ @MSN samples (based on FE-SEM images). Means with the same upper letters (a, b, c) are not statistically different based on the least significant difference at $p < 0.05$	73
<i>Table 5.1.</i> The mesoporous shell thickness (nm) of dSiO ₂ @MSN particles versus the molar ratio of non-ionic surfactants with CTAB in mixed micelles.....	84
<i>Table 6.1.</i> Weight loss (%) of HMSN and HMSN-Plu by temperature ranges through thermogravimetric analysis	98
<i>Table 6.2.</i> Loading capacity (DLC) and loading efficiency (DLE) for Doxorubicin (DOX) and Quercetin (QUE) of HMSN and HMSN-Plu	99
<i>Table 6.3.</i> Summary of physicochemical characteristics, drug loading capacity and drug release properties of the synthesized silica nanoparticles	110

INTRODUCTION

Mesoporous silica nanoparticles (MSNs) have been known to be widely studied materials for biomedical applications, especially drug delivery due to their suitable properties such as high surface area, large pore volume, adjustable pore size, high biocompatibility and easy surface modification. As a member of the MSN family, hollow mesoporous silica nanoparticles (HMSN) consisting of two main parts, the outer mesoporous shell and the inner hollow cavity. Therefore, besides the characteristic properties of MSN, HMSN also has another outstanding advantage that is its superior drug carrying capacity compared to MSN thanks to the hollow cavity.

HMSNs can be synthesized by different methods, of which hard templating is known as the most popular method thanks to the following advantages: (1) Predictable particle morphology, (2) narrow size distribution and uniform product morphology, (3) good control and high repeatability. With this hard templating, three common characteristics of HMSNs that can be adjusted are hollow cavity volume, mesoporous shell thickness and mesopore diameter. The volume of hollow cavity has been reported to be adjusted through controlling the hard template size. However, the mesoporous shell thickness and mesopore diameter - factors that have important influence on drug loading and drug release properties of the materials have not been thoroughly studied yet. Moreover, HMSN particles with open pores would cause drug leakage during transportation. To overcome this drawback, several studies have modified the HMSNs' surface with different agents to form the caps for the open pores were conducted. Even though, other approaches which denatured the HMSNs' surface with targeting and stimulus response agents seem to be better for not only enhance drug loading capacity and controlled drug release, but also improve the targeting ability, thereby increasing the therapeutic effect of the nanocarriers.

In this study, in order to produce a silica-based nanocarrier system for anti-cancer drug delivery, the thesis focused on synthesizing spherical HMSN particles with the desired size in the range of 100 nm. The mesoporous shell thickness and mesopore diameter of HMSNs would be controlled using different polymers in the

shell coating step to accommodate the delivery and release of therapeutic agents with different sizes. In addition, different pluronics and targeting agents would be modified on HMSNs' surface for the enhancement of their drug loading capacity, encapsulated drug storage ability, drug release controllability and targeting ability. From the above analysis, the thesis "*Structure-adjustable synthesis of hollow mesoporous silica nanoparticles and its surface modification for anti-cancer drug delivery*" would contribute to perfecting the drug carrier system based on HMSN.

Objectives of the thesis

Research on synthesis of hollow mesoporous nanostructured drug carrier materials based on silica (HMSN) with the size of about 100 nm, and controllabe thickness of mesoporous shell and mesopore diameter, along with surface modifications with Pluronics to improve the cancer treatment efficiency of the drug carrier system.

Main contents of the thesis

1. Synthesis of HMSN with a diameter of less than 100 nm.
2. Investigate the influence of molecular weight and concentration of polyethylene glycol (PEG) on the mesoporous shell thickness of HMSNs.
3. Investigate the influence of different non-ionic surfactants on the mesopore diameter of HMSNs.
4. Modify HMSNs' surface with different Pluronics, evaluate physico-chemical and biological properties of HMSN-Plu systems in the improvement of drug delivery and drug release control.
5. Investigate the encapsulation and release profiles for dual drugs of HMSN-Plu.
6. Evaluate cytotoxicity of HMSN, HMSN-P, HMSN-S and HMSN-Plu and cancer cell killing efficiency of drug loading HMSN-Plu.

The thesis was presented in seven parts including:

Chapter 1: Literature Review

Chapter 2: Materials and Experimental Methods

Chapter 3: A Modified Hard-Template Method for Hollow Mesoporous Silica Nanoparticles Synthesis with Suitable Particle Size and Shortened Synthetic Time

Chapter 4: Simply and Effectively Control the Shell Thickness of Hollow Mesoporous Silica Nanoparticles by Polyethylene Glycol for Drug Delivery Applications

Chapter 5: Non-ionic Surfactants as Co-Templates to Control the Mesopore Diameter of Hollow Mesoporous Silica Nanoparticles for Drug Delivery Applications

Chapter 6: Surface Modification of Hollow Mesoporous Silica Nanoparticles with Pluronics for Dual Drug Delivery

Conclusions and Future Perspectives

CHAPTER 1. LITERATURE REVIEW

1.1. Overview of cancer and cancer treatment

1.1.1. Overview of cancer

Cancer ranks as the leading cause of death and detrimental to life expectancy in every country in the world. According to the Global Cancer Registry (Globocan) in 2020, it is estimated that 19.3 million new cancer cases and nearly 10 million deaths caused by cancer. Female breast cancer has surpassed lung cancer to be the most commonly diagnosed cancer, with an estimated 2.3 million new cases accounting for 11.7%. This is followed by lung cancer (11.4%), colon cancer (10.0%), prostate (7.3%) and stomach (5.6%). Lung cancer remains the leading cause for cancer death, with an estimated 1.8 million deaths accounting for 18%, followed by colorectal cancer (9.4%), and liver cancer (8.3%), stomach (7.7%) and breast cancer in women (6.9%). The global cancer burden is forecasted to be 28.4 million cases by 2040, increase by 47% from 2020, which is dominated by the increase in developing countries (from 64% to 95%) compared to the figure for developed countries (from 32% to 56%). Therefore, it is crucial to build sustainable infrastructure for the dissemination of cancer prevention measures and the delivery of cancer care in developing countries for the global cancer control (Figure 1.1) [1].

In Vietnam, the most common cancers in male consist of liver, lung, stomach, colorectal, and prostate cancers (accounting for 65.8%). Meanwhile, common cancers in female include breast, lung, colorectal, stomach, and liver cancers (accounting for 59.4%). For both sexes, the most common cancers are liver, lung, breast, stomach and colorectal cancers. In 2020, Globocan announced that Vietnam ranked 91/185 in terms of new incidence and 50/185 in mortality rate per 100,000 people. The corresponding ranking in 2018 is 99/185 and 56/185 respectively. There is an estimated 182,563 new cases and 122,690 cancer deaths. For every 100,000 people, 159 people are newly diagnosed with cancer and 106 people die from cancer.

Thus, it can be seen that the figures for the new cases and the deaths of cancer in Vietnam are increasing rapidly.

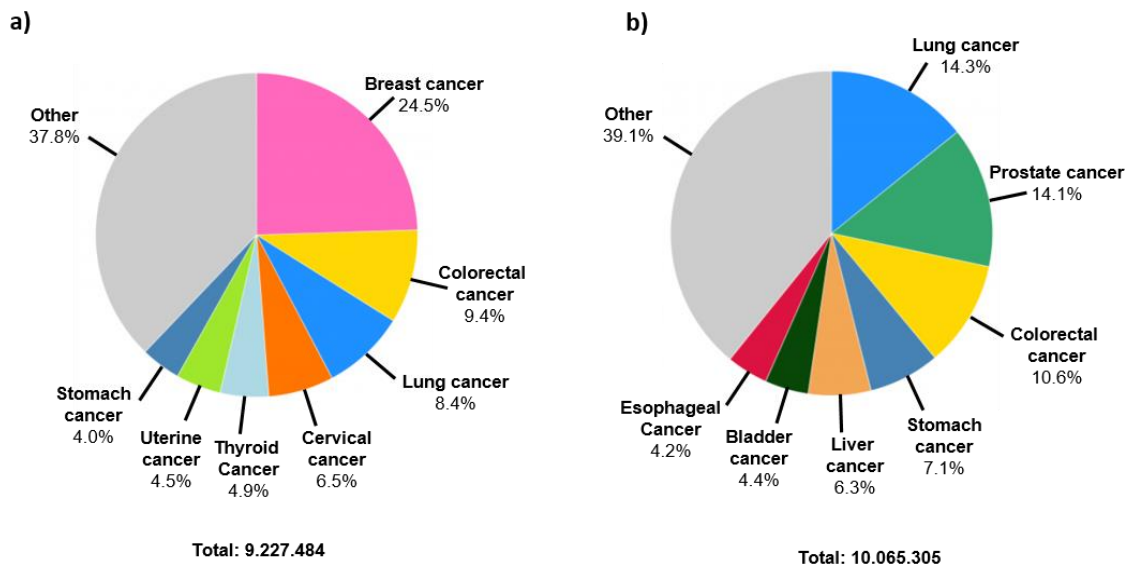


Figure 1.1. Global cancer data in 2020: a) Female, b) Male [1]

1.1.2. Common cancer treatment therapies

According to the US National Cancer Institute's Dictionary of Cancer Terms, a tumor is defined as an abnormal mass of tissue that occurs when cells divide more than normal or do not die. Tumors can be benign (non-cancerous), or malignant (cancerous). The main difference between benign and malignant tumors depends on their ability to detrimental affect other cells, tissues, and organs. Malignant tumors grow rapidly, enter the blood vessels and then spread into and invade other tissues and organs, this process is called metastasis. Cancer treatment has become difficult when the tumor metastasizes through different organs in the patient's body, and the possibility of recurrence after treatment. In contrast, benign tumors only form and do not spread to other tissues or organs. Therefore, these tumors can be removed, and no further treatment is required.

Cancer is caused by a series of gen mutations that change cell functions, in which proto-oncogenes are activated and tumor suppressor genes are inactivated. Proto-oncogenes include a group of genes that transform normal cells into cancer cells

when they are mutated. When proto-oncogenes' expression inappropriately rises, such genes turn into oncogenes. Proto-oncogenes encode proteins which involved in processes stimulate cell division, inhibit cell differentiation, and reduce apoptosis cell death. These processes (including stimulation of division, differentiation, and apoptosis) encourage normal human development and ensure the maintenance of tissues and organs. However, oncogenes that regulate the production of these proteins are elevated, induce cell division, reduce cell differentiation, and inhibit apoptosis cell death. All these effects induce the phenotype of the cancer cells. Thus, oncogenes are considered as potential molecular targets for anticancer drugs development

Cancer treatment depends on the type and origin of the cancer. Common cancer treatments include surgery, radiation therapy, immunotherapy, chemotherapy, and targeted therapy. In addition, there are some latest therapeutic approaches such as hormone therapy, stem cell transplantation and precision medicine (Figure 1.2) [2].

Hormone therapy has a strong association with breast cancer. Breast cancer was one of the first tumors found to be dependent on hormones (estrogens) and estrogen-lowering regulators. For example, tamoxifen, a selective estrogen receptor modulator (SERM), improved 10-year survival by 11% in patients with estrogen-positive cancer (ER+).

Non-metastatic solid tumors, such as skin tumors, can easily be treated by surgery. Surgery, compared with other treatments, is the only one with a cure rate close to 100% because all tumor cells are removed from the body and removed. However, surgery only applies to solid, non-metastatic tumors, and cannot be used for diffuse type such as blood cancer (leukemia). This is the most invasive method to treat cancer, but due to the removal of entire tumor tissue from the body, the risk of recurrence is low.

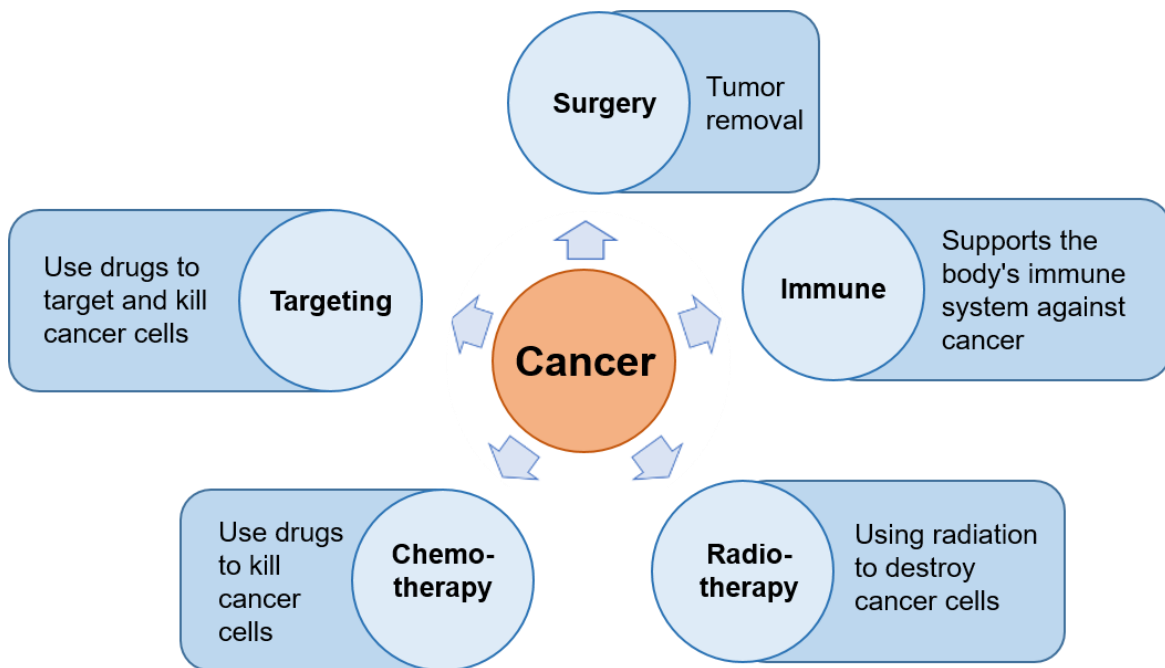


Figure 1.2. Common treatments for cancers [2]

For tumor tissues that metastasize to other tissues or organs, immunotherapy is used to utilize the body's immune system to defeat the cancer.

Radiation therapy uses doses of radiation to kill cancer cells and shrink tumors. With about 45% of new cancer cases receiving radiation therapy, it is mainly used for prostate, neck, breast, cervical and thyroid cancers because of their good accessibility. Due to the side effects consist of destruction of surrounding tissue, radiation therapy is often used with other cancer treatments.

The most prominent cancer treatment is chemotherapy. Small molecules are introduced into the stroma and exploited to destroy rapidly dividing cells. The drugs used in chemotherapy can be given by several methods such as oral, intravenous and other methods, making chemotherapy the least invasive cancer treatment available. However, this therapy causes some side effects, including killing healthy cells, fatigue and hair loss. Despite the severe side effects, chemotherapy can be used for all types of cancer with the highest success rate of treatment.

The latest cancer therapy is targeted therapy. Cancer cells are identified by several specific properties. Targeted therapy uses drugs that target these properties, resulting in less damage to surrounding healthy tissue and thus fewer side effects.

As can be seen, the priorities in cancer research are finding new drugs that are more effective against cancer cells or developing and improving drug delivery systems to reduce the effects side effects on healthy cells and increase the effectiveness of drugs against cancer cells.

1.2. Nanomaterials in cancer treatment

1.2.1. Nanomaterials in anti-cancer drug delivery applications

In the effort to develop drug delivery systems, nanotechnology has been explored as one of the main platforms and nanomaterials used as drug delivery agents are often referred to as nanomedicines. Nanomaterials can be defined as materials that are between 1 and 100 nanometers in size. However, nanodrugs' diameter can be up to several hundred nanometers. Nanodrugs were first developed in the early 1960s with liposomes served the function as carriers. Since then, different carriers have been developed to enhance the effectiveness of the treatment.

One of the advantages of nanodrugs is their ability to passively accumulate in solid tumor tissue due to their Enhanced Permeability and Retention (EPR) effects. In most healthy tissues, the size of the gaps in the endothelial lining is usually less than 2 nm. Meanwhile, since the growth of tumor requires angiogenesis, new blood vessels are formed near the tumor with sizes ranging from 100 to 800 nm [3-5]. Therefore, some free drug molecules can penetrate the endothelial gaps and be toxic to healthy cells. In contrast, drug-carrying nanosystems are large enough that they cannot penetrate the endothelial gaps of healthy cells but can easily penetrate tumor tissues, concentrating in the intercellular fluid surrounding the cancer cells and exert therapeutic effects on these cells.

Various nanomaterials have been researched and developed for drug delivery applications. Figure 1.3 presents the schematic diagram of different types of nano-carriers with diferente sizes commonly used in drug delivery, including inorganic nano-carriers (gold nanoparticles, mesoporous silica, carbon nanotubes, calcium phosphate), polymer nano-carriers (nano gels, solid lipid nanoparticles, micelles, dendrimers) and vesicular carriers (liposomes, nisosomes) [6].

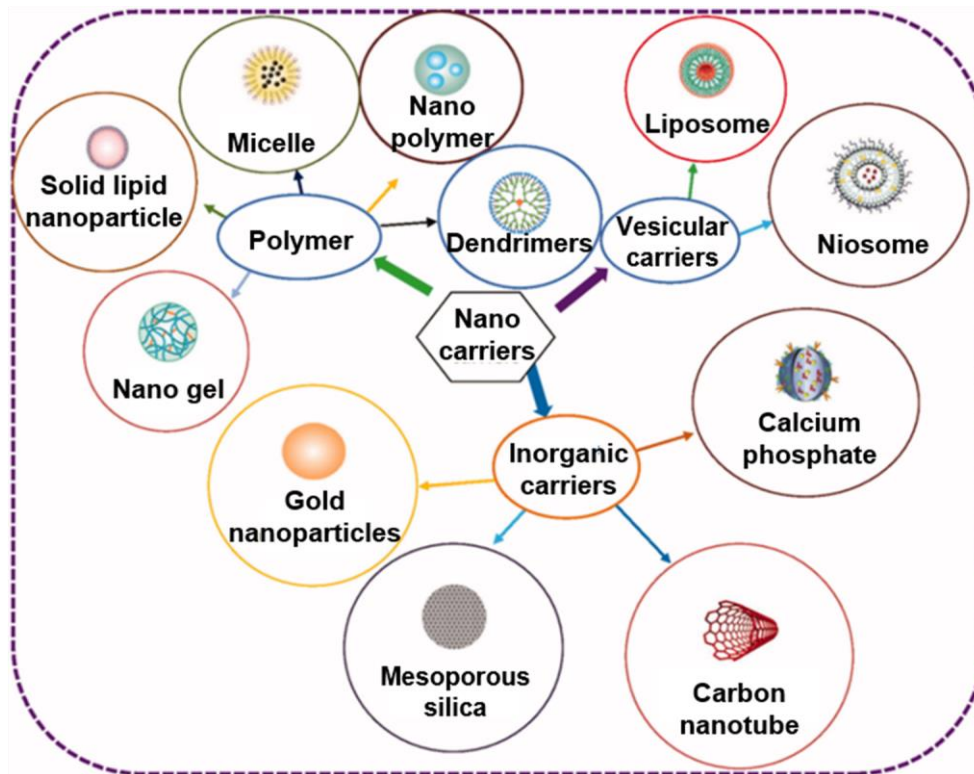


Figure 1.3. Popular nanomaterials applied in drug delivery [6]

1.2.2. Silica nanomaterials in anti-cancer drug delivery applications

One of the common inorganic materials in the development of chemotherapeutic agents delivery systems is silica nanoparticles, especially MSN. Silica nanoparticles are the amorphous white powder, composed of siloxane groups ($\text{Si} - \text{O} - \text{Si}$) inside and silanol groups ($\text{Si} - \text{OH}$) on the surface [7]. Meanwhile, MSN can be defined as silica nanoparticles containing pores with diameters from 2 to 50 nm.

The first mesoporous silica material, M41S, was discovered in 1990s by a researcher from the Mobil Oil company. The M41S family has three main members, Mobil Composition of Matter No. 41 (MCM-41), Mobil Composition of Matter No. 48 (MCM-48) and Mobil Composition of Matter No. 50 (MCM-50). They can be distinguished by their pore geometry, while MCM-41 has a hexagonal pore structure, MCM-48 has cubic shape and interwoven, continuous 3-D pore system, and MCM-50 has lamellar structure, consisting of silica sheets or porous aluminosilicate layers separated by surfactant layers (Figure 1.4). Among the three, MCM-41 is the most

widely studied because MCM-48 and MCM-50 are difficult to synthesize and thermally unstable.

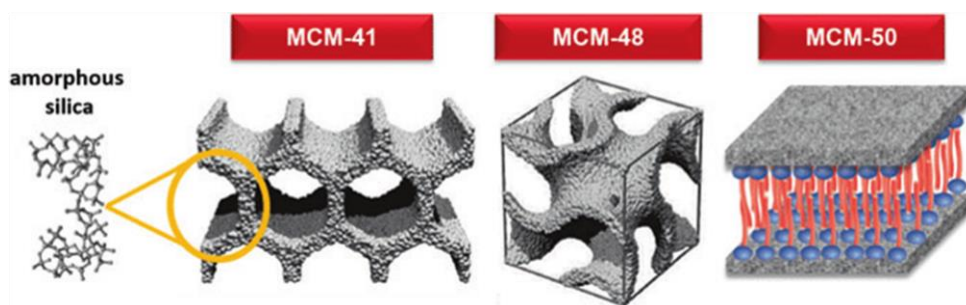


Figure 1.4. Members of the M41S family [8]

Due to the flexibility in synthesis, many different types of MSN have been developed. According to structure, MSN can be classified into conventional mesoporous particles, hollow mesoporous silica nanoparticles, core-shell mesoporous silica nanoparticles and yolk-shell mesoporous silica nanoparticles (Figure 1.5) [9].

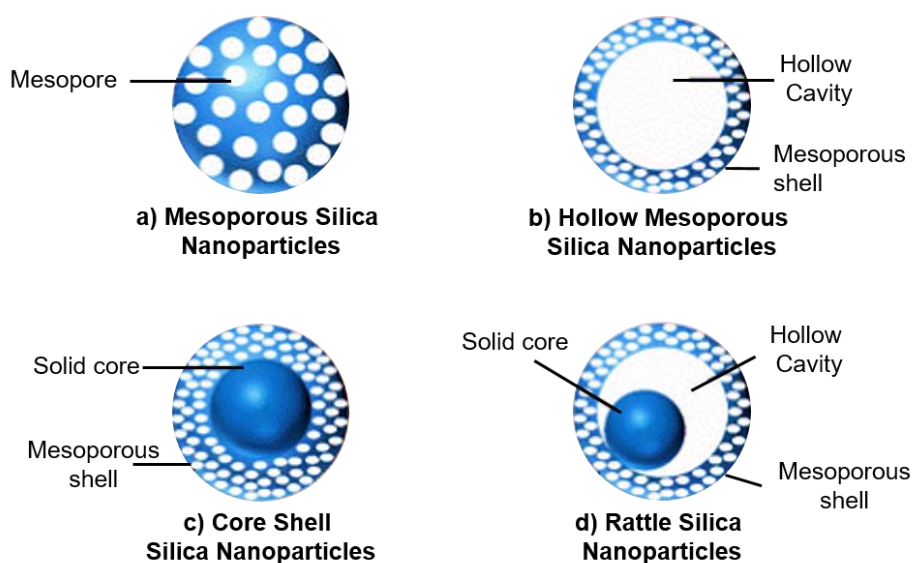


Figure 1.5. Structural classification of Mesoporous Silica Nanoparticles [9]

In 2001, MSN was first successfully applied as an ibuprofen carrier by Vallet-Regi and colleagues. The FDA (Food and Drug Administration) has recognized silica as "generally recognized as safe" (GRAS) for more than 50 years and it has been

used in pharmaceutical formulations as an excipient. The most promising development is when silica nanoparticles as imaging agents have been approved by the FDA for clinical trials in humans. This advance offers the hope that MSNs as drug delivery agents can be applied in clinical practice.

The popularity of MSN in drug delivery system development is due to its uncomplicated synthesis; particle morphology, particles size, and pore diameter can be adjusted through synthesis, particles' surface and pores' surface can be easily modified with functional groups, the porous structure of MSN can improve the loading capacity for poorly soluble drugs, and silica has been shown to protect the drug from enzymatic degradation [10, 11]. In particular, the pore diameter can be adjusted through synthesis making MSN selectively loaded with drugs. Finally, MSNs were well tolerated *in vitro* (at doses <100 µg/mL) [12-14] and *in vivo* (at doses <200 mg/kg) [13], their good compatibility has also been proven. Biocompatibility is considered as outstanding advantages of silica nanoparticles in drug delivery applications [15, 16].

Being a member of MSN family, HMSN, with a large cavity inside each particle, not only possess the advantages of MSN, but also show better drug loading capacity compared to the original non-hollow particles [17-20]. As the result of this, more and more research has been focused on the application of HMSN-based systems in drug delivery.

1.3. Recent progress of nano silica particle applications in drug delivery

1.3.1. International research

Since the first introduction of MSN as drug delivery systems in 2001, many scientists have attempted to improve the effectiveness of MSN in drug delivery. The number of studies on MSN drug-carrying applications has been constantly increasing [21], indicating that MSNs have always been attractive materials.

MSNs with adjustable shapes (sphere, rod, oval), particle size (from 20 to 50 nm) and pore size (from 2 to 6 nm) were successfully synthesized, mainly using sol-gel methods [22]. For example, Ya-Dong *et al.* reported the control of MSN particle size

using Taguchi statistical design method. The pH value, reaction time and silica precursor concentration were investigated. Results have shown that pH value of the reaction solution strongly effected the particle size as compared to the other two factors [23]. Naiara *et al.* synthesized MSN from Tetraethyl orthosilicate (TEOS) and Cetrimonium bromide (CTAB) as silica precursor and pore template, respectively. The particle morphology varied from spheres to rods increasing particle porosity in the presence of CTAB [24]. Kusum *et al.* prepared MSN by the sol-gel method using hexane/decane as pore expanders. The pore size of the obtained MSN increased from 2.5 to 5.2 nm, which was able to effectively deliver anticancer drug gemcitabine [25].

In addition, MSNs have been modified with a variety of ligands for better biocompatibility and effective delivery of different treating agents. For example, Chia-Hui *et al.* modified the surface of MSN with carboxylate groups via hydrazine bonds to improve the efficacy of Cisplatin in cancer treatment [26]. In another study, Anna and co-workers successfully modified the MSNs' pore walls with surface-hyperbranching polymerized poly(ethyleneimine) and used the obtained system as vectors for siRNA delivery [27]. Sahar *et al.* directly modified the surface of MSN with dielectric barrier discharge plasma in order to deliver Doxorubicin (DOX) in a dual-responsive behavior (pH and temperature) [28].

In 2004, the first hollow versions of MSN have been introduced. Zhu-Zhu *et al.* successfully prepared hollow porous silica nanoparticles via sol-gel method. CaCO_3 nanoparticles were used as the hard templates and Na_2SiO_3 was used as silica precursor. Brilliant Blue F was proved to be loaded in the hollow of the particles, resulting a better loading capacity and releasing controllability [29]. A similar approach was conducted by Jian-Feng *et al.* to fabricate porous hollow silica nanoparticles [30]. The hollow@shell structures of the particles in the two studies were illustrated by Transmission electron microscopy (TEM) images. Since then, a lot of research has been done to develop and create an ideal system based on HMSN for drug delivery.

1.3.2. National research

In recent years, research and development of silica nanomaterials has received much attention in Vietnam, including the research groups of Phan Bach Thang, Vong Binh Long and Nguyen Dai Hai.

The research group of Phan Bach Thang has successfully developed a biodegradable tetrasulfide-based organosilica nanomaterial BPMO (Biodegradable periodic mesoporous organosilica) for drug delivery applications in cancer treatment. The BPMO system was used to encapsulate daunorubicin (DNR) [31], reduced its size to enhance the loading efficiency of curcumin [32], and surface modified the surface to improve drug loading capacity and controlled release of cordycepin [33, 34].

Since 2014, Vong Binh Long has studied the synthesis of silica-containing redox nanoparticles (siRNP) for oral drug delivery and improved anti-inflammatory effects [35]. In 2017, the team continued to develop siRNPs loading BNS-22, a hydrophobic anti-cancer compound, with the ability to collect reactive oxygen species (ROS) to treat colitis-associated colorectal cancer [36]. In 2020, the team successfully developed siRNPs with a diameter of 50-60 nm to improve the bioavailability of silymarin (SM@siRNP). The results from the study indicated that SM@siRNP was a promising nanomedicine to enhance the anti-inflammatory activity of silymarin and had high potential in the treatment of inflammatory bowel disease [37].

Since 2013, the research team of Nguyen Dai Hai has taken the lead in researching and developing silica nanomaterials for biomedicine in Vietnam. The team successfully synthesized solid silica nanoparticles $dSiO_2$, then developed MSN and HMSN for anti-cancer drug delivery. The research team also successfully modified silica nanoparticles with active groups (amine) and polymers (PEG, heparin-PEG, chitosan-PEG and Pluronic F127) to increase the stability, improve drug capacity and drug release controllability of the carrier system [19, 38-44].

In this chapter, popular techniques in the synthesis and enhancement of HMSN for application in chemopreventive agents delivery were presented. The tunable properties of HMSNs, hybridized HMSNs and multidrug-carrying HMSNs was also

discussed. During the research and development of MSN carrier system, the achievements and the challenges were presented.

1.4. Hollow mesoporous silica nanoparticles (HMSN)

1.4.1. Structure of HMSN

As a member of MSN family, HMSN's structure consists of two main parts, the outer mesoporous shell and the inner hollow cavity (Figure 1.7). Therefore, beside the specific properties of MSN, HMSN exhibits excellent drug loading capacity thanks to the hollow cavity inside.

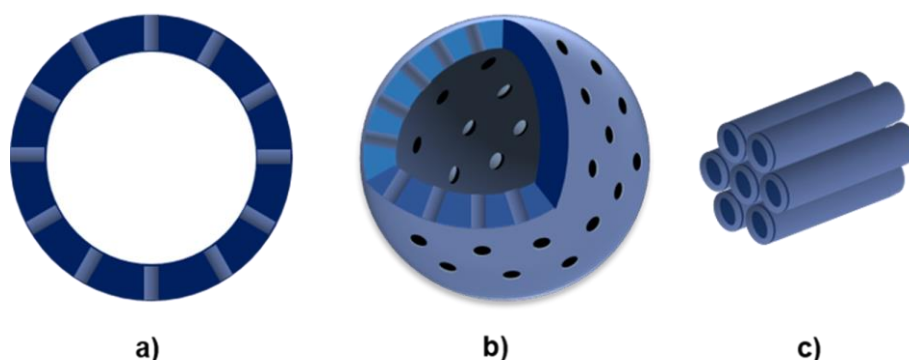


Figure 1.6. Structure of Hollow Mesoporous Silica Nanoparticle (HMSN): a) 2D radial section; b) 3D model; and c) Mesoporous structure of the shell

The template could be carbon nanoparticles, polystyrene nanoparticles, ferromagnetic nanoparticles, silica nanoparticles, After forming the shell, the template will be removed by physical methods or chemical methods to create the hollow cavity [45]. Meanwhile, the mesoporous shell covering the outside of the template is synthesized similar to synthesis procedure of MSN. The porous shell is made up of two main components, silica precursor and surfactant. The surfactant micelles act as the pore-template, the silica precursor is hydrolyzed and condensed on the template surface and around the micelles, forming the shell. The surfactant is then chemically or physically removed to form the shell with porous structure [46-48].

1.4.2. Synthesis methods of HMSN

HMSN synthesis followed a generally typical process:

- (1) Prepare the template;
- (2) Coating the shell over the template surface and thus creating a core@shell structure;
- (3) Remove the template to obtain a hollow structure.

Hollow mesoporous silica nanoparticle synthesis methods can be divided into three methods including hard template method, soft template method and self-template method (Figure 1.8). Accordingly, HMSN is classified into hard template HMSN, soft template HMSN and self-template HMSN.

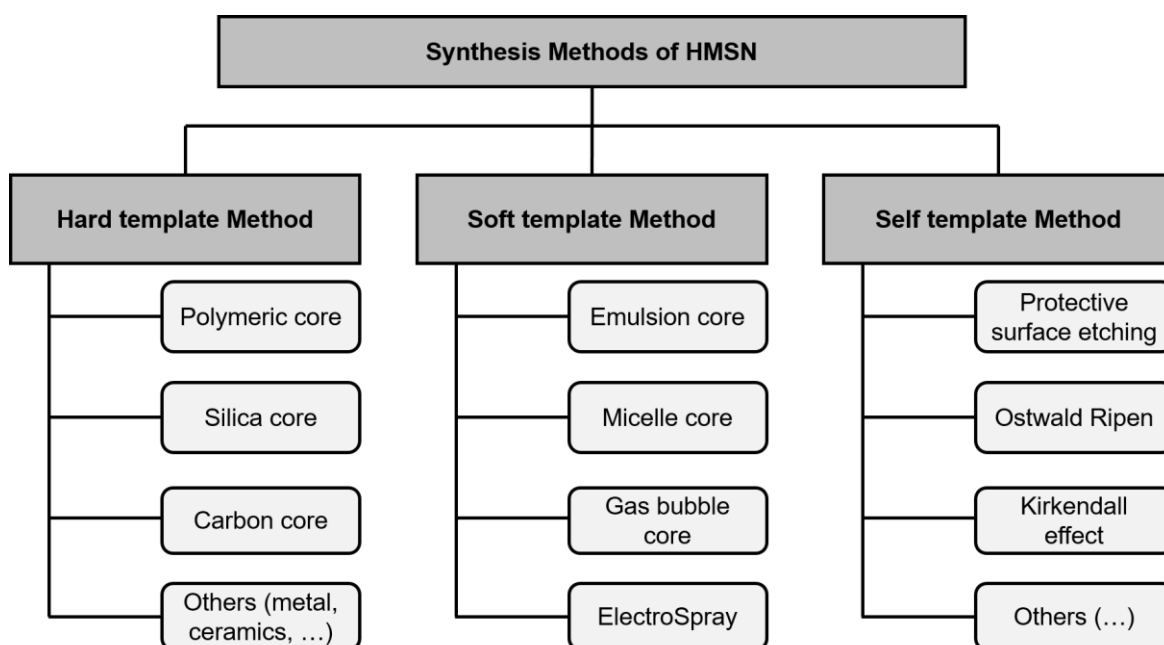


Figure 1.7. Synthesis methods of HMSN

1.4.2.1. Hard-template method

Hard-template HMSN is formed by using hard templates from inorganic compounds such as amorphous silica, metal carbonates, or polymers latex [49, 50]. The advantages of such type including the narrow size distribution, variety of sizes and configurations. When shell is formed on the template, the shape and size of the cavity are the same as the template used. Thus, the final morphology, structure and size of the particles after coating can be predicted. However, hard templates require

multi-step synthesis process as well as difficult thermal or chemical removal process, which is time-consuming and labor-intensive.

The synthesis of HMSN by hard template method consists of several main steps starting with forming a hard core compatible with the shell material, then creating mesoporous shell condensed on the core, and finally selectively removing the inner core to obtain HMSN.

Typical hard templates are inorganic compounds such as amorphous silica, metal carbonates, or polymers (latex) that can be chemically etched in the next step. Several methods, such as the sol-gel process, hydrothermal reaction, electrostatic assembly, and the chimie douce route have been used to agglomerate shell materials onto the surface of the template. Depending on the template and shell material, an additional surface modification step could be required to create compatibility between them. Template surface modification is usually chemical modification, which can improve compatibility with the shell by providing specific functional groups or by altering the charge distribution and template polarization, thereby efficiently condensing the shell material onto the template surface. To remove the template, the three main methods commonly used are chemical etching, heat treatment, or dissolution of the template in a suitable solvent based on the difference in composition between the template and the shell. Regardless of the approach, a reasonable choice of experimental conditions is necessary to prevent shell collapse during template removal process, by considering the properties of the hard template.

a) Hard template method based on polymer latex

Polymer latex particles are good option for the synthesis of HMSNs because they are uniform in size, and their size and surface properties can be easily adjusted during the synthesis. Polymer latex is also a common material, available and economical. After the silica shells are formed, they can be removed by heating or dissolving. Several types of latex polymers have been used as templates to synthesize HMSN such as polystyrene (PS), polyvinylpyrrolidone (PVP), poly (acrylic acid) (PAA), polymethylmethacrylate (PMMA).

b) Hard template method based on carbon and metal oxides

Unlike polymer latex templates, metal oxide and carbon templates have several advantages because they are polymorphic, organic solvents are not required during preparation, and surface properties are not needed to adjust prior to silica coating. Fuji *et al.* stated the ability to control the shape of hollow silica, using CaCO_3 as the template with various shapes such as cubes, rough surface spheres and rod-like particles. The internal size and shape of the synthesized hollow silica particles accurately reflect the outer size and shape of the template used [51].

c) Hard template method based on silica

Amorphous silica particles have been widely used as hard templates because they are available with high morphological uniformity and tunable particle size distribution at low cost. Typically, single-dispersed SiO_2 particles in the micrometer size range are synthesized by a classical sol-gel method (also known as Stöber's method) involving hydrolysis and condensation of silicon alkoxides in the mixture of water and alcohol and in the presence of a catalyst.

Homogeneous HMSNs could be synthesized from TEOS precursors by the silica-based hard-template method and etched by Na_2CO_3 through three main steps: (1) synthesis of homogenous dSiO_2 using the improved Stöber method; (2) synthesis of $\text{dSiO}_2@\text{MSN}$, in which cetyltrimethylammonium chloride (CTAC) is used as the porous template and triethanolamine (TEA) serves as the catalyst; (3) etching process to remove solid template of $\text{dSiO}_2@\text{MSN}$ with Na_2CO_3 and removed CTAC with 1% NaCl solution in methanol to obtain HMSN [52].

1.4.2.2. Soft template method

Soft template HMSNs are synthesized using liquid or gaseous soft templates such as emulsions, micelles and air bubbles [53, 54]. These soft templates help fill the template with dispersed functional groups or encapsulate guest molecules during shell formation process. However, it is more difficult, compared with hard-template HMSNs, to control the particle shape of soft-template HMSNs.

Using amphiphilic molecules containing both hydrophilic and hydrophobic part as templates for direct synthesis is known as the soft template method. This method is also known as the in situ template method because it takes only a short time to

prepare the soft template just before the silica coating process. In recent years, the soft template strategy has attracted researchers' attention due to the fact that the templates are relatively easy to prepare and remove. However, the hollow silica particles prepared by this method often have irregular shape and wide particle size distribution due to the malleability of the soft template.

a) Soft template method using emulsion

The emulsion method is one of the most classical soft-moulding methods and has a long history in the preparation of hollow silica. It is based on the formation of stabilized emulsion droplets by two or more incompatible solvents in the presence of a stabilizer. The dispersion of such immiscible liquids by the emulsification step leads to a dispersed phase and a continuous phase, where the boundary of the two phases is defined by an interface. Due to the low thermodynamic stability of these dispersions, amphiphilic molecules (surfactants) are used to reduce the interfacial tension. Depending on the composition of both phases, an emulsion can be defined as oil in water emulsion or water in oil emulsion. Similar to the hard template method, hydrolysis and condensation of the precursor occurs at the interface of the emulsion droplets to form a core@shell structure (emulsion@silica gel). Then, the soft templates are selectively removed and hollow silica spheres are formed.

Because of the agglomeration, it is difficult to obtain uniform droplets less than 100 nm in diameter by conventional emulsion methods. Meanwhile, the microemulsion method offers an advantage in producing homogeneous hollow silica spheres less than 100 nm in size because the microdroplets are thermodynamically stable and therefore being homogeneous [55].

b) Soft template using micelle

For the micelle soft template method, micelles can be formed by self-assembly of amphoteric molecules in a single-phase solvent. Self-assembly is occurred when the concentration of these molecules exceeds the critical micelle concentration (CMC). Through this method, hollow materials can be obtained by direct assembly of the precursors or through chemical interactions between the precursors molecular and the surface of the template. Similar to the emulsion method, depending on the

type of solvent, the micelle template can also be divided into water in oil or oil in water. Several reaction parameters can be investigated to prepare micelles/particles of variable shape, such as surfactant concentration, ionic strength, temperature, pH or chemical admixture.

Amphibian block copolymers can easily self-assemble into spherical, cylindrical micelles or many other shapes when the concentration is above CMC. One of the important examples is pluronic poly-(ethylene oxide)-poly(propylene oxide)-poly(ethylene oxide) (PEO-PPO-PEO). In aqueous solution, the hydrophobic PPO blocks will gather together as the micelle template, while the hydrophilic PEO blocks form a hydrated corona around the PPO. This template-corona-type structure formed from diblock-AB or triblock-ABA copolymers can be used as a soft template in hollow silica particle synthesis. Mandal *et al.* synthesized a family of hollow organosilica spherical particles and nanotubes using spherical and cylindrical micelles from Pluronic F127 and Pluronic P123 as the soft template, respectively. The internal cavity size of the obtained hollow silica particles is as small as 20 nm with a uniform cavity diameter [56].

c) Soft template using gaseous bubble

In the gaseous bubble soft template method, the dispersed air bubble in the liquid phase can be used as a soft template for the synthesis of hollow materials. This process involves the formation of bubble emulsions with subsequent deposition/adsorption of the precursor at the surface of the air bubbles. The template effect of the bubbles is affected by several parameters such as surface charge, particle size or hydrophilicity. Air-bubble emulsion systems can be obtained by several methods such as ultrasound, air blowing or chemical reaction [57].

1.4.2.3. Self template method

HMSNs can be synthesized directly by its self, independent of external template-generating agents, and thus the synthesis process is more concise. This method is often utilized to reduce production costs and facilitate large-scale synthesis. Several self-template methods can be used for direct synthesis of hollow structures including: surface protected etching, Ostwald ripening, Kirkendall effect, and ionic exchange

[49, 54]. In general, most of these methods are based on a two-step approach: (1) synthesis of a non-hollow material, (2) conversion of this material into a hollow structure. Direct synthesis (self-template) has several advantages over template-based synthesis, such as reproducibility and superior control over shell thickness and particle size distribution.

The self-template method is a process used to synthesize hollow silica nanoparticles without using another template. Several self-template methods that can be used for direct synthesis of hollow structures include: protective surface etching, Ostwald ripening, Kirkendall effect, and ionic exchange.

a) Protective surface etching

Surface protection etching is one of the popular self-template synthesis methods. The surface of the particles is covered with a protective layer that keeps the original particle size, while the sol-gel-derived porous structure allows etching agents to move inside and create cavity. This strategy allows fine control of the synthesis of complex hollow materials with enhanced catalytic performance [58].

b) Ostwald ripening method

For this method, the Ostwald ripening process in colloidal systems involves a heterogeneous structural change over time, that is the dissolution of small crystals or sol particles and the re-condensation of the sol particles these soluble fractions on the surface of larger crystals or sol particles. This thermodynamic process occurs because larger particles have an energetic advantage over smaller particles and increase the latter solubility. Under different experimental conditions for sol-forming particles in solution, many reversible chemical reactions take place on the solid/liquid boundary. Due to the variation in particle size, there is variation in the amount of solute. The uniformity of these concentration gradients will lead to complete dissolution of small particles and the growth of large particles, thereby forming voids as Ostwald ripening continues. This Ostwald ripening process is used under different conditions to synthesize hollow materials with variable shell thickness [59].

Through literature search on 3 different methods used to synthesize HMSN, the characteristics and limitations of each method group are summarized and presented in Table 1.1 below.

Table 1.1. Advantages and limitation of different HMSN synthesis methods

Method	Advantages	Limitations
Hard template	Particle morphology can be predicted Narrow size distribution, homogeneous particles' morphology Good control, high repeatability The most commonly used in synthesis of HMSN	The synthesis process is time consuming, going through many steps Hard templates are difficult to remove and require additional processing steps
Soft template	Simple technology The soft template is easy to prepare and remove	Irregular particle shape Wide particle size distribution The structure is less stable
Self template	The synthesis process is shortened because no template preparation is required The shell thickness and grain size can be controlled	There are few studies applied this method in synthesis of HMSN. More research data is required to verify the success and repeatability of the method

The hard template method shows advantages in terms of good synthesis control, predictable and uniform particles morphology, and highly reproducible results. This method has been verified for HMSN particles through many studies by scientists around the world. Department of Biomedical Materials - Institute of Applied Materials Science has succeeded in synthesizing HMSN by hard template method on SiO₂ template. The synthesis begins with the preparation of hard templates dSiO₂ spherical particles through the Stöber method with some modifications. In the second

step, a layer of mesoporous silica is coated on the surface of the SiO₂ particles using CTAB as the organic template. In the third step, the reaction solution was mixed with Na₂CO₃ solution to remove the sSiO₂ template, followed by CTAB removal by repeated washing with water to obtain HMSN particles [42].

From the above information, the silica-based hard-template method will be used to further study the synthesis of HMSN, in which the reaction mechanisms take place in each stage, including forming a hard template of silica, coating with silica mesoporous shell on the hard template surface, etching to remove the hard template to create a hollow mesoporous structure which will be presented in more detail in the next section.

1.4.3. Reaction mechanisms in the synthesis of HMSN by silica based hard-template method

1.4.3.1. Sol-gel process

The synthesis of dSiO₂ hard template or MSN porous shell was initiated by Stöber with the formation of single-dispersed spherical silica particles with sizes in the micrometer range. Stöber synthesis consists of four main components: water, base, alcohol and silica source. Particle dispersion is controlled through hydrolysis of alkyl silicates and subsequent condensation in the presence of alcohol [60]. To reduce the particle size to the nanometer range, various adjustments were made. The process of synthesis dSiO₂ hard template and MSN porous shell through the improved Stöber method (also known as the sol-gel method) is presented in Diagram 1.1.

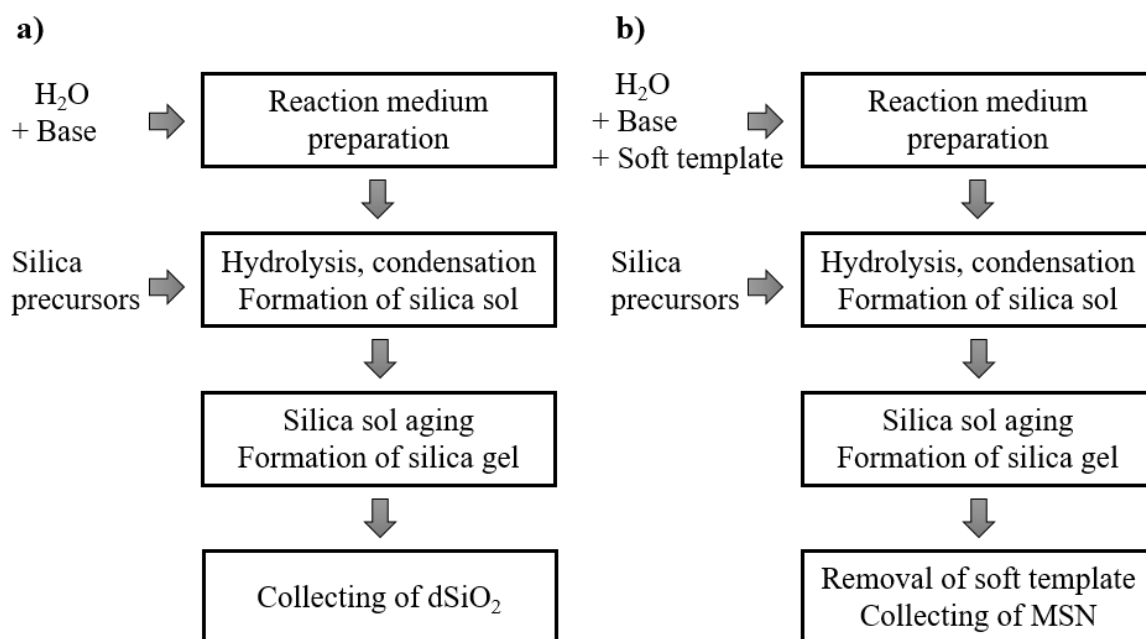


Diagram 1.1. Sol-Gel synthesis of a) hard template dSiO₂ and b) mesoporous shell MSN

The formation of silica particles from a metal alkoxide (Si(OR)₄) source such as TEOS in alcohol-water-ammonia medium can be described as follows: initially, ammonia and alcohol are added to the water reaction mixture. In particular, ammonia creates a base environment that catalyzes the hydrolysis and condensation of TEOS precursors, and alcohol helps to increase the solubility of TEOS and control the rate of hydrolysis. When TEOS is added to the mixture, TEOS molecules in a basic medium will be hydrolyzed to form silanol groups, followed by polymerization and agglomeration between the silanol groups or between the silanol groups and the epoxy group which produced siloxane bridges (Si – O – Si) (Figure 1.9) [61].

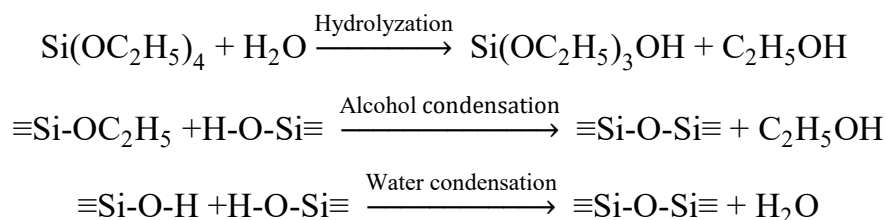


Figure 1.8. Hydrolysis and condensation of TEOS precursors in alcohol-water-ammonia medium

Silica particle growth can be explained by the multi-stage SFB method (Stober-Fink-Bohn), including nucleation stage, growth stage and shell development stage (Figure 1.10) [62].

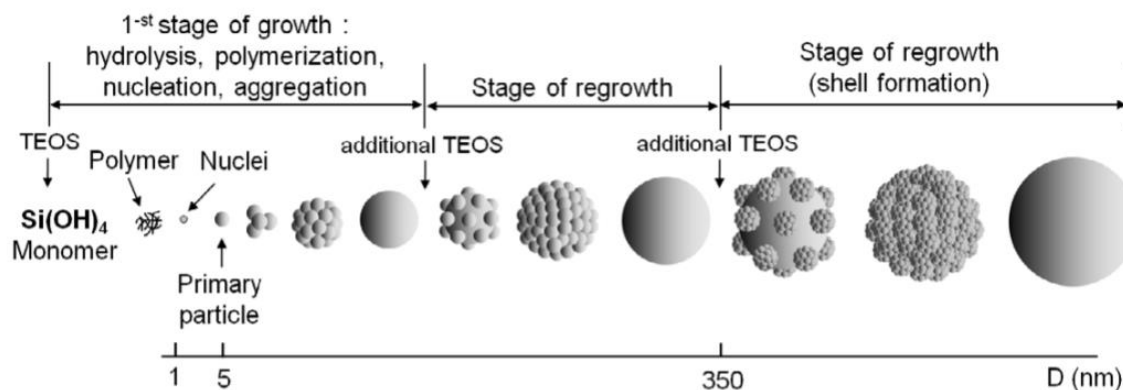


Figure 1.9. Multistage growth diagram of silica particles by hydrolysis of TEOS in alcohol-water-ammonia medium [62]

Grun *et al.* modified the Stober method by using additional surfactants to synthesize porous silica particles. Accordingly, the generated MSN has a spherical shape with MCM-41 properties [63]. Porosity patterning agents are usually cationic surfactants such as CTAB, CTAC or uncharged surfactants such as pluronics, PEG. Surfactants at higher concentrations than their CMC will form tubular micelles with the hydrophilic end facing outwards and the lipophilic end facing inward. In the reaction mixture with the presence of a positively charged CTAB surfactant micelle and a negatively charged dSiO₂ hard template, these micelles will link on the surface of the hard template by electrostatic attraction. When precursors are added to the reaction mixture, they are hydrolyzed and the siloxane bridges will condense around the CATB micelles to gradually form an entire mesoporous shell surrounding the hard template. The formation mechanism of MSN mesoporous shell is described in Figure 1.11 [18].

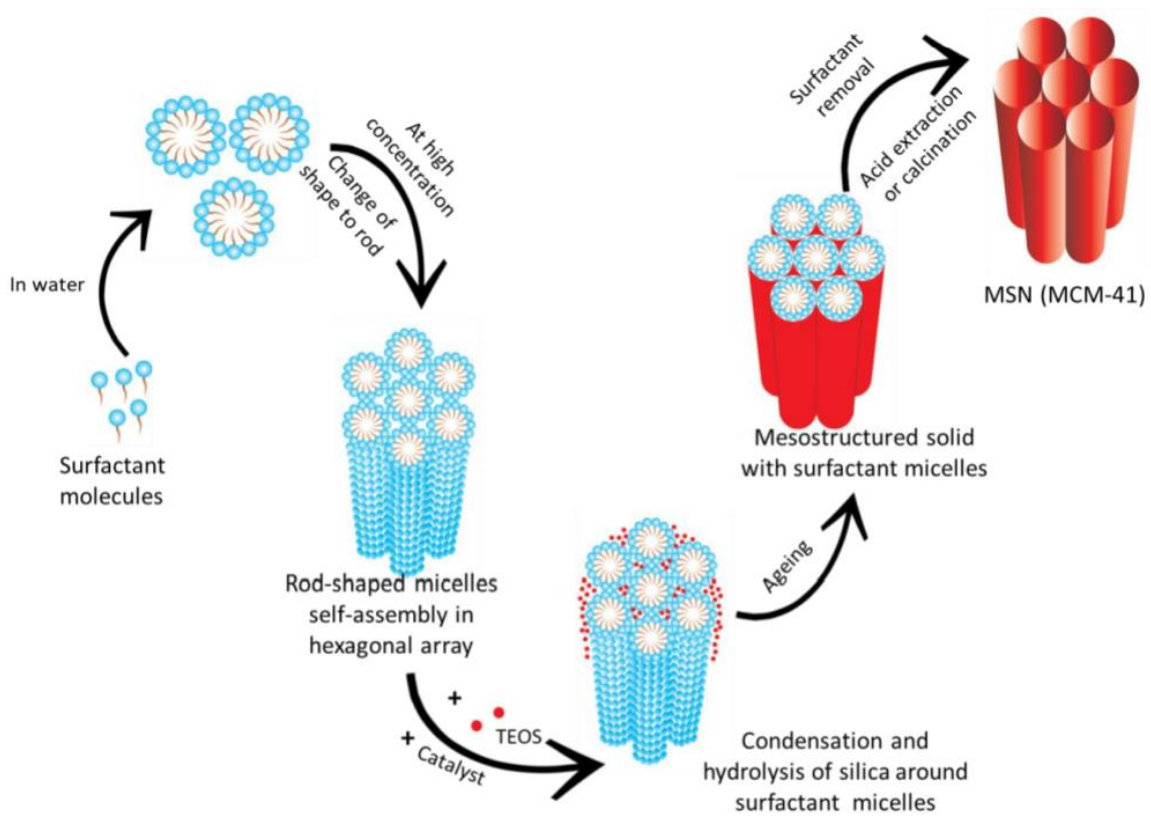


Figure 1.10. Illustration of the formation mechanism of the mesoporous shell (MCM-41) [18]

1.4.3.2. Etching of hard template and the role of CTAB in etching process

The hard template of the core@shell structure is etched using an alkaline etching agent in aqueous medium (Na_2CO_3). The etching process will occur through 2 stages (Figure 1.12).

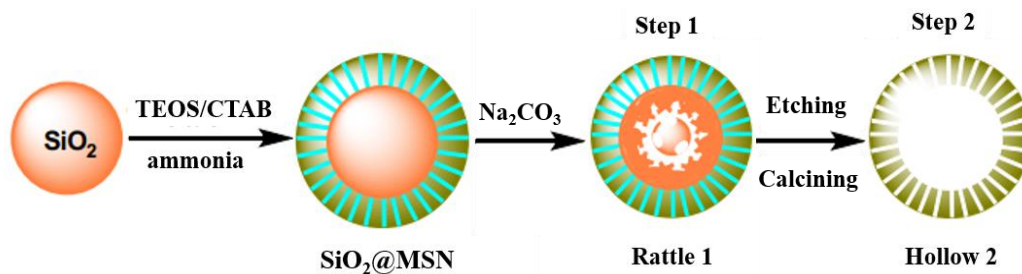


Figure 1.11. Etching process of hard template dSiO_2 by Na_2CO_3 [64]

Etching will begin when the water-soluble alkaline etching agent approaches the region near the template surface and the etching reaction occurs that forms rattle balls with a double shell structure (Rattle 1). Then the etching process will expand on both sides to continue to demolish the inner shell and rattles parts (both are belong to hard templates), forming a hollow structure (Hollow 2) [64].

The role of CTAB in the pores is illustrated in Figure 1.13. During the porous shell coating process, the tubular micelles of CTAB with outward-facing hydrophilic ends and inward-facing hydrophobic tails bond to the template surface. After hydrolysis and deposition of TEOS on the surface of the hard silica template as well as around the CTAB micelles, capillary mesopores are formed. At this time, CTAB presencing in the pores forms hydrophobic pore walls. Therefore, the etching agent will first pass through these capillary channels and the inner template will be etching first without appreciable effect on the porous silica shell.

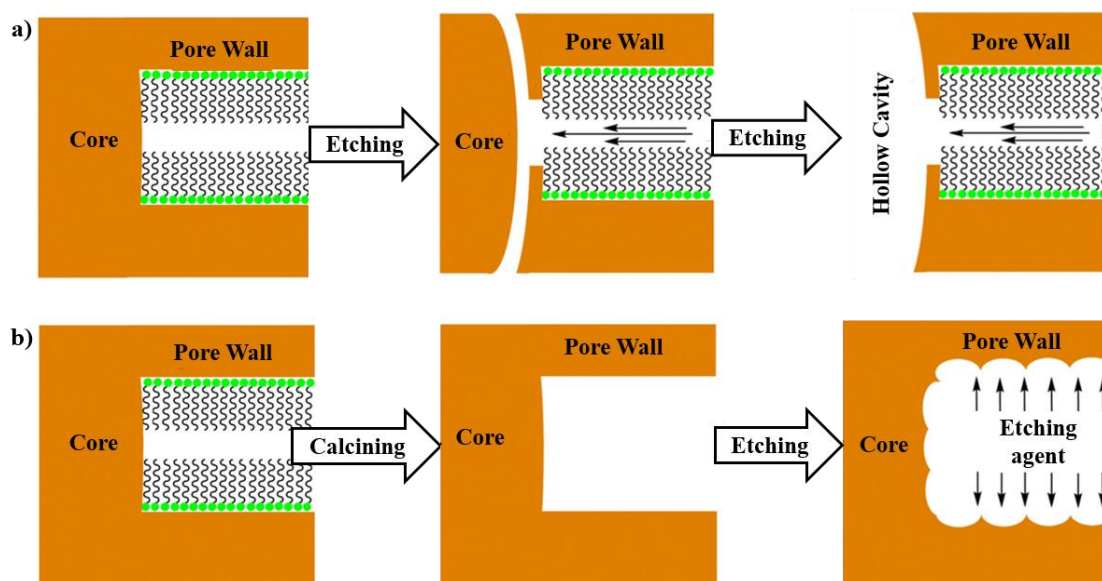


Figure 1.12. Etching mechanism of hard template dSiO₂ to form HMSN by Na₂CO₃: a) Etching process with the presence of CTAB micelles, and b) Etching process without CTAB micelles [64]

After the hard template is completely etching, the CTAB in the capillary tubes can be removed by calcination or washing, forming HMSN particles with a hollow template and porous shell structure (Figure 1.13a). In contrast, if CTAB in the

capillary channels is removed first, then the etching agents not only directly contact with the surface of the hard template, but also directly contact with the surface of the capillary channels. As a result, both the capillary channels wall and template surface are etched, where the porous shell with many capillary tubes carrying the etching agent will collapse more rapidly (Figure 1.13b) [64].

1.4.4. Modular factors in HMSN fabrication

One of the outstanding advantages of HMSN, making them versatile and potential in biomedical applications is their feasibility and ease of tuning. The three most commonly adjustable properties of HMSNs are particle size, cavity volume, porous shell thickness, and pore diameter (Figure 1.14).

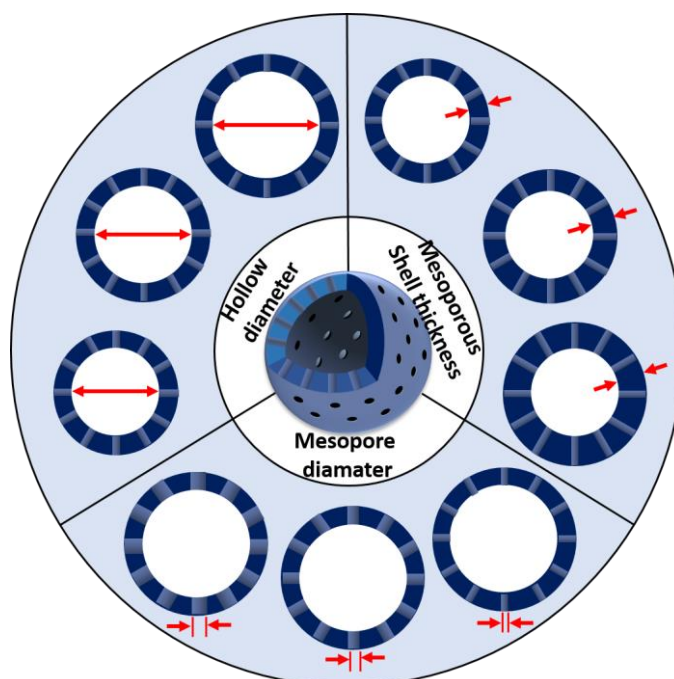


Figure 1.13. Modular factors of the HMSN

1.4.4.1. HMSN particle size and hollow cavity volume

HMSN particle size is one of the most important characteristics that need to be considered in synthesis process for drug delivery applications. It has been shown that particles with a diameter less than 10 nm tend to be rapidly eliminated by the kidneys, meanwhile particles 200 nm or larger tend to be removed from circulation quicker

[65]. There have been several reports about the successful synthesis of spherical HMSN with diameter around 134 to 150 nm [40, 52]. However, 100 nm nanoparticles exhibited the greatest uptake compared to larger diameter particles [66]. Therefore, the optimum size for HMSN should be nearly 100 nm. At this size, HMSN could not only load a sufficient amount of drug, but also prolong the circulation time during the administration.

In addition, it can be said that the hollow cavity of HMSN is the place to store the drug and the pores are the ways to help drugs released from the hollow cavity to the outside environment. Thus, adjusting the cavity volume will directly affect the drug loading capacity of HMSN. Based on the synthesis method presented in the previous section, the cavity volume of HMSN synthesized by the hard template method can be controlled through adjusting the size of the hard template (dSiO₂). There are different approaches to control dSiO₂ particle size, which mainly focused on the parameters in the sol-gel reaction and were well investigated by Nguyen Thi Ngoc Tram. The factors affecting the size of dSiO₂ were determined as: (1) concentration of silica precursors, (2) concentration of ethanol, (3) concentration of ammonia, (4) reaction time, and (5) reaction temperature. Based on these survey results, a parameter adjustment in the synthesis of dSiO₂ particles was made to reduce dSiO₂ size, thereby indirectly reducing the HMSN size to the desired size.

Furthermore, besides the well-known advantages of the hard-template synthesis method, time consuming is one of its drawbacks that need to be improved. For example, HMSN was prepared with the published hard-template method in about 21 hours for the main reactions (6 hours for dSiO₂ preparation, 6 hours for dSiO₂@MSN preparation and 9 hours for dSiO₂ etching) [42, 67]. Therefore, a modified method shortening the synthetic time would be meaningful for scientists who study on silica nanoparticles as well as for industrial scale production.

Interestingly, Feng *et al.* have published a hard-template method for HMSN synthesis with the main reaction time shortened to only 3 hours [52]. The hard template dSiO₂ with a diameter of 100 nm was prepared in 1 hour, the core@shell

structure dSiO₂@MSN was prepared in 1 hour more, and the etching step was conducted in 30 minutes to obtain the HMSN particles with a diameter of 150 nm. This publication is an important reference in modifying the synthesis process to shorten the HMSN synthetic time in the current doctoral thesis.

From the above reviews, a modified synthesis process is proposed with the expectation to generate HMSN particles with size less than 100 nm in a shorter time, including: (1) synthesis of dSiO₂ according to the adjusted process surveyed by Nguyen Thi Ngoc Tram [42, 67], (2) create core@shell structure dSiO₂@MSN according to Feng's published process [52], and (3) hard template etching to obtain HMSN according to Feng's published process [52]. The methods used to carry out this study are described in detail in Chapter 2 and the corresponding results are presented in Chapter 3.

1.4.4.2. Mesoporous shell thickness

a) Research status of controlling mesoporous shell thickness of MSN

The mesoporous shell thickness has been reported to be one of the main factors affecting the drug release profile of HMSN particles. Therefore, modulating the mesoporous shell thickness is a potential approach to be able to fabricate HMSN materials with desired drug release profiles [68, 69]. Basically, the adjustment of mesoporous shell thickness is similar to the control of diameters of dSiO₂ and MSN particles through the reaction parameters during the sol-gel process.

D. Deepika *et al.* synthesized hollow template – mesoporous shell silica nanoparticles with size of 230 ± 30 nm based on soft templates of PS (150 ± 20 nm) (Figure 1.15). The mesoporous shell was synthesized by the sol-gel method, using CTAB as a structural guide for the shell. The results showed that the meso porous shell thickness could be adjusted from 15 to 30 nm through adjusting the concentration of silica precursor TEOS [70].

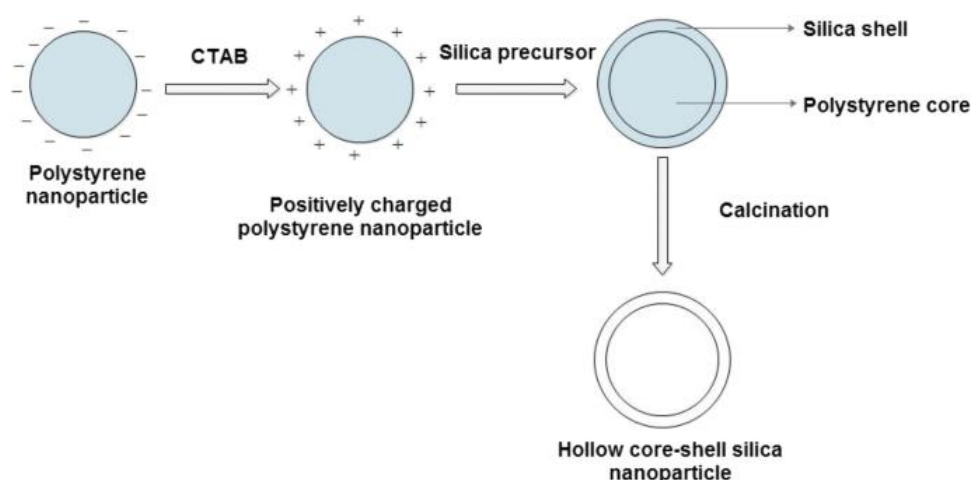


Figure 1.14. Adjustable shell thickness of microporous hollow core@shell silica nanoparticles for controlled release of doxorubicin [70]

The size of MSN particles was controlled by varying the amount of TEA, where a decrease in the amount of TEA resulted in a decrease in the MSN particle diameter [71, 72]. Yismaw and colleagues studied the effect of the catalyst by comparing MSNs generated using ammonia and TEA. MSN particles synthesized using ammonia have a larger diameter than TEA synthesis. This suggested that TEA acted as both a catalyst and a grain growth control additive [73].

Mai Ngoc Xuan Dat and his co-workers reduced the particle diameter of a biodegradable periodic mesoporous organosilica (PMO) called E4S through adjusting the amounts of the alkaline catalyst. E4S particle size decreased to less than 50 nm (Figure 1.16) [74].

The particle size of MSN can also be controlled using particle growth inhibitors. Pluronic P123 was added to the reaction solution as a growth inhibitor. By increasing its concentration from 0 to 0.1 mol, the MSNs particle size decreased from 200 nm to 40 nm [75]. The synthetic temperature also affects the particle size of MSNs, where larger particles were produced at higher synthetic temperatures [76].

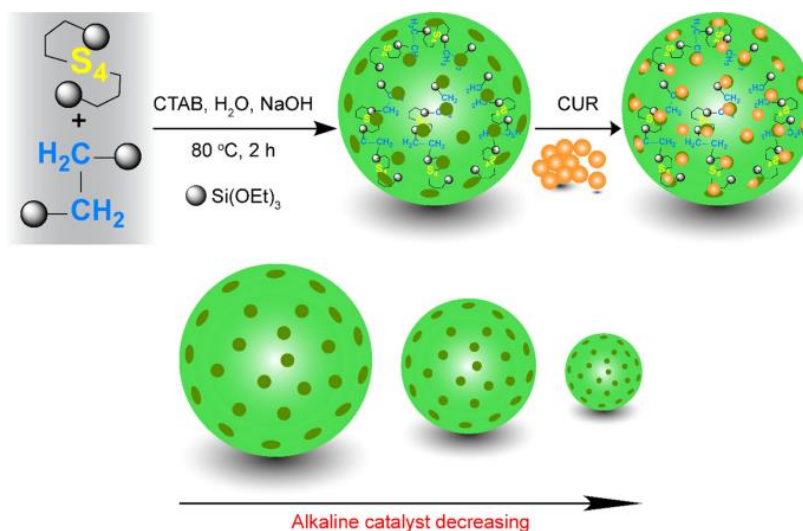


Figure 1.15. The size of biodegradable silica nanoparticles was reduced for efficient curcumin loading [74]

In general, there are approaches that have been used to control the particle size of HMSN such as varying the concentration of synthesis components (silica precursors and catalysts), changing reaction conditions (temperature, pH), and addition of dispersing agents or capping agents [70, 73, 75, 76]. Among these, capping agents seems to be a simple and effective method where molecules are added into the synthesis mixture to absorb selectively onto particles' surface, decrease the particle surface energy and consequently promote the growth of the particles [77].

b) Polyethylene Glycol (PEG) as a dispersant in nanoparticle synthesis

PEG is a synthetic polyether compound with the structural formula $H-(O-CH_2-CH_2)_n-OH$. PEG is colorless, inert, odorless and non-volatile, and can dissolve extremely well in water and organic solvents such as benzene, carbon tetrachloride and chloroform. Thanks to its good biocompatibility, hydrophilicity and rapid degradability, PEG has been commonly used as a capping agent in colloidal syntheses to control the size of nanoparticles [78-81].

PEG molecular weight and concentration were reported to have a complex effect on the nanoparticle synthesis [82]. For example, Francesco *et al.* used PEG 600 as a shape and size control agent of SrTiO₃ particles synthesized by hydrothermal method

(Figure 1.17). The study showed that PEG 600 had a great influence on the morphology of SrTiO₃ crystals, which changed both shape and size, depending on its concentration during hydrothermal synthesis. A low amount (5g) facilitates the growth of large particles with sizes above 800 nm and a clear cubic shape. As the PEG concentration increased (10 g and 20 g), the crystals decreased in size to 570 and 175 nm, respectively, and a linear dependence of size was observed on the PEG 600 concentration [83]. In another study, Miao Yu and co-workers successfully synthesized finely dispersed Mg(OH)₂ nanoparticles by direct precipitation method using PEG 6000 as a dispersant with the optimum concentration of 1.5 g/mol [84].

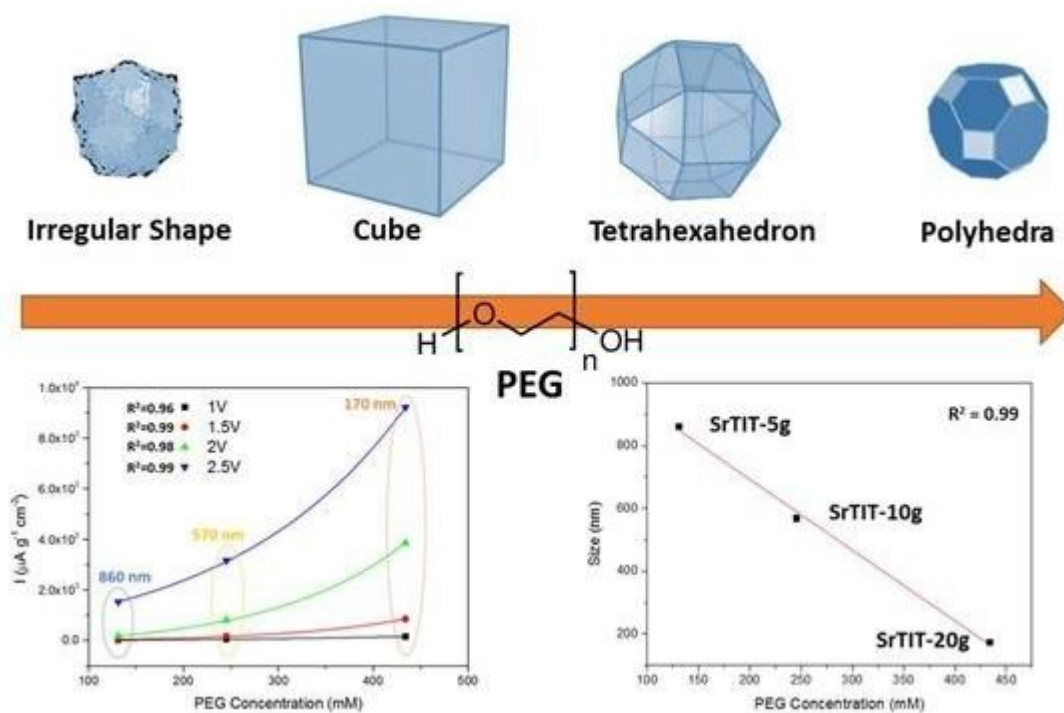


Figure 1.16. The effect of polyethylene glycol on shape and size of SrTiO₃ nanoparticles [83]

Dispersibility and stability of nanoparticles are also related to the molecular weight (corresponding to different lengths of the molecular chain) of PEG. For example, Li Chao *et al.* investigated the effect of PEG on the stability of nano SiO₂ particles in aqueous suspension by settling experiment, a well dispersed solution was obtained by adding a mixture of high molecular weight PEG and low molecular

weight PEG, as a complete and dense adsorption layer has been formed on the surface of the nanoparticles [85]. Vidyasagar *et al.* prepared ZnO powder by solid mechanical method in the presence of PEG 400. The study showed the size, structure, crystallinity and to some extent morphology of the nanoparticles. ZnO depends on the nature of the surfactant used. PEG 400 helped to improve the crystallinity and increase the particle size of ZnO powder [78].

For silica nanoparticles, PEG also have been initially employed to create particles with optimum size and good dispersion. Li Chao *et al.* studied the effect of PEG on the stability of silica nanoparticles in aqueous suspension by settling experiment. A well dispersed solution was obtained by adding a mixture of high molecular weight PEG and low molecular weight PEG because a complete and dense adsorption layer was formed on the surface of the nanoparticles [85]. Chapa-González and co-workers reported that the presence of PEG 400 and fixed PEG/Na₂SiO₃ ratio of 2:1(w/w) in the synthesis of silica nanoparticles from Na₂SiO₃ reduced the particle size and narrowed the size distribution of the obtained silica nanoparticles [86].

Although there have been studies using PEG as capping agents in silica nanoparticle synthesis to control the particle size, the number of these studies is very limited. Moreover, PEG molecular weight and concentration were usually fixed in each study. Importantly, to the best of the author knowledge, there has been no publication on the use of PEG to control the shell thickness of HMSN. Therefore, the research direction which uses PEG as a particle size controller in silica nanoparticle synthesis still has great deal of work.

Through the above literature review, it can be seen that a complete and systematic study on the influence of molecular weight and concentration of PEG on the mesoporous shell thickness of HMSN particles will contribute scientific and practical significance, providing more reference information for the desired processing of mesoporous silica nanomaterials. The methods used to carry out this study are described in detail in Chapter 2 and the corresponding results are presented in Chapter 4.

1.4.4.3. Mesopore diameter

a) Research status of controlling mesopore diameter of MSN

To be able to encapsulate desired agents with different molecular size such as drugs, nucleic acids, polysaccharides and proteins ... into the hollow cavity, the control of HMSN's meso-channel diameter is one of the pioneering and decisive factors [65, 87-91]. Generally, synthesized MSN particles have a pore size of 2–3 nm, which is sufficient to transport through and carry small molecules [92]. However, this pore diameter cannot be applied for larger molecules (> 1000 Dalton), thus limiting the applications of MSNs in general and HMSNs in particular in drug delivery field. Therefore, researchers have been devoting their efforts to enlarge the pore diameter of these nanoparticles. Basically, the pore diameter of MSN can be controlled by varying the synthesis parameters.

Xiaoyu Hong *et al.* reported that the pore size could be adjusted by varying the concentration of TEOS in cyclohexane, and they controlled to obtain MSNs with pore sizes from 7.8 nm to 12.9 nm [87]. In another study by Yongju He *et al.*, MSNs with larger diameter pores were obtained by varying the ratio of n-octadecyltrimethoxysilane (C18TMS)/TEOS or the ethanol/water volume ratio in the water-ethanol-ammonia system. In which, C18TMS serves as the structure-directing agent, TEOS as the silica precursors, ammonia as the catalyst, EtOH and H₂O as the solvents. The results show that the synthesized MSN has a spherical shape with a diameter ranging from 100 to 200 nm, and the pore size of MSN can be easily adjusted from 2.4 to 6.5 nm by changing the ratio. Molar ratio C18TMS/TEOS from 0.32 to 0.74 and volume ratio ethanol/water from 3.6 to 7.5 [93].

Interestingly, the diameter of mesopores is dependent on its template size, therefore, it is possible to control the MSN's pore size by adjusting the diameter of the soft template micelles. CTAB is the most commonly positively charged surfactant used as a soft template for meso-channels in MSN synthesis [94, 95] [40]. Therefore, using another surfactant to form a mixed micelle with CTAB whose larger

micelle diameter and then use this mixed micelle as a porous template in MSN synthesis could be a potential approach to control the mesopore size.

b) Mixed micelles of CTAB as controller of MSN's mesopores

As previously mentioned, using a mixed micelle of CTAB with another surfactant to increase the mixed micelle diameter, and then using this mixed micelle as a porous template in MSN synthesis could be a potentially alternative approach to tune the pore diameter of HMSN. With this idea, Xianbin Liu *et al.* reported a method to synthesize Santa Barbara Amorphous-15 (SBA-15) silica nanoparticles with large pore diameter using CTAB and pluronic P123 as porous co-templates. CTAB and P123 self-assembled in aqueous medium, forming a tubular micelle with a larger diameter than the original CTAB micelle. As a result, SBA-15 porous silica nanoparticles with pore diameter can be enlarged up to 8.2 nm without affecting the structural order of the particles (Figure 1.18) [96]. Even so, the approach to controlling pore diameter of MSN by modulating the soft-template micelle seems not to have been fully investigated. In addition, research on controlling mesopore diameter of the hollow member of MSN family (HMSN) appear to be rare.

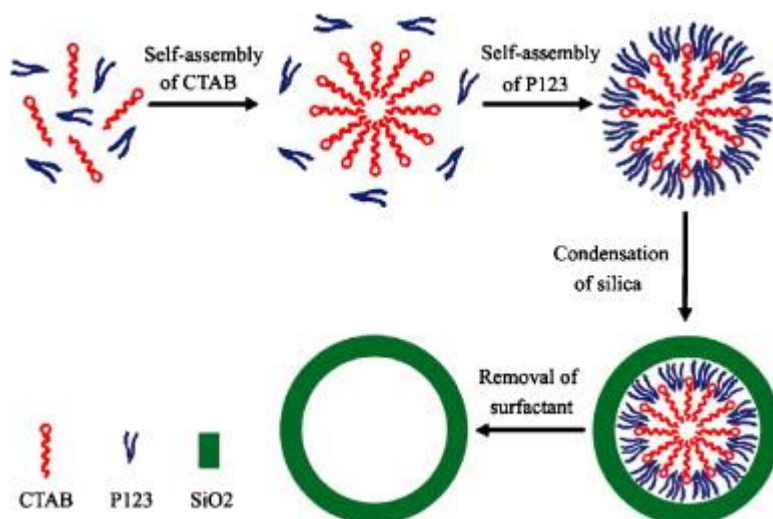


Figure 1.17. Self-assembly of mixed micelle of CTAB and P123 used as mesoporous templates in MSN particle synthesis [96]

The stability of mixed micelles depends on two factors: (1) coulombic interaction between ionic head groups and (2) chain length of the surfactant tail groups [97]. CTAB molecule is a positively charged surfactant, with a structure consisting of an alkyl chain in the form of a hydrophobic tail (16C) and a hydrophilic positive quaternary ammonium head. Moreover, the mixed micelle of CTAB should have a positive charge to form an electrostatic attraction between the mixed micelle and the hard template surface $dSiO_2$, creating favorable conditions for the formation of the mesoporous shell of the HMSN. As a result, non-ionic surfactants with a structure consistent with the above two factors are expected to create a mixed micelle system with CTAB being stable, positively charged and suitable for HMSN particle synthesis. Sujan Chatterjee *et al.* prepared a mixed micelle of CTAB with non-ionic surfactants including polyoxyethylene (20) cetyl ether (Brij 58), polysorbate 20 (Tween 20) and polysorbate 80 (Tween 80) in proportions in aqueous solution to study their stability and ideality. The adsorption between surfaces, the minimum area per surfactant molecule at the interface, the thermodynamics of the micelleization, and the stability of the mixed micelles were investigated. The effect of hydrophobic and hydrophilic chain lengths on the stability of mixed micelles was also included in this study [97]. The results of this study have contributed useful basic information for the development of mixed micelles of CTAB and non-ionic surfactants, which could be applied in the HMSN synthesis process.

Through the above literature review, a complete and systematic study on the influence of the type of non-ionic surfactant and its molar ratio to CTAB in the mixed micelle system to the pore diameter of HMSN particles will have scientific and practical significance, providing necessary and valuable information for the synthesis of desired HMSNs. The methods used to carry out this study are described in detail in Chapter 2 and the corresponding results are presented in Chapter 5.

1.4.5. Modifications of HMSN

Although different strategies have been conducted to exploit the applicability of MSN in anti-cancer drug delivery, the clinical applications of MSN remain a

challenge due to several limitations [21]. MSN particles have shown certain limitations that need to be improved and overcome. In terms of particle structure, the open pore of MSN causes the drug to be washed away after loading and leaked during circulation. This leads to the decrease in actual drug delivery capacity and the rise of side effects of the drug-carrying system when circulating in the body [40]. In term of chemical properties, the silanol groups on the surface of MSN interact with the phospholipids on the red blood cell membranes leading to hemolysis [98]. Therefore, surface modification of HMSN with appropriate ligands would help to over come these drawbacks. The modified ligands firstly would "cap" the openings pores, thereby improving drug retention and limiting drug leakage of HMSN in circulation, secondly eliminate the hemolytic effect of surface silanol groups.

The ability to modify HMSNs is due to their surface chemistry with the silanol groups present on the particle surface. These silanol groups can be modified with various compounds to improve and expand the application of HMSN in the biomedical field. Methods to modify silica nanosurface include co-condensation method and grafting method [99]. Normally, modification of HMSN by grafting method takes place through 2 steps: (1) denaturing HMSN surface with active functional groups; (2) grafting the hybrid material to the surface of the activated HMSNs through the functional groups. The advantage of this technique is the specificity of modification sites such as particle surface and pore surface [99].

The amino group is the most commonly used functional group for surface modification of HMSN. This group can be used as precursors to graft other compounds. Nguyen Thi Ngoc Tram and her colleagues used (3-Aminopropyl)triethoxysilane (APTES) with amine groups to denature HMSNs. The effect of APTES concentration on the properties of HMSN were also investigated, founding that the particle size and amino group density increased with the concentration of APTES. Moreover, DOX loading capacity and controlled release of HMSN were well improved after the amination (Figure 1.19) [40].

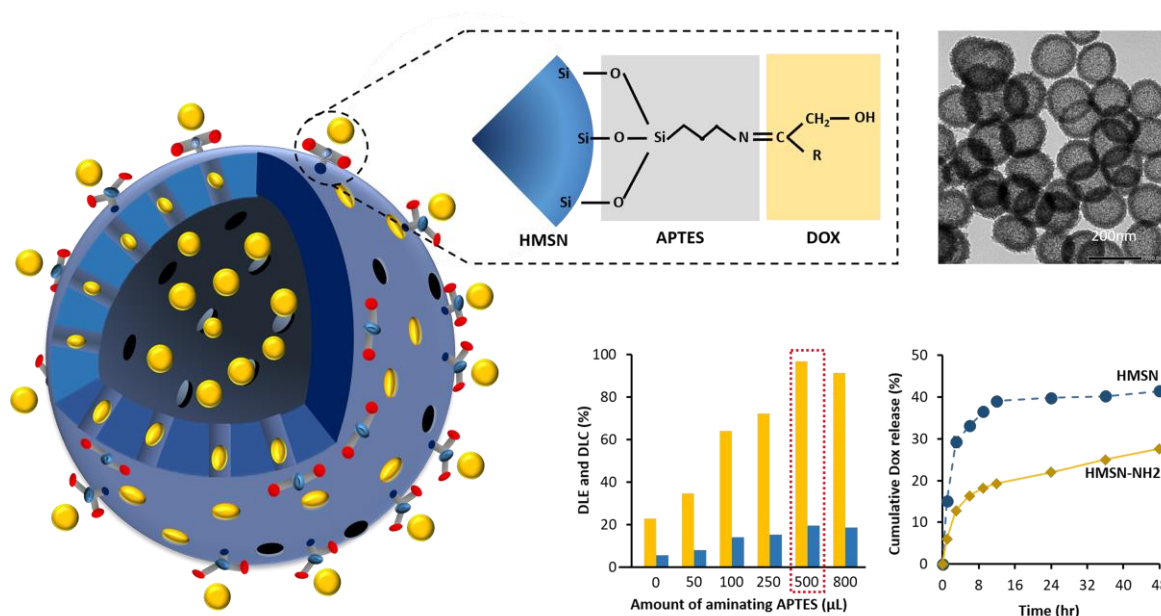


Figure 1.18. Aminated HMSN using 3-Aminopropyltriethoxysilane for better DOX loading capacity and controlled release [40]

Zaharudin N.S. *et al.* reported that the surface of MSN was successfully modified with amino, thiol or carboxyl groups for application in hydrophilic and hydrophobic drug delivery [100]. Besides, Yismaw and colleagues modified MSN with an acrylate functional group [101]. The aldehyde functional group has been successfully grafted onto the surface of dendritic MSNs using triethoxysilyl butyraldehyde to create a pH-responsive protein drug delivery system [102]. The disulfide group has been successfully functionalized on MSN through co-condensation with bis(triethoxysilylpropyl) disulfide (BTES) as the precursor of the functional group [103].

For drug delivery applications, MSNs are often functionalized with the polymer because it improves the drug carrier performance and the therapeutic effect of the carrier. The polymer type is selected for hybridization with MSN based on desired outcomes such as biocompatibility, specific targeting, ability to respond to stimuli or controlled drug release [104]. Some common polymers used for hybridization with MSN can be named such as PEG, Pluronic, dendrimer, chitosan, ...

PEG is a biocompatible, non-toxic, water-soluble polymer that is most widely used in biomaterials, biotechnology and drugs. PEG has been approved for use by the FDA and is one of the most commonly used polymers for hybridization with MSNs. When being PEGylated on the surface, the carrier can prevent nonspecific protein adsorption, reduce renal excretion, reduce toxicity, change biodistribution, improve stability and increase circulation time in blood. These factors are important for effective drug delivery [105]. PEG can be hybridized onto the MSN surface through previously modified MSNs with amino groups [105]. A modified system of HMSNs with PEG through amino intermediates has been successfully synthesized by Nguyen Thi Ngoc Tram *et al.* DOX was used as the model drug to evaluate the effect of PEGylation on the loading capacity and release profiles of the systems. Due to the capping effect of the PEG molecules on the pores of HMSN, the synthetic system could carry a higher DOX amount and establish a better controlled drug release profile [41].

Pluronic are amphiphilic tri-block copolymers which were FDA-approved and have long been described in pharmaceutical and clinical applications [106]. Their molecules compose of a central hydrophobic poly(propylene oxide) (PPO) template flanked by hydrophilic poly(ethylene oxide) (PEO) chains (Figure 1.20). This structure on the one hand makes pluronic good biocompatibility, on the other hand can improve the solubility of encapsulated poorly soluble drugs [107]. Recently, Pluronic have been modified with several nanoparticles for drug delivery applications. These poloxamers have been studied to denature on the surface of nanocarriers such as dendrimer or MSN to improve drug release profiles in cancer treatment. In particular, for the carrier system with a open pore structure, pluronic is expected to act as caps to keep the drug inside the pores after encapsulation, avoiding drug leakage during transportation, and induce a controlled release of the drug [108, 109].

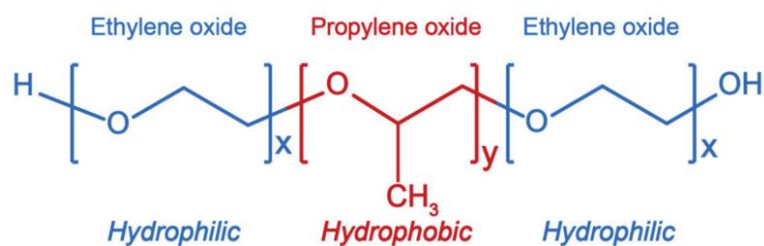


Figure 1.19. Molecular structure of Plurionics

Adem *et al.* reported a modifying system between hydrophobic MSN (modified with Octyl) with Pluronic F127. The modified MSN particles with F127 were dispersible in both water and phosphate-buffered saline (PBS), while the conventional MSNs readily agglomerated and precipitated. Improved biocompatibility of F127 hybrid MSN has been demonstrated through assays for cytotoxicity, hemolytic activity, and thrombogenic potential [110]. Besides, there have been several studies using Plurionics to encapsulate poorly soluble drugs. Rajib *et al.* reported the use of Pluronic F127 micelles for the encapsulation of hydrophobic drugs including ibuprofen, aspirin, and erythromycin [111].

In another study, Nguyen Thi Tram Chau and her co-workers successfully prepared plurionics-conjugated polyamidoamine dendrimer nanocarriers for hydrophobic drugs (Figure 1.21) [108]. Four kinds of plurionics (P123, F68, F127 and F108) were conjugated on 4th generation of polyamidoamine dendrimer (PAMAM G4.0). The results obtained from Fourier-transform infrared (FT-IR), ^1H NMR and Gel Permeation Chromatography (GPC) showed that the plurionics were successfully conjugated on the dendrimer. The molecular weights of the four PAMAM G4.0-Plurionics and their morphology are in the range of 200.15–377.14 kDa and the diameter is about 60–180 nm according to TEM, respectively. The loading and release efficiency of the hydrophobic anticancer drug fluorouracil (5-FU) was evaluated by HPLC. Interestingly, the G4.0-P123 system of dendrimer PAMAM in combination with P123 exhibited a higher drug loading efficiency (up to 76.25%) compared with other plurionics. The cytotoxicity test showed that all the conjugated nanocarriers are highly biocompatible. The drug-loaded nanocarriers also

showed inhibitory activity on MCF-7 breast cancer cells. The obtained results demonstrate the great potential of nanocarriers conjugated with pluronics in general and lipophilic pluronics specifically in hydrophobic drug delivery for biomedical applications.

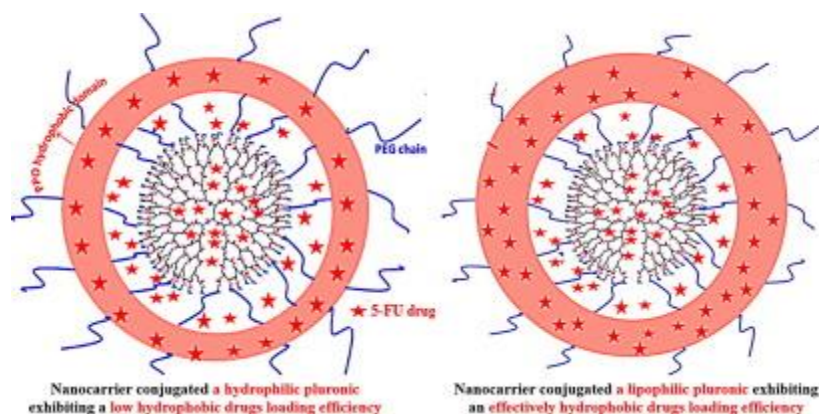


Figure 1.20. Conjugation of polyamidoamine dendrimer and pluronics for hydrophobic drug delivery [108]

1.4.6. Multiple-Drug Loading HMSN

Chemotherapy is a systemic treatment that has a therapeutic effect on tumors that have a tendency to metastasize to advanced tumors. However, some problems such as: (1) Side effects, (2) Low solubility and poor drug stability, (3) Poor distribution and (4) Multidrug resistance (MDR), are the disadvantages of chemotherapy that need to be overcome [112]. It has been reported that the use of multiple drugs in combination can increase the effectiveness of treatment and inhibit tumor growth. For example, co-distribution of Quercetin (QUE) with Doxorubicin (DOX) was proved to not only reduce the required dose of DOX but also reduce the cardiotoxicity produced by DOX [113, 114]. This combination has also been shown to overcome multidrug resistance in the MDA-MB-231/MDR1 cell line [115]. Importantly, the specific distribution and adequate accumulation of drugs into tumor by a nanocarrier could reduce the damage to normal organs and enhance the antitumor efficiency [116].

There have been several reports of using MSN as a carrier to deliver two anticancer drugs for treatment. Zhang and colleagues reported the use of hollow mesoporous organosilica nanoparticle (MON) for drug delivery of doxorubicin and cisplatin. The results showed the enhanced antitumor activity when two drugs were used [117]. For the treatment of acute myelogenous leukemia, MSN coated with the folic acid modified PEGylated lipid bilayer to carry paclitaxel and tanshinone IIA [118]. The MSN carrier system is composed of polydopamine, and the rattle-structured upconversion nanoparticles are synthesized to deliver doxorubicin and hydroxycamptothecin. This carrier can deliver both hydrophilic (doxorubicin) and hydrophobic (hydroxycamptothecin) drugs, where MSN is used for doxorubicin and polydopamine for the hydroxycamptothecin shell, respectively [119]. However, studies on application of HMSN in dual drug delivery are still very limited. Meanwhile, there have been no reports on dual-drug loading systems based on HMSN modifying with Pluronic - a polymer with proven dual-drug encapsulating potential.

Considering the above-mentioned issues, the development of a nano system based on HMSN modifying with Pluronics for dual drugs loading would address the obstacles of both HMSN and chemotherapy in cancer treatment. Modified Pluronic firstly would "cap" the openings pores, thereby improving drug retention and limiting drug leakage of HMSN in circulation, secondly eliminate the hemolytic effect of surface silanol, and finally enhance the encapsulation of drugs with different properties to increase the therapeutic effect. In this doctoral thesis, HMSN was surface modified with different Pluronics including L64, F68 and F127 for the investigation of dual drugs loading capacity, loading efficiency and *in vitro* release behavior. The model drugs were DOX as a hydrophilic drug and QUE as a hydrophobic drug. The methods used to carry out this study are described in detail in Chapter 2 and the corresponding results are presented in Chapter 6.

In conclusion, researching the best method to fight cancer is an ongoing process. The approach is through finding a more effective drug or improving the carrier, where the effectiveness of the drug would be worthless without the best transporter.

Therefore, finding and improving delivery materials to increase the effectiveness of drugs is very important. HMSN is one of the carriers that can overcome the problems posed by current treatments. It has many desirable properties such as high surface area, adjustable particle size and morphology and easy surface functionalization. These properties may increase drug loading capacity, improve circulation time, and develop multifunctional carriers. Although the application as an anticancer drug delivery agent of HMSN is potential, the properties of HMSN materials such as particle size, pore diameter, and shell thickness still need to be completed and optimized with the desired drug/agent. Additionally, modified HMSN systems still need more studies to verify their activities *in vitro* as well as expand understanding of the behavior of drug carrier hybrid HMSN systems *in vivo* conditions in general and humans in particular. Therefore, there is still a lot of work to develop HMSN with the favorable properties for anti-cancer treatment. With the time and improvement, HMSN is expected to become one of the most effective and potential anticancer drug delivery systems.

CHAPTER 2. MATERIALS AND EXPERIMENTAL METHODS

2.1. Materials

2.1.1. Chemicals

The chemicals used in the study were analytical grade which are listed in Table 2.1.

Table 2.1. List of used chemicals

Order No.	Chemicals' names	Origin	Purity
1	Ammonia solution	Merck	25-28%
2	Cetyltrimethylammonium bromide (CTAB)	Sigma	$\geq 98\%$
3	Ethanol	Vietnam	96%
4	Absolute Ethanol	Chemsol	99.5%
5	Deioned water (DI)	Vietnam	
6	Sodium carbonate	Merck	$\geq 99.9\%$
7	Tetraethyl orthosilicate (TEOS)	Sigma	$\geq 98\%$
8	Acid Acetic	Fisher	99.5%
9	(3-aminopropyl)triethoxysilane (APTES)	Sigma	$\geq 98\%$
10	Triethanolamine (TEA)	Merck	$\geq 99\%$
11	Polyethylene glycol 1000 (PEG 1000)	Sigma	
12	Polyethylene glycol 1000 (PEG 2000)	Sigma	

13	Polyethylene glycol 1000 (PEG 4000)	Sigma	
14	Polyethylene glycol 1000 (PEG 6000)	Sigma	
15	Polyoxyethylene (10) stearyl ether (Brij S10)	Sigma	
16	Polysorbate 20 (Tween 20)	Fisher	$\geq 95\%$
17	Polysorbate 80 (Tween 80)	Fisher	$\geq 95\%$
18	Pluronic F127	Sigma	
19	Pluronic F68	Sigma	
20	Pluronic L64	Sigma	
21	Dulbecco's Modified Eagle Medium (DMEM)	Sigma	endotoxin, tested
22	Fetal bovine serum (FBS)	Sigma	≤ 10 EU/mL endotoxin
23	Penicillin-Streptomycin	Sigma	1000 U/mL
24	Thiazolyl Blue Tetrazolium Bromide (MTT)	Sigma	98%
25	Doxorubicin (DOX)	Sigma	$\geq 98\%$
26	Rose Bengal (RB)	Sigma	95%
27	Quercetin (QUE)	Sigma	$\geq 95\%$

2.1.2. Equipments

The equipments used in the study were at the Institute of Applied Materials Science (IAMS) and other national research institutions which are listed in Table 2.2.

Table 2.2. List of used equipments

Order No.	Equipments' name	Origin
1	Refrigerated Centrifuge Hermle Z 32 HK	Germany
2	Bench Top Freeze Dryer Eyela FDU-1200	Japan
3	Zetasizer Horiba SZ-100	Japan
4	Transmission electron microscopy Jeol JEM-1400	Japan
5	Field Emission Scanning electron microscope with Energy Dispersive X-ray microanalysis	Japan
6	NMR Spectrometer Bruker 500 MHz	Germany
7	X-ray Diffractometer Bruker D2 Advance	Germany
8	Thermogravimetric Analyzer Mettler Toledo TGA-DSC 3+	Switzerland
9	Surface Area and Porosimetry Analyzer Micromeritics TriStar II Plus (Version 3.03)	USA
10	UV/Visible Scanning Spectrophotometer Shimadzu UV/Vis-1800	Japan
11	Bruker Equinox 55 FT-IR spectrometer	Germany
12	CelCulture CO ₂ Incubators	Japan
13	Tissue culture hood	Japan
14	Confocal microscopy	USA

2.2. Synthesis Methods

2.2.1. Synthesis of HMSN

HMSN were synthesized by hard-template method through three main steps, including (1) the preparation of the hard template dSiO₂ using Stober method, (2) the preparation of core@shell structure dSiO₂@MSN using sol-gel technique, and (3) the selective etching of dSiO₂@MSN to form HMSN [52]. The synthesis processes are presented in the following Diagram 2.1, Diagram 2.2 and Diagram 2.3.

In the first step, dSiO₂ as hard templates were prepared by a modified Stober method [41]. To control the HMSN particle diameter below 100 nm, the particle size

of dSiO₂ was reduced through the synthesis components such as the concentration of silica precursor TEOS, the concentration of catalyst agent NH₃ and the amount of EtOH [42, 67]. Typically, 70.0 mL of absolute ethanol was mixed with 10.0 mL DI and 3.0 mL of ammonia and stirred for about 15 minutes at 60 °C. Then 6.0 mL of TEOS was added to the mixture and the reaction was allowed to happen for 6 hours. After that, the time of mesoporous silica coating step and hard template silica etching step would be shortened through reactional parameters such as temperature and catalyst agent [52].

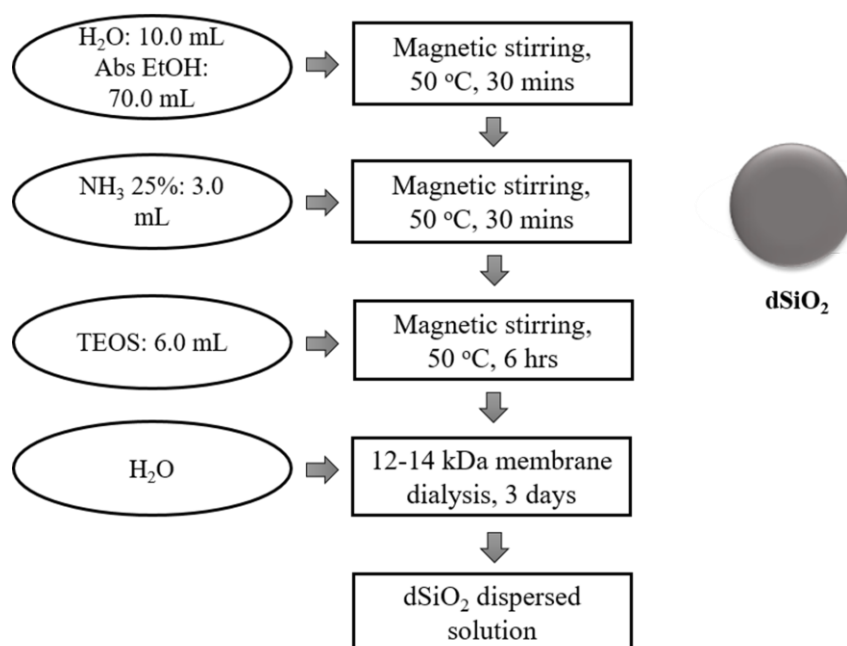


Diagram 2.1. The preparation of the hard template dSiO₂

In the second step, mesoporous silica layer was coated on the hard-templates using sol-gel method [52]. A solution including 3.0 g of CTAB, 50.0 mg of TEA and 20.0 mL of DI was prepared. Then, 10 mL of the dSiO₂ solution obtained in the first step was added and stirred at room temperature for 1 hour. The mixture was alternately heated to 80 °C, added 0.5 mL of TEOS and stirred for 1 hour to form dSiO₂@MSN.

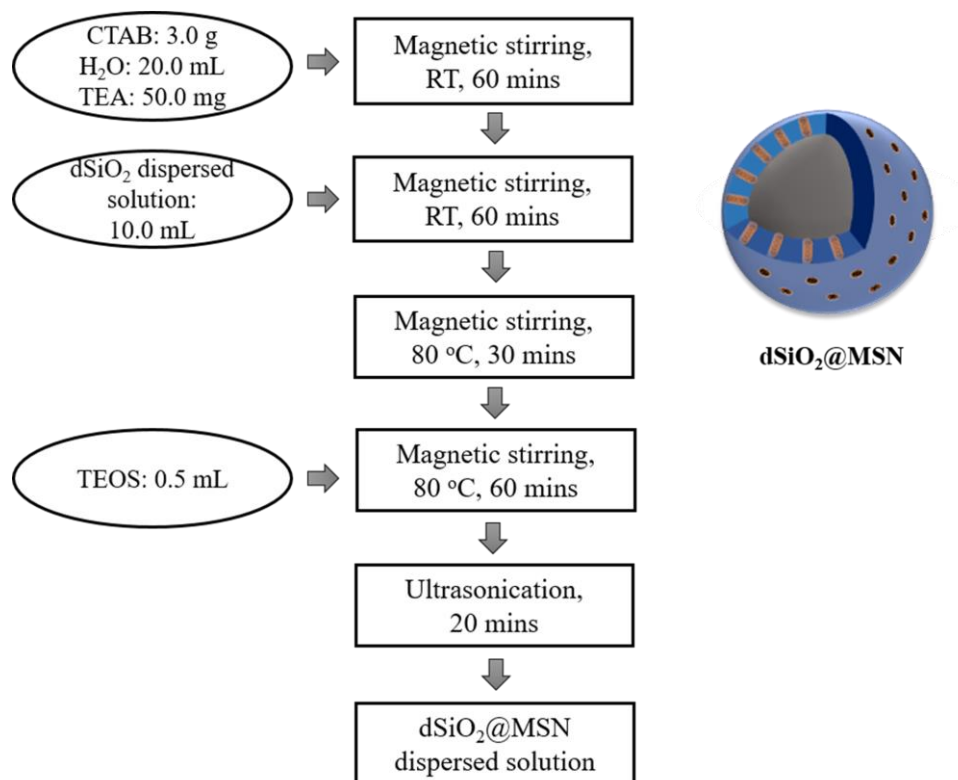


Diagram 2.2. The preparation of core@shell structure dSiO₂@MSN

In the third step, the hard-templates were removed via etching process using an aqueous Na₂CO₃ solution [20, 62]. The mixture obtained in the second step was cooled down to 50 °C before the addition of Na₂CO₃ (to reach the concentration of 21.2 mg/mL) and then stirred continuously to let the etching process happen. To study the etching of silica hard-template over time, a certain volume of the reaction mixture was aspirated every 30 minutes. The collected samples, named by the etching time including HMSN 30, HMSN 60, HMSN 90, HMSN 120, HMSN 150 and HMSN 180, were dialyzed by 12 x 14 kDa membranes against ethanol and distilled water in 3 days before lyophilized. After that, the particle size, morphology and particle structure of the samples were evaluated via Scanning electron microscope (SEM) and TEM images in order to choose suitable etching time. The chosen HMSN (with suitable etching time) was characterized FT-IR, Thermogravimetric analysis (TGA), Brunauer-Emmett-Teller (BET), Barret Joyner and Halenda (BJH), Dynamic Light Scattering (DLS), zeta potential, X-ray

Diffraction (XRD), Energy-dispersive X-ray spectroscopy (EDX) and MTT analytical methods.

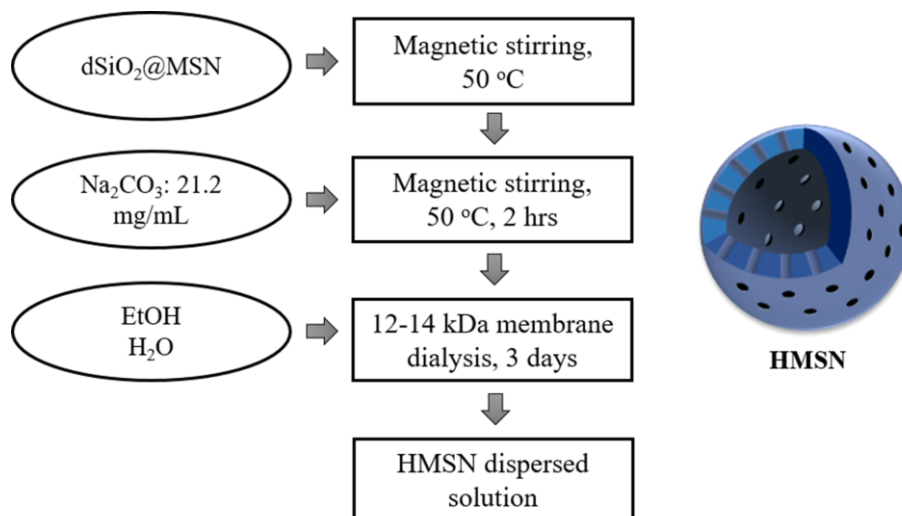


Diagram 2.3. The selective etching of dSiO₂@MSN to form HMSN

2.2.2. The effect of PEG on the mesoporous shell thickness of HMSN

To investigate the effects of PEG on the mesoporous shell thickness of HMSN, PEG with difference molecular weight (1000, 2000, 4000 and 6000 g/mol) and weight percentage (from 1% to 5%) was added into the reaction mixture in the second step of the synthesis process of HMSN as described in Diagram 2.4.

A part of the achieved solution after the second step was dialyzed by 12 x 14 kDa membranes against ethanol and distilled water in 3 days before being lyophilized to obtain dSiO₂@MSN. The post- lyophilized dSiO₂@MSN samples were calcined at 600 °C for 2 hours to removal of residual organic components for further experiments. These dSiO₂@MSN samples were measured DLS and SEM to determine the morphology and diameter of the particles. Based on the DLS particle diameter of dSiO₂ and dSiO₂@MSN, the thickness of the mesoporous shell would be calculated following the equation:

$$T_s = \frac{d_{\text{dSiO}_2@\text{MSN}} - d_{\text{dSiO}_2}}{2} \quad (1)$$

Where: TS: the thickness of mesoporous shell (nm)

$d_{\text{dSiO}_2@\text{MSN}}$: diameter of dSiO₂@MSN particles (nm)

d_{dSiO_2} : diameter of dSiO₂ particles (nm)

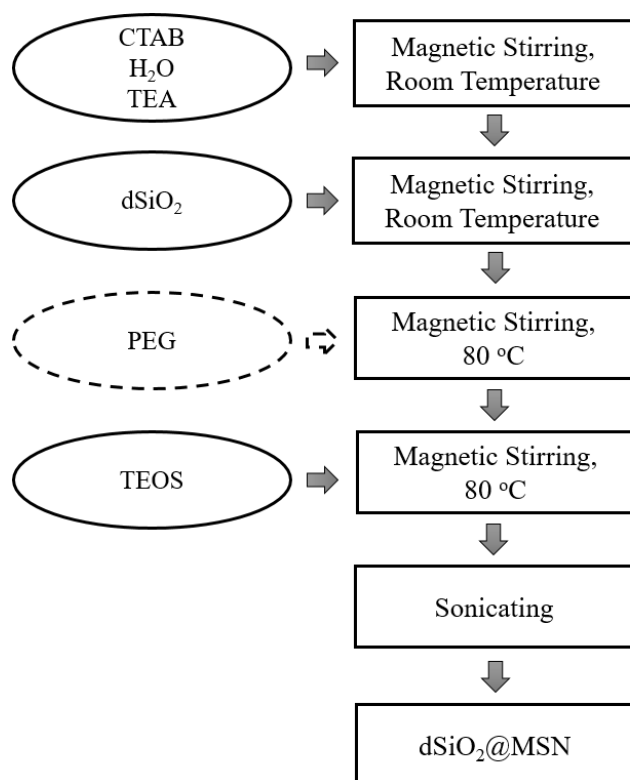


Diagram 2.4. Mesoporous silica layer coating step in HMSN synthesis process with the presence of PEG

The rest of the dSiO₂@MSN solution was continued to conduct the third step to obtain HMSN. The post- lyophilized HMSN samples were calcined at 600 °C for 2 hours to complete removal of residual organic components for further experiments.

In order to better clarify the role of PEG in the HMSN synthesis, characteristics of synthesized HMSNs with and without PEG named as HMSN-0 and HMSN-P, respectively, were determined and compared via SEM, TEM, BET, FT-IR, EDX, DLS and Zeta potential analysis.

The drug loading capacity (DLC) and drug loading efficiency (DLE) as well as drug release profiles of HMSN-0 and HMSN-P were investigated using DOX as a model drug and DOX amount was identified using UV-Vis spectrometer at 480 nm. Finally, cytotoxicity of the synthesized HMSN-0 and HMSN-P was evaluated through the MTT assay on MCF-7 cell line.

2.2.3. The effect of non-ionic surfactants on the mesopore diameter of HMSN

Non-ionic surfactants with different hydrophobic tails and hydrophilic heads including Tween 20 (T20), Tween 80 (T80) and Brij S10 (BS10) (Figure 2.1) were used as co-templates for mesopores in the preparation of HMSN. Tween 20 and Tween 80 have similar hydrophilic heads and different hydrophobic tails, while Brij S10 and Tween 80 have similar hydrophobic tails and different hydrophilic heads. The use of these nonionic surfactants would help to evaluate the effect of their structure on the formation of mixed micelles with CTAB, and accordingly on the mesopore diameter of HMSN.

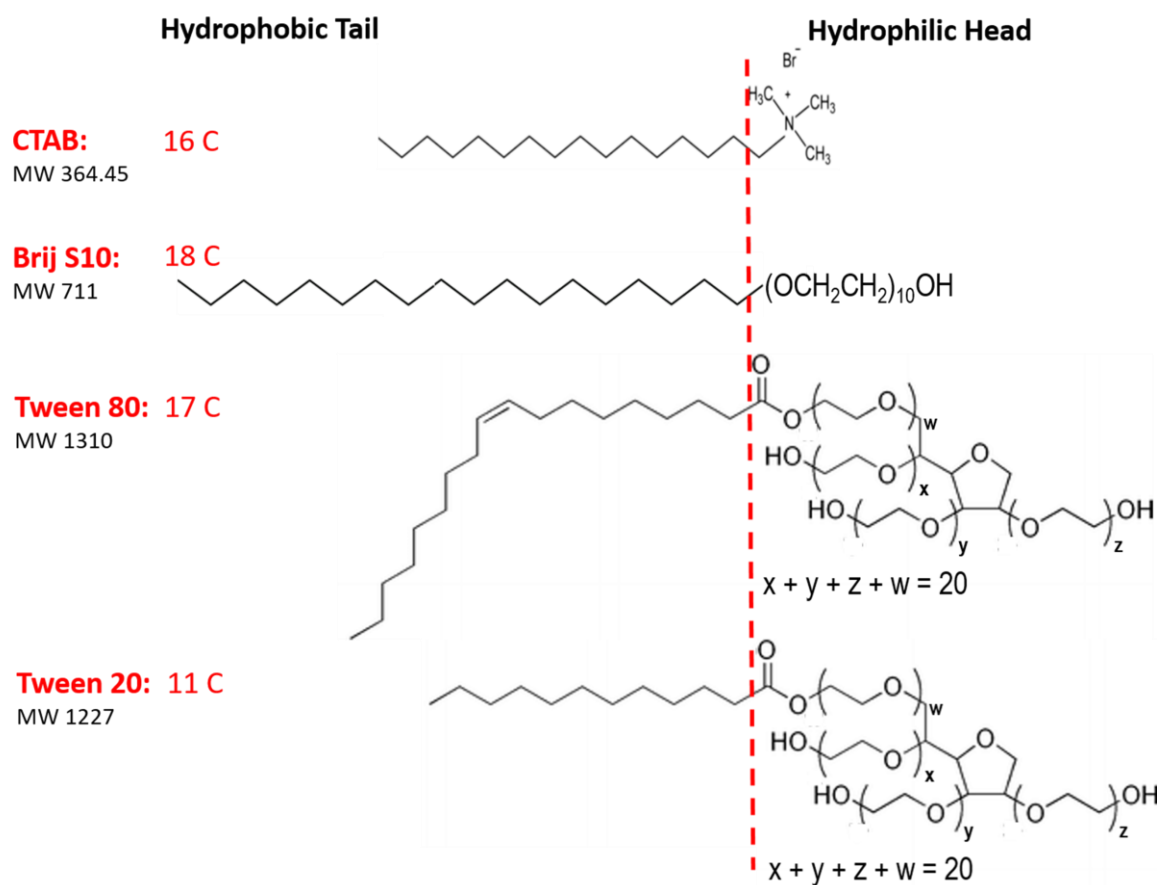


Figure 2.1. Molecular formulas of the used non-ionic surfactants versus CTAB

The mixed micelles of non-ionic surfactants at difference molar ratio with the constant CTAB (0:1, 1:4, 1:3, 1:2 and 1:1) were used in the second step of the HMSN synthesis process as co-templates to coat the mesoporous shell onto the hard template dSiO₂. The mesoporous shell coating process was described in Diagram 2.5.

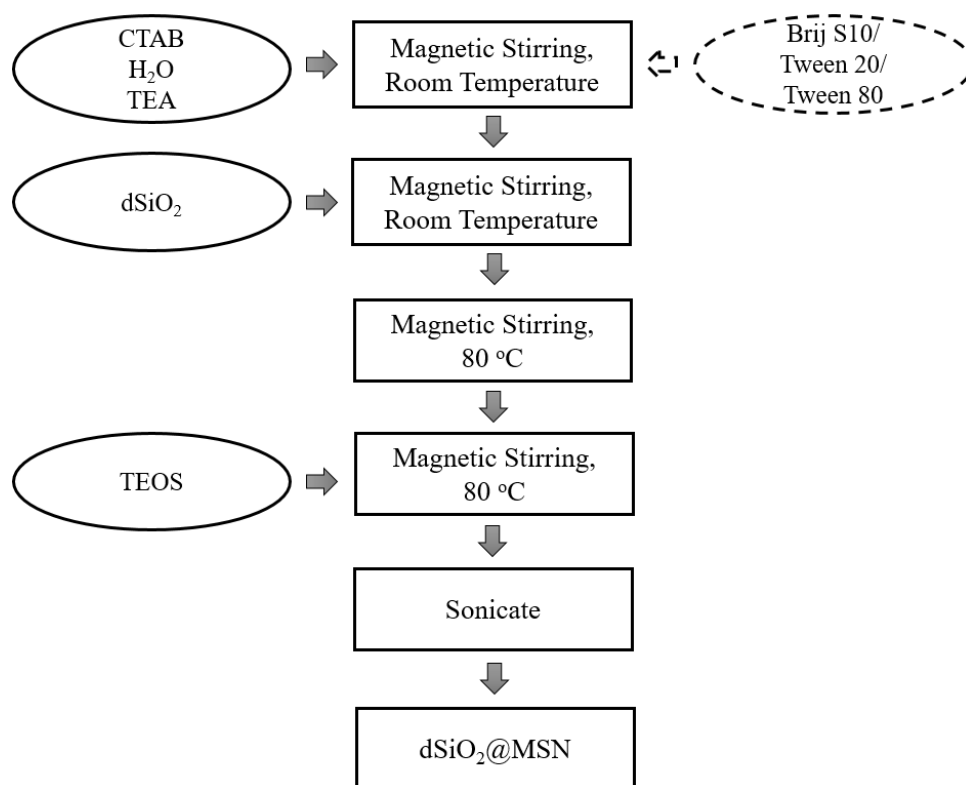


Diagram 2.5. Mesoporous silica layer coating step in HMSN synthesis process with the presence of non-ionic surfactants as co-templates

A part of the achieved solution after the second step was dialyzed by 12 x 14 kDa membranes against ethanol and distilled water in 3 days before being lyophilized to obtain dSiO₂@MSN. These dSiO₂@MSN samples were measured DLS size, BET Surface Area Analysis and BJH Pore Size and Volume Analysis to determine the morphology and diameter of the particles as well as diameter of meso-pores.

The thickness of the mesoporous was calculated based on the particle diameter of dSiO₂ and dSiO₂@MSN and the Equation (1). Based on the BET and BJH analysis, the meso-pore diameter of dSiO₂@MSN samples were determined and compared. The rest of the dSiO₂@MSN solution was continued to conduct the third step to obtain HMSN and the products were characterized via SEM, TEM, Zeta potential, XRD and FT-IR analysis.

The DLC and DLE values as well as drug release profiles of HMSN and HMSN-S (HMSN-BS10, HMSN-T20 and HMSN-T80) were investigated. To evaluate the

ability of the particles to load cargos with bigger size, Rose Bengal (RB) (MW 1017.64 g/mol, as twice higher than that of DOX) was used as the model drug and loaded into the particles using equilibrium dialysis method [120]. To quantify and calculate the released drug in dialysis systems, the collected samples were subjected to UV-Vis spectrophotometry at 546 nm [42]. Additionally, cytotoxicity of the obtained HMSN and HMSN-S was evaluated using MTT assay on MCF-7 cell line.

2.2.4. Surface Modification Method of HMSNs with Pluronics

To modify the surface of HMSN with Pluronic, HMSN and Pluronic molecules need to be activated. For HMSNs, the nanoparticle surface was impregnated with a more active amine group by modification with APTES to form HMSN-NH₂ [121, 122]. For pluronic, the -OH groups at the ending terminals were activated with 4-Nitrophenyl chloroformate (NPC). Then, the two- activated terminals of Pluronic were reacted with 3-amino-1-propanol to form an -OH group at one end and a nitro group at the other end, forming NPC-Plu-OH [123, 124]. Finally, HMSN-NH₂ was reacted with NPC-Plu-OH to form the product HMSN-Plu. The methodology of modification HMSN with Pluronic was inherited from doctoral thesis of Nguyen Thi Ngoc Tram.

2.2.4.1. Activation HMSNs' surface with APTES

The prepared HMSN were functionalized its surface with amine groups by the reaction with APTES. Firstly, 200 mg of the prepared HMSN was dispersed in 20 mL ethanol and sonicated for 20 min. The dispersion was then moved to a round bottom flask and stirred for 15 min. A mixture of APTES : EtOH (1:1, v/v) was added drop by drop into the HMSN dispersed solution. The reaction was carried out with continuous stirring for 24 h at room temperature. Finally, the particles HMSN-NH₂ were collected and washed by centrifuging with ethanol and water for 10 min at 10000 rpm. The HMSN activating process was shown in Diagram 2.6.

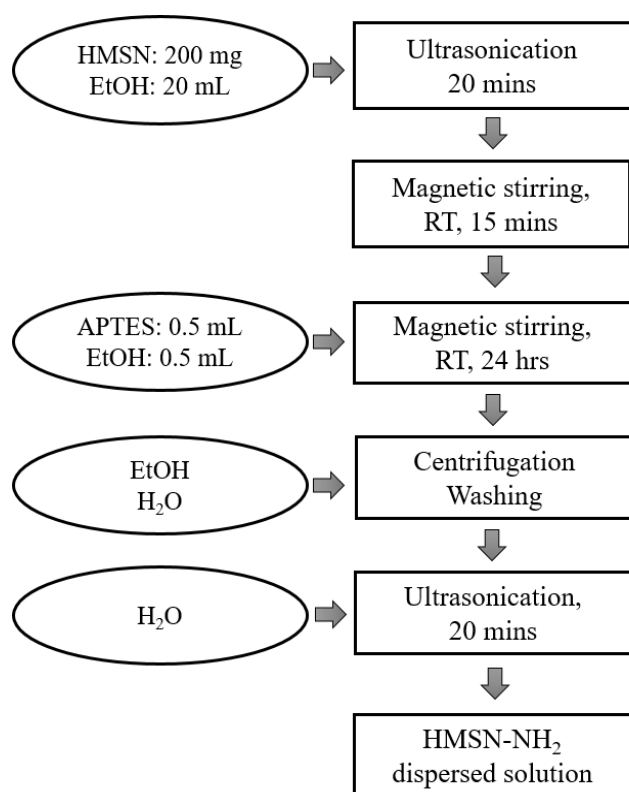


Diagram 2.6. The surface activation of HMSN with APTES

2.2.4.2. Activation of Pluronic with NPC

Firstly, 5 g of Pluronic was heated in vacuum environment for 1.5 h in a 250 mL round bottom flask to ensure that Pluronic was totally melted and dehumidified. After that, a sufficient amount of NPC was added into the melted Pluronic and stirred at the same temperature for 5 h in a nitrogen atmosphere. The mixture was then cooled down to room temperature, added by 10 mL of THF and stirred for another 16 h. Consequently, amino-1-propanol diluted in 10 mL of THF was dropped little by little into the mixture and stirred slowly in 5 h more. The resulting solution was precipitated in 250 mL of cold diethyl ether and vacuum-filtered. The product NP-Plu-OH was evaporated to completely remove the remaining solvent [125]. The activating process of Pluronic was shown in Diagram 2.7.

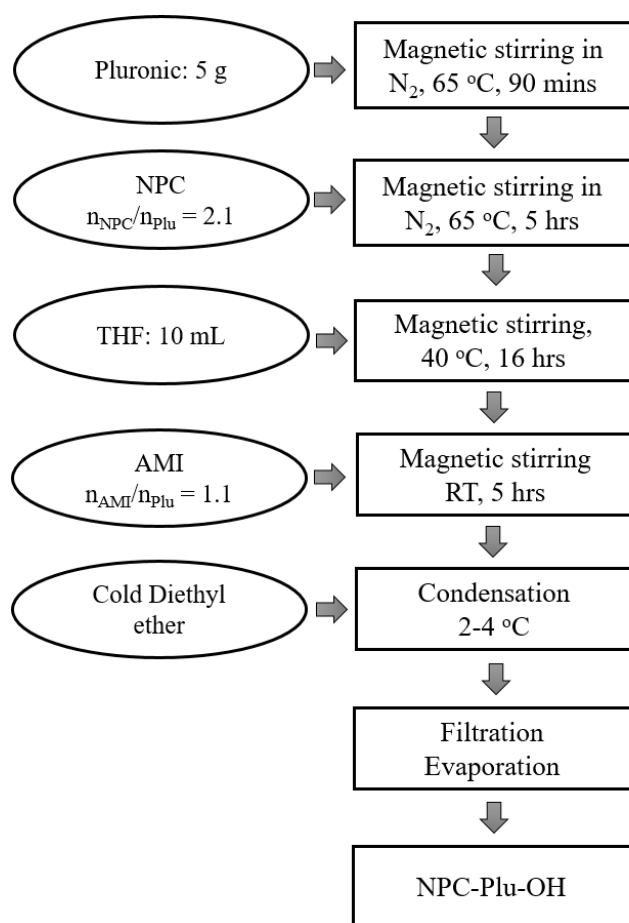


Diagram 2.7. The activation of Pluronic with NPC

2.2.4.3. Modification of HMSN-NH₂ with NPC-Plu-OH

HMSN-Plu was synthesized by the reaction between the prepared HMSN-NH₂ and activated NPC-Plu-OH [126, 127]. Firstly, 50 mg of HMSN-NH₂ was dispersed in 10 mL of DI, soicated in 15 min and moved to a round bottom flask, which was named mixture A. For the moment, 100 mg of NPC-Plu-OH was dissolved in another 10 mL of DI, named mixture B. Then, B was added drop by drop into A under continuous magnetic stirring for 2 h at 350 rpm. The product HMSN-Plu was dialyzed by 12 x 14 kDa membranes against distilled water before lyophilized. The process was shown in Diagram 2.8.

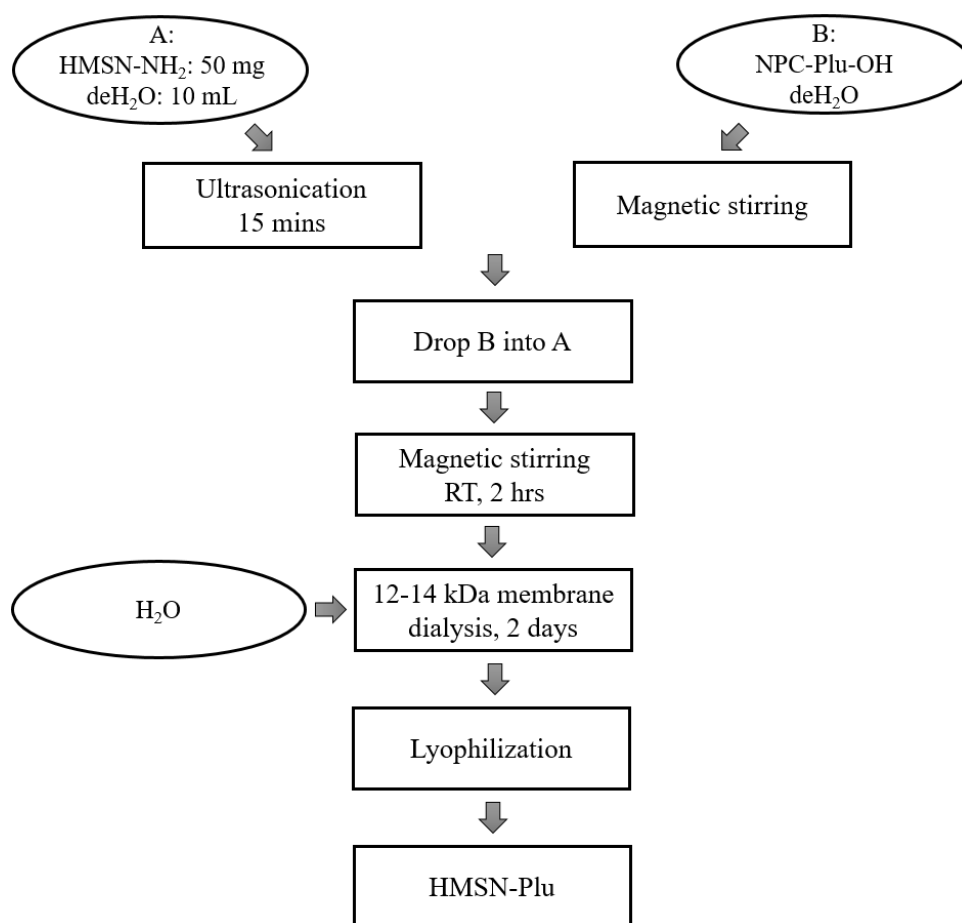


Diagram 2.8. The preparation of HMSN-Plu from HMSN-NH₂ and NPC-Plu-OH

2.2.5. The effect of Pluronics on dual-drugs delivery characteristics of HMSN-Plu

Pluronics with different number of hydrophilic blocks (PEO) and hydrophilic blocks (PPO) including L64, F68 and F127 (Table 2.3) were activated and denatured on the surface of HMSN particles. HMSN-Plu systems were then identified their properties including DLS, Zeta potential, morphology and porosity to evaluate the influence of different types of Pluronic on the physico-chemical properties of HMSN particles after the surface modification.

Moreover, DOX as hydrophilic drug and QUE as hydrophobic drug were used as the model drugs in drug loading capacity, drug release profiles and cytotoxicity experiments to evaluate the influence of these Pluronics on the biological properties of the conventional HMSN. DOX was encapsulated first in HMSN-Plu systems using

DI as the solvents. After that, QUE was loaded into the DOX@HMSN-Plu using DI:MeOH (1:1, v/v) as the solvents.

Table 2.3. Characteristics of the used Pluronics

Pluronics	Average number of PEO units (x)	Average number of PPO units (y)	Molar mass (Da)
L64	14	31	2900 [128]
F68	82	31	8400 [129]
F127	95	62	12600 [129]

2.3. Physicochemical Analysis Methods

The particle size distribution was determined by DLS, meanwhile the zeta potential (ζ) was determined through a Helium-neon (He-Ne) laser beam with the setting detection angle of 90°, temperature of 25 °C and wavelength of 532 nm using a Zetasizer Nano SZ (SZ-100, Horiba, Kyoto, Japan) at the Institute of Applied Materials Science.

To evaluate the particle size, morphology and hollow@shell structure of the synthesized samples, Scanning Electron Microscopy (SEM) and Transmission electron microscope (TEM) images were taken on FE-SEM S-4800 (HITACHI, Tokyo, Japan) and JEM-1400 (JEOL, Tokyo, Japan), respectively. Moreover, Energy dispersive X-ray spectroscopy (EDX) analytical method was used for chemical characterization using FE-SEM S-4800.

To study the components and evaluate the purity of the synthesized particles, FT-IR and thermal gravimetric analysis (TGA) were carried out. FT-IR investigation was performed on Bruker Equinox 55 FT-IR spectrometer (Bruker, Ettlingen, Germany) using KBr pellet method. Additionally, TGA investigation was performed with a TGA Analyzer (Mettler Toledo, Switzerland) under a nitrogen flow with temperature program from 30 to 800 °C at the increasing speed of 10 °C/minute.

XRD experiment was performed on a Bruker D2 Phaser diffractometer (Germany) using mono-chromated $\text{CuK}\alpha$ radiation to investigate the molecular structure of HMSN.

Brunauer-Emmett-Teller (BET) Surface Area Analysis and Barrett-Joyner-Halenda (BJH) Pore Size and Volume Analysis were operated on TriStar II Plus (Version 3.03, Micromeritics, GA, USA).

Drug amount including Doxorubicin (DOX), Rose Bengal (RB) and Quecertain (QUE) was determined by measuring the absorbance at 480, 546 and 380 nm, respectively, using a UV/Visible Scanning Spectrophotometer UV/Vis-1800 (Shimadzu, Japan).

2.4. Drug loading and *in vitro* release study

The DLC and DLE values as well as drug release profiles of nano particles were investigated. Model drug was loaded into the particles using equilibrium dialysis method [120]. Initially, 20 mg of the nanocarriers was dispersed in 8 mL of appropriate solvent (DI, EtOH, MeOH or DMSO) and 2 mg of the drug was dissolved in another 2 mL of the solvent. Then, drug solution was added into the mixture and stirred at room temperature for 24 h. After that, the loaded particles were collected by centrifuging at 10.000 rpm in 30 min. The supernatant was collected and checked for unloaded drug by UV-Vis.

The free drug standard curves were established by measuring the absorbance of known concentration drug solutions (5-50 ppm and 0-5 ppm) at corresponding wavelength using a UV/Vis-1800 spectrophotometer (Jasco Co., Tokyo, Japan) [42]. DLE and DLC values for each drug were calculated using the equations below:

$$\text{DLE (\%)} = \frac{20 - W_{\text{non-D}}}{20} \times 100\% \quad (2)$$

$$\text{DLC (\%)} = \frac{20 - W_{\text{non-D}}}{(W_{\text{particles}} + 20 - W_{\text{non-D}})} \times 100\% \quad (3)$$

Where: 20 (mg) is the initial amount of drug used in the loading experiment
 $W_{\text{non-D}}$ the total amount of unloaded drug detected in the dialysis solution

$W_{\text{particles}}$ is the dried weight of the carrier system

The drug release profiles of free drug and loaded drug were assessed in PBS buffer using dialysis method which was described in the previous study [41]. First, 1 mL of free drug or loaded drug suspended in PBS was transferred to a 12-14 kDa dialysis bag and immersed in a vial containing 20 mL of the release medium. Then, the vial was placed in an orbital shaker bath maintained at 100 rpm continuous shaking. At the marked times, 2 mL of the release medium was collected and an equal volume of fresh medium was added. The collected release medium was analyzed by UV-Vis spectroscopy to determine the released drug [42].

2.5. Cell culture and MTT assay

Cytotoxicity of the synthesized particles and killing cancer cell effect of drug loading particles was evaluated through the MTT assay. Human breast cancer (MCF-7) cells and Human cervical cancer cells (Hela) were used as model cell lines. Both MCF-7 and Hela cell lines were supplied by ATCC (Manassas, VA). The cells were cultivated in complete DMEM (10% FBS, 100 IU/mL penicillin, and 0.1 mg/mL streptomycin) in a 5% CO₂ humidified incubator. The cells were seeded into a 96-well culture plate with a density of 3×10^4 cells/well. After 24 h being incubated with the culture media, the cells were treated with the synthesized particles at different concentrations from 10 $\mu\text{g/mL}$ to 250 $\mu\text{g/mL}$, or were treated with free drug and loaded drug at different concentrations from 0.1 to 50 $\mu\text{g/mL}$ for 48 h. Then, 20 μL of 5 mg/mL MTT solution were added to each well and incubated for 4 h more at 37 °C. The culture medium was discarded, DMSO was added with the amount of 100 μL /well and subsequently shaken for 2 min. Then the absorbance was measured in a microplate reader at the wavelength of 570 nm [40]. The cell viability was calculated using the following equation:

$$\text{Cell viability (\%)} = \frac{\text{Abs}_{\text{sample}} - \text{Abs}_{\text{blank}}}{\text{Abs}_{\text{control}} - \text{Abs}_{\text{blank}}} \times 100\% \quad (4)$$

2.6. Statistical analysis

Each experiment was performed in triplicate. The calculated results were presented as mean \pm standard deviation (SD). Testing for significant differences

between means was carried out using one-way ANOVA with Bonferroni's post-test ($p < 0.05$).

CHAPTER 3. A MODIFIED HARD-TEMPLATE METHOD FOR HOLLOW MESOPOROUS SILICA NANOPARTICLES SYNTHESIS WITH SUITABLE PARTICLE SIZE AND SHORTENED SYNTHETIC TIME

3.1. Synthesis of silica hard-template

The dSiO₂ particles were obtained after the first step of the HMSN synthesis process. Characteristics of the obtained dSiO₂ including zeta potential and hydrodynamic size were showed in Figure 3.1a and Figure 3.1b. The synthesized hard-templates had a zeta potential of -45.8 ± 0.4 mV, which was consistent with the previous reports of silica nanoparticles [130]. The hydrodynamic size of dSiO₂ was determined as 96.8 ± 0.3 nm with polydispersity index (PI) of 0.072. Low PI value (< 0.1) indicated that the obtained dSiO₂ was highly uniform with respect to the particle size [131].

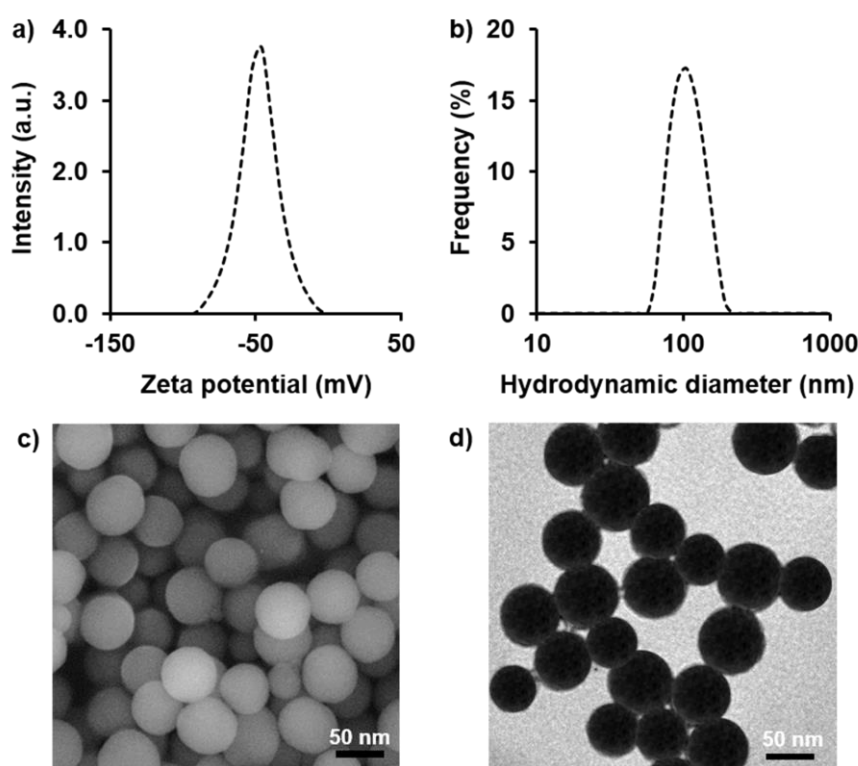


Figure 3.1. Characterizations of the synthesized hard-template dSiO₂: a) Zeta potential; b) DLS particle size distribution; c) SEM image; d) TEM image

The morphology of the dSiO₂ particles was presented via SEM and TEM images in Figure 3.1c and Figure 3.1d. As can be seen from SEM and TEM images, the dSiO₂ particles are mono-disperse spheres with particle diameter of 65.3 ± 0.4 nm. Compare to the previous studies, the hard template dSiO₂ diameter reduced from more than 100 nm to about 65 nm [52, 67]. The reduction of the hard template diameter is expected to lead to the reduction of the synthesized HMSN.

3.2. Etching over time of silica hard-template in the synthesis of HMSN

HMSN particles which was under different etching time from 30 to 180 minutes were taken SEM and TEM image (Figure 3.2). SEM images presented the outside appearance of HMSN, showing that the particles had non-hollow structure after 30 and 60 minutes of etching. The hollow structure of HMSN was visible after 90 minutes and most obvious after 120 minutes of etching. However, after 150 minutes of etching, the shell appeared to have some holes in it, indicating that it had begun to be corroded but the particles was still spherical. Finally, after 180 minutes of etching, the particles lost their spherical shape and the shell was collapsed.

TEM images showed the status of the hard template which could help explain how the etching process occurred. When the etching agent accessed the template, the rattle-type spheres with double-shell structure would be first obtained (HMSN 30, HMSN 60). After that, the cavity extended toward both sides and consequently the hollow structure was formed (HMSN 90, HMSN 120). When the hard template was totally corroded, the mesoporous shell would be corroded and destroyed by the etching agent (HMSN 150, HMSN 180). This observed phenomenon was consistent with the mechanism of selective etching in the previous report [64]. As previously mentioned, CTAB at sufficient concentration (21.2 mg/mL) would acted as a protector for the mesoporous shell and uniform HMSNs with clear hollow cavity would be obtained when the etching process was done (in this case the suitable etching time was determined as 120 min). However, too long etching time (150 and 180 min) would cause over-etching, leading to the etching of the shells and resulting aggregated particles with rough surfaces. Gradually, the shell became thinner, was destroyed and the particle structure collapsed as seen in Figure 3.2.

These results suggested that the suitable etching time was 120 minutes, consequently the HMSN 120 would be used for further experiment. Importantly, the synthetic time of HMSN for the main reactions in the current study decreased from 21 hours to 9 hours. In details, hard-template preparation time was remained for 6 hours, mesoporous shell coating time shortened to 1 hour and hard-template etching time shortened to 2 hours [67]. This modified hard-template method with shorter synthetic time would be meaningful for scientists who study on silica nanoparticles as well as for industrial scale production.

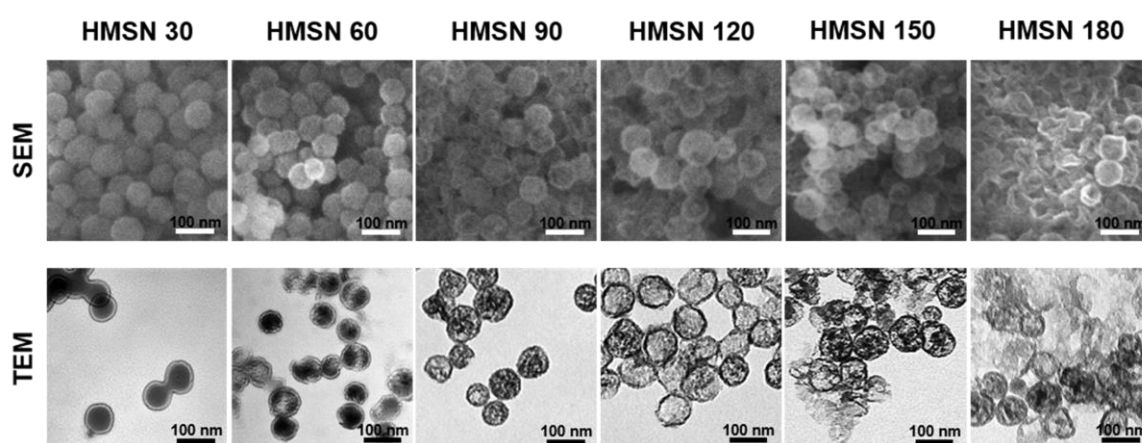


Figure 3.2. SEM and TEM images of HMSN over etching time

3.3. Characterizations of synthesized HMSN

The synthesized HMSN particles were characterized via TEM, BET, BJH, FT-IR, EDX, Zeta potential, DLS, XRD and TGA analysis whose results were showed in Figure 3.3 and Figure 3.4.

TEM images of the synthesized $\text{dSiO}_2\text{@MSN}$ and HMSN 120 were presented in Figure 3.3a and Figure 3.3b. Based on TEM image, $\text{dSiO}_2\text{@MSN}$ particles showed core@shell structure: the inner dark region is the solid template and the surrounding brighter region is the mesoporous shell. Meanwhile, HMSN's TEM image clearly showed the hollow@shell structure of the chosen HMSN 120 particles with the particle diameter of 80.2 ± 1.3 nm, the hollow diameter of 65.3 ± 0.9 nm, and the mesoporous shell thickness of about 7.5 nm. Compare to the previous studies, the particle size of the synthesized HMSN reduced from over 134 nm to about 80 nm

[52, 67]. Recently, nanomaterials have been surface modified with different polymers and functional groups to increase their biocompatibility, drug loading capacity and targeting ability, the particle diameter consequently will increase after being denatured [65]. Therefore, this obtained HMSN would be a appropriate material for a complete nano-carrier preparation.

As a consequence, on the one hand, this study has reduced the hard template size dSiO₂ by changing the ratio of reactants including TEOS, EtOH and DI. On the other hand, the study has determined the appropriate etching time of hard template for the HMSNs synthesized from this reduced-size template. The highlight of this study was that the modified synthesis process of HMSN particles by hard template method to both achieve the desired HMSN particle size and shorten the time and corresponding cost of synthesis.

The N₂ adsorption–desorption isotherms and the pore size distributions of HMSN were shown in Figure 3.3c and Figure 3.4d. As can be seen, the HMSN's isotherms was classified as Langmuir type IV isotherm curve and type H₂ hysteresis loop according to IUPAC, proving mesoporous nature of the synthesized HMSN [132, 133]. Additionally, the surface area and the pore diameter of HMSN were determined as about 767.2 m²/g and 2.5 nm, respectively. These results are in relative agreement with the previous publications [68, 134].

As seen from the FT-IR spectrum (Figure 3.4a), the strong absorption bands at 1103 cm⁻¹, 814 cm⁻¹ and 467 cm⁻¹ were attributed to the anti-symmetric stretching vibration, symmetric stretching vibration and bending vibration of Si-O-Si, respectively. The characteristic absorption peaks at 3500 cm⁻¹ and 951 cm⁻¹ corresponded to the bending vibration of Si-OH [135]. The elemental composition on the surface of HMSN was identified via EDX analysis (Figure 3.4b). The EDX pattern showed the presence of oxygen and silicon elements with the atomic percentages of 68.82 and 31.18, respectively, predicting that CTAB and other reacted reagents were well removed [136].

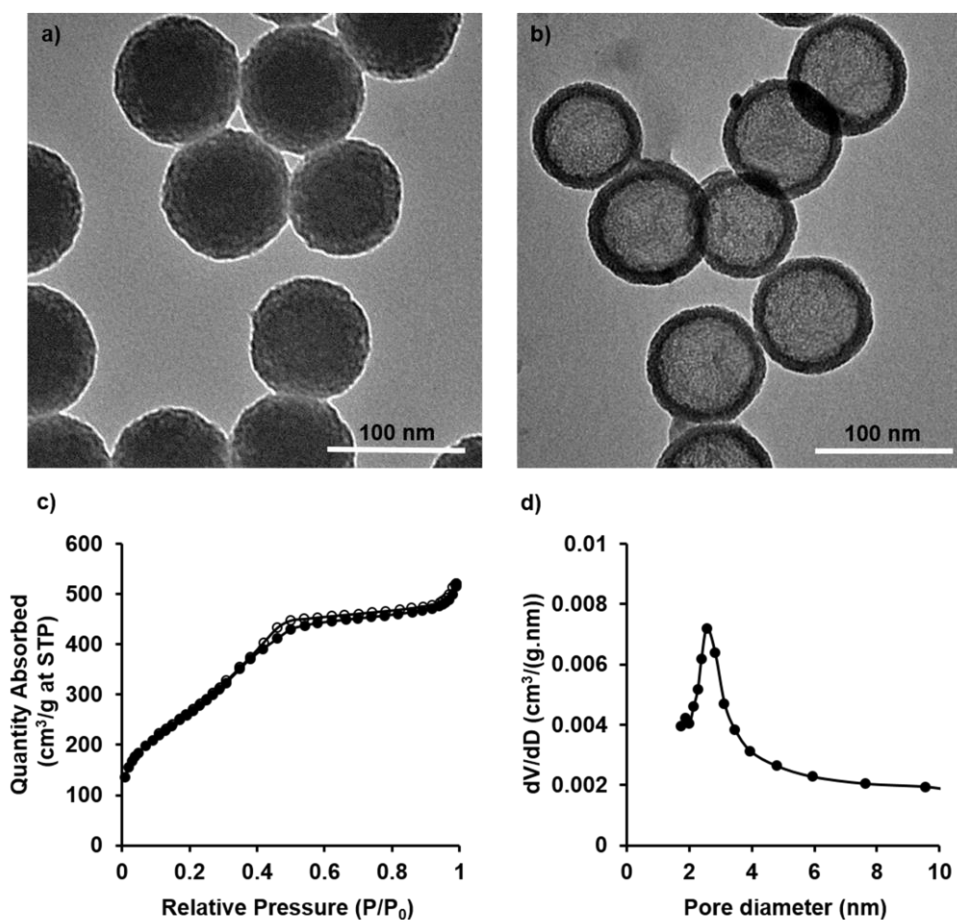


Figure 3.3. a) TEM image of dSiO₂@MSN; b) TEM image of HMSN, c) N₂ adsorption-desorption isotherms of HMSN and d) Pore size distributions of HMSN

The synthesized HMSN had a zeta potential of -46.6 ± 0.7 mV (Figure 3.4c), which was other than -30 mV to $+30$ mV, would help prevent agglomeration and kept the particles dispersed well [137]. DLS analysis determined the hydrodynamic size of HMSN was 108.2 ± 1.8 nm and PI was 0.083 (Figure 3.4d). Low PI value (< 0.1) indicated that the obtained HMSN was highly uniform with respect to the particle size [131]. Figure 3.4e showed the XRD pattern of HMSN with un-sharp peak at $2\theta = 23.9^\circ$, confirming the amorphous nature of silica particles [138]. Figure 3.4f presented the TGA graph HMSN. The initial weight loss at temperature below 200°C , which was about 4.6%, could be attributed to the physically adsorbed water. In the range of $200 - 800^\circ\text{C}$, no loss of weight was observed, indicating that CTAB and other reacting reagents were well removed.

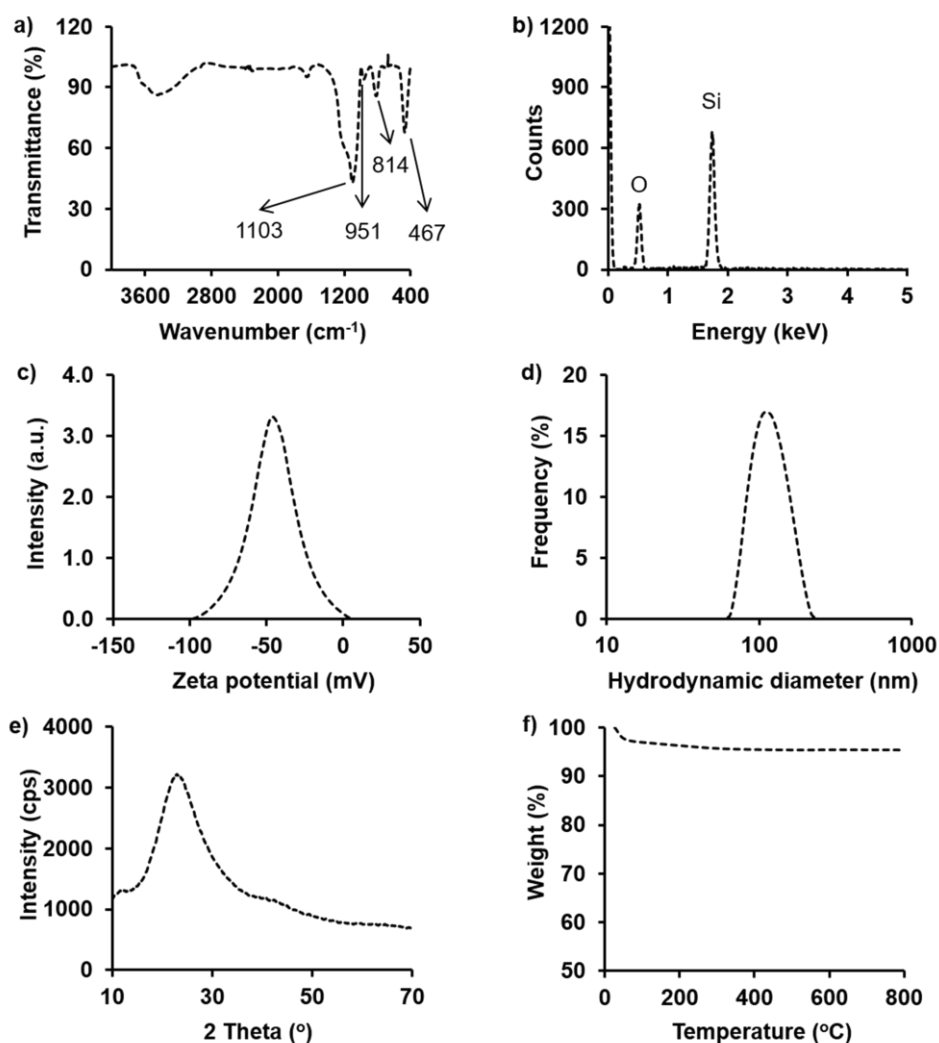


Figure 3.4. Characterizations of the synthesized HMSN: a) FT-IR spectrum; b) EDX pattern; c) Zeta potential; d) DLS particle size distribution; e) XRD pattern; and f) TGA graph

3.4. Cytotoxicity of synthesized HMSN

MTT assays on MCF-7 cell line were carried out to evaluate the cytotoxicity of the synthesized HMSN and the results were shown in Figure 3.5. As can be seen from the figure, the cell viability was 100% when being treated with 10 $\mu\text{g/mL}$ HMSN. When the treated concentration of HMSN increased to 250 $\mu\text{g/mL}$, the cell viability gradually decreased but remained higher than 80%. This meant the synthesized HMSN had no obvious toxicity on MCF-7 cells in a range of concentrations from 10 to 250 $\mu\text{g/mL}$, demonstrating that the synthesized HMSN in the current study could be regarded as a biocompatible nanocarrier.

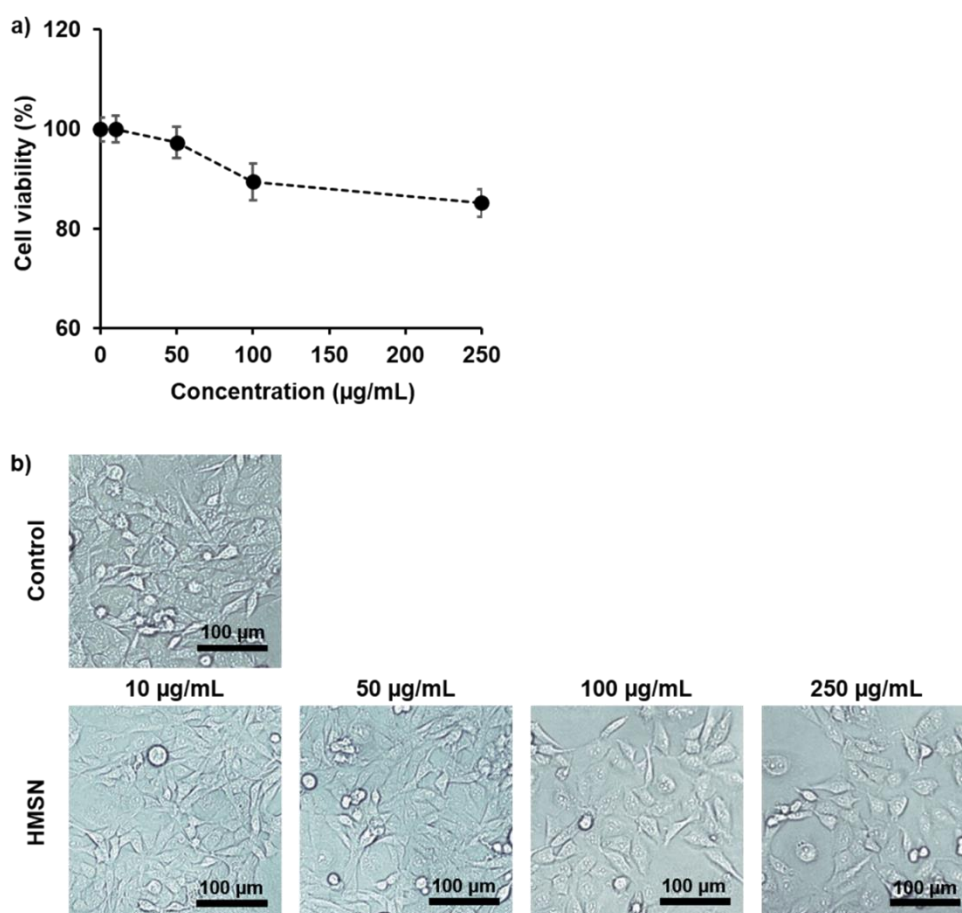


Figure 3.5. a) Cell viability assay by MTT assay with variable concentrations of HMSN on MCF-7 cells; b) Morphology of MCF-7 cells treated by HMSN at different concentrations

3.5. Summary

The HMSN particles with an optimal diameter were successfully prepared by the modified hard-templating in a shortened synthetic time. The obtained HMSN particles showed high uniform morphology as spheres with hollow core-mesoporous shell structure, having the particle diameter of about 80 nm, the hollow diameter of about 65 nm, and the mesoporous shell thickness of about 7.5 nm. The observation via SEM and TEM images of hard-template etching over time in the hollow mesoporous silica nanoparticle synthesis has shown that the suitable etching time has been determined to be 120 minutes. The synthetic time for the main reactions was shortened by more than half from 21 hours to 9 hours. Moreover, the synthesized HMSN performed as a biocompatible material with no *in vitro* toxicity at the

concentration up to 250 $\mu\text{g/mL}$. This modified hard-template method with shorter synthetic time and nearly 100 nm obtained particle diameter would be meaningful for scientific research and industrial scale production.

The research results of this content have been accepted for publication in Vietnam Journal of Science and Technology, ISSN 2525-2518, 0866-708X with the title “**A Modified Hard-Templating for Hollow Mesoporous Silica Nanoparticles Synthesis with Suitable Particle Size and Shortened Synthesis Time**”. Accepted notification in 20 August 2022.

CHAPTER 4. SIMPLY AND EFFECTIVELY CONTROL THE SHELL THICKNESS OF HOLLOW MESOPOROUS SILICA NANOPARTICLES BY POLYETHYLENE GLYCOL FOR DRUG DELIVERY APPLICATIONS

4.1. Effect of PEG molecular weight on the mesoporous shell thickness of $\text{dSiO}_2\text{@MSN}$

To investigate the effect of molecular weight of PEG on the mesoporous shell thickness of $\text{dSiO}_2\text{@MSN}$, PEG with molecular weights of 1000, 2000, 4000 and 6000 g/mol was added at a concentration of 3% (w/v) into the reaction mixture. The obtained samples were designated as $\text{dSiO}_2\text{@MSN-P1k}$, $\text{dSiO}_2\text{@MSN-P2k}$, $\text{dSiO}_2\text{@MSN-P4k}$ and $\text{dSiO}_2\text{@MSN-P6k}$ and their DLS size and FE-SEM images were shown in Figure 4.1.

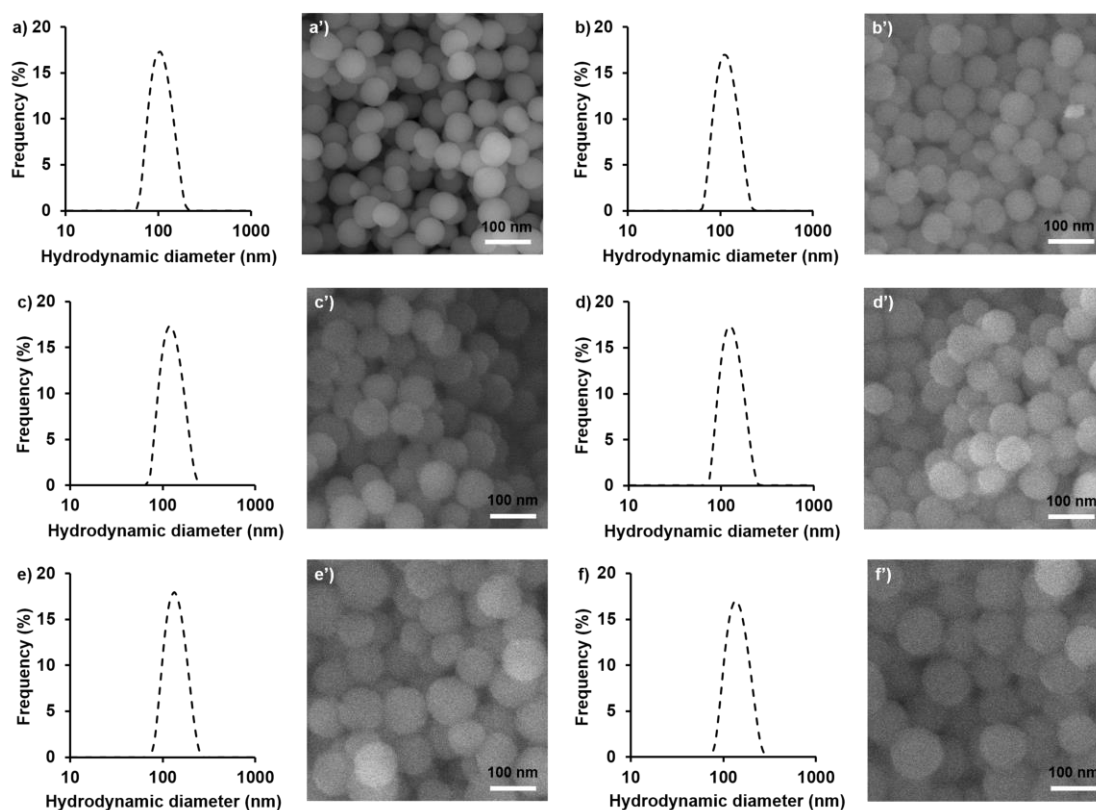


Figure 4.1. Size dispersion by DLS measurement and field-emission scanning electron microscopy (FE-SEM) images of (a, a') dSiO_2 , (b, b') $\text{dSiO}_2\text{@MSN}$, (c, c') $\text{dSiO}_2\text{@MSN-P1k}$, (d, d') $\text{dSiO}_2\text{@MSN-P2k}$, (e, e') $\text{dSiO}_2\text{@MSN-P4k}$ and (f, f') $\text{dSiO}_2\text{@MSN-P6k}$

First, all the samples including hard template dSiO₂ and mesoporous shell-coated particles samples dSiO₂@MSN and dSiO₂@MSN-P_xk (x was 1, 2, 4 and 6) were obtained with spherical shape, monodisperse, and highly narrow size distribution (polydispersity index (PI) ranged from 0.072 to 0.123). In addition, the FE-SEM images showed that dSiO₂ particles had clear boundaries and fine surface. Meanwhile, dSiO₂@MSN and dSiO₂@MSN-P_xk particles performed less clear boundaries and slightly rough surface. This suggested that mesoporous shell had been successfully coated on the hard template dSiO₂.

The particle diameter of dSiO₂, dSiO₂@MSN and dSiO₂@MSN-P_xk samples was calculated from FE-SEM images using ImageJ. Subsequently, the mesoporous shell thickness was calculated using the equation (1). The results are presented in Table 4.1.

Table 4.1. Effect of PEG molecular weight (1000, 2000, 4000 and 6000) at 3% (w/v) on the particle diameter and mesoporous shell thickness of dSiO₂@MSN samples (based on FE-SEM images). Means with the same upper letters (^a, ^b, ^c) are not statistically different based on the least significant difference at $p < 0.05$

Particles	Diameter (nm)	Shell thickness (nm)
dSiO ₂	65.3 ± 1.99	-
dSiO ₂ @MSN	75.8 ± 1.83 ^a	5.25
dSiO ₂ @MSN-P1k	79.1 ± 1.93 ^{a, b}	6.90
dSiO ₂ @MSN-P2k	85.2 ± 0.65 ^b	9.95
dSiO ₂ @MSN-P4k	94.1 ± 3.87 ^c	14.40
dSiO ₂ @MSN-P6k	97.7 ± 4.77 ^c	16.20

The results showed that at the same concentration of 3% (w/v) in the reaction mixture, when PEG molecular weight increased from 1000 to 6000 g/mol, the mesoporous shell thickness gradually increased from 6.90 nm to 16.20 nm, respectively. ANOVA analysis and Bonferroni Correction showed that there was no

statistically significant difference between the pairs dSiO₂@MSN versus dSiO₂@MSN-P1k, dSiO₂@MSN-P1k versus dSiO₂@MSN-P2k, and dSiO₂@MSN-P4k versus dSiO₂@MSN-P6k ($p < 0.05$).

For HMSNs with the same cavity volume, the one has a thicker mesoporous shell (means longer meso-channels) is expected to have more space for drug encapsulation and more sustained drug release profile. Moreover, in order to ensure a certain mechanical stability for HMSNs, they should have a sufficiently thick mesoporous shell so as not to break during handling and administration. Mechanical stability of HMSN was studied and proved to depend on the thickness of the mesoporous shell by Lasio *et al.* [139]. Accordingly, HMSNs with shell thickness from 14 to 18 nm with complete shells were broken under pressure from 103.0 to 123.6 MPa. Therefore, HMSN particles in the current study with mesoporous shell thickness in the range of 14.40 to 16.20 nm, which were obtained in the presence of 3% (w/v) PEG 4000 and PEG 6000, were expected to meet the above mentioned characteristics. PEG 6000 was chosen to prepare HMSN for further studies.

4.2. Effect of PEG weight percentage on the mesoporous shell thickness of dSiO₂@MSN

To investigate the effect of PEG weight percentage on the mesoporous shell thickness of dSiO₂@MSN, PEG 6000 was added to the reaction mixture at difference concentrations from 1% to 5% (w/v). The obtained samples were named as dSiO₂@MSN-Py% (y was from 1 to 5) and their DLS size and FE-SEM images were shown in Figure 4.2.

Similar to the previous experiment on the effect of PEG molecular weight on the mesoporous shell thickness, the dSiO₂@MSN-Py% samples were spherical, monodisperse, and highly uniform in particle size (PI ranged from 0.062 to 0.133). The mesoporous shell was successfully coated onto the hard template dSiO₂ particles with unclear boundaries and slightly rough surface. Based on the particle diameter of dSiO₂, dSiO₂@MSN and dSiO₂@MSN-Py% determined from FE-SEM images, the mesoporous shell thickness was calculated using the equation (1). The results are presented in Table 4.2.

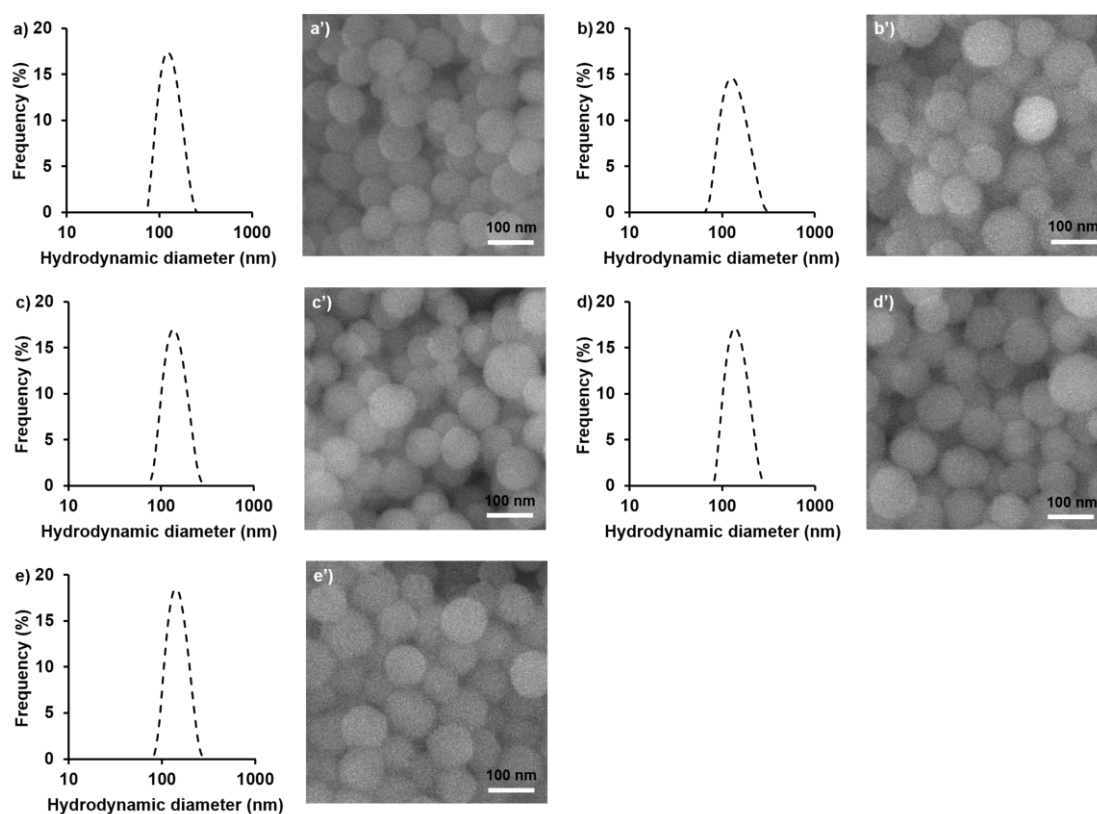


Figure 4.2. Size dispersion by DLS measurement and field-emission scanning electron microscopy (FE-SEM) images of (a, a') dSiO₂@MSN-P1%, (b, b') dSiO₂@MSN-P2%, (c, c') dSiO₂@MSN-P3%, (d, d') dSiO₂@MSN-P4% and (e, e') dSiO₂@MSN-P5%

When the concentration of PEG 6000 increased from 1% to 5% (w/v), the mesoporous shell thickness corresponding increased from 10.45 to 18.25 nm. These results once again confirmed that the presence of PEG in the reaction system would increase the mesoporous shell thickness of HMSN particles. However, ANOVA analysis and Bonferroni Correction showed no statistically significant difference between the samples dSiO₂@MSN-P2%, dSiO₂@MSN-P3%, dSiO₂@MSN-P4% and dSiO₂@MSN-P5%.

It was reported that in aqueous solution, ether oxygen atoms of PEG (–O–) formed hydrogen bonds with water molecules. Therefore, separate zigzag chains of PEG (Figure 4.3a) through hydrogen bonds with water molecules would form an ordered net structure (Figure 4.3b) [140-142]. At the same concentration in the reaction system, the high PEG molecular weight resulted in enlarged the PEG net

structure horizontally. Meanwhile, when the concentration in the reaction system of the same PEG increases, its ordered net structure will expand vertically.

Table 4.2. Effect of weight percentage of PEG 6000 (1% - 5%) on the particle diameter and mesoporous shell thickness of dSiO₂@MSN samples (based on FE-SEM images). Means with the same upper letters (^a, ^b, ^c) are not statistically different based on the least significant difference at $p < 0.05$

Particles	Diameter (nm)	Shell thickness (nm)
dSiO ₂	65.3 ± 1.99	-
dSiO ₂ @MSN	75.8 ± 1.83	5.25
dSiO ₂ @MSN-P1%	86.2 ± 1.01	10.45
dSiO ₂ @MSN-P2%	94.3 ± 0.87 ^a	14.50
dSiO ₂ @MSN-P3%	97.7 ± 4.77 ^a	16.20
dSiO ₂ @MSN-P4%	99.8 ± 2.46 ^a	17.25
dSiO ₂ @MSN-P5%	101.8 ± 1.68 ^a	18.25

When the amount of PEG added is greater than the saturation adsorption of the nanoparticles in solution, this ordered net structure could change the particle growth kinetics which promotes nucleation and facilitates the particle agglomeration [143]. Therefore, growing the PEG network in the solution either vertically (increase the PEG concentration) or horizontally (increase the PEG molecular weight) could promote the nucleation and agglomeration of silica nanoparticles. In addition, as an inert polymer, PEG has been commonly used to reduce surface intension [144]. The reduced surface intension of the shell coating solution might contribute to the promotion of nucleation and condensation of silica nanoparticles. For these reason, the mesoporous shell thickness increased as the PEG molecular weight or the PEG concentration in the reaction system increased. However, with a specific amount of TEOS precursors under a determined reaction conditions, to a certain limit, continuing to increase PEG molecular weight or PEG concentration could not further

enhance the nucleation and agglomeration of the nanoparticles. This result was consistent with the previous publications about the role of PEG on nanoparticle crystallization [78, 83].

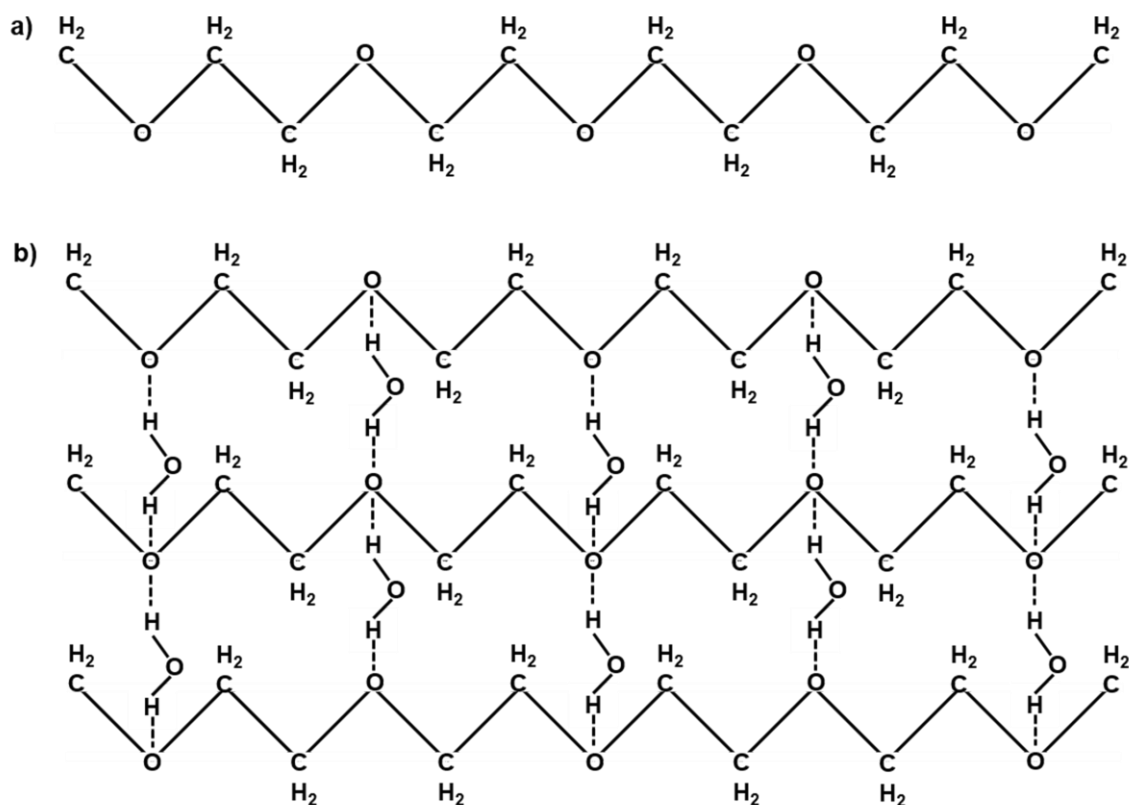


Figure 4.3. The structure of PEG changes from a) zigzag chains to b) ordered net structure in the solution

Based on the calculated mesoporous shell thickness in Table 4.2 and statistical analysis, PEG 6000 at the concentration of 2% (w/v) was selected to synthesize HMSN for further experiments. In order to better evaluate the role of PEG on the properties of the synthesized HMSN materials, the obtained particles with the presence of PEG in the synthesis – HMSN-P2% would be characterized in the comparison with HMSN-0.

4.3. Characterizations of the synthesized HMSNs

The synthesized HMSN particles with and without the presence of PEG were characterized via TEM, Zeta potential, FT-IR and EDX analysis. The characterization results were showed in Figure 4.4 and Figure 4.5.

In Figure 4.4, both $\text{dSiO}_2\text{@MSN}$ and HMSN samples with and without PEG were morphologically monodispersed spherical particles. Statistical results based on TEM images showed that the HMSN-0 particles had a diameter of 80.2 nm and a mesoporous shell thickness of 7.5 nm, and HMSN-P had a diameter of 94.3 nm and a 14.5 nm-thick mesoporous shell. This result was relatively consistent with the results presented in section 3.2, which was calculated based on DLS size and Equation (4). In addition, zeta potential of both HMSN-0 and HMSN-P had negative values near -50 mV, indicating that PEG was well removed from the synthesized HMSN-P samples.

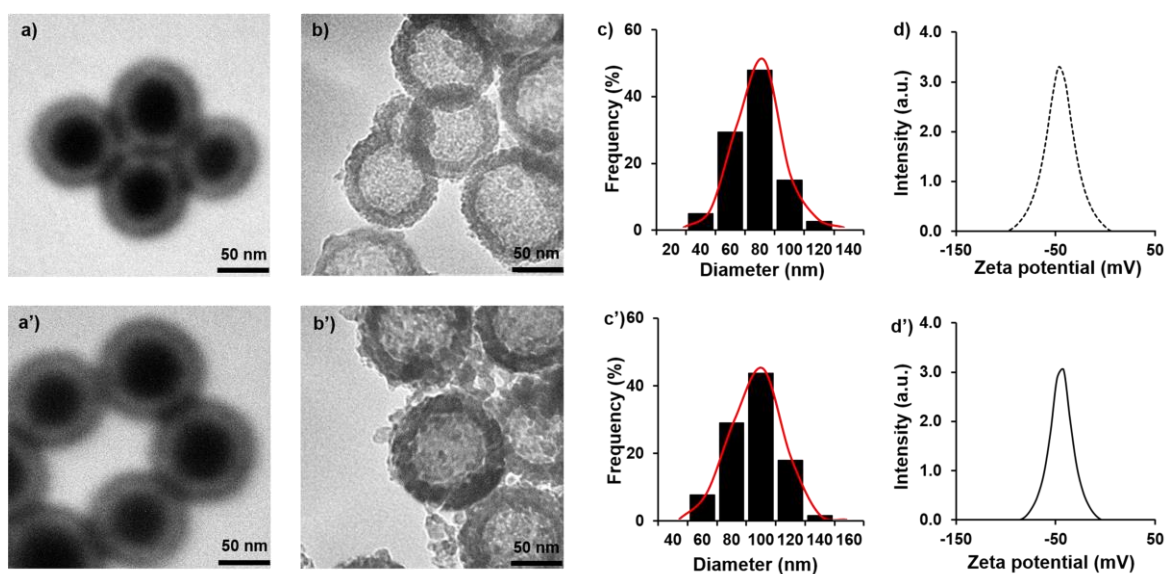


Figure 4.4. Characterizations of the synthesized silica nanoparticles: a) TEM images of $\text{dSiO}_2\text{@MSN}$ -0 and a') $\text{dSiO}_2\text{@MSN}$ -P; TEM images of b) HMSN-0 and b') HMSN-P; Size distribution of c) HMSN-0 and c') HMSN-P; Zeta potential of d) HMSN-0 and d') HMSN-P

BET and BJH analysis were conducted to evaluate the surface area and mesopore diameter of the two samples. The results were presented in Figure 4.5. According to IUPAC classification, the adsorption isotherms of both $\text{dSiO}_2\text{@MSN}$ -0 and $\text{dSiO}_2\text{@MSN}$ -P were Langmuir type IV isotherm curve and type H_2 hysteresis loop, which is characterized by mesoporous materials [132, 133]. This result suggested that the presence of PEG in the reaction mixture during the mesoporous shell coating

step did not alter the nature of the nitrogen adsorption-desorption isotherms of the original particle [40].

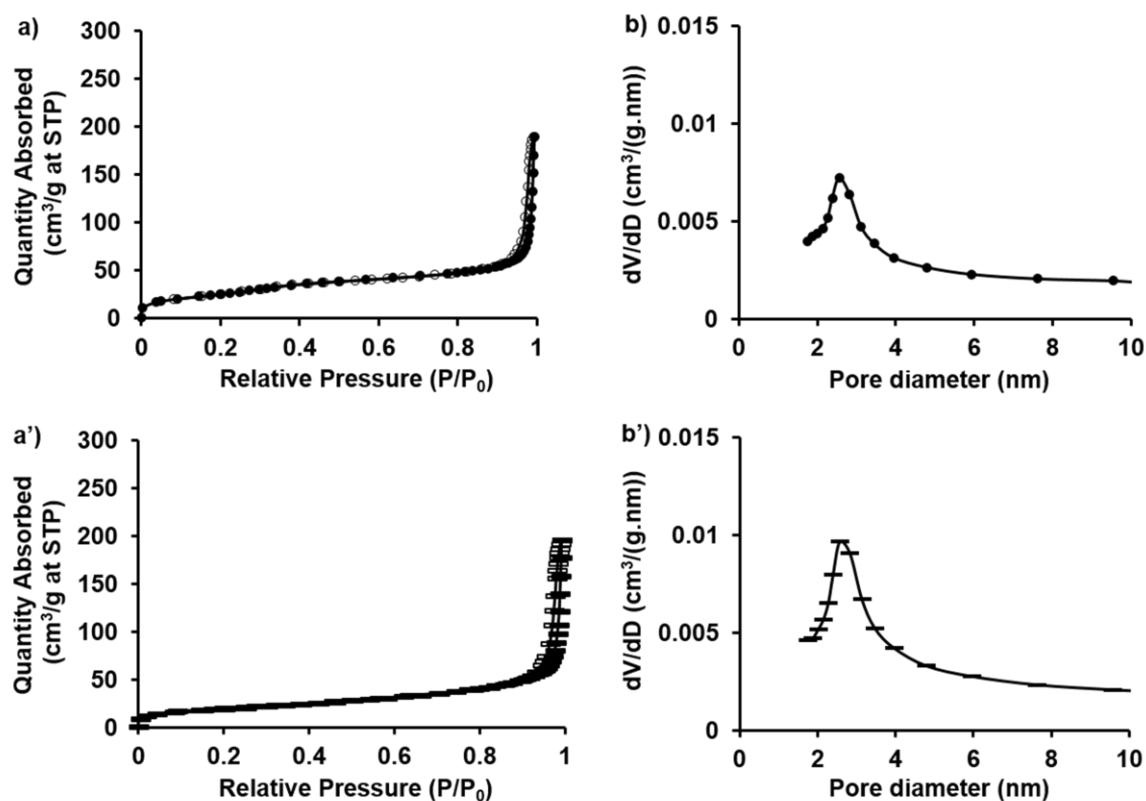


Figure 4.5. The N₂ adsorption-desorption isotherms and pore size distributions of dSiO₂@MSN (a and b) and dSiO₂@MSN-P (a' and b')

The mesopore diameter of dSiO₂@MSN-0 and dSiO₂@MSN-P were determined as 2.5 nm, which was in agreement with the previous reports using CTAB micelle as soft template for mesochannels [145, 146]. Meanwhile, the N₂ adsorption capacity and BJH Adsorption dV/dD pore volume of dSiO₂@MSN-P were higher than those of dSiO₂@MSN-0. Corresponding to these, the surface area of dSiO₂@MSN-P was 76.1 m²/g, higher than that of dSiO₂@MSN-0 (67.2 m²/g). The increase of the N₂ adsorption capacity and BJH Adsorption dV/dD pore volume as well as surface area of dSiO₂@MSN-P compared to dSiO₂@MSN-0 was due to the increase of its mesoporous shell thickness. Together with the result of DLS, SEM and TEM, it can be concluded that the presence of PEG in the shell coating step of HMSN synthesis helped increase the mesoporous shell thickness.

The elemental composition on the surface of HMSN-0 and HMSN-P was identified using EDX analysis (Figure 4.6a). The EDX patterns showed the presence of oxygen elements at 0.53 keV and silicon elements at 1.75 keV. The atomic percentages of oxygen and silicon were 70.6 and 29.4 for HMSN-0 and were 74.2 and 25.8 for HMSN-P, respectively. These results were consistent with the atomic ratio of silicon dioxide (SiO_2) molecular, proving that CTAB, PEG and other reacted reagents were well removed [136]. It could be seen from the FT-IR spectra (Figure 4.6b) that the strong absorption bands at 1103 cm^{-1} , 814 cm^{-1} and 467 cm^{-1} were assigned to the anti-symmetric stretching vibration, symmetric stretching vibration and bending vibration of Si-O-Si, respectively. Moreover, two characteristic absorption peaks for the bending vibration of Si-OH were witnessed at 3500 cm^{-1} and 951 cm^{-1} [135].

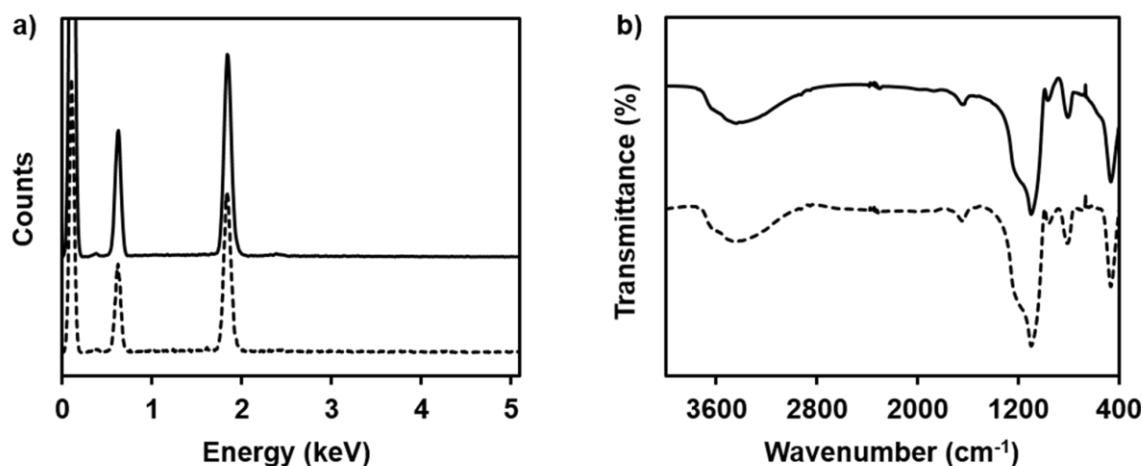


Figure 4.6. Characterizations of the synthesized HMSN-0 (square dot) and HMSN-P (solid): a) EDX patterns; b) FT-IR spectra.

4.3.1. Drug loading and in vitro drug release study of the synthesized HMSN

DLE and DLC values for DOX of HMSN-0 and HMSN-P were measured and presented in Figure 4.7a. The results showed that DLE and DLC values of HMSN-P slightly lower than those of HMSN-0. This might be due to the fact that although HMSN-0 and HMSN-P had the same hollow cavity volume, HMSN-P had a thicker shell than HMSN-0. Therefore, HMSN-P had a smaller number of particles in the

same particle mass than HMSN-0. This meant that for the same mass of particles, HMSN-0 had more space for DOX to be loaded than HMSN-P, leading to slight decrease in DLC and DLE values of HMSN-P. However, there was no statistical difference of DLC and DLE between the two samples ($p < 0.05$). This result showed that although the mesoporous shell thickness increased in the presence of PEG, the drug loading capacity of HMSN materials was still maintained.

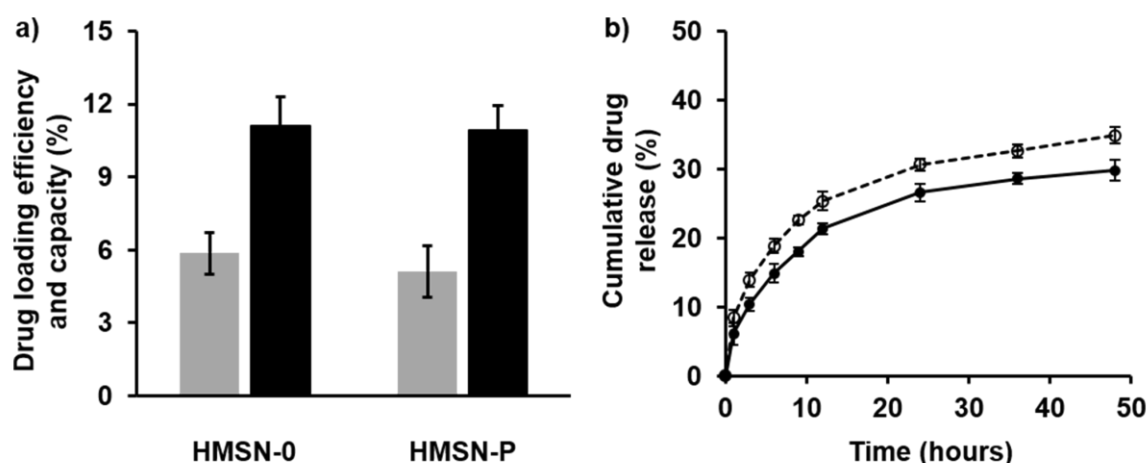


Figure 4.7. DOX loading capacity (DLC - grey) and DOX loading efficiency (DLE - black) of HMSN-0 and HMSN-P (a); *In vitro* release profile of Dox@HMSN-0 (empty circle) and Dox@HMSN-P (solid circle) (b). The marked points correspond to 0, 1, 3, 6, 9, 12, 24, 36 and 48 h, respectively

The drug release profile of Dox@HMSN-0 and Dox@HMSN-P in microenvironmental conditions was presented in Figure 4.7b. Both HMSN-0 and HMSN-P showed sustainable release profiles with no more than 35% of the initial DOX was released by each within 48 h. However, from the 12-hour mark onwards, the amount of drug released from HMSN-P was about 4-5% lower than from HMSN-0. This suggested that with similar drug loading, HMSN-P had longer meso-channels and exhibited better controlled release pattern than HMSN-0. The reason for this might be that the drug took longer to pass through the longer meso-channels to the outside [68, 69].

4.4. Cytotoxicity of the synthesized HMSN

The cytotoxicity of the synthesized HMSN-0 and HMSN-P were evaluated by MTT assays on MCF-7 cell line. The results were illustrated in Figure 4.8. As can be seen from the figure, the cell viability remained 100% when being treated with 10 $\mu\text{g/mL}$ of both synthesized materials while the cell viability witnessed a gradual decrease, yet it still remained higher than 80% in the cell viability when the treated concentration was increased to 250 $\mu\text{g/mL}$. This indicated that there was no cytotoxicity from the synthesized nanocarriers was observed on MCF-7 cell in the range of concentration from 10 to 250 $\mu\text{g/mL}$, therefore emphasizing that HMSN-0 and HMSN-P in the current study could be recognized as a biocompatible nanocarriers.

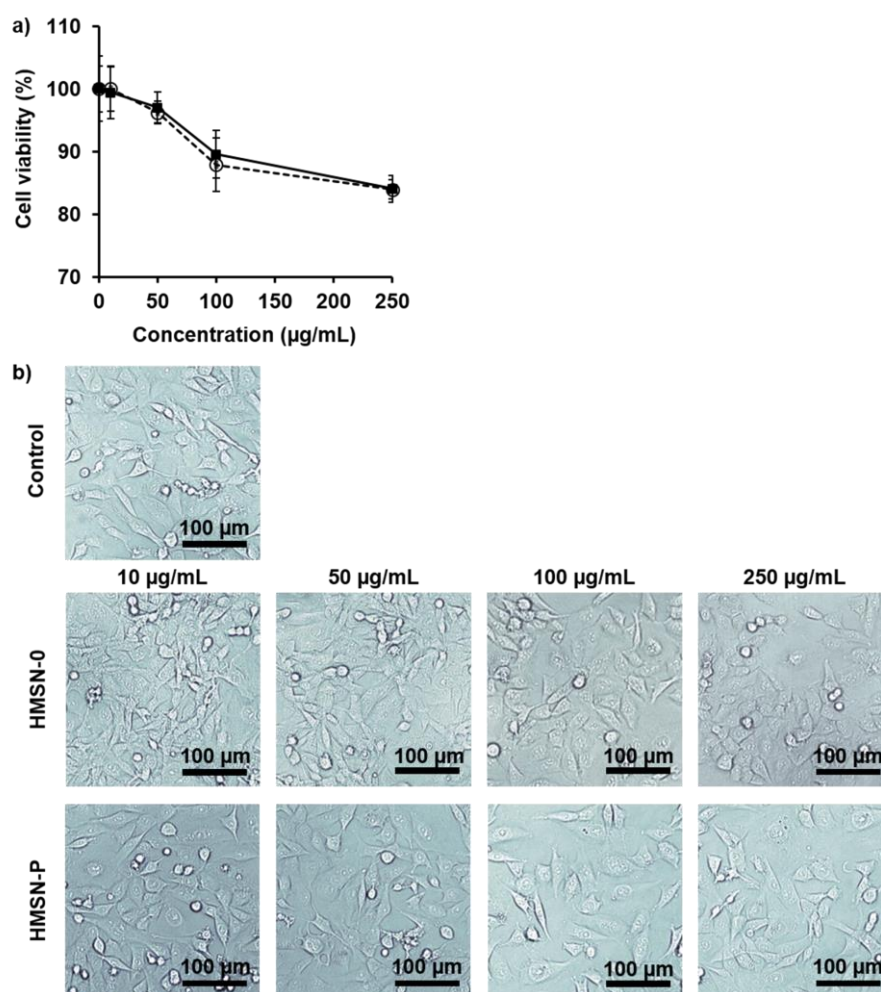


Figure 4.8. Cell viability by MTT assay with variable concentrations of HMSN-0 and HMSN-P on MCF-7 cells (a); MCF-7 cells treated by HMSN-0 and HMSN-P at different concentrations (b)

4.5. Summary

This study reported the synthesis of HMSN by hard template method with the presence of PEG in the mesoporous shell coating step as the capping agent. PEG with different molecular weights and concentrations showed notable influence on the HMSN's size. As the PEG molecular weight increased from 1000 to 6000 g/mol at the concentration of 3% or the PEG 6000 concentration increased from 1% to 5% (w/v), the mesoporous shell thickness gradually raised from 6.90 to 16.20 nm and from 10.45 to 18.25 nm, respectively (based on FE-SEM image size). dSiO₂@MSN-P synthesized in the presence of 2% PEG 6000 retained the monodispersed spherical morphology with a particle diameter of 94.3 nm and a mesoporous shell thickness of 14.5 nm, which was about 7.0 nm thicker than that of dSiO₂@MSN-0. The pore size and surface area of dSiO₂@MSN-0 and dSiO₂@MSN-P were determined as 2.5 nm, 67.2 m²/g and 2.5 nm, 76.9 m²/g, respectively. HMSN-P showed a slightly lower drug loading capacity but exhibited a better controlled drug release profile than HMSN-0. In addition, both HMSN-0 and HMSN-P performed no *in vitro* cytotoxicity at the concentration up to 250 µg/mL, demonstrating that they were biocompatible materials. These results contributed useful and meaningful information to the basic theory of hollow mesoporous silica nanoparticle synthesis for drug delivery applications.

The research results of this content have been published in the Journal of Applied Polymer Science, SCIE/SSCI, Q2, H index 175, IF 3.125, ISSN 0021-8995 (print); 1097-4628 (web) with the title “**Simply and Effectively Control the Shell Thickness of Hollow Mesoporous Silica Nanoparticles by Polyethylene Glycol for Drug Delivery Applications**”. DOI: <https://doi.org/10.1016/j.colsurfa.2022.130218>.

CHAPTER 5. NON-IONIC SURFACTANTS AS CO-TEMPLATES TO CONTROL THE MESOPORE DIAMETER OF HOLLOW MESOPOROUS SILICA NANOPARTICLES FOR DRUG DELIVERY APPLICATIONS

5.1. Preparation of mixed micelles of non-ionic surfactants with CTAB

The non-ionic surfactants Brij S10, Tween 20 and Tween 80 were used to prepare mixed micelles with the constant amount of CTAB so that the molar ratio of the surfactants and CTAB ($nS:nCTAB$) gradually increased. The obtained mixed micelles were determined viscosity and DLS diameter. The results were presented in Figure 5.1.

For the viscosity, each mixture was kept at their prepared concentration and measured the viscosity by Brookfield DV III Rheometer using spindle CP40 at 250 rpm. There was a similarity in the viscosity change of the mixed micelle solution T20-CTAB and T80-CTAB. The viscosity of the micelle solutions decreased from the origin when one of these two surfactants was added. Although the viscosity of the mixed micelle solution polysorbate-CTAB increased as the molar ratio $nS:nCTAB$ increased, ranging from about 3 to 30 cP, this increase was not significant compared to the viscosity of the original CTAB micelle solution (57.1 cP). In contrast to the polysorbates, the presence of high molar ratio of BS10 markedly increased its mixed micelle solution viscosity, raising from 57.1 to 484.0 cP. Viscosity is one of the factors that reflect the mechanical and physical properties of the medium that can affect the reaction process. Therefore, the information of the viscosity of mixed micelle solutions explains the results of the synthesis.

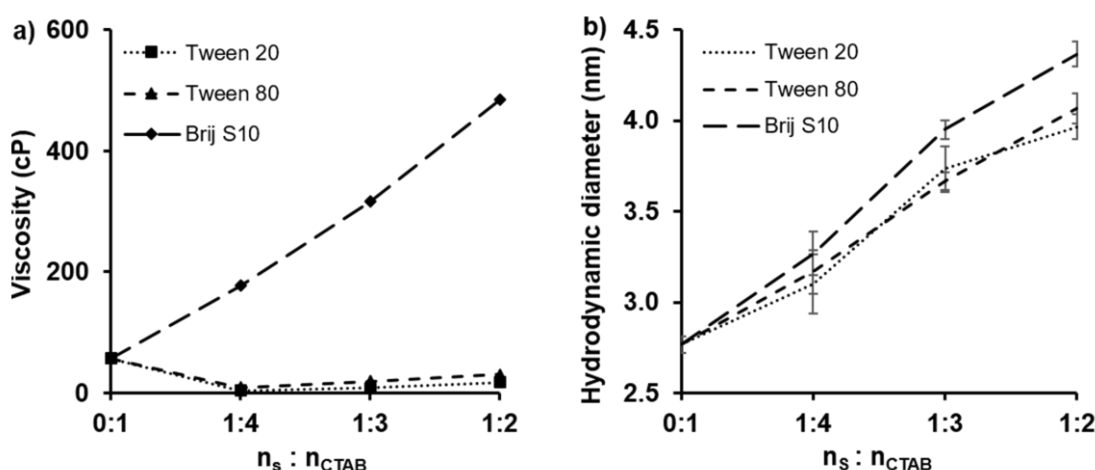


Figure 5.1. a) Viscosity of mixed micelles versus molar ratio of non-ionic surfactants and CTAB. Molar concentration of CTAB remained constantly at 0.02 M. b) Hydrodynamic diameter of mixed micelles versus molar ratio. Molar concentration of CTAB in each mixture was 50 mM in the presence of 1 mM KBr

At the concentration of 0.02 M, much higher than CMC of CTAB and its binary combinations with non-ionic surfactants [75], these mixed micelles had cylindrical forms [147]. To simply estimate the correlation between the cylindrical micelle diameters with molar ratios of non-ionic surfactants with CTAB, each solution was diluted to the CTAB concentration of 50 mM, at which they form spherical micelles [148, 149], and measured their hydrodynamic size of formed spherical micelles by Horiba SZ-100. In general, the mixed micelle diameter was significantly higher than that of micelle CTAB (Figure 5.1b). For each binary combination, the micelle diameter increased by the increasing of the molar ratio $nS:nCTAB$. There was a similarity in micelle size change by the molar ratios $nS:nCTAB$ between the mixed micelle T20-CTAB and T80-CTAB. When the $nS:nCTAB$ ratio increased from 1:4 to 1:2, the diameter of T20 and T80 mixed micelles increased gradually from 3.1 nm to 4.0 nm, while those of mixed micelle BS10-CTAB increased from 3.2 nm to 4.2 nm. The above results on the spherical mixed micelle diameter would help predicting the mesopore diameter of the synthesized hollow mesoporous materials using mixed micelle as soft-templates.

5.2. Effect of non-ionic surfactants on the mesoporous shell thickness of dSiO₂@MSN

To investigate the effect of Tween 20, Tween 80 and Brij S10 in mixed micelles on the mesoporous shell thickness of dSiO₂@MSN, mixed micelles of the three non-ionic surfactants with CTAB at different molar ratios were used as co-templates in the shell coating step. The obtained samples dSiO₂@MSN-S were determined DLS size (Figure 5.2).

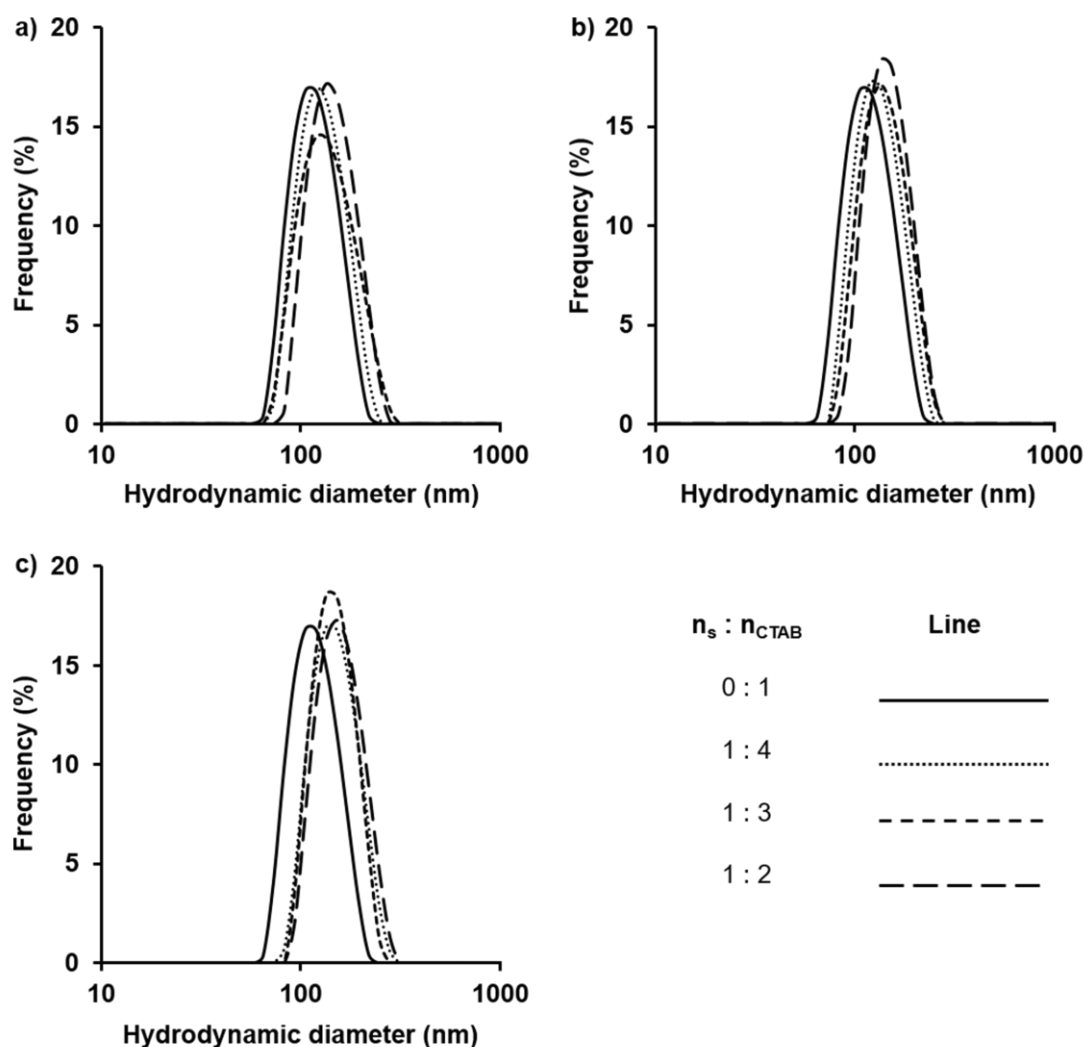


Figure 5.2. Size distribution by DLS measurement of a) dSiO₂@MSN-T20, b) dSiO₂@MSN-T80, and c) dSiO₂@MSN-BS10

The DLS diameter of dSiO₂@MSN and dSiO₂@MSN-S samples were higher than that of dSiO₂, proving that the mesoporous shell was successfully coated onto

the hard templates dSiO₂ and the obtained particles were spherical, monodisperse, and highly uniform in particle size (PI ranged from 0.062 to 0.133). Based on the DLS diameter of dSiO₂ (reported as 96.8 ± 1.99 nm in Chapter 3), dSiO₂@MSN and dSiO₂@MSN-S, the mesoporous shell thickness was calculated using the equation (4) and presented in Table 5.1.

Table 5.1. The mesoporous shell thickness (nm) of dSiO₂@MSN particles versus the molar ratio of non-ionic surfactants with CTAB in mixed micelles

Surfactants	Tween 20	Tween 80	Brij S10
n_S:n_{CTAB}			
0 : 1	4.65	4.65	4.65
1 : 4	9.45	10.45	18.70
1 : 3	13.60	13.80	20.50
1 : 2	16.70	17.45	21.10

For each non-ionic surfactant, the mesoporous shell thickness gradually increased when its molar ratio with CTAB increased. This suggested that the higher the presence of non-ionic surfactants in the mixed micelle, the larger the mixed micelle diameter and the thicker the mesoporous shell. This phenomenon could be explained through the model in Figure 5.3 as follow: when the diameter of micelles used as co-templates of mesopore increased, the residual surface area as well as the space around the dSiO₂ templates for the siloxane bridges to condense was narrowed, leading to the increase in the thickness of the mesoporous shell.

For further investigation on the influence of non-ionic surfactants on mesopore diameter of HMSN, three synthesized dSiO₂@MSN samples using mixed micelles of T20, T80 or BS10 with CTAB at the molar ratio n_S:n_{CTAB} of 1:2 was determined their surface area and mesopore diameter.

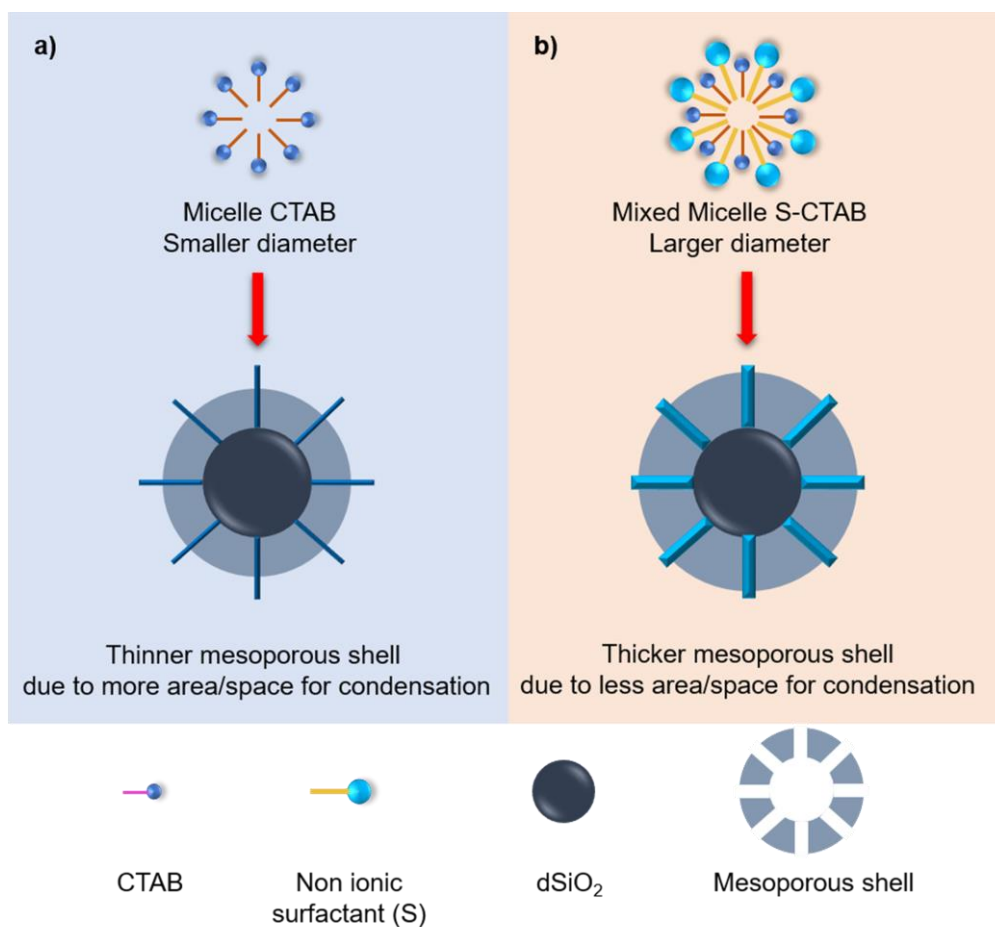


Figure 5.3. Illustration of the effect of non-ionic surfactants in mixed micelles on the mesoporous shell thickness of dSiO₂@MSN

5.3. Effect of non-ionic surfactants on the mesopore diameter of dSiO₂@MSN

As mentioned in the previous section, the mesopore diameter could be predicted based on the diameter of mixed micelle S-CTAB. However, to be certain about the mesopore size distribution, the BET method and BJH model are useful tools. The N₂ adsorption–desorption isotherms and the pore size distributions of dSiO₂@MSN samples were shown in Figure 5.4. According to IUPAC classification, the adsorption isotherms of the four samples were Langmuir type IV isotherm curve and type H₂ hysteresis loop. This type of pathway is characterized by mesoporous materials [132, 133], suggesting that the presence of non-ionic surfactants in the mixed micelle during the mesoporous shell coating step did not change the nature of the nitrogen adsorption-desorption isotherms of the original particle [40].

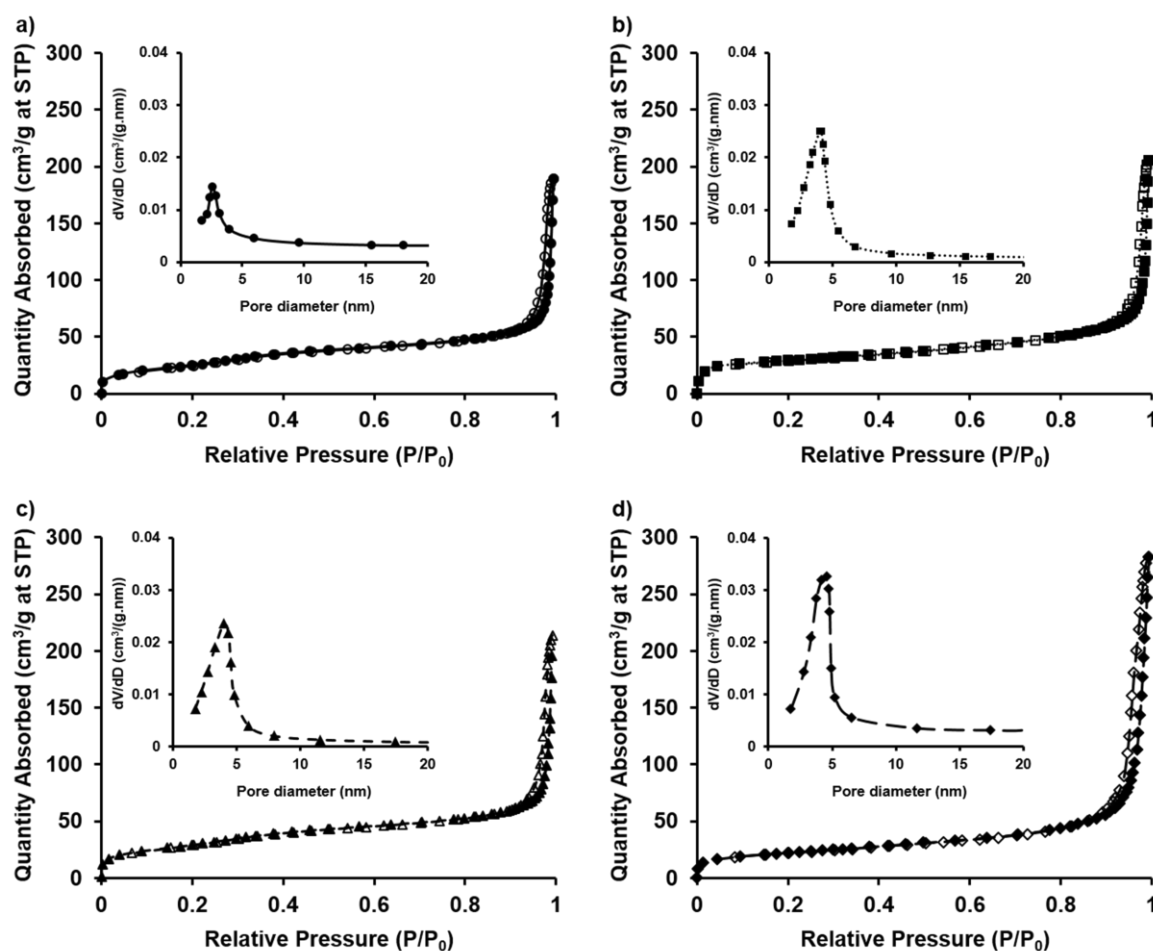


Figure 5.4. The N_2 adsorption-desorption isotherms and pore size distributions of a) $dSiO_2@MSN$, b) $dSiO_2@MSN-T20$, c) $dSiO_2@MSN-T80$ and d) $dSiO_2@MSN-BS10$

It was found that the N_2 adsorption capacity and the pore size of the samples gradually increased when the micelles CTAB, T80-CTAB, T20-CTAB and BS10-CTAB as soft templates were used. With the presence of the non-ionic surfactant in the micelle as soft template, the pore diameter significantly increased from 2.5 nm to more than 4.0 nm, of which, there was no notably different between the two samples $dSiO_2@MSN-T20$ and $dSiO_2@MSN-T80$ (4.1 nm and 4.0 nm), meanwhile $dSiO_2@MSN-BS10$ owned the biggest mesopores (4.5 nm). Corresponding to the increase in pore diameter, the surface area of $dSiO_2@MSN$, $dSiO_2@MSN-T20$, $dSiO_2@MSN-T80$ and $dSiO_2@MSN-BS10$ samples were 67.2, 91.8, 92.2 and 106.7 m²/g, respectively. The pore diameter results are in relative agreement with the mixed

micelle diameter results. Together with the illustration in Figure 5.3, the influence of non-ionic surfactants on mesopore diameter and mesoporous shell thickness has been clarified.

5.4. Characterizations of the synthesized HMSNs

The synthesized HMSN particles with and without the presence of non-ionic surfactants (at the molar ratio nS:nCTAB of 1:2) were characterized via SEM, TEM, particle size distribution, Zeta potential (Figure 5.5), XRD and FT-IR (Figure 5.6).

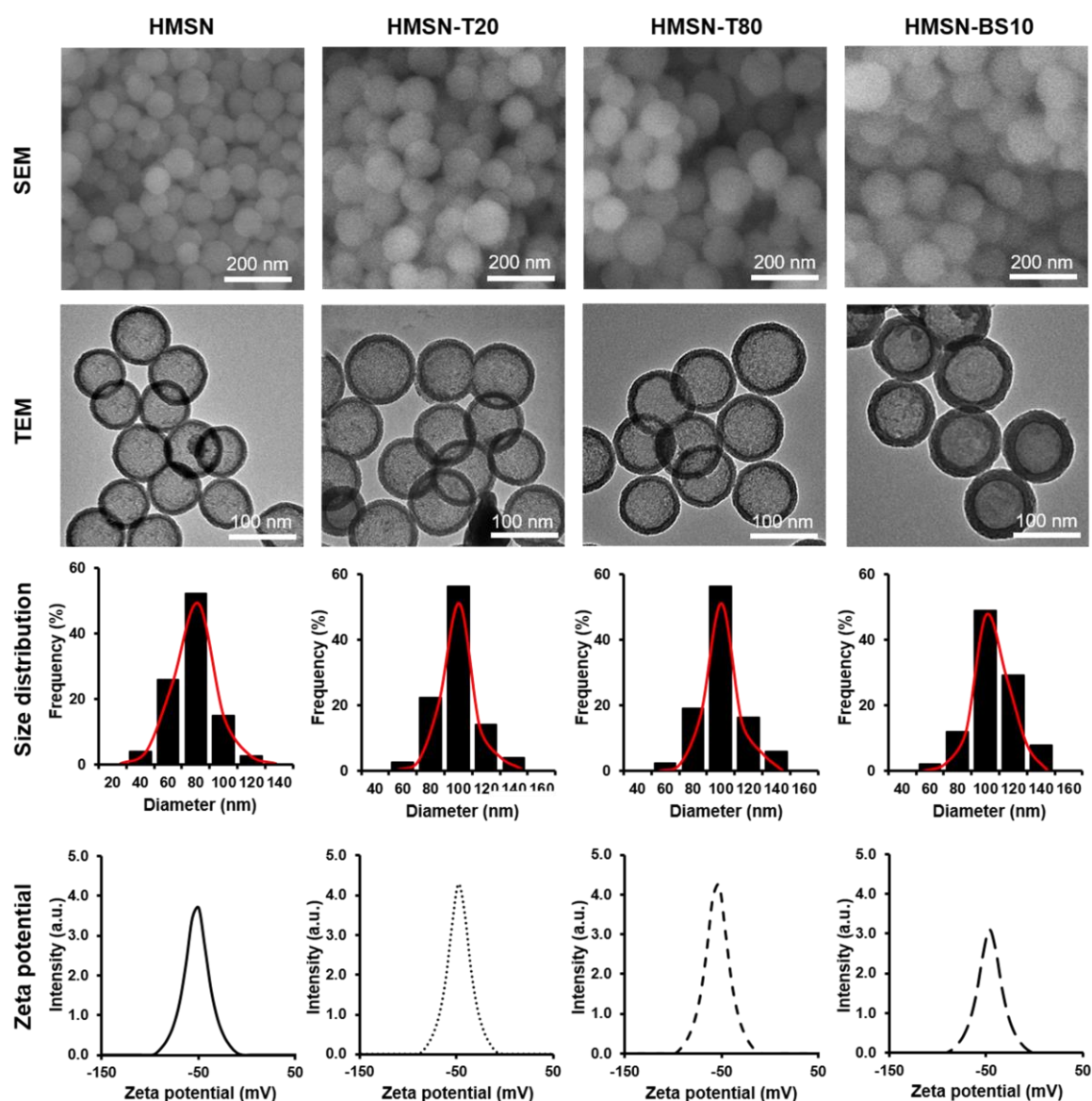


Figure 5.5. SEM images, TEM images, Size distribution and Zeta potential of HMSN, HMSN-T20, HMSN-T80 and HMSN-BS10

As could be seen, all the synthesized HMSN samples with and without non-ionic surfactants were morphologically monodispersed spherical particles. SEM images confirmed the spherical, monodisperse and narrow size distribution of the formed particles. Besides, they showed that the particles HMSN, HMSN-T20, HMSN-T80 and HMSN-BS10 had diameters, respectively, of 80.2, 99.3, 100.8 and 110.4 nm, which were consistent with the size of TEM images. Moreover, TEM images suggested that the synthesized HMSN with the presence of non-ionic surfactants remained its hollow@shell structure. Additionally, zeta potential of the four samples HMSN, HMSN-T20, HMSN-T80 and HMSN-BS10 had negative values around -50 mV, indicating that CTAB and other non-ionic surfactants were well removed from the synthesized HMSNs.

The XRD patterns in Figure 5.6a showed un-sharp peaks at about $2\theta = 23^\circ$, confirming that after being synthesized with and without non-ionic surfactants, the obtained HMSN samples remained the amorphous nature of silica particles [41].

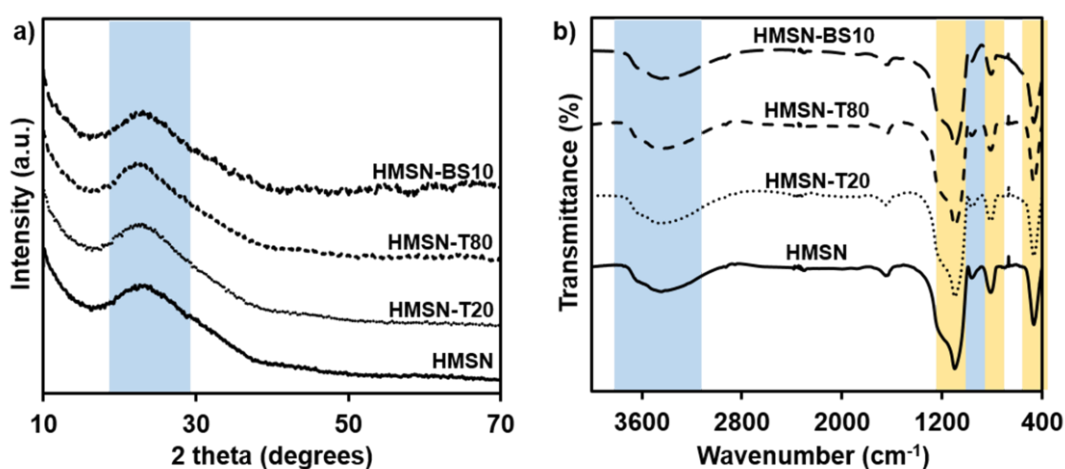


Figure 5.6. a) XRD patterns and b) FT-IR spectra of HMSN, HMSN-T20, HMSN-T80 and HMSN-BS10

In addition, the lack of other peaks in the XRD patterns proving that the synthesized HMSNs were highly pure. FT-IR spectra in Figure 5.6b provides information about the involved functional groups. The strong absorption bands at $1098\text{--}1105\text{ cm}^{-1}$, $807\text{--}811\text{ cm}^{-1}$ and $466\text{--}468\text{ cm}^{-1}$ were attributed to the presence of anti-symmetric stretching vibration, symmetric stretching vibration and bending

vibration of Si-O-Si, respectively. In addition, two characteristic absorption peaks for the bending vibration of Si-OH were witnessed, as respective wavenumbers at 3430-3440 cm^{-1} and 955-963 cm^{-1} [135].

5.5. Drug loading and *in vitro* drug release study of the synthesized HMSNs

DLE and DLC values for RB of HMSN, HMSN-T20, HMSN-T80 and HMSN-BS10 were measured and presented in Figure 5.7a. The results showed that both DLE and DLC values of HMSN were significant lower than those of HMSN-S. This might be due to the difference between the mesopore diameter and the cargo size. In the previous report, with Doxorubicin (DOX) (MW of 543.52 g/mol and molecular size of 1.5 nm [94]), HMSN (mesopore diameter of 2.5nm) performed relative good DLE and DLC values of 5.87% and 11.09%, respectively. In contrast, RB used in the current study had MW of 1017.64 g/mol, which was twice higher than that of DOX, would therefore own larger molecular size compared to DOX and be hard to pass through the mesopores of the original HMSN. The low values DLC and DLE of HMSN, which were 1.95% and 3.82%, respectively, were mainly the amount of RB adsorbed on the surface of the particles. Meanwhile, thanks to the presence of non-ionic surfactants, the mesopore diameter of HMSN-T20, HMSN-T80 and HMSN-BS10 were enlarged up to more than 4.0 nm, leading to an easy passage of RB through the mesoporous channels and higher amount of cargos loaded inside the hollow cavity. The similarity of DLC and DLE between HMSN-T20 and HMSN-T80 was explained by the fact that they had mesopores with similar diameters while HMSN-BS10 performed the best DLE and DLC because it had the largest mesoporous channels (as presented in the BET and BJH results).

For the drug release profiles (Figure 5.7b), RB@HMSN-S showed similar cumulative amount of released drug over the time, suggesting better control release profiles compared to that of RB@HMSN. The burst release of RB@HMSN might be due to RB was absorbed on the surface but unloaded inside the particles. Meanwhile it took time for the loaded RB in RB@HMSN-S to be released from the hollow through longer meso-channel to the outside [68, 69]. Among the three systems RB@HMSN-S, RB@HMSN-BS10 showed slightly faster release profile

compared to the others. This phenomenon was consistent with the largest mesopore diameter of HMSN-BS10 which was reported in the previous section.

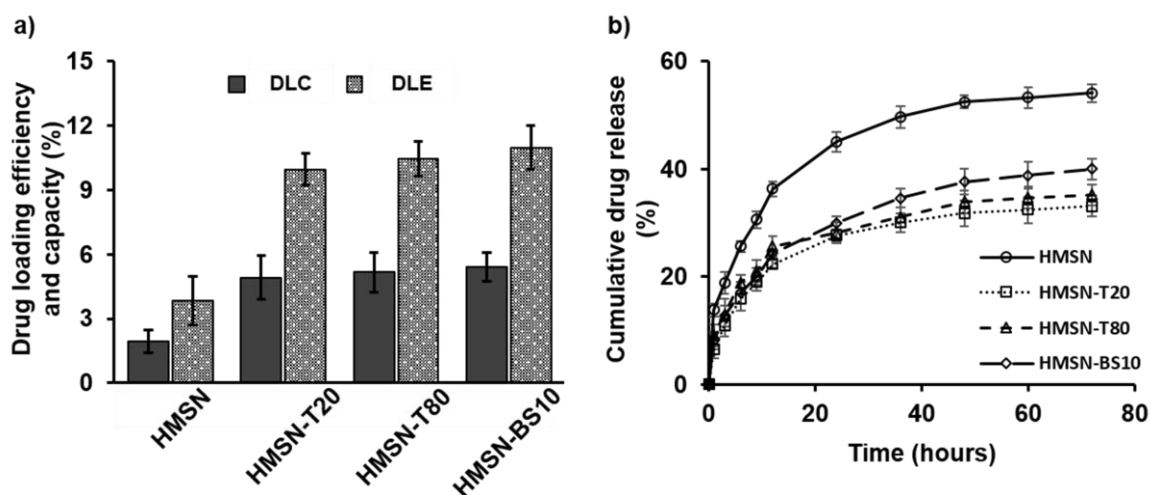


Figure 5.7. (a) Rose bengal (RB) loading capacity (DLC - grey) and loading efficiency (DLE - black) of HMSN, HMSN-T20, HMSN-T80 and HMSN-BS10; (b) *In vitro* release profile of RB from HMSN, HMSN-T20, HMSN-T80 and HMSN-BS10. The marked points correspond to 0, 1, 3, 6, 9, 12, 24, 36, 48, 60 and 72 h, respectively

5.6. Cytotoxicity of the synthesized HMSNs

The cytotoxicity of the synthesized HMSN and HMSN-S were evaluated by MTT assays on MCF-7 cell line. The results were illustrated in Figure 5.8. As can be seen from the figure, the cell viability remained 100% when being treated with 10 $\mu\text{g}/\text{mL}$ of both synthesized materials. Although the cell viability witnessed a gradual decrease, it still remained higher than 80% in the cell viability when the treated concentration increased to 250 $\mu\text{g}/\text{mL}$. Such observation states that there was no cytotoxicity recorded from the synthesized nanocarriers on MCF-7 cell in the aforementioned range from 10 to 250 $\mu\text{g}/\text{mL}$, and emphasizes that HMSN synthesized with or without the presence of non-ionic surfactants in this study could be both recognized as biocompatible nanocarriers.

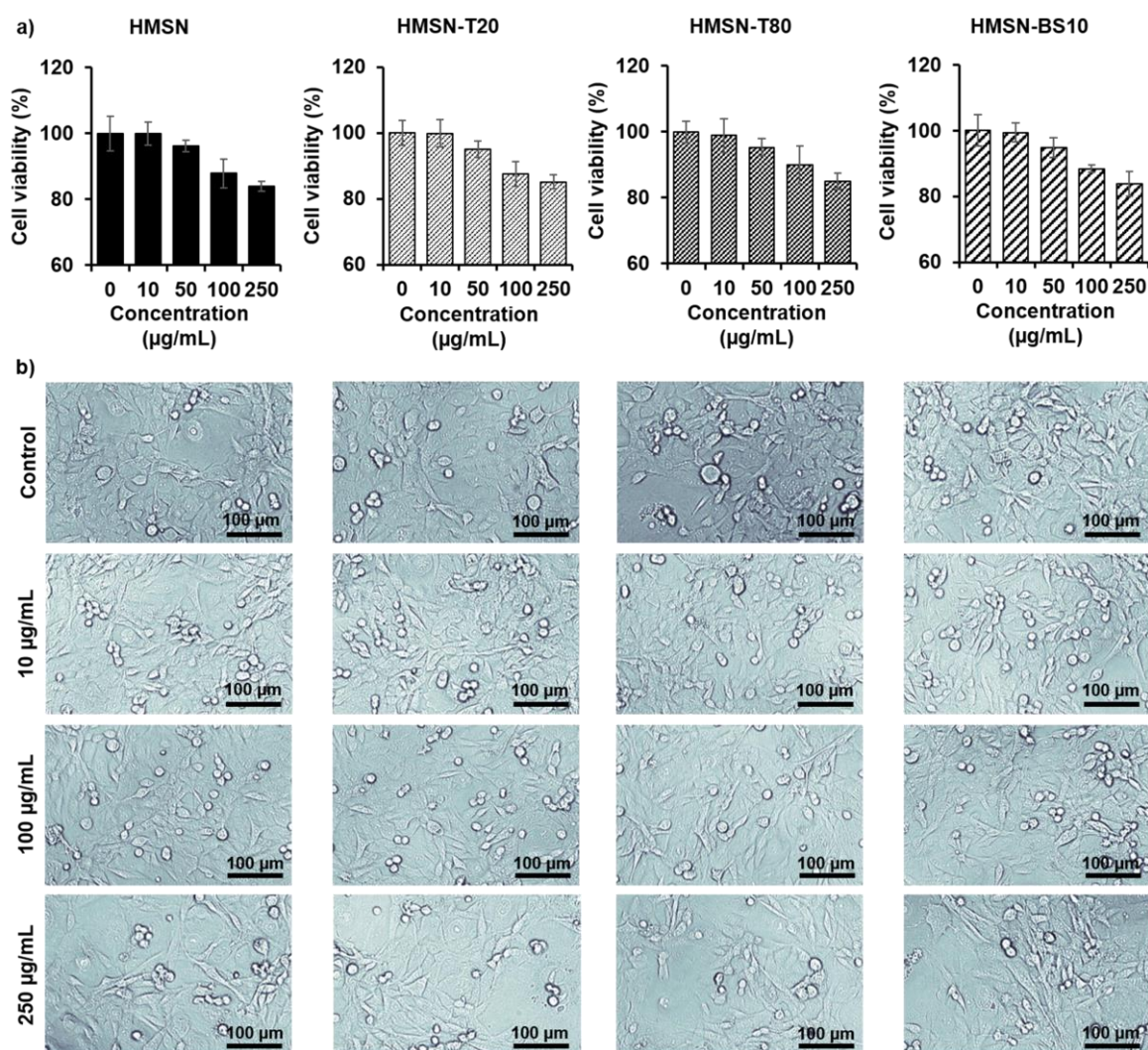


Figure 5.8. a) Cell viability by MTT assay on MCF-7 cells; and b) MCF-7 cells treated by HMSN, HMSN-T20, HMSN-T80 and HMSN-BS10 at different concentrations

5.7. Summary

Three non-ionic surfactants including Tween 20, Tween 80 and Brij S10 were successfully used as co-templates with CTAB at different molar ratios to adjust the mesopore diameter through the synthesis of HMSN by hard template method. The HMSN-S synthesized with mixed micelles S-CTAB owned significantly larger mesopores, of which, at the molar ratio nS:nCTAB of 1:2, HMSN-T20 and HMSN-T80 had 4.0 nm diameter meso-channels and HMSN-BS10 had 4.5 nm diameter meso-channels, compared to the original HMSN with mesopore diameter of 2.5 nm.

Besides, the increase in mesoporous shell thickness of the corresponding HMSN as its mesopore diameter increased was proved and explained. In addition, all the synthesized HMSNs were characterized and could be regarded as biocompatible materials. These results contributed useful and meaningful information to the basic theory of hollow mesoporous silica nanoparticle synthesis for drug delivery applications.

The research results of this content have been published in the journal *Colloids and Surfaces A: Physicochemical and Engineering Aspects*, SCIE/SSCI, Q2, H index 179, IF 5.518, ISSN 0927-7757 with the title “**Non-ionic Surfactants as Co-Templates to Control the Mesopore Diameter of Hollow Mesoporous Silica Nanoparticles for Drug Delivery Applications**”. DOI: <https://doi.org/10.1016/j.colsurfa.2022.130218>.

CHAPTER 6. SURFACE MODIFICATION OF HOLLOW MESOPOROUS SILICA NANOPARTICLES WITH PLURONICS FOR DUAL DRUGS DELIVERY

6.1. Activation Pluronic with NPC

Three Pluronics including L64, F68 and F12 were activated with NPC. The FT-IR spectra (Figure 6.1) of the activated NPC-Plu-OH samples appeared the absorption signals at 2878 cm^{-1} , 1468 cm^{-1} , and 1109 cm^{-1} , which attributed to the characteristic oscillations of $-\text{OCH}_2\text{-CH}_2-$, $-\text{NO}_2$, and C-O , respectively. This result proved that the three Pluronic were successfully activated with NPC [150].

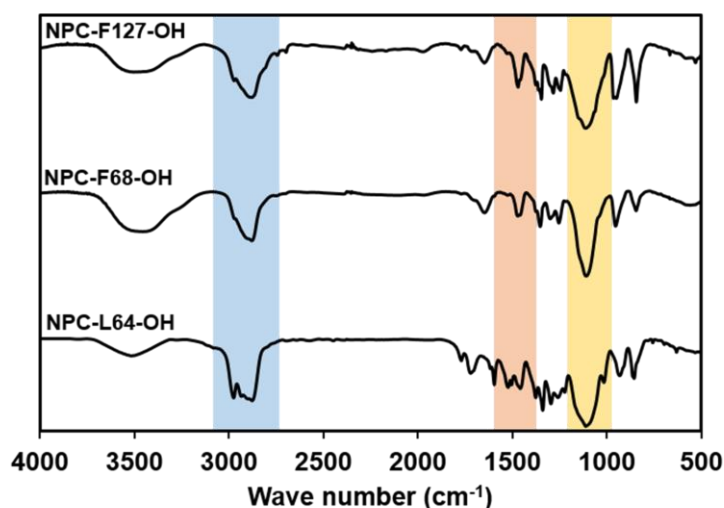


Figure 6.1. FT-IR spectra of NPC-Plu-OH

The structures of the NPC-Plu-OH samples were analyzed via $^1\text{H-NMR}$ analysis (Figure 6.2). The spectra had chemical shift signals at $\delta\text{H} = 3.34\text{ ppm}$ of $\underline{\text{H}}\text{C-O-}$ (d), $\delta\text{H} = 3.80 - 3.35\text{ ppm}$ of $-\text{O-}\underline{\text{C}}\text{H}_2\text{-CH-}$ (OCH_2)-(CH₃) (e), $\delta\text{H} = 3.83 - 3.82\text{ ppm}$ of $-\text{O-}\underline{\text{C}}\text{H}_2\text{-CH}_2\text{-OCOO-}$ (c), $\delta\text{H} = 4.46 - 4.44\text{ ppm}$ of $-\text{O-CH}_2\text{-}\underline{\text{C}}\text{H}_2\text{-OCOO-}$ (c', c''), $\delta\text{H} = 7.47 - 7.45\text{ ppm}$ (b), and $\delta\text{H} = 8.33 - 8.31\text{ ppm}$ (a). These signals were consistent with the structure of NPC-Plu-OH, once again confirming the successful activation of Pluronics by NPC [151, 152].

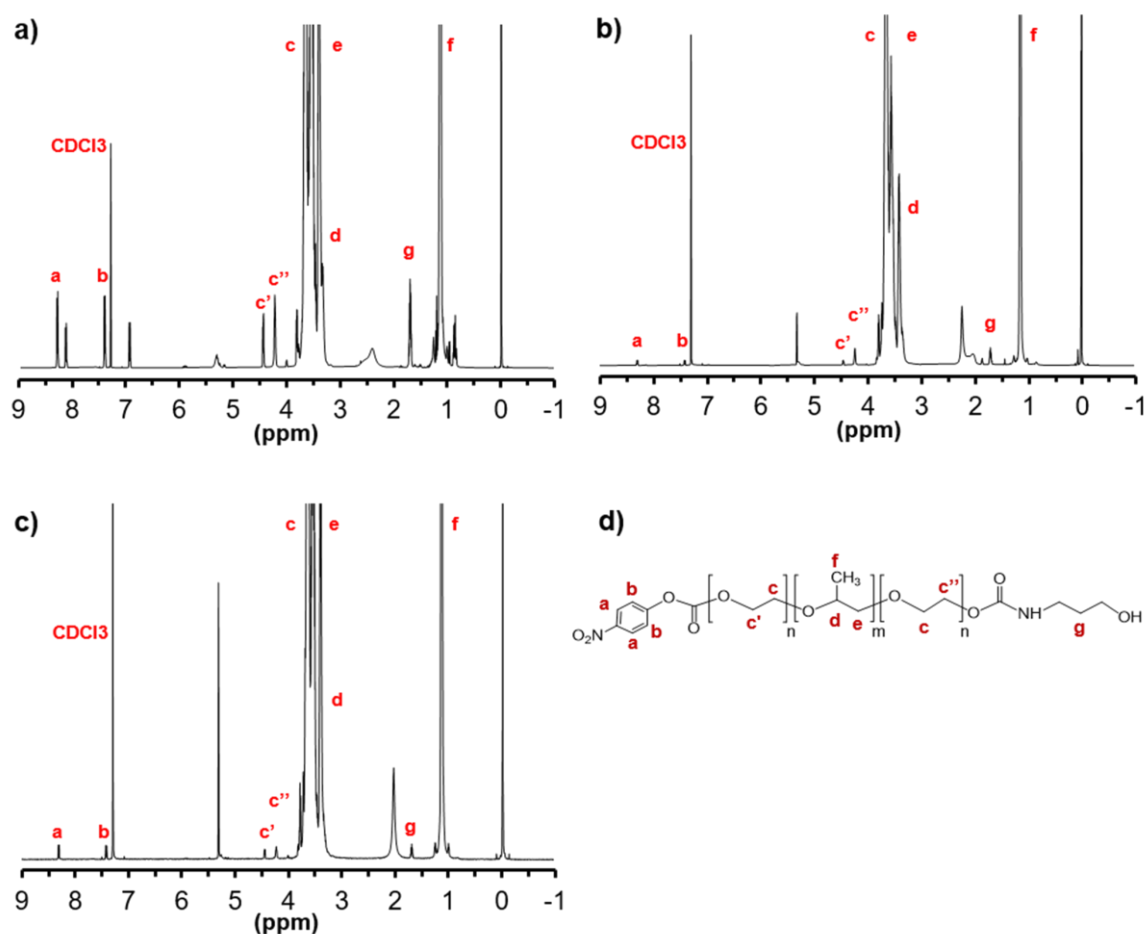


Figure 6.2. ¹H-NMR spectra of NPC-Plu-OH: a) NPC-L64-OH, b) NPC-F68-OH, c) NPC-F127-OH, d) Annotation the molecular structure of NPC-Plu-OH

6.2. Amination of HMSNs' surface

The HMSN particles after being surface modified with APTES were characterized to demonstrate successful amination through zeta potential, total amount of amine groups, DLS, FT-IR and EDX analysis.

The surface charge of HMSNs was identified as -46.6 mV (Figure 6.3a). This negative charge value was due to the presence of hydroxyl groups on the HMSNs' surface. After the amination, amine groups were protonated into NH₃⁺, a positive charge group, thereby resulting in a positive charge value of the obtained particles as 49.6 mV. The switch from negative value to positive value of the particles' surface charge demonstrated that APTES was successfully denatured on the HMSNs' surface.

The amount of amine groups on the surface of HMSN-NH₂ was determined by conducting a Kaiser test. The distinctive pink complex produced by the reaction between ninhydrin and -NH₂ was formed and then measured its UV absorbance at 570 nm and calculated against a standard curve to quantify the surface -NH₂ groups [40, 153]. The result of the analysis was identified 78.62 μg per 100 mg of HMSN-NH₂, which was consistent with the previous publication [40].

The hydrodynamic diameter of HMSN and HMSN-NH₂ were determined as 108.2 nm and 109.6 nm, respectively (Figure 6.3b). The similarity of the hydrodynamic diameter of HMSN and HMSN-NH₂ was thought to be due to the small molecular weight of APTES (221.37 g/mol).

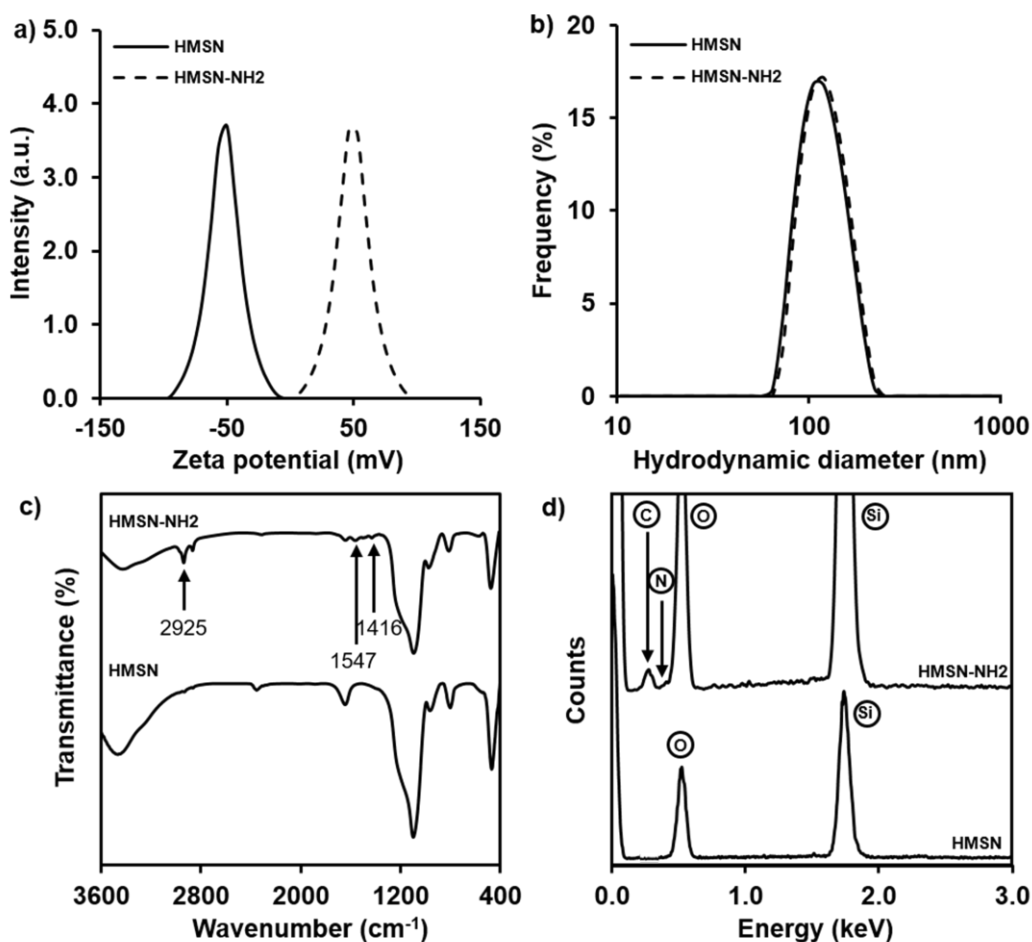


Figure 6.3. Characterizations of HMSN and HMSN-NH₂: a) Zeta potential; b) Hydrodynamic particle diameter; c) FT-IR spectra; and d) EDX patterns

The FT-IR spectra of HMSN and HMSN-NH₂ both showed adsorption bands at 1090 cm⁻¹, 952 cm⁻¹ and 801 cm⁻¹, which were recognized as the stretching vibrations of Si-O-Si, asymmetric bending and stretching of Si-OH (Figure 6.3c). In addition, broad bands at about 3300 - 3500 cm⁻¹ presented the OH stretching of the silanol groups, meanwhile peaks at 1629 cm⁻¹ corresponded to the OH stretching of water. These signals indicated the presence of silicon in the two samples. Moreover, the FT-IR spectrum of HMSN-NH₂ appeared new signals at wavenumbers of 2925 cm⁻¹ and 1416 cm⁻¹, which were signals of C-H tensile and bending vibrations of aminopropyl group. Besides, the amine group were also determined through a weak absorption peak at wavenumber 1547 cm⁻¹ presenting the bending vibration of NH₂ group. The FT-IR results demonstrated that the HMSN surface has been successfully aminated [154-156].

The EDX pattern (Figure 6.3d) of HMSNs showed the presence of only silica and oxygen elements with the atomic percentages of 68.82 and 31.18, respectively [136]. Meanwhile, carbon and nitrogen were the two more elements observed in the EDX pattern of HMSN-NH₂ sample. The atomic percentages of Si, O, C and N on the surface of HMSN-NH₂ were determined as 22.96, 53.85, 16.19 and 7.00%, respectively, confirming the success of the modification of APTES on HMSNs' surface.

6.3. Modification of HMSNs' surface with Pluronics via amine intermediate

The modification of HMSNs' surface with 3 types of Pluronics including L64, F68 and F127 were conducted by the reactions of HMSN-NH₂ with the activated NPC-Plu-OH. The obtained samples HMSN-L64, HMSN-F68 and HMSN-F127 were characterized using zeta potential, DLS size, FT-IR and TGA analysis. The results were presented in Figure 6.4.

Zeta potential of the three samples HMSN-L64, HMSN-F68 and HMSN-F127 were identified as 37.8 mV, 30.2 mV and 20.2mV, respectively (Figure 6.4a). They were all positive but lower than that of HMSN-NH₂. This could be due to the reaction between the activated Pluronics with amine groups on the surface of HMSN-NH₂, leading to a decrease in the amount of amine groups on the obtained nanoparticles'

surface. Moreover, zeta potential of the three HMSN-Plu were more than 15 mV, these particles, therefore, were expected to be stable from electrostatic consideration [157].

Hydrodynamic diameter of HMSN-Plu samples was measured and presented in Figure 6.4b. There was a gradual increase in DLS size from 127.9 nm to 142.1 nm and 172.7 nm when HMSN particles were conjugated to Pluronic of increasing molecular weight (from 2900 kDa to 8400 kDa and 12600 kDa). This was thought to be due to the corresponding increase of the chain length of Pluronic molecules. The results of zeta potential and DLS suggested that Pluronic were successfully denatured on HMSNs' surface.

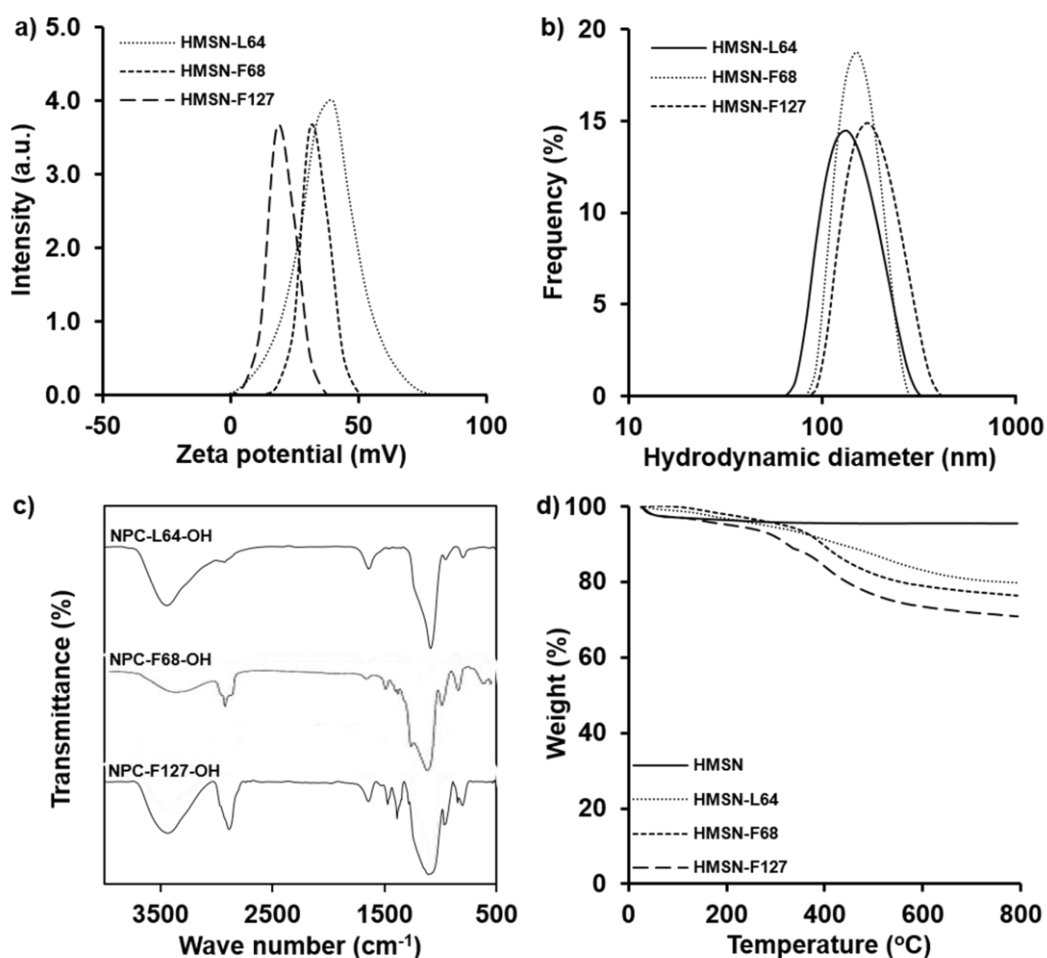


Figure 6.4. Characterizations of HMSN-L64, HMSN-F68 and HMSN-F127: a) Zeta potential; b) Hydrodynamic particle diameter; c) FT-IR spectra; and d) TGA graphs

To better confirm the successful Pluronics denaturation on HMSN surface, FT-IR and TGA experiments were performed. In Figure 6.4c, the FT-IR spectra of HMSN-Plu appeared the absorption signals of both naked HMSN particles by amine group (Figure 6.3c) and activated NPC-Plu-OH (Figure 6.1). The absorption peaks at $3300\text{-}3500\text{ cm}^{-1}$ and 1089 cm^{-1} corresponded to the -OH and Si-O-Si groups of the naked HMSN. Meanwhile, the three FT-IR spectra of HMSN-Plu also had absorption peaks at 2888 cm^{-1} and 1111 cm^{-1} which together attributed to the group $\text{-OCH}_2\text{-CH}_2\text{-}$ of the Pluronics [133, 158, 159].

Figure 6.4d showed the TGA graphs of HMSN and HMSN-Plu. The initial mass loss at temperature below $200\text{ }^\circ\text{C}$ could be ascribed to the removal of humidity and to the condensation of surface silanols. Meanwhile, the loss of weight at temperature above $200\text{ }^\circ\text{C}$ could be directly related to the extent of surface functionalization [160]. From the TGA data, the weight loss values of HMSN and HMSN-Plu in the temperature ranges of $0\text{-}200\text{ }^\circ\text{C}$ and $200\text{-}800\text{ }^\circ\text{C}$ were calculated and presented in Table 6.1. The weight loss values at the temperature range $200\text{-}800\text{ }^\circ\text{C}$ of HMSN-L64, HMSN-F68 and HMSN-F127 were determined, respectively, as 14.56, 17.61 and 19.05%, hence, could be ascribed to amount of the corresponding Pluronic modifying in the HMSNs' surface. TGA result, together with FT-IR, zeta potential and DLS results, demonstrated that the three Pluronics were successfully modified on the HMSNs' surface.

Table 6.1. Weight loss (%) of HMSN and HMSN-Plu by temperature ranges through thermogravimetric analysis

Temperture range	0 – 200 °C	200 – 800 °C
Particles	Weight loss (%)	
HMSN	4.62	-
HMSN-L64	3.33	14.56
HMSN-F68	2.23	17.61
HMSN-F127	4.91	19.05

6.4. Dual-drug loading capacity and in vitro release behavior of HMSN-Plu

DOX and QUE were respectively encapsulated into the conventional HMSN and the modified HMSN-Plu. Their loading capacity and loading efficiency were presented in Table 6.2 as follow:

Table 6.2. Loading capacity (DLC) and loading efficiency (DLE) for Doxorubicin (DOX) and Quercetin (QUE) of HMSN and HMSN-Plu

Particles	DLC (%)		DLE (%)	
	DOX	QUE	DOX	QUE
HMSN	5.87 ± 0.64	2.34 ± 1.03	15.15 ± 0.94	9.60 ± 0.78
HMSN-L64	7.04 ± 0.81	9.80 ± 1.16	19.88 ± 1.02	43.44 ± 1.18
HMSN-F68	6.79 ± 0.59	9.83 ± 0.79	19.28 ± 0.87	43.82 ± 1.05
HMSN-F127	6.97 ± 0.97	17.80 ± 0.85	19.50 ± 1.13	86.83 ± 0.98

From the results in Table 6.2, it could be seen that the loading capacity for DOX of the three samples HMSN-Plu slightly increased compared to that of HMSN. The difference could be due to the ability of DOX to bind with the remaining amine groups on the HMSN-Plu surface via imine forming reaction [40].

Meanwhile, there was a clearly noticeable difference between QUE loading capacity values among the samples. HMSN owned the lowest DLC value (2.34%), HMSN-L64 and HMSN-F68 showed better loading capacity for QUE with DLC value of 9.80% and 9.83%, respectively, and HMSN-F127 performed the highest DLC values of 17.80%.

The relative similarity in DOX loading capacity of the samples was due to the fact that DOX was previously encapsulated, when the cavities and pores of the materials were empty. Thus, DOX, a hydrophilic drug, could reside in these empty spaces without any competition. QUE was then loaded into the DOX encapsulated materials. At this time, the remaining space inside the materials for QUE was not as much as for DOX. That was the reason why the DLC value for QUE of HMSN was the lowest. Fortunately, hydrophobic blocks PPO of the Pluronic molecules on

HMSN-Plu's surface was the sites where QUE, a poorly soluble drug, could be effectively encapsulated through physical interaction, resulting in marked enhancement of QUE loading capacity of HMSN-Plu. When considering the structure of L64, F68 and F127, it was possible to find a correlation between QUE loading capacity and the number of PPO blocks. The more PPO units a Pluronic had, the higher QUE loading capacity a HMSN-Plu showed. Consequently, HMSN-F127 performed the equivalent DLC value for DOX and the highest DLC value for QUE.

6.5. In vitro drug release behavior of HMSN-Plu

In vitro drug release behavior of free drugs and loaded drugs was investigated in different conditions including [37 °C, pH 7.4], [18 °C, pH 7.4] and [37 °C, pH 5.5]. The results were showed in Figure 6.5. By comparing the percentage of cumulative drug release in the two conditions [37 °C, pH 7.4] and [18 °C, pH 7.4], release behavior in response to temperature of the samples could be assessed. In contrast, the comparison of the cumulative drug release percentage in the two conditions [18 °C, pH 7.4] and [37 °C, pH 5.5] could support to judge the release behavior by pH values of the samples.

For DOX release, at the three conditions, free DOX was released the fastest, followed by DOX from HMSN, whereas HMSN-Plu showed better controlled DOX release profiles. This proved that the modified Pluronics on HMSNs' surface had come into play as the caps to reduce the opening of the mesoporous channels, slowing down the movement of DOX from the hollow cavity out to the environment.

After 72 h, although the released DOX amount from HMSN-Plu samples generally increased when the temperature reduced from 37 to 18 °C (at the same pH value of 7.4), the differences were not significant. Meanwhile, there were notable increases in the amount of cumulative DOX release after 72 h at pH 5.5. This phenomenon was attributed to the dimerization of DOX in PBS pH 7.4 where DOX interacted with the buffer and formed covalently bonded DOX dimers [161]. The results suggested that the three HMSN-Plu systems released DOX in response to pH, in which HMSN-Plu systems performed slow DOX release rates in physiological condition and higher rates in tumor microenvironment condition.

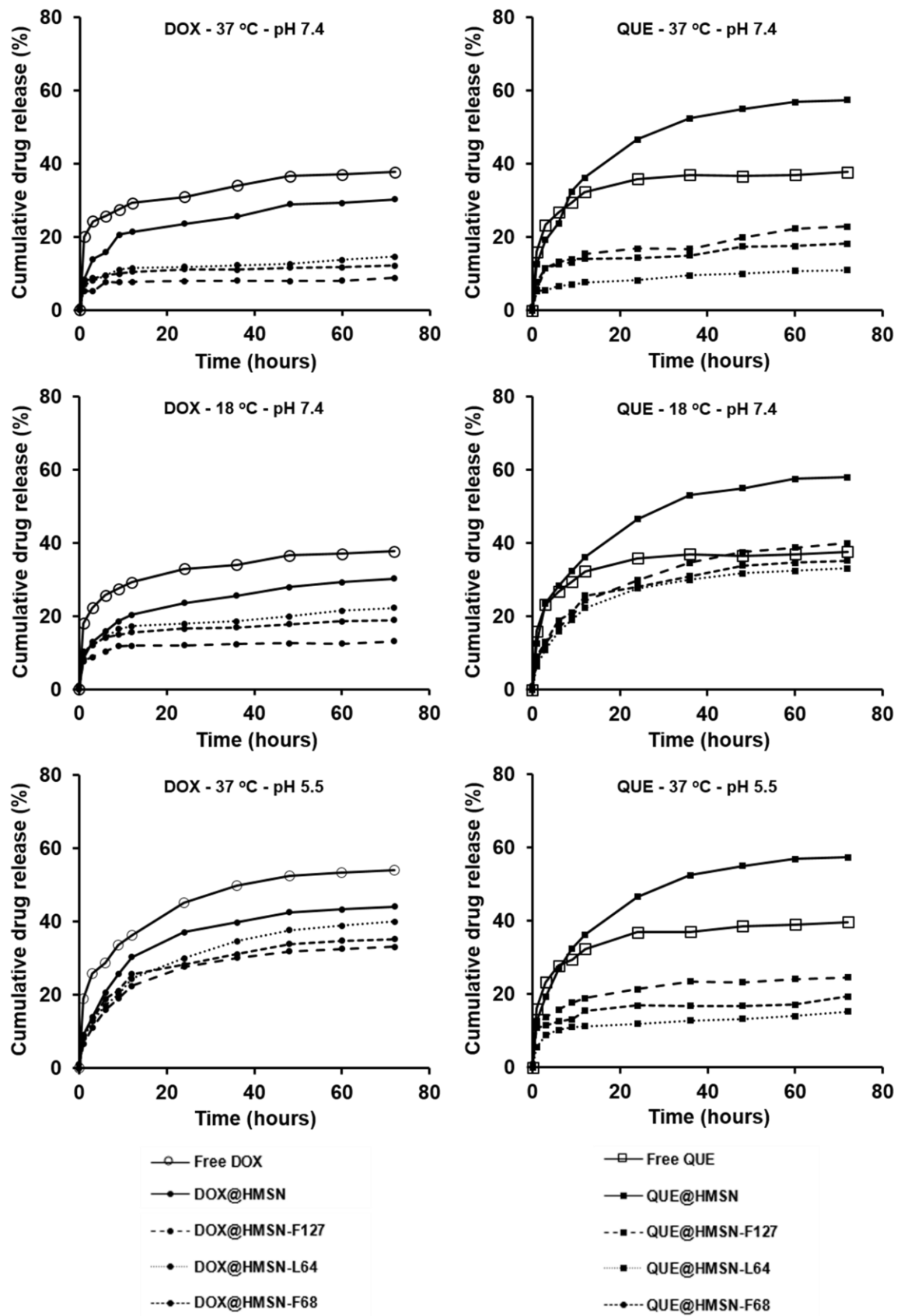


Figure 6.5. *In vitro* release behaviour of free drugs and loaded drugs in different conditions of temperatures and pH values

For QUE release, HMSN showed burst release profiles at all tested conditions. This was due to the loaded QUE was mainly adsorbed on the HMSNs's surface. Meanwhile, the drug release rate (%) was calculated as the percentage of cumulative released drug with the loaded drug. Therefore, although HMSN showed high percentages of drug released, the absolute mass of drug released was very small.

Free QUE and loaded QUE from HMSN-Plu were released more slowly than those from HMSN. This could be due to the high initial amount of QUE (free or loaded in the materials) and its poor solubility. This is an advantage of the HMSN-Plu loading QUE systems because they can limit the leakage of QUE when circulating in the body under the physiological condition.

Besides, HMSN-Plu also showed improvement in drug release rate at low temperature (18 °C). This phenomenon could be explained by the stretching of Pluronic chains at low temperature, causing the encapsulated QUE molecules in the hydrophobic PPO blocks to be released easily out to the environment by the concentration difference. The results suggested that the three HMSN-Plu systems released QUE in response to temperature, in which HMSN-Plu systems performed slow QUE release rates in physiological temperature and higher rates at cooler temperatures. Among the three systems, HMSN-F127 showed relatively good controllability of drug release and effective response to temperature and pH compared to the other HMSN-Plu systems. The release behavior of HMSN-Plu in different conditions was illustrated in Figure 6.6.

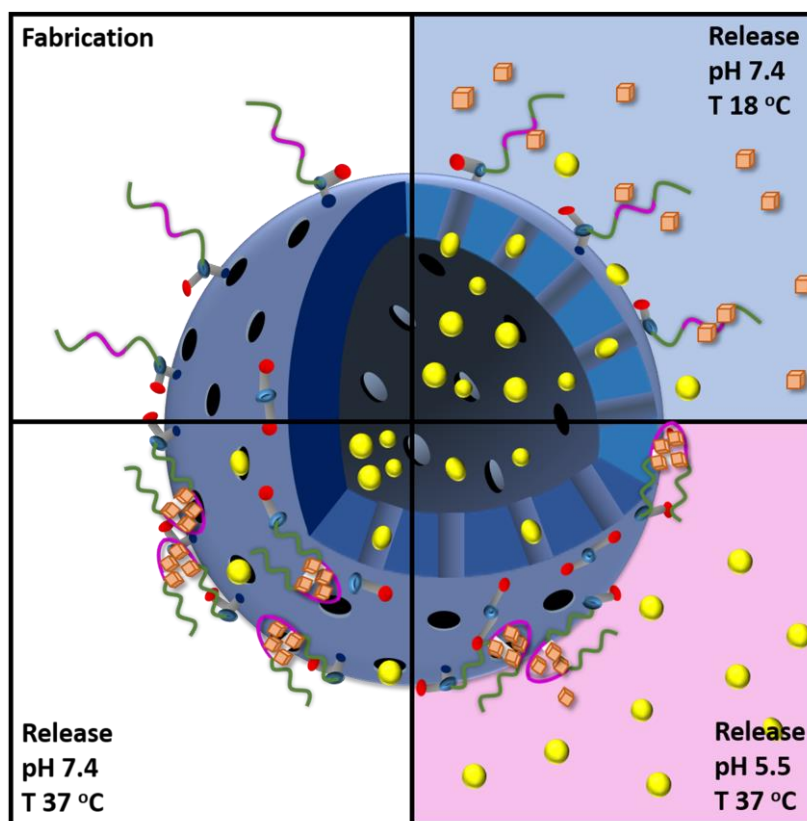


Figure 6.6. Illustration of release behavior of HMSN-Plu in different conditions

6.6. Cytotoxicity of HMSN-Plu

MTT assays on HeLa cell line were carried out to evaluate the cytotoxicity of the nanocarriers HMSN-Plu. As shown in Figure 6.7, HMSN-L64, HMSN-F68 and HMSN-F127 exhibited no obvious toxicity on HeLa cells at the concentrations up to 250 $\mu\text{g}/\text{mL}$. Therefore, HMSN-Plu can be regarded as biocompatible nanocarriers.

In terms of zeta potential value, DLS size and biocompatibility, HMSN-L64, HMSN-F68 and HMSN-F127 satisfy the required characteristics of a drug delivery system. In terms of the ability to encapsulate dual drugs with different solubility, HMSN-F127 showed as the most potential candidate among the three HMSN-Plu samples when possessing the equivalent DLC value for DOX and the highest value for QUE. Moreover, HMSN-F127 showed good controllability of drug release and effective response to temperature and pH. Therefore, HMSN-F127 sample was selected for further studies.

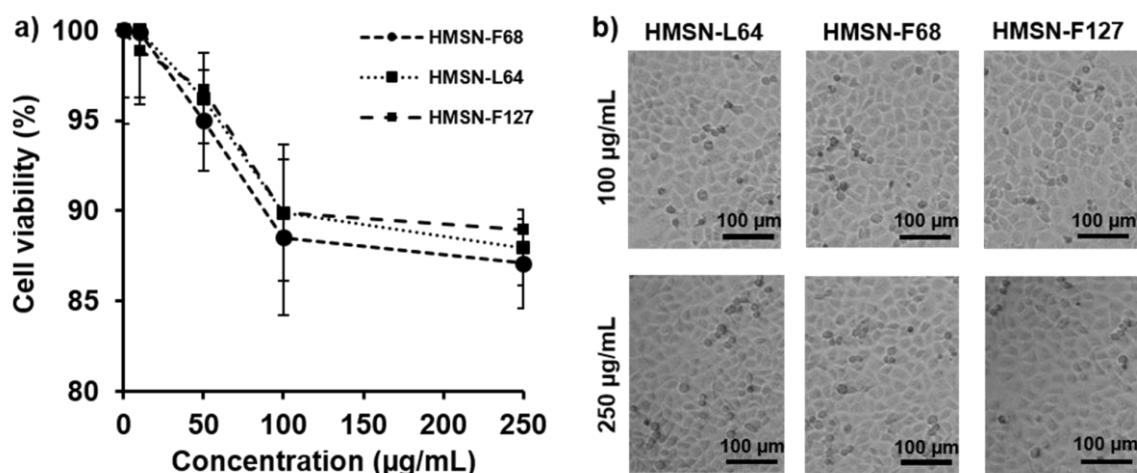


Figure 6.7. a) Cytotoxicity by MTT assay of HMSN-Plu on HeLa cells; b) Morphology of HeLa cells treated by HMSN at different concentrations

6.7. Characterizations of HMSN-F127

The synthesized HMSN-F127 was previously analyzed in terms of zeta potential, DLS size, FT-IR, TGA, loading capacity and release profile. After being selected as the appropriate nanocarrier for dual-drug delivery, the morphology of HMSN-F127 was characterized through TEM images, porosity through BJH analysis, structure through XRD analysis and cytotoxicity through MTT assay.

TEM images showed that both HMSN and HMSN-F127 were spherical monodisperse particles (Figure 6.8). The particle diameters of HMSN and HMSN-F127 were determined as 77.16 nm and 119.75 nm, respectively. The particles HMSN-F127 with such an appropriate size could not only load a sufficient amount of drug, but also prolong the circulation time during the administration.

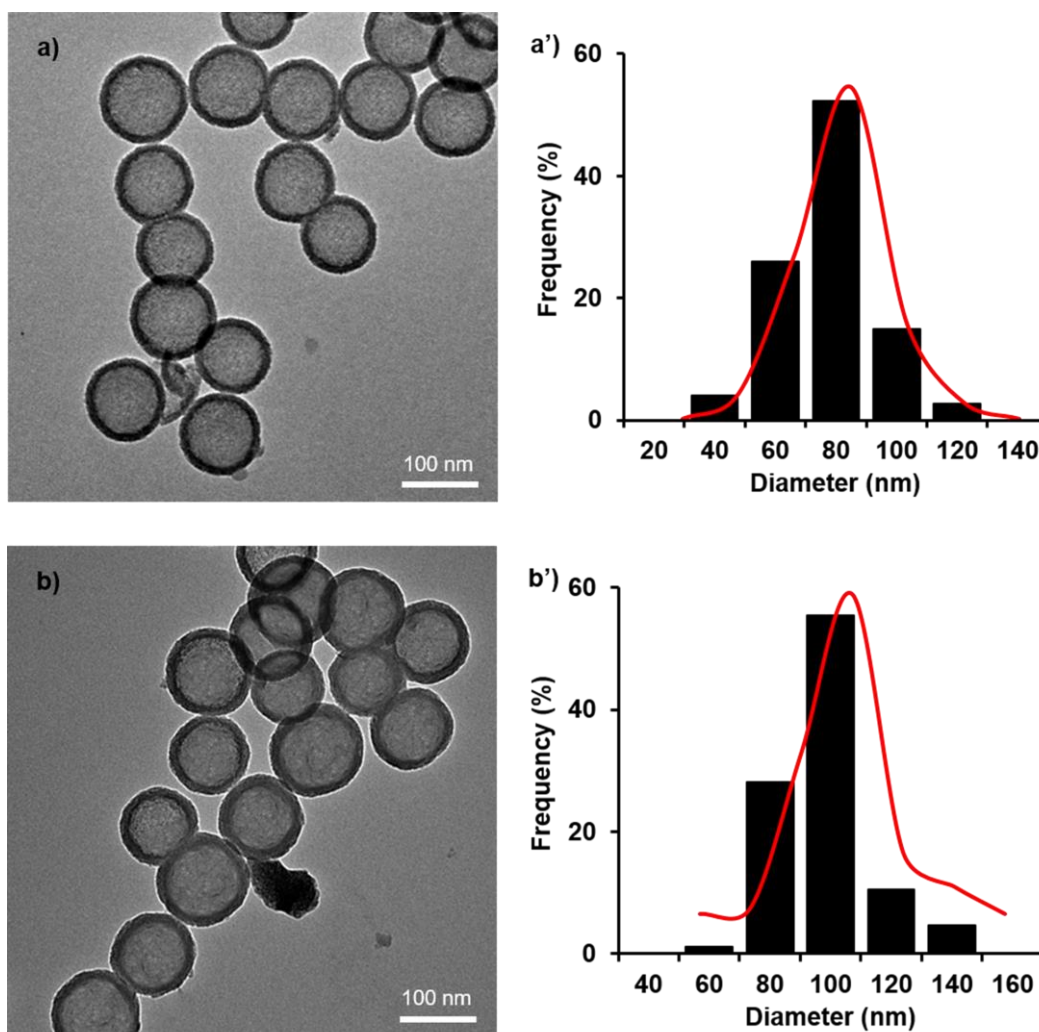


Figure 6.8. TEM images and Size distribution of a), a') HMSN and b), b') HMSN-F127

The isotherms of N_2 adsorption–desorption and the distributions of pore diameter were shown in Figure 6.9. The nitrogen sorption isotherms of HMSN and HMSN-F127 were both Langmuir type IV isotherm curves, according to IUPAC classification, which were characterized by mesoporous materials [132, 133]. In addition, the large hysteresis loops in the relative pressure range (P/P_0) of 0.5–1.0 suggested the hollow structure of the two particle systems [162]. HMSN possessed a higher BET surface area ($767 \text{ m}^2/\text{g}$) compared to that of HMSN-F127 ($446 \text{ m}^2/\text{g}$). Moreover, even though the pore diameters of HMSN and HMSN-F127 were similar (2.5 and 2.2 nm, respectively), dV/dD value of HMSN was significantly higher than that of HMSN-F127. The decrease of BET surface area and BJH pore volume of

HMSN-F127 was due to the fact that F127 molecules presented on HMSNs' surface and acted as capping agents of the open pores.

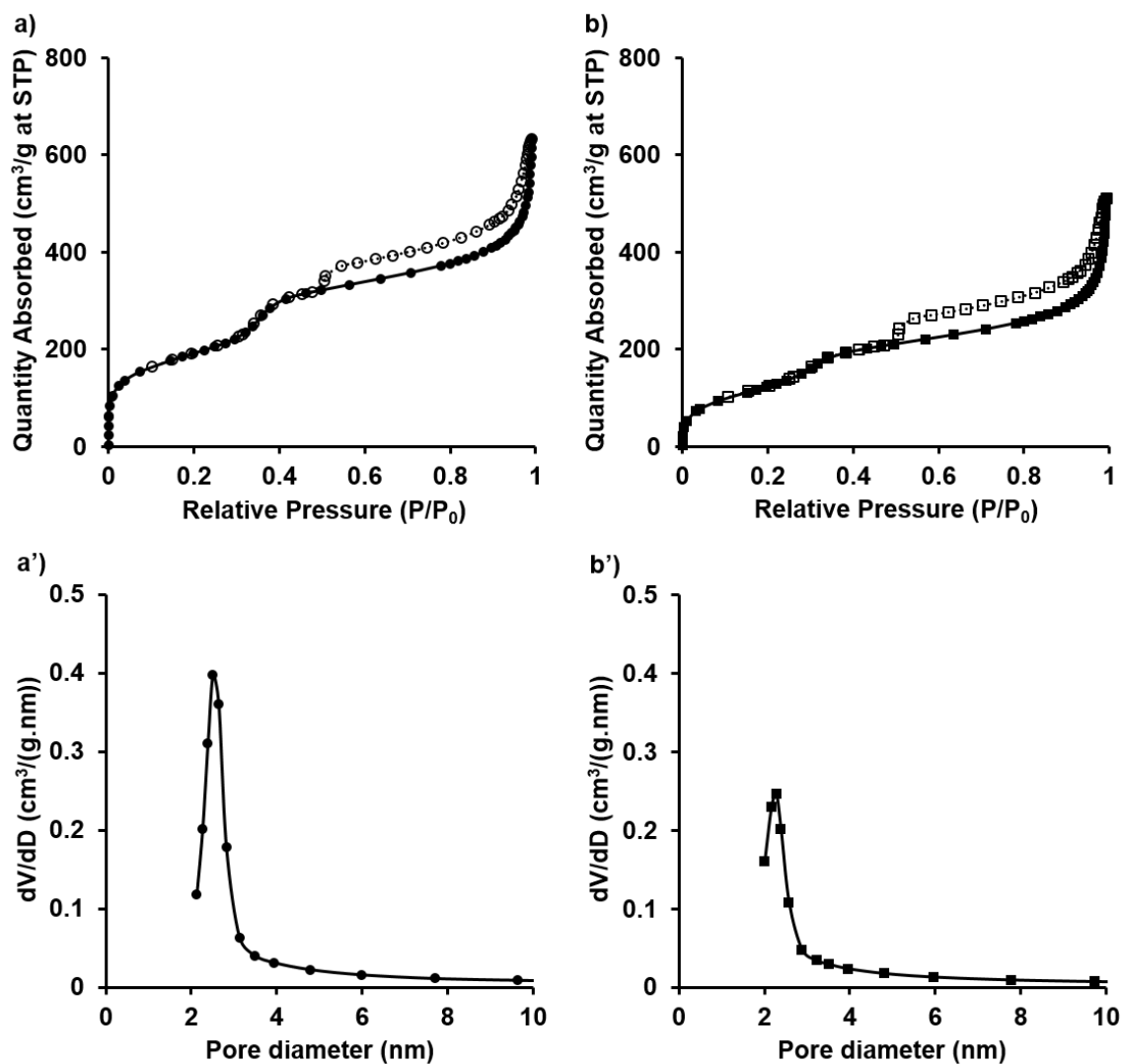


Figure 6.9. The N₂ adsorption-desorption isotherms and pore size distributions of HMSN (a, a') and HMSN-F127 (b, b')

Figure 6.10a showed the XRD patterns of naked HMSN and HMSN-F127 which were analyzed using the software OriginPro with the expected accuracy of $\pm 0.02^\circ$ throughout the entire measuring range and achievable peak width $< 0.05^\circ$ (Figure 6.10b and Figure 6.10c).

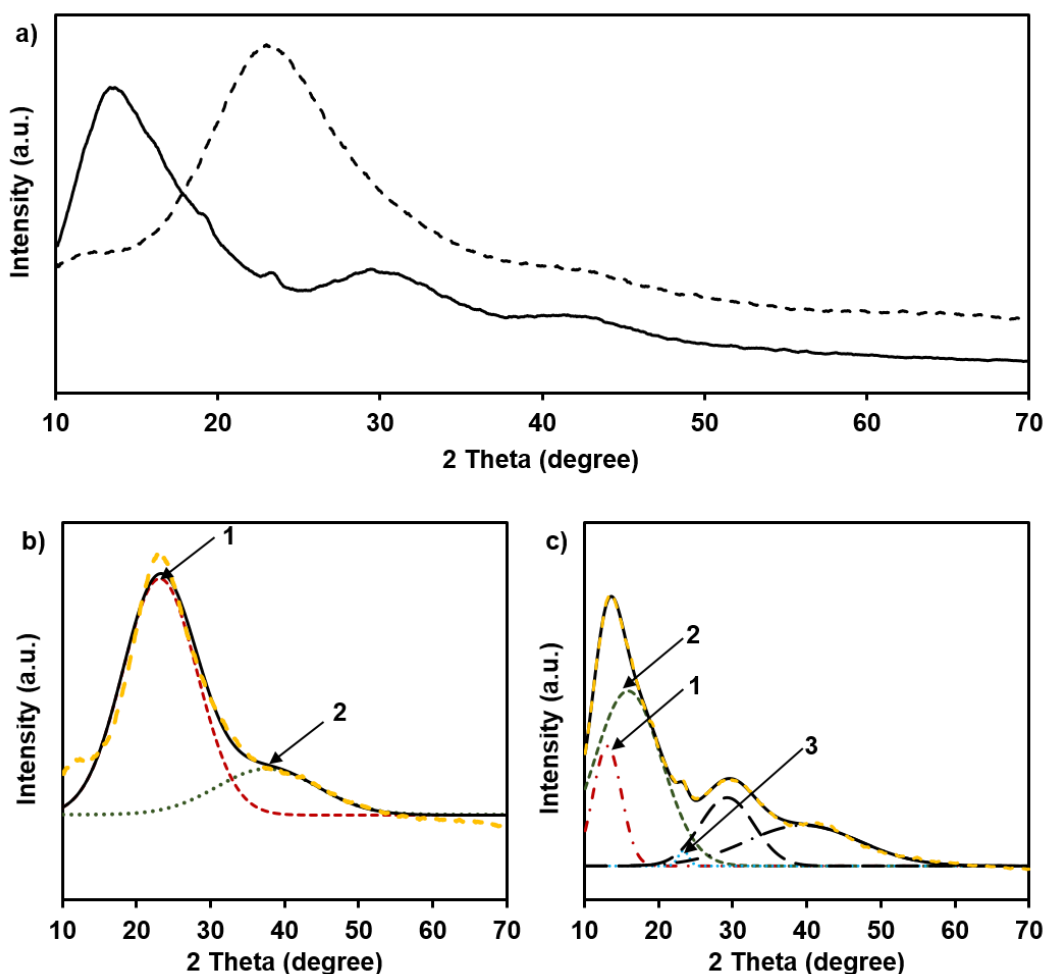


Figure 6.10. (a) XRD patterns of HMSN (dash line) and HMSN-F127 (solid line); (b) Fitting XRD peaks of HMSN (XRD pattern – Dash; Cumulative fit peak – Solid line); and (c) Fitting XRD peaks of HMSN-F127 (XRD pattern – Dash; Cumulative fit peak – Solid line)

The XRD patterns of HMSN and HMSN-F127 showed un-sharp peaks with 2θ at 23.5° and 13.9° , respectively. In the fitting XRD diffractogram of HMSN (Figure 6.10b), the fitting peak 2 with 2θ at 23.18° could be ascribed to amorphous silica. Meanwhile, the peak 3 with 2θ at 23.35° in the fitting XRD diffractogram of HMSN-F127 (Figure 6.10c), characterizing for HMSN, decreased the intensity. This might be due to the intercalation of silane moieties on the surface of HMSN after the activation of HMSN by APTES [163]. Additionally, the fitting peak 1 with 2θ at 13.08° could be attributed for APTES and the fitting peak 2 with 2θ at 15.89° could be attributed for F127 [41, 164]. Both the XRD patterns with un-sharp peaks

confirmed the amorphous nature of silica particles and revealed that the conjugated F127 had no impact on the structure of the silica particles [138].

6.8. Cancer cell killing ability of DOX.QUE@HMSN-Plu

In vitro cancer cell killing ability of free DOX, free QUE and DOX.QUE@HMSN-F127 against Hela cells was evaluated and presented in Figure 6.11.

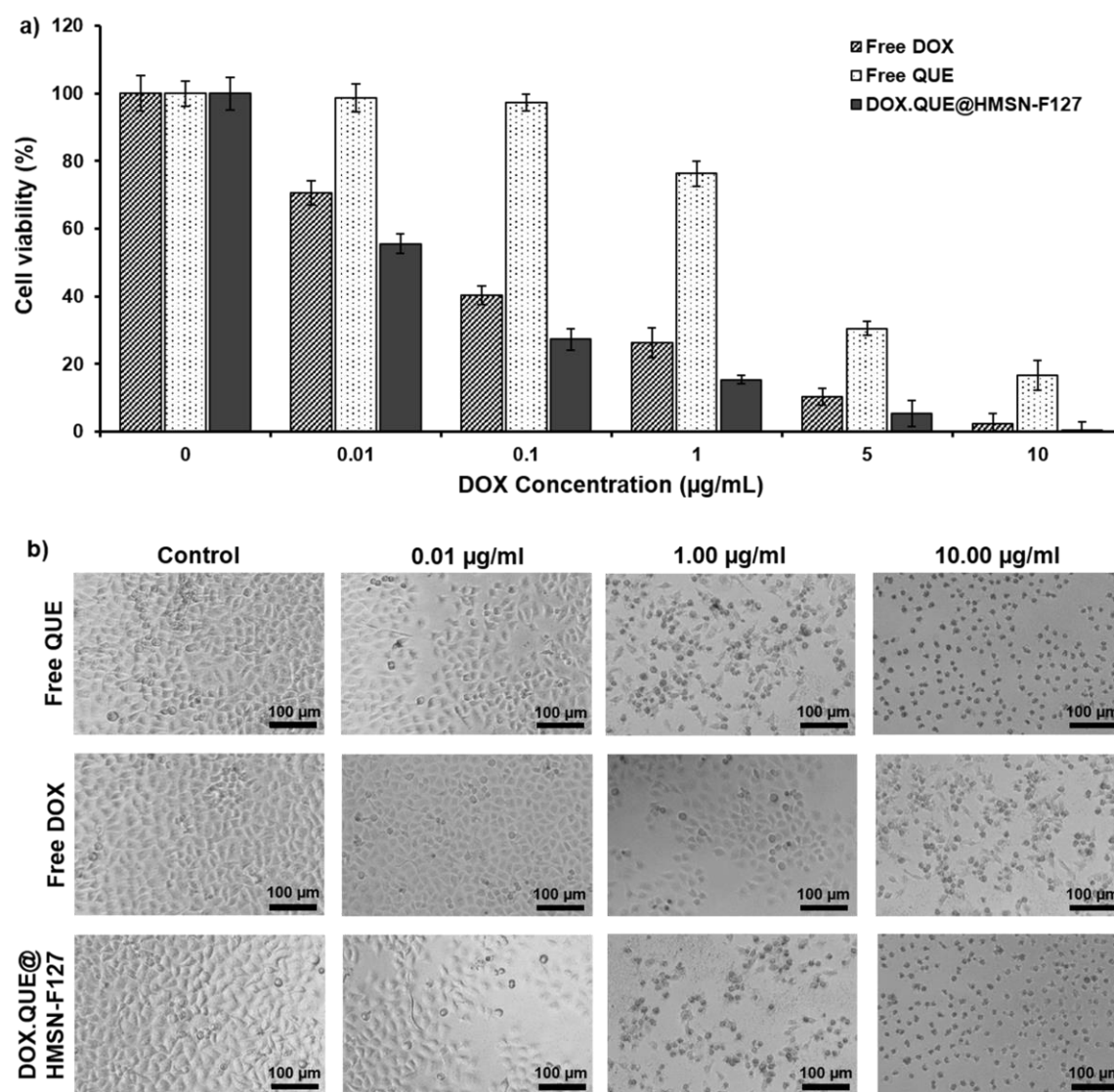


Figure 6.11. a) Cell viability and b) Morphology of Hela cells treated by Free DOX, Free QUE and DOX.QUE@HMSN-F127

Overall, the free DOX, free QUE and DOX.QUE@HMSN-F127 samples induced cell death in concentration-dependent manners. Free QUE showed the lowest cytotoxicity on Hela cells with IC₅₀ value of 3.29 µg/mL, while free DOX killed 50% of the cultured Hela cells at the concentration of 0.07 µg/mL. DOX.QUE@HMSN-F127 performed the strongest effect on the cells. The IC₅₀ of DOX in DOX.QUE@HMSN-F127 was identified as 0.03 µg/mL, which was as half as that of free DOX. Although DOX was released at a slower rate from the nanocarrier HMSN-F127, the system simultaneously released QUE, which was proved to reduce the required dose as well as the side effect of DOX [113, 114]. That's the reason why the system DOX.QUE@HMSN-F127 showed the best cancer killing effect against Hela cells.

6.9. Summary

Three nanocarrier systems based on HMSN modified with Pluronic including L64, F68 and F127 have been successfully synthesized for dual drug delivery application. HMSN-Plu samples, which were proved and characterized via specific techniques, showed to be potential candidates for drug delivery with zeta potentials over 20 mV, DLS diameters below 120 nm and no toxicity at concentrations up to 250 µg/mL. In addition, HMSN-Plu greatly enhanced loading capacity as well as release controllability for DOX and QUE. Among them, HMSN-F127 showed as the most potential candidate due to its great loading capacity for DOX and especially QUE. Moreover, HMSN-F127 showed good controllability of drug release with temperature responsive release for QUE and pH responsive release for DOX. Importantly, DOX.QUE@HMSN-F127 demonstrated a strong killing effect against Hela cell line. These findings suggested that HMSN-F127 would be a potential nanocarrier for effectively dual drugs delivery in cancer treatment.

The physicochemical characteristics, drug loading capacity and drug release properties of the synthesized carrier systems in this study were summarized in Table 6.3.

Table 6.3. Summary of physicochemical characteristics, drug loading capacity and drug release properties of the synthesized silica nanoparticles

Particle	Particles' DLS diameter (nm)	Particles' TEM diameter (nm)	Mesoporous diameter (nm)	DLC (%)	Release rate* (%)
dSiO ₂	96.8	65.3	-	-	-
HMSN	108.2	80.2	2.5	Single loading DOX: 5.87 RB: 1.95	DOX: 34.9 RB: 52.5 QUE: 55.03
				Dual loading DOX: 5.87 QUE: 2.34	
HMSN-P **	124.7	94.3	2.5	Single loading DOX: 5.13	DOX: 29.8
HMSN-T20 ***	130.2	99.3	4.1	Single loading RB: 4.92	RB: 31.3
HMSN-T80 ***	131.7	100.8	4.0	Single loading RB: 5.17	RB: 33.9
HMSN-BS10 ***	139.0	110.4	4.5	Single loading RB: 5.41	RB: 37.6
HMSN-L64	127.9	-	-	Dual loading DOX: 7.04 QUE: 9.80	DOX: 12.62 QUE: 9.96
HMSN-F68	142.1	-	-	Dual loading DOX: 6.79 QUE: 9.83	DOX: 11.59 QUE: 17.37
HMSN-F127	172.7	119.7	2.2	Dual loading DOX: 6.97 QUE: 17.80	DOX: 7.94 QUE: 19.82

*: Cumulative drug released after 48 hours at 37°C and pH 7.4

** : P was PEG 6000 kDa at 2% (w/v)

*** : The molar ratio of non-ionic surfactants with CTAB was 1:2

CONCLUSIONS AND FUTURE PERSPECTIVES

Conclusion

To sum up, the current thesis has completed the set objectives. HMSN materials were firstly synthesized by hard-templating with shortened synthetic time and optimal particle size, secondly modulated mesoporous shell thickness and mesopore diameter, and finally surface modified with Pluronics for anti-cancer drugs delivery applications. In detail:

- The synthesis method of HMSN was successfully modified to shorten the synthetic time by more than half from 21 hours to 9 hours and reduce the HMSN particle size to about 80 nm.
- Mesoporous shell thickness of HMSN was successfully controlled using PEG in the shell coating step. As the molecular weight (1000, 2000, 4000 and 6000 Da) or concentration (1, 2, 3, 4 and 5%) of PEG increased, the shell thickness tended to increase. HMSN-P synthesized in the presence of 2% PEG 6000 has a particle diameter of 94.3 nm and a mesoporous shell thickness of 14.5 nm, showing a slightly lower DOX loading capacity but a better controlled DOX release profile than the original HMSN.
- Mesopore diameter of HMSN was successfully controlled using non-ionic surfactants (Tween 20, Tween 80 and Brij S10) as co-templates for mesopores in the shell coating step. For each non-ionic surfactant, as the molar ratios S : CTAB increased, the mesoporous shell thickness of HMSN gradually increased. HMSN-T20, HMSN-T80 and HMSN-BS10 synthesized at the molar ratio S : CTAB of 1:2, respectively owned the enlarged mesopore diameters of 4.1, 4.0 and 4.5 nm, performing significantly higher loading capacity and better release controllability for Rose Bengal - a high molecular weight agent, compared to the original HMSN.
- Three types of Pluronics including L64, F68 and F127 were successfully modified on HMSNs' surface. The obtained HMSN-Plu systems significantly

enhanced loading capacity as well as release controllability for DOX and QUE. HMSN-F127 showed great loading capacity for DOX (6.97%) and QUE (17.80%) compared to those of HMSN (5.87% for DOX and 2.34% for QUE). Moreover, HMSN-F127 showed good release controllability with temperature responsive release for QUE and pH responsive release for DOX.

- HMSN, HMSN-P, HMSN-S and HMSN-Plu were biocompatible nanocarriers with no observed cytotoxicity at concentrations up to 250 $\mu\text{g}/\text{mL}$, proved by MTT assays. Moreover, the great inhibition activity against human cervical cancer Hela cell line of the dual drug loading system DOX.QUE@HSMN-F127 was illustrated with IC₅₀ value for DOX of 0.03 $\mu\text{g}/\text{mL}$, which was as half as that of free DOX.

Novelty of the thesis

The hard-template synthesis method of HMSN was successfully modified to reduce the particle size below 100 nm with shortened synthetic time.

PEG with different molecular weights and concentrations were investigated and used as capping agents in the shell coating step to control the mesoporous shell thickness of HMSN.

Mixed micelles of non-ionic surfactants and CTAB were investigated and used as soft templates in the shell coating step to enlarged the mesopore diameter of HMSN.

Pluronic with different numbers of PPO and PEO units were used to modify the surface of HMSN particles for dual drug loading application. The loading capacity of drug with different solubility (DOX and QUE) as well as the drug release profile in response to temperature and pH of the HMSN-Plu systems were evaluated to select the most effective dual drug delivery HMSN-Plu system.

Future perspective

Researching the best method to fight cancer is an ongoing process and HMSN has been one of the carriers that can overcome the problems posed by current treatments. A further research objective will include denaturing the HMSN-Plu

system with ligands such as folic acid for active targeting. In addition, the modification of HMSN with different stimulus-responsive agents to improve stimulus-responsive delivery of the system. Furthermore, the *in vitro* activities as well as *in vivo* behavior of the modified HMSN systems need to be verified and expanded understanding.

LIST OF PUBLICATIONS

- 1. Ngoc Hoi Nguyen, Cuu Khoa Nguyen, Dai Hai Nguyen, “A Modified Hard-Templating for Hollow Mesoporous Silica Nanoparticles Synthesis with Suitable Particle Size and Shortened Synthesis Time”, Vietnam Journal of Science and Technology, ISSN 2525-2518, 0866-708X, Accepted 20 August 2022.**
- 2. Ngoc Hoi Nguyen, Dieu Linh Tran, Ngoc-Hang Truong-Thi, Cuu Khoa Nguyen, Dai Hai Nguyen, “Simply and Effectively Control the Shell Thickness of Hollow Mesoporous Silica Nanoparticles by Polyethylene Glycol for Drug Delivery Applications”, Journal of Applied Polymer Science, SCIE/SSCI, Q2, H index 175, IF 3.125, ISSN 0021-8995 (print); 1097-4628 (web). DOI: <http://doi.org/10.1002/app.53126>.**
- 3. Ngoc Hoi Nguyen, Ngoc-Hang Truong-Thi, Dinh Tien Dung Nguyen, Yern Chee Ching, Ngoc Trinh Huynh, Dai Hai Nguyen, “Non-ionic Surfactants as Co-Templates to Control the Mesopore Diameter of Hollow Mesoporous Silica Nanoparticles for Drug Delivery Applications”, Colloids and Surfaces A: Physicochemical and Engineering Aspects, SCIE/SSCI, Q2, H index 179, IF 5.518, ISSN 0927-7757. DOI: <https://doi.org/10.1016/j.colsurfa.2022.130218>**
- 4. Ngoc Hoi Nguyen, Dai Hai Nguyen, “A Research on Drug Delivery System based on Mesoporous Silica Nanoparticles for Anti-Cancer”, The International Chemistry and Its Applications Conference 2022.**

REFERENCES

1. H. Sung, J. Ferlay, R.L. Siegel, M. Laversanne, I. Soerjomataram, A. Jemal, and F. Bray, *Global cancer statistics 2020: GLOBOCAN estimates of incidence and mortality worldwide for 36 cancers in 185 countries*. CA: a cancer journal for clinicians **2021**.71(3), p. 209-249.
2. E. Bidram, Y. Esmaeili, H. Ranji-Burachaloo, N. Al-Zaubai, A. Zarrabi, A. Stewart, and D.E. Dunstan, *A concise review on cancer treatment methods and delivery systems*. Journal of Drug Delivery Science and Technology **2019**.54, p. 101350.
3. Y. Luo, G. Prestwich, *Cancer-targeted polymeric drugs*. Current cancer drug targets **2002**.2(3), p. 209-226.
4. C.K. Nguyễn, *Vật liệu polyme thông minh và ứng dụng trong y sinh*. 2016, NXB Khoa học Tự nhiên và Công nghệ. 446-455.
5. C.K. Nguyen, N.Q. Tran, T.P. Nguyen, and D.H. Nguyen, *Biocompatible nanomaterials based on dendrimers, hydrogels and hydrogel nanocomposites for use in biomedicine*. Advances in Natural Sciences: Nanoscience and Nanotechnology **2017**.8(1), p. 015001.
6. A.K. Jain, S. Thareja, *In vitro and in vivo characterization of pharmaceutical nanocarriers used for drug delivery*. Artificial cells, nanomedicine, and biotechnology **2019**.47(1), p. 524-539.
7. H. Gao, J. Yang, *Nanoscale silicon dioxide prepared by sol-gel process*. Modern applied science **2010**.4(9), p. 152.
8. A.J. Schwanke, R. Balzer, and S. Pergher, *Microporous and mesoporous materials from natural and inexpensive sources*. Handbook of ecomaterials **2017**, p. 1-22.
9. F. Arriagada, S. Nonell, and J. Morales, *Silica-based nanosystems for therapeutic applications in the skin*. Nanomedicine **2019**.14(16), p. 2243-2267.
10. D.Ş. Karaman, H. Kettiger, *Silica-based nanoparticles as drug delivery systems: Chances and challenges*, in *Inorganic Frameworks as Smart Nanomedicines*. 2018, Elsevier. p. 1-40.
11. M. Gonçalves, *Sol-gel silica nanoparticles in medicine: A natural choice. Design, synthesis and products*. Molecules **2018**.23(8), p. 2021.
12. S.P. Hudson, R.F. Padera, R. Langer, and D.S. Kohane, *The biocompatibility of mesoporous silicates*. Biomaterials **2008**.29(30), p. 4045-4055.
13. J. Lu, M. Liang, Z. Li, J.I. Zink, and F. Tamanoi, *Biocompatibility, biodistribution, and drug-delivery efficiency of mesoporous silica nanoparticles for cancer therapy in animals*. Small **2010**.6(16), p. 1794-1805.

14. Z. Tao, M.P. Morrow, T. Asefa, K.K. Sharma, C. Duncan, A. Anan et al., A.-K. Souid, *Mesoporous silica nanoparticles inhibit cellular respiration*. Nano letters **2008**.8(5), p. 1517-1526.
15. Y. Zhao, X. Sun, G. Zhang, B.G. Trewyn, I.I. Slowing, and V.S.-Y. Lin, *Interaction of mesoporous silica nanoparticles with human red blood cell membranes: size and surface effects*. ACS nano **2011**.5(2), p. 1366-1375.
16. K.K. Cotí, M.E. Belowich, M. Liong, M.W. Ambrogio, Y.A. Lau, H.A. Khatib et al., J.F. Stoddart, *Mechanised nanoparticles for drug delivery*. Nanoscale **2009**.1(1), p. 16-39.
17. Y. Zhou, G. Quan, Q. Wu, X. Zhang, B. Niu, B. Wu et al., C. Wu, *Mesoporous silica nanoparticles for drug and gene delivery*. Acta pharmaceutica sinica B **2018**.8(2), p. 165-177.
18. R. Narayan, U.Y. Nayak, A.M. Raichur, and S. Garg, *Mesoporous Silica Nanoparticles: A Comprehensive Review on Synthesis and Recent Advances*. Pharmaceutics **2018**.10(3), p. 118.
19. T.T.N. Thi, T.V. Tran, N.Q. Tran, C.K. Nguyen, and D.H. Nguyen, *Hierarchical self-assembly of heparin-PEG end-capped porous silica as a redox sensitive nanocarrier for doxorubicin delivery*. Materials Science and Engineering: C **2017**.70, p. 947-954.
20. Y. Chen, *Synthesis of hollow mesoporous silica nanoparticles by silica-etching chemistry for biomedical applications*, in *Design, Synthesis, Multifunctionalization and Biomedical Applications of Multifunctional Mesoporous Silica-Based Drug Delivery Nanosystems*. 2016, Springer. p. 31-46.
21. M. Vallet-Regí, M. Colilla, I. Izquierdo-Barba, and M. Manzano, *Mesoporous silica nanoparticles for drug delivery: Current insights*. Molecules **2018**.23(1), p. 47.
22. F. Ahmadi, A. Sodagar-Taleghani, P. Ebrahimnejad, S.P.H. Moghaddam, F. Ebrahimnejad, K. Asare-Addo, and A. Nokhodchi, *A review on the latest developments of mesoporous silica nanoparticles as a promising platform for diagnosis and treatment of cancer*. International Journal of Pharmaceutics **2022**, p. 122099.
23. Y.-D. Chiang, H.-Y. Lian, S.-Y. Leo, S.-G. Wang, Y. Yamauchi, and K.C.-W. Wu, *Controlling particle size and structural properties of mesoporous silica nanoparticles using the Taguchi method*. The Journal of Physical Chemistry C **2011**.115(27), p. 13158-13165.
24. N.I. Vazquez, Z. Gonzalez, B. Ferrari, and Y. Castro, *Synthesis of mesoporous silica nanoparticles by sol-gel as nanocontainer for future drug delivery applications*. Boletín de la Sociedad Española de Cerámica y Vidrio **2017**.56(3), p. 139-145.

25. K. Saini, R. Prabhuraj, and R. Bandyopadhyaya, *Development of mesoporous silica nanoparticles of tunable pore diameter for superior gemcitabine drug delivery in pancreatic cancer cells*. Journal of Nanoscience and Nanotechnology **2020**.20(5), p. 3084-3096.
26. C.-H. Lin, S.-H. Cheng, W.-N. Liao, P.-R. Wei, P.-J. Sung, C.-F. Weng, and C.-H. Lee, *Mesoporous silica nanoparticles for the improved anticancer efficacy of cis-platin*. International journal of pharmaceutics **2012**.429(1-2), p. 138-147.
27. A. Slita, A. Egorova, E. Casals, A. Kiselev, and J.M. Rosenholm, *Characterization of modified mesoporous silica nanoparticles as vectors for siRNA delivery*. Asian journal of pharmaceutical sciences **2018**.13(6), p. 592-599.
28. S. Porrang, N. Rahemi, S. Davaran, M. Mahdavi, B. Hassanzadeh, and A.M. Gholipour, *Direct surface modification of mesoporous silica nanoparticles by DBD plasma as a green approach to prepare dual-responsive drug delivery system*. Journal of the Taiwan Institute of Chemical Engineers **2021**.123, p. 47-58.
29. Z.-Z. Li, L.-X. Wen, L. Shao, and J.-F. Chen, *Fabrication of porous hollow silica nanoparticles and their applications in drug release control*. Journal of Controlled Release **2004**.98(2), p. 245-254.
30. J.-F. Chen, H.-M. Ding, J.-X. Wang, and L. Shao, *Preparation and characterization of porous hollow silica nanoparticles for drug delivery application*. Biomaterials **2004**.25(4), p. 723-727.
31. N.X.D. Mai, A. Birault, K. Matsumoto, H.K.T. Ta, S.G. Intasa-ard, K. Morrison et al., F. Tamanoi, *Biodegradable Periodic Mesoporous Organosilica (BPMO) Loaded with Daunorubicin: A Promising Nanoparticle-Based Anticancer Drug*. ChemMedChem **2020**.
32. K.M. Le, N.-T. Trinh, V.D.-X. Nguyen, T.-D. Van Nguyen, T.-H. Thi Nguyen, T. Van Vo et al., L.B. Vong, *Investigating the Anti-Inflammatory Activity of Curcumin-Loaded Silica-Containing Redox Nanoparticles*. Journal of Nanomaterials **2021**.2021.
33. N.X.D. Mai, U.-C.N. Le, L.H.T. Nguyen, H.T.K. Ta, H. Van Nguyen, T.M. Le et al., T.L.H. Doan, *Facile synthesis of biodegradable mesoporous functionalized-organosilica nanoparticles for enhancing the anti-cancer efficiency of cordycepin*. Microporous and Mesoporous Materials **2021**.315, p. 110913.
34. N.X.D. Mai, T.-H.T. Nguyen, L.B. Vong, M.-H.D. Dang, T.T.T. Nguyen, L.H.T. Nguyen et al., T.L.H. Doan, *Tailoring chemical compositions of biodegradable mesoporous organosilica nanoparticles for controlled slow release of chemotherapeutic drug*. Materials Science and Engineering: C **2021**.127, p. 112232.

35. M.A. Hossain, M. Yamashita, L.B. Vong, Y. Ikeda, and Y. Nagasaki, *Silica-installed redox nanoparticles for novel oral nanotherapeutics–improvement in intestinal delivery with anti-inflammatory effects*. *Journal of drug targeting* **2014**.22(7), p. 638-647.
36. L.B. Vong, S. Kimura, and Y. Nagasaki, *Newly Designed Silica-Containing Redox Nanoparticles for Oral Delivery of Novel TOP2 Catalytic Inhibitor for Treating Colon Cancer*. *Advanced healthcare materials* **2017**.6(20), p. 1700428.
37. T.-H.T. Nguyen, N.-T. Trinh, H.N. Tran, H.T. Tran, P.Q. Le, D.-N. Ngo et al.. Y. Nagasaki, *Improving Silymarin oral bioavailability using silica-installed redox nanoparticle to suppress inflammatory bowel disease*. *Journal of Controlled Release* **2020**.
38. T.T.N. Thi, Tran, T. V., Tran, N. Q., Nguyen, C. K., & Nguyen, D. H., *Hierarchical self-assembly of heparin-PEG end-capped porous silica as a redox sensitive nanocarrier for doxorubicin delivery*. *Materials Science and Engineering: C* **2017**.70, p. 947-954.
39. T.T.H. Thi, T.N.Q. Nguyen, D.T. Hoang, and D.H. Nguyen, *Functionalized mesoporous silica nanoparticles and biomedical applications*. *Materials Science and Engineering: C* **2019**.99, p. 631-656.
40. T.N.T. Nguyen, N.T.T. Le, N.H. Nguyen, B.T.K. Ly, T.D. Nguyen, and D.H. Nguyen, *Aminated hollow mesoporous silica nanoparticles as an enhanced loading and sustained releasing carrier for doxorubicin delivery*. *Microporous and Mesoporous Materials* **2020**.309, p. 110543.
41. T.N.T. Nguyen, D.-H. Nguyen-Tran, L.G. Bach, T.H. Du Truong, N.T.T. Le, and D.H. Nguyen, *Surface PEGylation of hollow mesoporous silica nanoparticles via aminated intermediate*. *Progress in Natural Science: Materials International* **2019**.29(6), p. 612-616.
42. N.-T. Nguyen-Thi, L.P. Pham Tran, N.T.T. Le, M.-T. Cao, N.T. Nguyen, C.H. Nguyen et al.. N.Q. Trung, *The Engineering of Porous Silica and Hollow Silica Nanoparticles to Enhance Drug-loading Capacity*. *Processes* **2019**.7(11), p. 805.
43. N.T.N. Thi, D.H. Nguyen, *Hollow mesoporous silica nanoparticles fabrication for anticancer drug delivery*. *Vietnam Journal of Science and Technology* **2020**.58(1), p. 39.
44. U.V. Vo, V.C. Nguyen, X.V.D. Vo, M.K.T. Vo, H.A. Le Pham, T.T.N. Tran et al.. C.K. Nguyen, *Synthesize and survey the drug loading efficiency of the porous nano silica modified by gelatin*. *Advances in Natural Sciences: Nanoscience and Nanotechnology* **2019**.10(3), p. 035017.
45. Y. Chen, H.-R. Chen, and J.-L. Shi, *Construction of homogenous/heterogeneous hollow mesoporous silica nanostructures by*

- silica-etching chemistry: principles, synthesis, and applications*. Accounts of chemical research **2014**.47(1), p. 125-137.
46. D. Mahony, A. Cavallaro, K. Mody, L. Xiong, T. Mahony, S. Qiao, and N. Mitter, *In vivo delivery of bovine viral diarrhoea virus, E2 protein using hollow mesoporous silica nanoparticles*. Nanoscale **2014**.6(12), p. 6617-6626.
 47. Y. Zhang, C.Y. Ang, M. Li, S.Y. Tan, Q. Qu, Z. Luo, and Y. Zhao, *Polymer-coated hollow mesoporous silica nanoparticles for triple-responsive drug delivery*. ACS applied materials & interfaces **2015**.7(32), p. 18179-18187.
 48. Y. Feng, N. Panwar, D.J.H. Tng, S.C. Tjin, K. Wang, and K.-T. Yong, *The application of mesoporous silica nanoparticle family in cancer theranostics*. Coordination Chemistry Reviews **2016**.319, p. 86-109.
 49. X. Wang, J. Feng, Y. Bai, Q. Zhang, and Y. Yin, *Synthesis, properties, and applications of hollow micro-/nanostructures*. Chemical reviews **2016**.116(18), p. 10983-11060.
 50. J. Hu, M. Chen, X. Fang, and L. Wu, *Fabrication and application of inorganic hollow spheres*. Chemical Society Reviews **2011**.40(11), p. 5472-5491.
 51. M. Fuji, T. Shin, H. Watanabe, and T. Takei, *Shape-controlled hollow silica nanoparticles synthesized by an inorganic particle template method*. Advanced Powder Technology **2012**.23(5), p. 562-565.
 52. F. Chen, H. Hong, S. Shi, S. Goel, H.F. Valdovinos, R. Hernandez et al., W. Cai, *Engineering of hollow mesoporous silica nanoparticles for remarkably enhanced tumor active targeting efficacy*. Scientific reports **2014**.4(1), p. 1-10.
 53. A.K. Meka, P.L. Abbaraju, H. Song, C. Xu, J. Zhang, H. Zhang et al., C. Yu, *A Vesicle Supra-Assembly Approach to Synthesize Amine-Functionalized Hollow Dendritic Mesoporous Silica Nanospheres for Protein Delivery*. Small **2016**.12(37), p. 5169-5177.
 54. S.F. Soares, T. Fernandes, A.L. Daniel-da-Silva, and T. Trindade, *The controlled synthesis of complex hollow nanostructures and prospective applications*. Proceedings of the Royal Society A **2019**.475(2224), p. 20180677.
 55. B. Peng, M. Chen, S. Zhou, L. Wu, and X. Ma, *Fabrication of hollow silica spheres using droplet templates derived from a miniemulsion technique*. Journal of colloid and interface science **2008**.321(1), p. 67-73.
 56. M. Mandal, M. Kruk, *Family of single-micelle-templated organosilica hollow nanospheres and nanotubes synthesized through adjustment of organosilica/surfactant ratio*. Chemistry of Materials **2012**.24(1), p. 123-132.

57. H. Wang, X. Liu, O. Saliy, W. Hu, and J. Wang, *Robust Amino-Functionalized Mesoporous Silica Hollow Spheres Templated by CO₂ Bubbles*. *Molecules* **2022**.27(1), p. 53.
58. S. Yu, B. Liu, Q. Wang, Y. Gao, Y. Shi, X. Feng et al., J. Zhang, *Ionic liquid assisted chemical strategy to TiO₂ hollow nanocube assemblies with surface-fluorination and nitridation and high energy crystal facet exposure for enhanced photocatalysis*. *ACS applied materials & interfaces* **2014**.6(13), p. 10283-10295.
59. L. Zhang, H. Wang, *Interior structural tailoring of Cu₂O shell-in-shell nanostructures through multistep Ostwald ripening*. *The Journal of Physical Chemistry C* **2011**.115(38), p. 18479-18485.
60. W. Stöber, A. Fink, and E. Bohn, *Controlled growth of monodisperse silica spheres in the micron size range*. *Journal of colloid and interface science* **1968**.26(1), p. 62-69.
61. G. Bogush, C. Zukoski Iv, *Studies of the kinetics of the precipitation of uniform silica particles through the hydrolysis and condensation of silicon alkoxides*. *Journal of Colloid and Interface Science* **1991**.142(1), p. 1-18.
62. V. Masalov, N. Sukhinina, E. Kudrenko, and G. Emelchenko, *Mechanism of formation and nanostructure of Stöber silica particles*. *Nanotechnology* **2011**.22(27), p. 275718.
63. M. Grün, I. Lauer, and K.K. Unger, *The synthesis of micrometer- and submicrometer-size spheres of ordered mesoporous oxide MCM-41*. *Advanced Materials* **1997**.9(3), p. 254-257.
64. W. Li, Y. Tian, C. Zhao, B. Zhang, H. Zhang, Q. Zhang, and W. Geng, *Investigation of selective etching mechanism and its dependency on the particle size in preparation of hollow silica spheres*. *Journal of Nanoparticle Research* **2015**.17(12), p. 1-11.
65. M.J. Mitchell, M.M. Billingsley, R.M. Haley, M.E. Wechsler, N.A. Peppas, and R. Langer, *Engineering precision nanoparticles for drug delivery*. *Nature Reviews Drug Discovery* **2021**.20(2), p. 101-124.
66. M.P. Desai, V. Labhassetwar, E. Walter, R.J. Levy, and G.L. Amidon, *The mechanism of uptake of biodegradable microparticles in Caco-2 cells is size dependent*. *Pharmaceutical research* **1997**.14(11), p. 1568-1573.
67. N.T.N. Thi, D.H. Nguyen, *Hollow mesoporous silica nanoparticles fabrication for anticancer drug delivery*. *Vietnam Journal of Science and Technology* **2020**.58(1), p. 39-39.
68. Y. Jiao, J. Guo, S. Shen, B. Chang, Y. Zhang, X. Jiang, and W. Yang, *Synthesis of discrete and dispersible hollow mesoporous silica nanoparticles with tailored shell thickness for controlled drug release*. *Journal of Materials Chemistry* **2012**.22(34), p. 17636-17643.

69. A.M. El-Toni, A. Khan, M.A. Ibrahim, J.P. Labis, M. Al-Hoshan, S. Yin, and T. Sato, *Synthesis of double mesoporous core-shell silica spheres with tunable core porosity and their drug release and cancer cell apoptosis properties*. Journal of colloid and interface science **2012**.378(1), p. 83-92.
70. D. Deepika, J. Ponnannettiappan, *Synthesis and characterization of microporous hollow core-shell silica nanoparticles (HCSNs) of tunable thickness for controlled release of doxorubicin*. Journal of Nanoparticle Research **2018**.20(7), p. 1-15.
71. L. Haddick, W. Zhang, S. Reinhard, K. Möller, H. Engelke, E. Wagner, and T. Bein, *Particle-size-dependent delivery of antitumoral miRNA using targeted mesoporous silica nanoparticles*. Pharmaceutics **2020**.12(6), p. 505.
72. K. Möller, T. Bein, *Degradable drug carriers: vanishing mesoporous silica nanoparticles*. Chemistry of Materials **2019**.31(12), p. 4364-4378.
73. S. Yismaw, R. Kohns, D. Schneider, D. Poppitz, S.G. Ebbinghaus, R. Gläser et al., D. Enke, *Particle size control of monodispersed spherical nanoparticles with MCM-48-type mesostructure via novel rapid synthesis procedure*. Journal of Nanoparticle Research **2019**.21(12), p. 1-13.
74. N.X.D. Mai, Y.T. Dang, H.K.T. Ta, J.-S. Bae, S. Park, B.T. Phan et al., T.L.H. Doan, *Reducing particle size of biodegradable nanomaterial for efficient curcumin loading*. Journal of Materials Science **2021**.56(5), p. 3713-3722.
75. S.M. Mousavi Elyerdi, M.N. Sarvi, and A.J. O'Connor, *Synthesis of ultra small nanoparticles (< 50 nm) of mesoporous MCM-48 for bio-adsorption*. Journal of Porous Materials **2019**.26(3), p. 839-846.
76. F. Catalano, P.P. Pompa, *Design Rules for Mesoporous Silica toward the Nanosize: A Systematic Study*. ACS Applied Materials & Interfaces **2019**.11(50), p. 47237-47246.
77. T.-D. Nguyen, T.-O. Do, *Size- and shape-controlled synthesis of monodisperse metal oxide and mixed oxide nanocrystals*. Nanocrystal **2011**.2, p. 55-84.
78. C. Vidyasagar, Y.A. Naik, *Surfactant (PEG 400) effects on crystallinity of ZnO nanoparticles*. Arabian Journal of Chemistry **2016**.9(4), p. 507-510.
79. C. Iacovita, R. Stiufiuc, T. Radu, A. Florea, G. Stiufiuc, A. Dutu et al., C.M. Lucaciu, *Polyethylene glycol-mediated synthesis of cubic iron oxide nanoparticles with high heating power*. Nanoscale research letters **2015**.10(1), p. 1-16.
80. K. Shameli, M. Bin Ahmad, S.D. Jazayeri, S. Sedaghat, P. Shabanzadeh, H. Jahangirian et al., Y. Abdollahi, *Synthesis and characterization of polyethylene glycol mediated silver nanoparticles by the green method*. International journal of molecular sciences **2012**.13(6), p. 6639-6650.
81. Y. Hatakeyama, T. Morita, S. Takahashi, K. Onishi, and K. Nishikawa, *Synthesis of gold nanoparticles in liquid polyethylene glycol by sputter*

- deposition and temperature effects on their size and shape.* The Journal of Physical Chemistry C **2011.115**(8), p. 3279-3285.
82. Q.W. Zhu, M.G. Ou. *The function of PEG in the synthesis of nanomaterials.* in *Applied Mechanics and Materials*. 2014. Trans Tech Publ.
 83. F. Pellegrino, F. Sordello, L. Mino, M. Prozzi, U. Mansfeld, V.-D. Hodoroba, and C. Minero, *Polyethylene glycol as shape and size controller for the hydrothermal synthesis of SrTiO₃ cubes and polyhedra.* *Nanomaterials* **2020.10**(9), p. 1892.
 84. Y. Miao, G. Chen, H. Wang, and X.-w. GUO, *Synthesis of nanometer magnesium hydroxide by direct precipitation method with PEG 6000 as dispersant [J].* Journal of Henan Normal University (Natural Science Edition) **2011.39**(5), p. 110-113.
 85. C. Li, J.-H. Du, and W.-Z. Han, *Effects of Polyethylene Glycol on Stability of Nano Silica in Aqueous Suspension.* Zhuangjiabing Gongcheng Xueyuan Xuebao (Journal of Academy of Armored Force Engineering) **2007.21**(3), p. 74-77.
 86. C. Chapa-González, A.L. Piñón-Urbina, and P.E. García-Casillas, *Synthesis of controlled-size silica nanoparticles from sodium metasilicate and the effect of the addition of PEG in the size distribution.* *Materials* **2018.11**(4), p. 510.
 87. X. Hong, X. Zhong, G. Du, Y. Hou, Y. Zhang, Z. Zhang et al., X. Sun, *The pore size of mesoporous silica nanoparticles regulates their antigen delivery efficiency.* *Science advances* **2020.6**(25), p. eaaz4462.
 88. J. Li, S. Shen, F. Kong, T. Jiang, C. Tang, and C. Yin, *Effects of pore size on in vitro and in vivo anticancer efficacies of mesoporous silica nanoparticles.* *RSC advances* **2018.8**(43), p. 24633-24640.
 89. P. Horcajada, A. Ramila, J. Perez-Pariente, and M. Vallet-Regí, *Influence of pore size of MCM-41 matrices on drug delivery rate.* *Microporous and Mesoporous Materials* **2004.68**(1-3), p. 105-109.
 90. R.G. Tilkin, J.G. Mahy, A.P. Monteiro, A. Belet, J. Feijóo, M. Laird et al., C. Grandfils, *Protein encapsulation in mesoporous silica: Influence of the mesostructured and pore wall properties.* *Colloids and Surfaces A: Physicochemical and Engineering Aspects* **2022.642**, p. 128629.
 91. Y. Wu, X. Sun, H. Wang, J. Shen, and Y. Ke, *Pore size control of monodisperse mesoporous silica particles with alkyl imidazole ionic liquid templates for high performance liquid chromatography applications.* *Colloids and Surfaces A: Physicochemical and Engineering Aspects* **2022.637**, p. 128200.
 92. L. Chen, X. Zhou, and C. He, *Mesoporous silica nanoparticles for tissue-engineering applications.* *Wiley Interdisciplinary Reviews: Nanomedicine and Nanobiotechnology* **2019.11**(6), p. e1573.

93. Y. He, J. Li, M. Long, S. Liang, and H. Xu, *Tuning pore size of mesoporous silica nanoparticles simply by varying reaction parameters*. Journal of Non-Crystalline Solids **2017**.457, p. 9-12.
94. P. Bilalis, L.-A. Tziveleka, S. Varlas, and H. Iatrou, *pH-Sensitive nanogates based on poly (l-histidine) for controlled drug release from mesoporous silica nanoparticles*. Polymer Chemistry **2016**.7(7), p. 1475-1485.
95. C. Vautier-Giongo, H.O. Pastore, *Micellization of CTAB in the presence of silicate anions and the exchange between bromide and silicate at the micelle surface: A step to understand the formation of mesoporous molecular sieves at extremely low surfactant and silicate concentrations*. Journal of colloid and interface science **2006**.299(2), p. 874-882.
96. X. Liu, L. Li, Y. Du, Z. Guo, T.T. Ong, Y. Chen et al., Y. Yang, *Synthesis of large pore-diameter SBA-15 mesostructured spherical silica and its application in ultra-high-performance liquid chromatography*. Journal of Chromatography A **2009**.1216(45), p. 7767-7773.
97. S. Chatterjee, P. Sen, K. Das, S. Bhattacharya, and R. Palepu, *Mixed micellization of ionic and nonionic surfactants in aqueous solution*. Journal of dispersion science and technology **2006**.27(5), p. 751-759.
98. C. Bharti, U. Nagaich, A.K. Pal, and N. Gulati, *Mesoporous silica nanoparticles in target drug delivery system: A review*. International journal of pharmaceutical investigation **2015**.5(3), p. 124.
99. N. Mizoshita, T. Tani, and S. Inagaki, *Syntheses, properties and applications of periodic mesoporous organosilicas prepared from bridged organosilane precursors*. Chemical Society Reviews **2011**.40(2), p. 789-800.
100. N.S. Zaharudin, E.D.M. Isa, H. Ahmad, M.B.A. Rahman, and K. Jumbri, *Functionalized mesoporous silica nanoparticles templated by pyridinium ionic liquid for hydrophilic and hydrophobic drug release application*. Journal of Saudi Chemical Society **2020**.24(3), p. 289-302.
101. S. Yismaw, S.G. Ebbinghaus, M. Wenzel, D. Poppitz, R. Gläser, J. Matysik et al., D. Enke, *Selective functionalization of the outer surface of MCM-48-type mesoporous silica nanoparticles at room temperature*. Journal of Nanoparticle Research **2020**.22(9), p. 1-15.
102. Z. Tian, Y. Xu, and Y. Zhu, *Aldehyde-functionalized dendritic mesoporous silica nanoparticles as potential nanocarriers for pH-responsive protein drug delivery*. Materials Science and Engineering: C **2017**.71, p. 452-459.
103. D. Díaz-García, L. Sommerova, A. Martisova, H. Skoupilova, S. Prashar, T. Vaculovic et al., S. Gómez-Ruiz, *Mesoporous silica nanoparticles functionalized with a dialkoxide diorganotin (IV) compound: In search of more selective systems against cancer cells*. Microporous and Mesoporous Materials **2020**.300, p. 110154.

104. K.K. Bansal, D.K. Mishra, A. Rosling, and J.M. Rosenholm, *Therapeutic potential of polymer-coated mesoporous silica nanoparticles*. Applied Sciences **2020**.10(1), p. 289.
105. I. Garrido-Cano, V. Candela-Noguera, G. Herrera, J.M. Cejalvo, A. Lluch, M.D. Marcos et al., R. Martínez-Mañez, *Biocompatibility and internalization assessment of bare and functionalised mesoporous silica nanoparticles*. Microporous and Mesoporous Materials **2021**.310, p. 110593.
106. I. Jarak, C.L. Varela, E.T. da Silva, F.F. Roleira, F. Veiga, and A. Figueiras, *Pluronic-based nanovehicles: Recent advances in anticancer therapeutic applications*. European Journal of Medicinal Chemistry **2020**.206, p. 112526.
107. A. Pitto-Barry, N.P. Barry, *Pluronic® block-copolymers in medicine: from chemical and biological versatility to rationalisation and clinical advances*. Polymer Chemistry **2014**.5(10), p. 3291-3297.
108. T.T.C. Nguyen, C.K. Nguyen, T.H. Nguyen, and N.Q. Tran, *Highly lipophilic pluronics-conjugated polyamidoamine dendrimer nanocarriers as potential delivery system for hydrophobic drugs*. Materials Science and Engineering: C **2017**.70, p. 992-999.
109. J.D. Kim, Y.J. Jung, C.H. Woo, Y.C. Choi, J.S. Choi, and Y.W. Cho, *Thermo-responsive human α -elastin self-assembled nanoparticles for protein delivery*. Colloids and Surfaces B: Biointerfaces **2017**.149, p. 122-129.
110. A. Yildirim, G.B. Demirel, R. Erdem, B. Senturk, T. Tekinay, and M. Bayindir, *Pluronic polymer capped biocompatible mesoporous silica nanocarriers*. Chemical Communications **2013**.49(84), p. 9782-9784.
111. R. Basak, R. Bandyopadhyay, *Encapsulation of hydrophobic drugs in Pluronic F127 micelles: effects of drug hydrophobicity, solution temperature, and pH*. Langmuir **2013**.29(13), p. 4350-4356.
112. M.A. Cerqueira, B.W. Souza, J. Simões, J.A. Teixeira, M.R.M. Domingues, M.A. Coimbra, and A.A. Vicente, *Structural and thermal characterization of galactomannans from non-conventional sources*. Carbohydrate polymers **2011**.83(1), p. 179-185.
113. S.R. Khalil, A.T. Mohammed, A.H. Abd El-fattah, and A.W. Zagloul, *Intermediate filament protein expression pattern and inflammatory response changes in kidneys of rats receiving doxorubicin chemotherapy and quercetin*. Toxicology Letters **2018**.288, p. 89-98.
114. S. Hassanzadeh, Z. Feng, T. Pettersson, and M. Hakkarainen, *A proof-of-concept for folate-conjugated and quercetin-anchored pluronic mixed micelles as molecularly modulated polymeric carriers for doxorubicin*. Polymer **2015**.74, p. 193-204.
115. S. Liu, R. Li, J. Qian, J. Sun, G. Li, J. Shen, and Y. Xie, *Combination therapy of doxorubicin and quercetin on multidrug-resistant breast cancer and their*

- sequential delivery by reduction-sensitive hyaluronic acid-based conjugate/d- α -tocopheryl poly (ethylene glycol) 1000 succinate mixed micelles*. *Molecular pharmaceutics* **2020**.17(4), p. 1415-1427.
116. S. Dahiya, R. Dahiya, and E. Hernández, *Nanocarriers for anticancer drug targeting: recent trends and challenges*. *Critical Reviews™ in Therapeutic Drug Carrier Systems* **2021**.38(6).
 117. J. Zhang, L. Weng, X. Su, G. Lu, W. Liu, Y. Tang et al.. L. Wang, *Cisplatin and doxorubicin high-loaded nanodrug based on biocompatible thioether- and ethane-bridged hollow mesoporous organosilica nanoparticles*. *Journal of colloid and interface science* **2018**.513, p. 214-221.
 118. Z. Li, Y. Zhang, C. Zhu, T. Guo, Q. Xia, X. Hou et al.. N. Feng, *Folic acid modified lipid-bilayer coated mesoporous silica nanoparticles co-loading paclitaxel and tanshinone IIA for the treatment of acute promyelocytic leukemia*. *International journal of pharmaceutics* **2020**.586, p. 119576.
 119. X. Chen, L. Song, X. Li, L. Zhang, L. Li, X. Zhang, and C. Wang, *Co-delivery of hydrophilic/hydrophobic drugs by multifunctional yolk-shell nanoparticles for hepatocellular carcinoma theranostics*. *Chemical Engineering Journal* **2020**.389, p. 124416.
 120. U.V. Vo, C.K. Nguyen, V.C. Nguyen, T.V. Tran, B.Y.T. Thi, and D.H. Nguyen, *Gelatin-poly (ethylene glycol) methyl ether-functionalized porous Nanosilica for efficient doxorubicin delivery*. *Journal of Polymer Research* **2019**.26(1), p. 6.
 121. J. Liu, Z. Luo, J. Zhang, T. Luo, J. Zhou, X. Zhao, and K. Cai, *Hollow mesoporous silica nanoparticles facilitated drug delivery via cascade pH stimuli in tumor microenvironment for tumor therapy*. *Biomaterials* **2016**.83, p. 51-65.
 122. Z. Luo, K. Cai, Y. Hu, L. Zhao, P. Liu, L. Duan, and W. Yang, *Mesoporous silica nanoparticles end-capped with collagen: redox-responsive nanoreservoirs for targeted drug delivery*. *Angewandte Chemie International Edition* **2011**.50(3), p. 640-643.
 123. N. Gorochovceva, R. Kulbokaite, R. Juskenas, and R. Makuska, *Synthesis and study of chitosan and poly (ethylene glycol) graft copolymers containing triazine moiety*. *Chemija* **2004**.15(1), p. 22-27.
 124. X. Teng, S. Cheng, R. Meng, S. Zheng, L. Yang, Q. Ma et al.. J. He, *A facile way for fabricating PEGylated hollow mesoporous silica nanoparticles and their drug delivery application*. *Journal of Nanoscience and Nanotechnology* **2015**.15(5), p. 3773-3779.
 125. D.H.T. Nguyen, D.Y.P. Nguyen, L.P.T. Pham, T.N.N. Vo, D.H. Nguyen, and K.D. Park. *Preparation and Characterization of Redox-Sensitive Pluronic F127-Based Nanogel as Effective Nanocarrier for Drug Delivery*. in

- International Conference on the Development of Biomedical Engineering in Vietnam*. 2018. Springer.
126. W. Rao, H. Wang, J. Han, S. Zhao, J. Dumbleton, P. Agarwal et al., D.L. Zynger, *Chitosan-decorated doxorubicin-encapsulated nanoparticle targets and eliminates tumor reinitiating cancer stem-like cells*. ACS nano **2015**.9(6), p. 5725-5740.
 127. Y. He, L. Luo, S. Liang, M. Long, and H. Xu, *Amino-functionalized mesoporous silica nanoparticles as efficient carriers for anticancer drug delivery*. Journal of biomaterials applications **2017**.32(4), p. 524-532.
 128. D. Liu, M. Yang, D. Wang, X. Jing, Y. Lin, L. Feng, and X. Duan, *DPD Study on the Interfacial Properties of PEO/PEO-PPO-PEO/PPO Ternary Blends: Effects of Pluronic Structure and Concentration*. Polymers **2021**.13(17), p. 2866.
 129. J. Yu, H. Qiu, S. Yin, H. Wang, and Y. Li, *Polymeric drug delivery system based on pluronics for cancer treatment*. Molecules **2021**.26(12), p. 3610.
 130. A. Sikora, A.G. Shard, and C. Minelli, *Size and ζ -potential measurement of silica nanoparticles in serum using tunable resistive pulse sensing*. Langmuir **2016**.32(9), p. 2216-2224.
 131. M. Danaei, M. Dehghankhold, S. Ataei, F. Hasanzadeh Davarani, R. Javanmard, A. Dokhani et al., M. Mozafari, *Impact of particle size and polydispersity index on the clinical applications of lipidic nanocarrier systems*. Pharmaceutics **2018**.10(2), p. 57.
 132. D.H. Guston, *Encyclopedia of nanoscience and society*. 2010: SAGE Publications, Inc. 1024.
 133. D. Peer, J. Kar, S. Hong, O. Farokhazad, and L.R. Margalit, *Nanocarriers as an emerging platform for cancer therapy*. Nature **2007**.2, p. 10.
 134. K. Cheng, Y. Zhang, Y. Li, Z. Gao, F. Chen, K. Sun et al., B. Sun, *A novel pH-responsive hollow mesoporous silica nanoparticle (HMSN) system encapsulating doxorubicin (DOX) and glucose oxidase (GOX) for potential cancer treatment*. Journal of Materials Chemistry B **2019**.7(20), p. 3291-3302.
 135. M. Khoeini, A. Najafi, H. Rastegar, and M. Amani, *Improvement of hollow mesoporous silica nanoparticles synthesis by hard-templating method via CTAB surfactant*. Ceramics International **2019**.45(10), p. 12700-12707.
 136. R. Dubey, Y. Rajesh, and M. More, *Synthesis and characterization of SiO₂ nanoparticles via sol-gel method for industrial applications*. Materials Today: Proceedings **2015**.2(4-5), p. 3575-3579.
 137. E. Joseph, G. Singhvi, *Multifunctional nanocrystals for cancer therapy: a potential nanocarrier*. Nanomaterials for drug delivery and therapy **2019**, p. 91-116.

138. N.V. Scarlett, I.C. Madsen, *Effect of microabsorption on the determination of amorphous content via powder X-ray diffraction*. Powder Diffraction **2018**.33(1), p. 26-37.
139. J. Lasio, A.M. Allgeier, C.D. Chan, J.D. Londono, E. Najafi, and F.J. Woerner, *Control of Mechanical Stability of Hollow Silica Particles, and Its Measurement by Mercury Intrusion Porosimetry*. Langmuir **2017**.33(19), p. 4666-4674.
140. M.A. Bag, L.M. Valenzuela, *Impact of the hydration states of polymers on their hemocompatibility for medical applications: A review*. International journal of molecular sciences **2017**.18(8), p. 1422.
141. O. Philippova, S. Kuchanov, I. Topchieva, and V. Kabanov, *Hydrogen bonds in dilute solutions of poly (ethylene glycol)*. Macromolecules **1985**.18(8), p. 1628-1633.
142. S. Lüsse, K. Arnold, *The interaction of poly (ethylene glycol) with water studied by 1H and 2H NMR relaxation time measurements*. Macromolecules **1996**.29(12), p. 4251-4257.
143. S.-C. Liufu, H.-N. Xiao, Y.-P. Li, and Z.-R. Hu, *Polyethylene glycol adsorption behavior on nanoparticulate TiO₂ and its stability in aqueous dispersions*. Journal of Inorganic Materials **2005**.20(2), p. 310-316.
144. F. Beiranvand, S.H. Najibi, and B. Hashemi Shahraki, *Experimental measurement of equilibrium surface tension of an aqueous solution of polyethylene glycol and a surfactant*. Iranian Journal of Oil and Gas Science and Technology **2020**.9(3), p. 26-43.
145. Y. Wu, Y. Long, Q.-L. Li, S. Han, J. Ma, Y.-W. Yang, and H. Gao, *Layer-by-layer (LBL) self-assembled biohybrid nanomaterials for efficient antibacterial applications*. ACS Applied Materials & Interfaces **2015**.7(31), p. 17255-17263.
146. X. Li, C.-H. Wong, T.-W. Ng, C.-F. Zhang, K.C.-F. Leung, and L. Jin, *The spherical nanoparticle-encapsulated chlorhexidine enhances anti-biofilm efficiency through an effective releasing mode and close microbial interactions*. International journal of nanomedicine **2016**.11, p. 2471.
147. V. Patel, N. Dharaiya, D. Ray, V.K. Aswal, and P. Bahadur, *pH controlled size/shape in CTAB micelles with solubilized polar additives: a viscometry, scattering and spectral evaluation*. Colloids and Surfaces A: Physicochemical and Engineering Aspects **2014**.455, p. 67-75.
148. K. Kuperkar, L. Abezgauz, D. Danino, G. Verma, P. Hassan, V. Aswal et al., P. Bahadur, *Viscoelastic micellar water/CTAB/NaNO₃ solutions: rheology, SANS and cryo-TEM analysis*. Journal of colloid and interface science **2008**.323(2), p. 403-409.

149. T. Movchan, I. Soboleva, E. Plotnikova, A. Shchekin, and A. Rusanov, *Dynamic light scattering study of cetyltrimethylammonium bromide aqueous solutions*. Colloid Journal **2012**.74(2), p. 239-247.
150. P. Kalsi, *Organic reactions stereochemistry and mechanism (Through Solved Problems)*. 2007: New Age International.
151. P. Kerativitayanan, J.K. Carrow, and A.K. Gaharwar, *Nanomaterials for engineering stem cell responses*. Advanced healthcare materials **2015**.4(11), p. 1600-1627.
152. D.H. Guston, *Encyclopedia of nanoscience and society*. Vol. 1. 2010: Sage.
153. E. Kaiser, R.L. Colescott, C.D. Bossinger, and P.I. Cook, *Color test for detection of free terminal amino groups in the solid-phase synthesis of peptides*. Anal Biochem **1970**.34(2), p. 595-8.
154. H. Wei, L. Han, J. Ren, and L. Jia, *Anticoagulant surface coating using composite polysaccharides with embedded heparin-releasing mesoporous silica*. ACS applied materials & interfaces **2013**.5(23), p. 12571-12578.
155. L. Potgieter, M. McCracken, F. Hopkins, R. Walker, and J. Guy, *Experimental production of bovine respiratory tract disease with bovine viral diarrhoea virus*. American journal of veterinary research **1984**.45(8), p. 1582-1585.
156. E. Dietrich, H. Oudadesse, A. Lucas-Girot, Y. Le Gal, S. Jeanne, and G. Cathelineau, *Effects of Mg and Zn on the surface of doped melt-derived glass for biomaterials applications*. Applied Surface Science **2008**.255(2), p. 391-395.
157. B. White, S. Banerjee, S. O'Brien, N.J. Turro, and I.P. Herman, *Zeta-potential measurements of surfactant-wrapped individual single-walled carbon nanotubes*. The Journal of Physical Chemistry C **2007**.111(37), p. 13684-13690.
158. W. Ahmed, M.J. Jackson, *Emerging nanotechnologies for manufacturing*. 2 ed. 2014: William Andrew. 576.
159. M. Yu, J. Zhao, and S. Feng, *Vitamin E TPGS prodrug micelles for hydrophilic drug delivery with neutroprotective effects*. International Journal of Pharmaceutic **2012**.438(1), p. 9.
160. V. Nairi, S. Medda, M. Piludu, M.F. Casula, M. Vallet-Regi, M. Monduzzi, and A. Salis, *Interactions between bovine serum albumin and mesoporous silica nanoparticles functionalized with biopolymers*. Chemical Engineering Journal **2018**.340, p. 42-50.
161. Y. Yamada, *Dimerization of doxorubicin causes its precipitation*. ACS omega **2020**.5(51), p. 33235-33241.
162. K. Rayappan, C. Murugan, S. Sundarraj, R.P. Lara, and S. Kannan, *Peptide-Conjugated Nano-Drug Delivery System to Improve Synergistic Molecular*

- Chemotherapy for Colon Carcinoma*. ChemistrySelect **2017**.2(27), p. 8524-8534.
163. C. Huo, J. Ouyang, and H. Yang, *CuO nanoparticles encapsulated inside Al-MCM-41 mesoporous materials via direct synthetic route*. Scientific reports **2014**.4, p. 3682.
164. R. Pradhan, S.Y. Kim, C.S. Yong, and J.O. Kim, *Preparation and characterization of spray-dried valsartan-loaded Eudragit® E PO solid dispersion microparticles*. asian journal of pharmaceutical sciences **2016**.11(6), p. 744-750.

APPENDIX

DLS size of dSiO₂

2022.07.19 16:03:13

HORIBA
Scientific

HORIBA SZ-100 for Windows [Z Type] Ver2.20

SZ-100

dSiO₂_001.nsz

Measurement Results

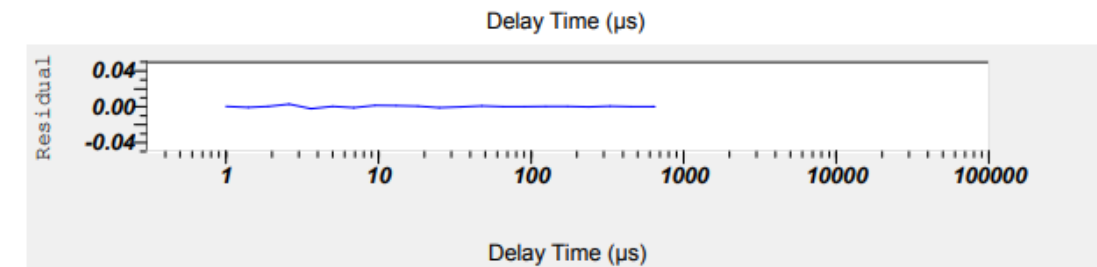
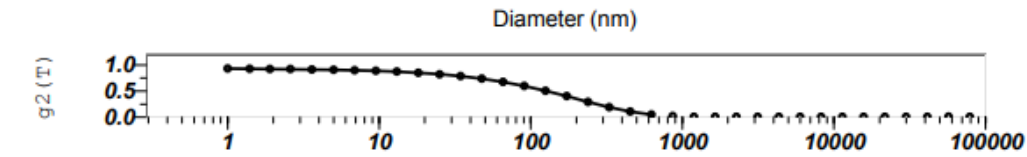
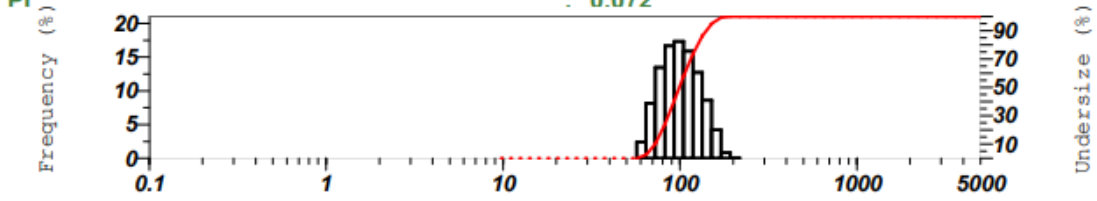
Date : Tuesday, July 19, 2022 15:59:24 PM
 Measurement Type : Particle Size
 Sample Name : dSiO₂
 Scattering Angle : 90
 Temperature of the Holder : 24.8 °C
 Dispersion Medium Viscosity : 0.898 mPa·s
 Transmission Intensity before Meas. : 26611
 Distribution Form : Standard
 Distribution Form(Dispersity) : Monodisperse
 Representation of Result : Scattering Light Intensity
 Count Rate : 2002 kCPS

Calculation Results

Peak No.	S.P.Area Ratio	Mean	S. D.	Mode
1	1.00	103.3 nm	26.0 nm	98.6 nm
2	---	--- nm	--- nm	--- nm
3	---	--- nm	--- nm	--- nm
Total	1.00	103.3 nm	26.0 nm	98.6 nm

Cumulant Operations

Z-Average : 96.8 nm
 PI : 0.072



DLS size of dSiO₂@MSN

2022.07.19 15:58:18



HORIBA SZ-100 for Windows [Z Type] Ver2.20

SZ-100

MSN@dSiO₂_001.nsz

Measurement Results

Date : Tuesday, July 19, 2022 15:54:21 PM
 Measurement Type : Particle Size
 Sample Name : MSN@dSiO₂
 Scattering Angle : 90
 Temperature of the Holder : 24.9 °C
 Dispersion Medium Viscosity : 0.897 mPa·s
 Transmission Intensity before Meas. : 25009
 Distribution Form : Standard
 Distribution Form(Dispersity) : Monodisperse
 Representation of Result : Scattering Light Intensity
 Count Rate : 1436 kCPS

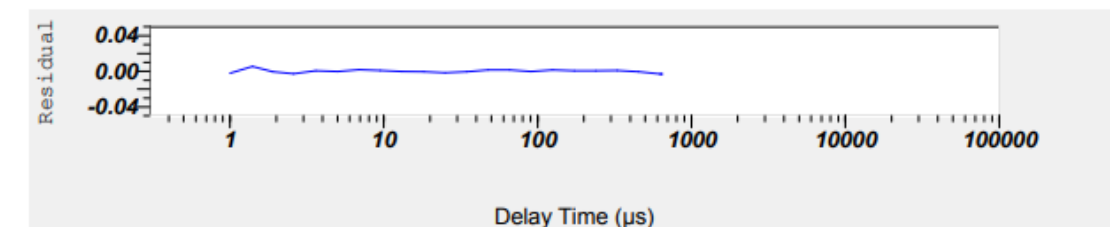
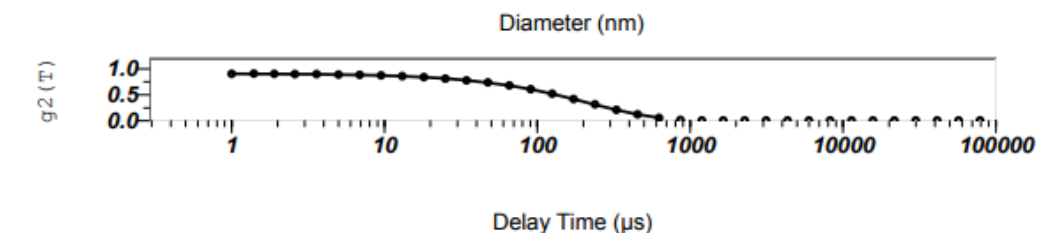
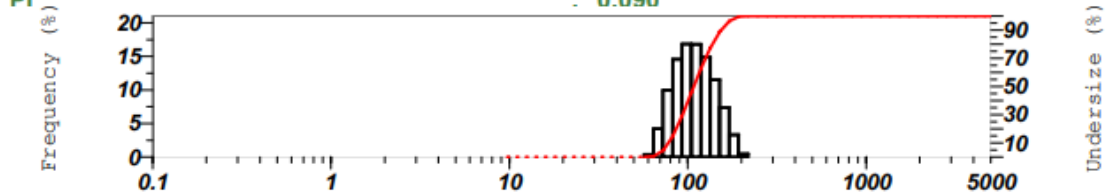
Calculation Results

Peak No.	S.P.Area Ratio	Mean	S. D.	Mode
1	1.00	112.7 nm	28.9 nm	99.7 nm
2	---	--- nm	--- nm	--- nm
3	---	--- nm	--- nm	--- nm
Total	1.00	112.7 nm	28.9 nm	99.7 nm

Cumulant Operations

Z-Average : 106.1 nm

PI : 0.090



DLS size of dSiO₂@MSN-PIk

2022.07.19 15:54:42



HORIBA SZ-100 for Windows [Z Type] Ver2.20

SZ-100

MSN@dSiO₂.PEG.1000.3%_001.nsz

Measurement Results

Date : Tuesday, July 19, 2022 15:49:11 PM
 Measurement Type : Particle Size
 Sample Name : MSN@dSiO₂.PEG.1000.3%
 Scattering Angle : 90
 Temperature of the Holder : 25.0 °C
 Dispersion Medium Viscosity : 0.895 mPa·s
 Transmission Intensity before Meas. : 26546
 Distribution Form : Standard
 Distribution Form(Dispersity) : Monodisperse
 Representation of Result : Scattering Light Intensity
 Count Rate : 1344 kCPS

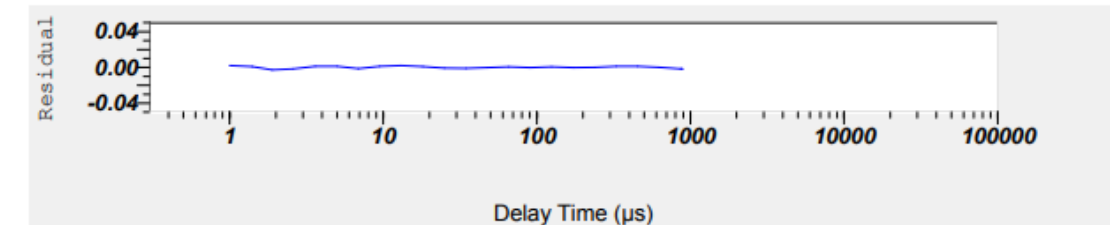
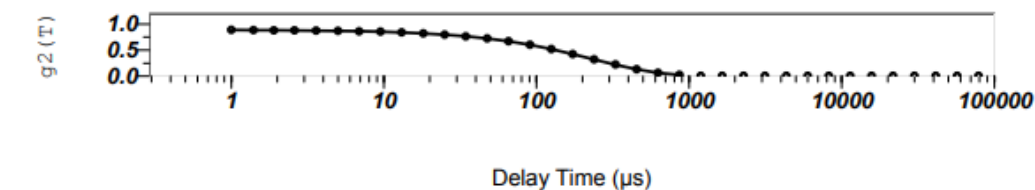
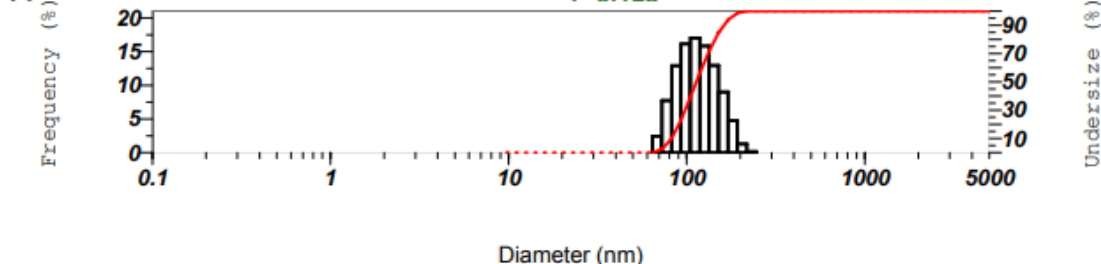
Calculation Results

Peak No.	S.P.Area Ratio	Mean	S. D.	Mode
1	1.00	118.2 nm	30.6 nm	111.6 nm
2	---	--- nm	--- nm	--- nm
3	---	--- nm	--- nm	--- nm
Total	1.00	118.2 nm	30.6 nm	111.6 nm

Cumulant Operations

Z-Average : 110.3 nm

PI : 0.123





SZ-100

MSN@dSiO₂.PEG.2000.3%_003.nsz

Measurement Results

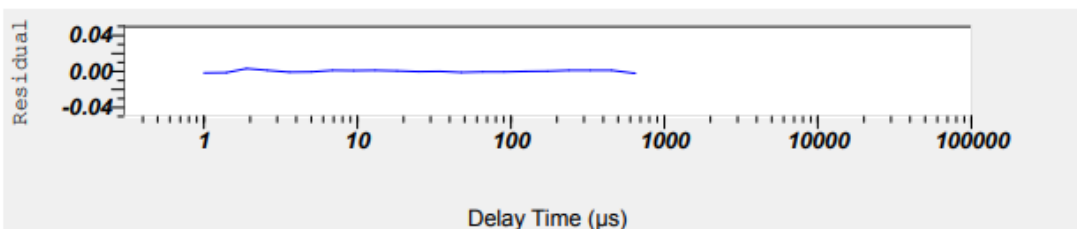
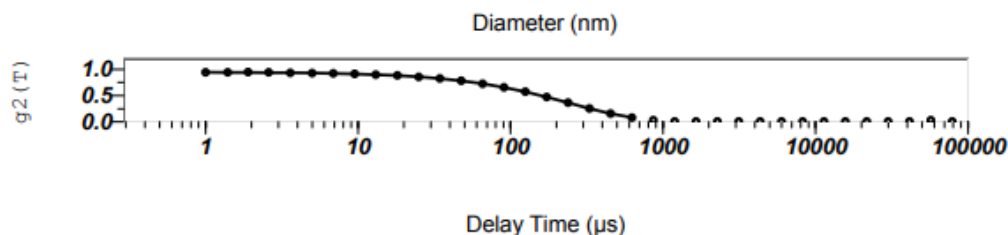
Date : Tuesday, July 19, 2022 15:46:09 PM
 Measurement Type : Particle Size
 Sample Name : MSN@dSiO₂.PEG.2000.3%
 Scattering Angle : 90
 Temperature of the Holder : 24.9 °C
 Dispersion Medium Viscosity : 0.897 mPa·s
 Transmission Intensity before Meas. : 28778
 Distribution Form : Standard
 Distribution Form(Dispersity) : Monodisperse
 Representation of Result : Scattering Light Intensity
 Count Rate : 2555 kCPS

Calculation Results

Peak No.	S.P.Area Ratio	Mean	S. D.	Mode
1	1.00	124.9 nm	31.4 nm	112.3 nm
2	---	--- nm	--- nm	--- nm
3	---	--- nm	--- nm	--- nm
Total	1.00	124.9 nm	31.4 nm	112.3 nm

Cumulant Operations

Z-Average : 116.3 nm
 PI : 0.133





SZ-100

MSN@dSiO₂.PEG.4000.3%_003.nsz

Measurement Results

Date : Tuesday, July 19, 2022 16:19:23 PM
 Measurement Type : Particle Size
 Sample Name : MSN@dSiO₂.PEG.4000.3%
 Scattering Angle : 90
 Temperature of the Holder : 24.9 °C
 Dispersion Medium Viscosity : 0.897 mPa·s
 Transmission Intensity before Meas. : 27171
 Distribution Form : Standard
 Distribution Form(Dispersity) : Monodisperse
 Representation of Result : Scattering Light Intensity
 Count Rate : 1784 kCPS

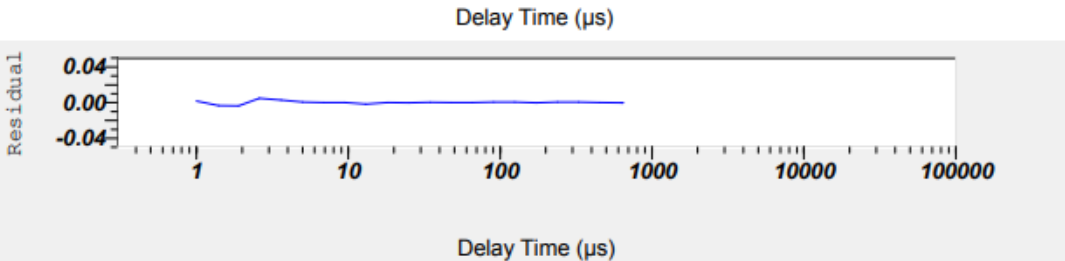
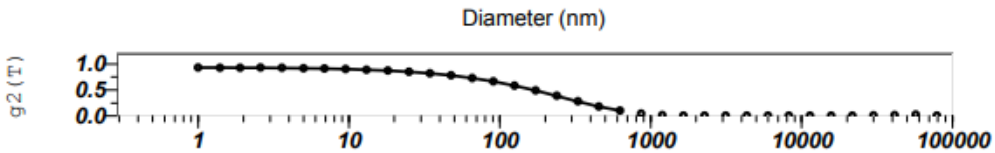
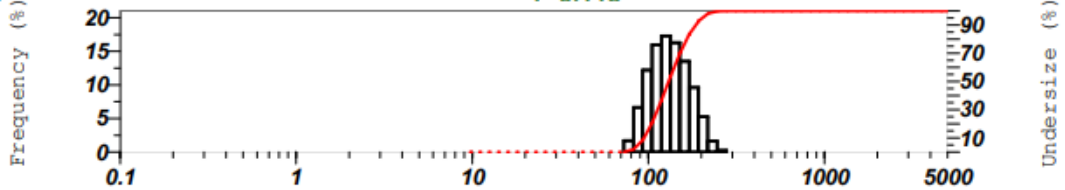
Calculation Results

Peak No.	S.P.Area Ratio	Mean	S. D.	Mode
1	1.00	136.0 nm	34.9 nm	126.4 nm
2	---	--- nm	--- nm	--- nm
3	---	--- nm	--- nm	--- nm
Total	1.00	136.0 nm	34.9 nm	126.4 nm

Cumulant Operations

Z-Average : 125.9 nm

PI : 0.116



DLS size of dSiO₂@MSN-P6k

2022.07.19 16:31:59



HORIBA SZ-100 for Windows [Z Type] Ver2.20

SZ-100

MSN@dSiO₂.PEG.6000.3%_003.nsz

Measurement Results

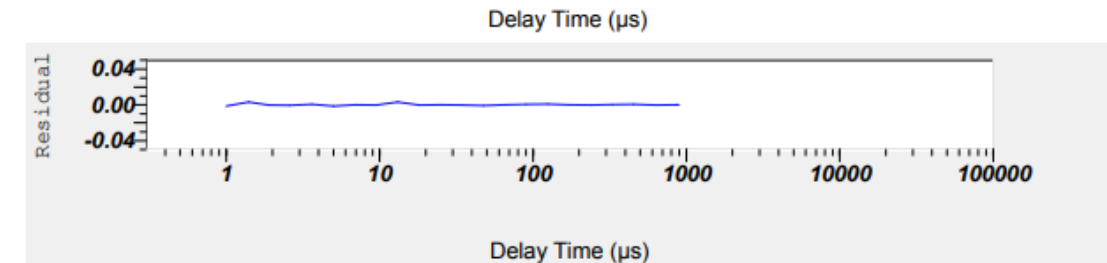
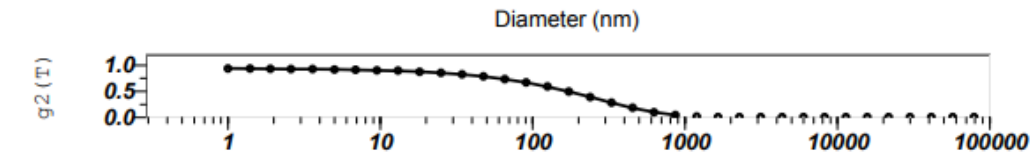
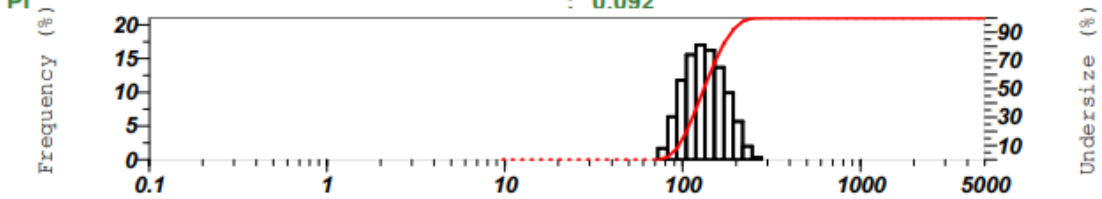
Date : Tuesday, July 19, 2022 16:29:39 PM
 Measurement Type : Particle Size
 Sample Name : MSN@dSiO₂.PEG.6000.3%
 Scattering Angle : 90
 Temperature of the Holder : 25.0 °C
 Dispersion Medium Viscosity : 0.895 mPa·s
 Transmission Intensity before Meas. : 27273
 Distribution Form : Standard
 Distribution Form(Dispersity) : Monodisperse
 Representation of Result : Scattering Light Intensity
 Count Rate : 1651 kCPS

Calculation Results

Peak No.	S.P.Area Ratio	Mean	S. D.	Mode
1	1.00	137.4 nm	35.7 nm	126.5 nm
2	---	--- nm	--- nm	--- nm
3	---	--- nm	--- nm	--- nm
Total	1.00	137.4 nm	35.7 nm	126.5 nm

Cumulant Operations

Z-Average : 128.7 nm
 PI : 0.092



DLS size of dSiO₂@MSN-P1%

2022.07.19 16:51:04



HORIBA SZ-100 for Windows [Z Type] Ver2.20

SZ-100

MSN@dSiO₂.PEG.6000.1%_003.nsz

Measurement Results

Date : Tuesday, July 19, 2022 16:34:47 PM
 Measurement Type : Particle Size
 Sample Name : MSN@dSiO₂.PEG.6000.1%
 Scattering Angle : 90
 Temperature of the Holder : 24.9 °C
 Dispersion Medium Viscosity : 0.897 mPa·s
 Transmission Intensity before Meas. : 28683
 Distribution Form : Standard
 Distribution Form(Dispersity) : Monodisperse
 Representation of Result : Scattering Light Intensity
 Count Rate : 2466 kCPS

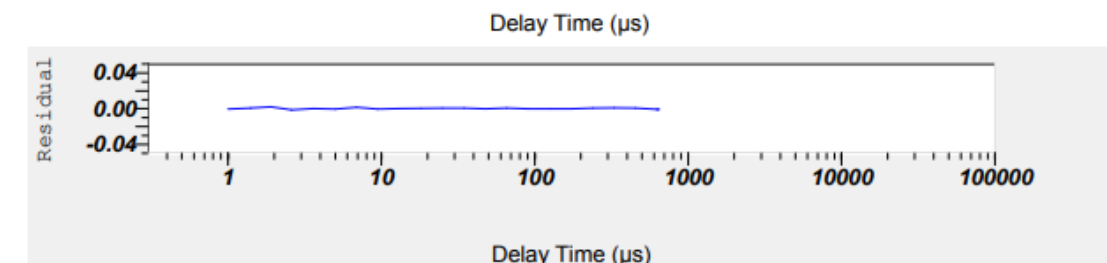
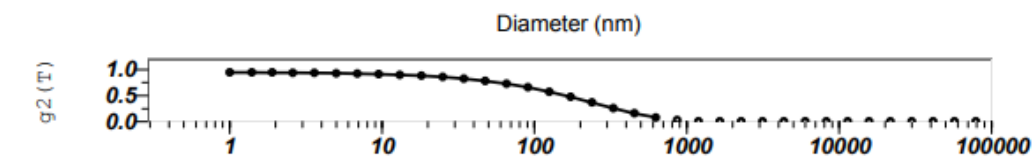
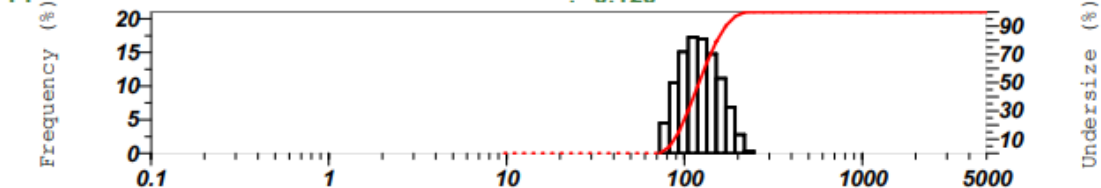
Calculation Results

Peak No.	S.P.Area Ratio	Mean	S. D.	Mode
1	1.00	126.0 nm	31.7 nm	112.5 nm
2	---	--- nm	--- nm	--- nm
3	---	--- nm	--- nm	--- nm
Total	1.00	126.0 nm	31.7 nm	112.5 nm

Cumulant Operations

Z-Average : 117.7 nm

PI : 0.120



DLS size of dSiO₂@MSN-P2%

2022.07.19 16:21:44



HORIBA SZ-100 for Windows [Z Type] Ver2. 20

SZ-100

MSN@dSiO₂.PEG.6000.2%_002.nsz

Measurement Results

Date : Tuesday, July 19, 2022 16:18:14 PM
 Measurement Type : Particle Size
 Sample Name : MSN@dSiO₂.PEG.6000.2%
 Scattering Angle : 90
 Temperature of the Holder : 25.0 °C
 Dispersion Medium Viscosity : 0.895 mPa·s
 Transmission Intensity before Meas. : 27171
 Distribution Form : Standard
 Distribution Form(Dispersity) : Monodisperse
 Representation of Result : Scattering Light Intensity
 Count Rate : 1836 kCPS

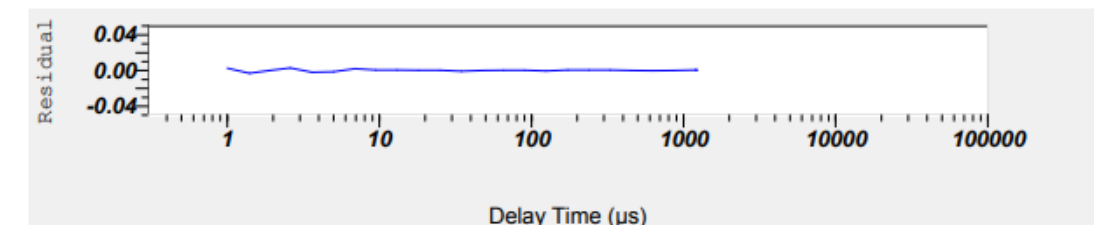
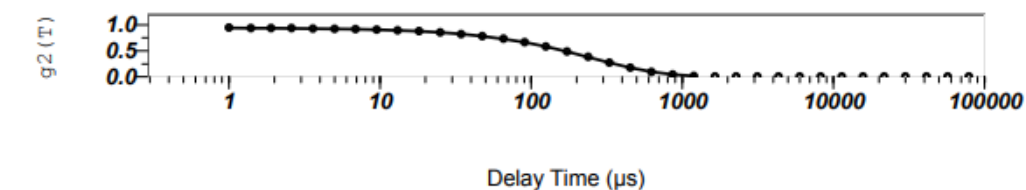
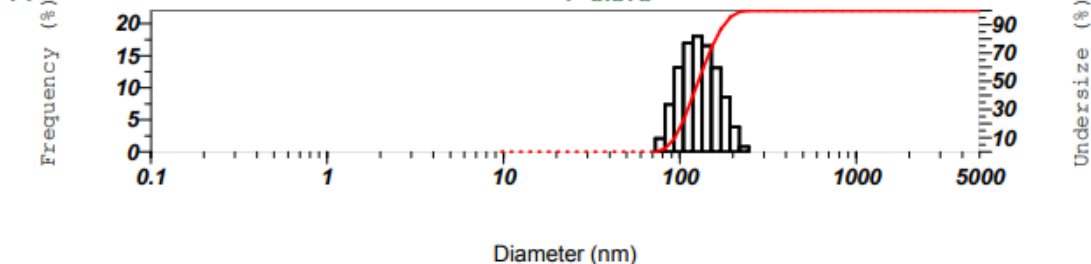
Calculation Results

Peak No.	S.P.Area Ratio	Mean	S. D.	Mode
1	1.00	132.2 nm	32.5 nm	126.0 nm
2	---	--- nm	--- nm	--- nm
3	---	--- nm	--- nm	--- nm
Total	1.00	132.2 nm	32.5 nm	126.0 nm

Cumulant Operations

Z-Average : 124.7 nm

PI : 0.079



DLS size of dSiO₂@MSN-P3%

2022.07.19 15:39:33



HORIBA SZ-100 for Windows [Z Type] Ver2. 20

SZ-100

MSN@dSiO₂.PEG.6000.3%_003.nsz

Measurement Results

Date : Tuesday, July 19, 2022 15:33:45 PM
 Measurement Type : Particle Size
 Sample Name : MSN@dSiO₂.PEG.6000.3%
 Scattering Angle : 90
 Temperature of the Holder : 25.0 °C
 Dispersion Medium Viscosity : 0.895 mPa·s
 Transmission Intensity before Meas. : 29061
 Distribution Form : Standard
 Distribution Form(Dispersity) : Monodisperse
 Representation of Result : Scattering Light Intensity
 Count Rate : 679 kCPS

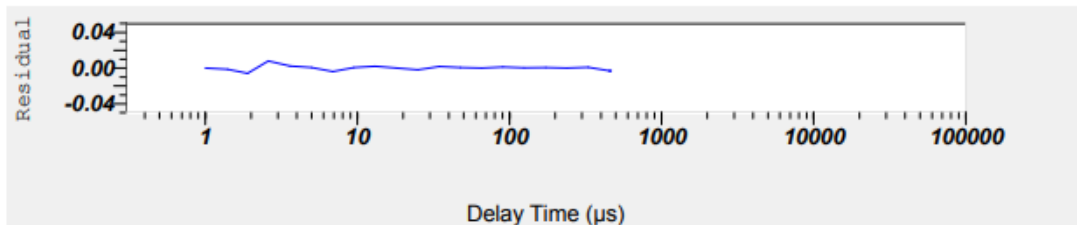
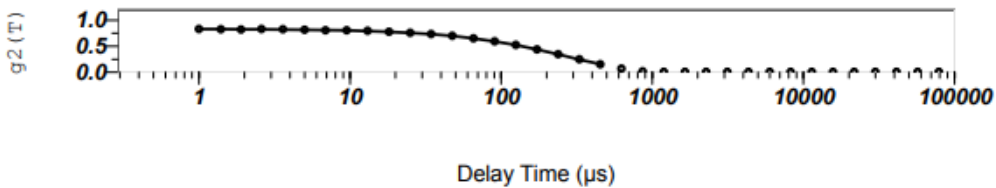
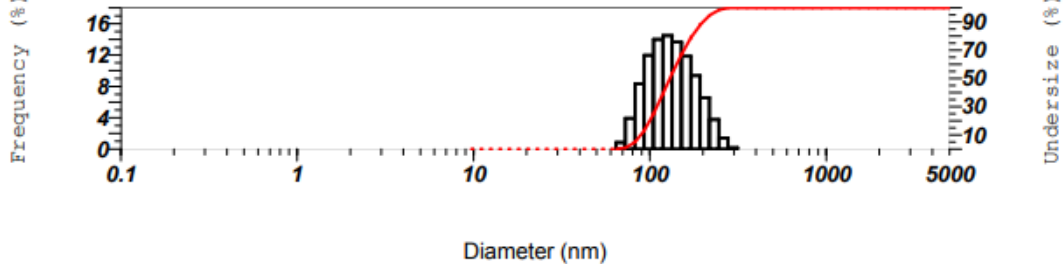
Calculation Results

Peak No.	S.P.Area Ratio	Mean	S. D.	Mode
1	1.00	138.2 nm	42.7 nm	126.0 nm
2	---	--- nm	--- nm	--- nm
3	---	--- nm	--- nm	--- nm
Total	1.00	138.2 nm	42.7 nm	126.0 nm

Cumulant Operations

Z-Average : 127.9 nm

PI : 0.129



DLS size of dSiO₂@MSN-P4%

2022.07.19 16:31:58



HORIBA SZ-100 for Windows [Z Type] Ver2. 20

SZ-100

MSN@dSiO₂.PEG.6000.4%_002.nsz

Measurement Results

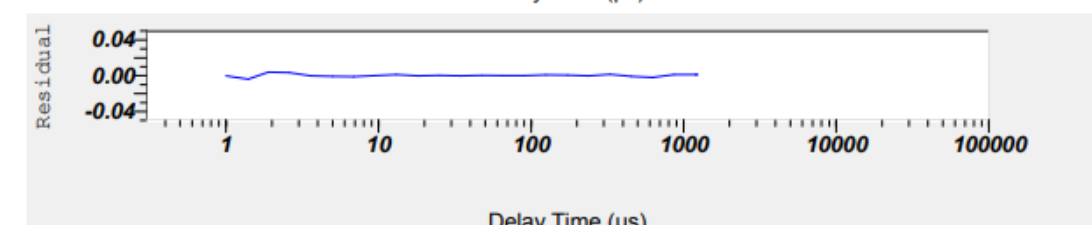
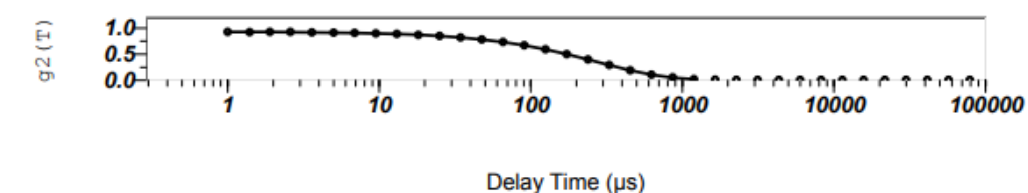
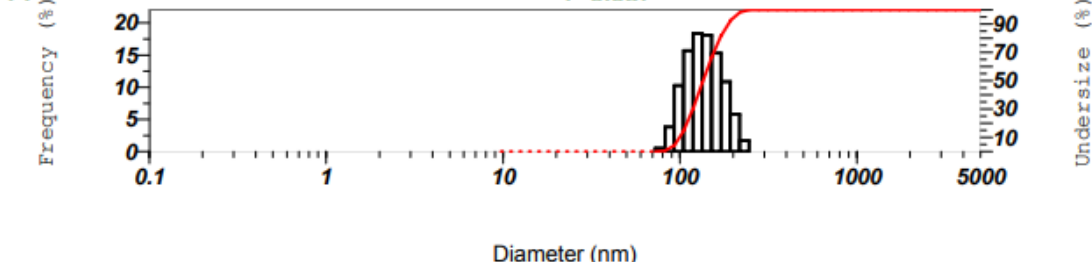
Date : Tuesday, July 19, 2022 16:28:29 PM
 Measurement Type : Particle Size
 Sample Name : MSN@dSiO₂.PEG.6000.4%
 Scattering Angle : 90
 Temperature of the Holder : 25.0 °C
 Dispersion Medium Viscosity : 0.895 mPa·s
 Transmission Intensity before Meas. : 27273
 Distribution Form : Standard
 Distribution Form(Dispersity) : Monodisperse
 Representation of Result : Scattering Light Intensity
 Count Rate : 1656 kCPS

Calculation Results

Peak No.	S.P.Area Ratio	Mean	S. D.	Mode
1	1.00	140.1 nm	33.3 nm	127.2 nm
2	---	--- nm	--- nm	--- nm
3	---	--- nm	--- nm	--- nm
Total	1.00	140.1 nm	33.3 nm	127.2 nm

Cumulant Operations

Z-Average : 131.7 nm
 PI : 0.087



DLS size of dSiO₂@MSN-P5%

2022.07.19 16:28:56



HORIBA SZ-100 for Windows [Z Type] Ver2.20

SZ-100

MSN@dSiO₂.PEG.6000.5%_002.nsz

Measurement Results

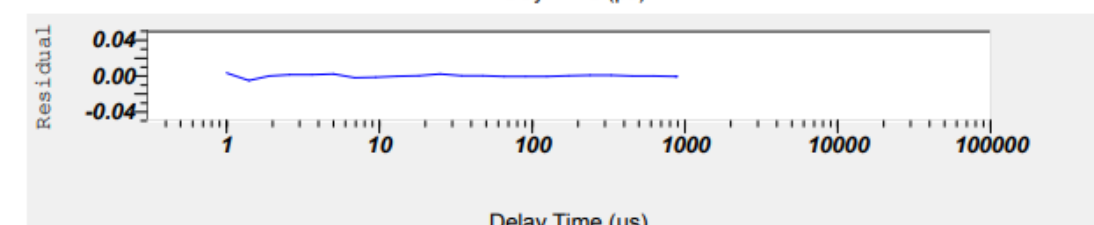
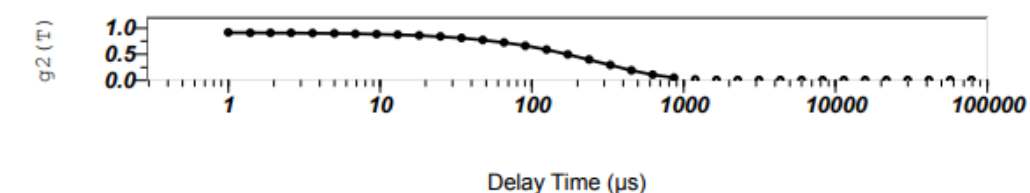
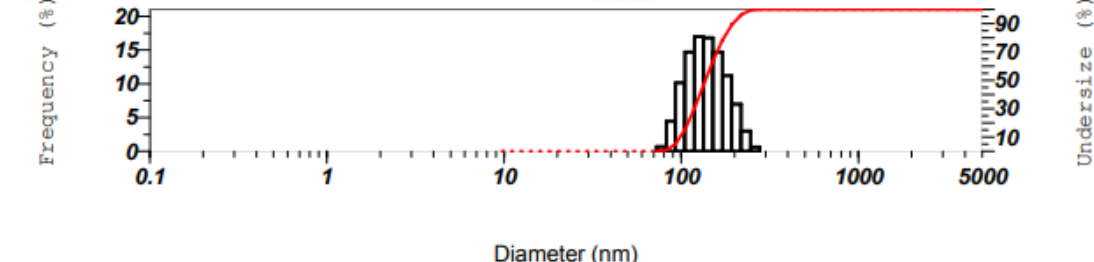
Date : Tuesday, July 19, 2022 16:23:22 PM
 Measurement Type : Particle Size
 Sample Name : MSN@dSiO₂.PEG.6000.5%
 Scattering Angle : 90
 Temperature of the Holder : 24.8 °C
 Dispersion Medium Viscosity : 0.899 mPa·s
 Transmission Intensity before Meas. : 29217
 Distribution Form : Standard
 Distribution Form(Dispersity) : Monodisperse
 Representation of Result : Scattering Light Intensity
 Count Rate : 1621 KCPS

Calculation Results

Peak No.	S.P.Area Ratio	Mean	S. D.	Mode
1	1.00	142.9 nm	37.0 nm	127.2 nm
2	---	--- nm	--- nm	--- nm
3	---	--- nm	--- nm	--- nm
Total	1.00	142.9 nm	37.0 nm	127.2 nm

Cumulant Operations

Z-Average : 134.2 nm
 PI : 0.086



DLS size of HMSN

2022.07.19 15:58:21



HORIBA SZ-100 for Windows [Z Type] Ver2.20

SZ-100

HMSN_002.nsz

Measurement Results

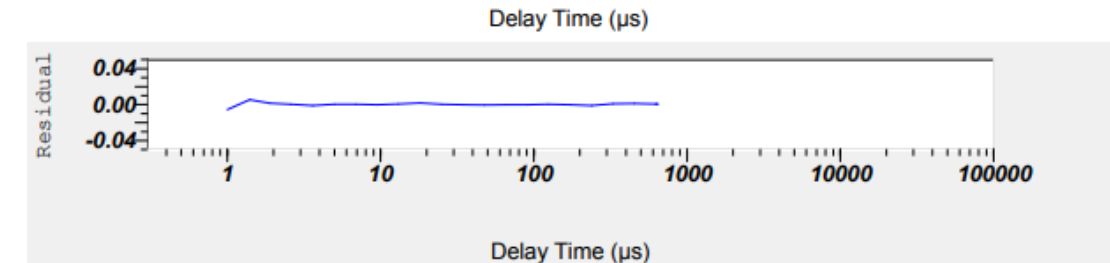
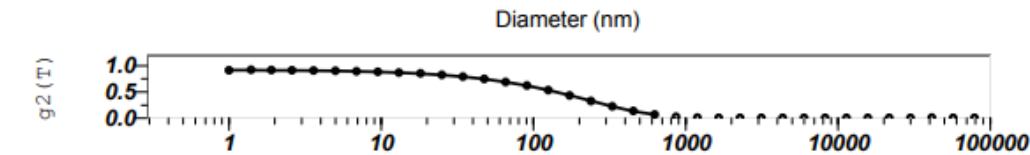
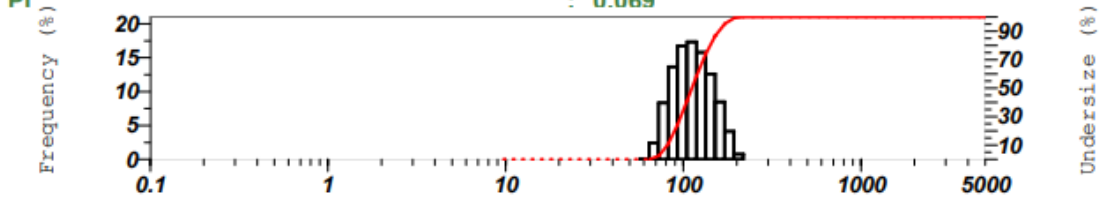
Date : Tuesday, July 19, 2022 15:55:21 PM
Measurement Type : Particle Size
Sample Name : HMSN
Scattering Angle : 90
Temperature of the Holder : 24.9 °C
Dispersion Medium Viscosity : 0.897 mPa·s
Transmission Intensity before Meas. : 25009
Distribution Form : Standard
Distribution Form(Dispersity) : Monodisperse
Representation of Result : Scattering Light Intensity
Count Rate : 1475 kCPS

Calculation Results

Peak No.	S.P.Area Ratio	Mean	S. D.	Mode
1	1.00	116.3 nm	29.3 nm	111.3 nm
2	---	--- nm	--- nm	--- nm
3	---	--- nm	--- nm	--- nm
Total	1.00	116.3 nm	29.3 nm	111.3 nm

Cumulant Operations

Z-Average : 108.8 nm
PI : 0.069



DLS size of HMSN-NH₂

2022.09.12 09:56:02



HORIBA SZ-100 for Windows [Z Type] Ver2.20

SZ-100

HMSN-NH2_1.nsz

Measurement Results

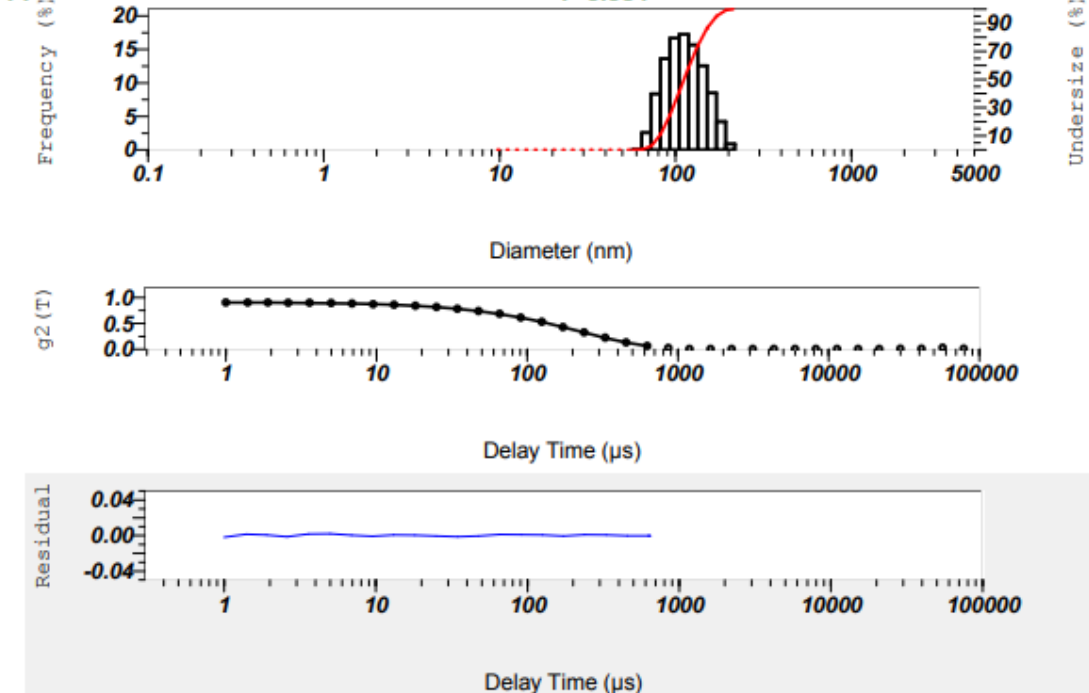
Date : Monday, September 12, 2022 9:39:54 AM
Measurement Type : Particle Size
Sample Name : HMSN-NH2
Scattering Angle : 90
Temperature of the Holder : 24.8 °C
Dispersion Medium Viscosity : 1.087 mPa·s
Transmission Intensity before Meas. : 25101
Distribution Form : Standard
Distribution Form(Dispersity) : Monodisperse
Representation of Result : Scattering Light Intensity
Count Rate : 1301 KCPS

Calculation Results

Peak No.	S.P.Area Ratio	Mean	S. D.	Mode
1	1.00	116.4 nm	29.5 nm	111.3 nm
2	--	-- nm	-- nm	-- nm
3	--	-- nm	-- nm	-- nm
Total	1.00	116.4 nm	29.5 nm	111.3 nm

Cumulant Operations

Z-Average : 109.6 nm
PI : 0.064



DLS size of HMSN-L64

2022.09.27 15:39:58



HORIBA SZ-100 for Windows [Z Type] Ver2.20

SZ-100

HMSN-L64_5.nsz

Measurement Results

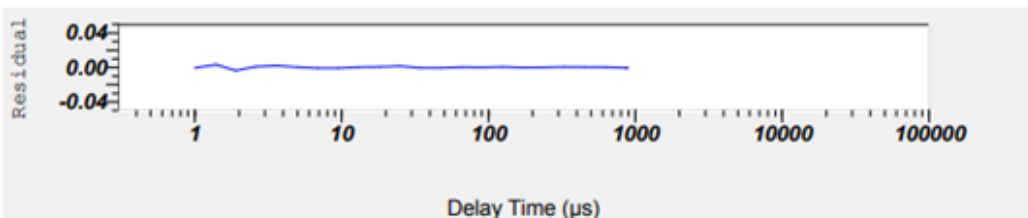
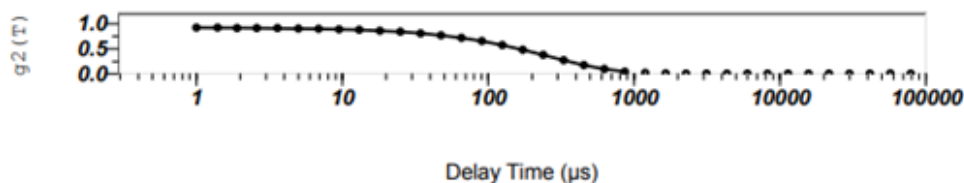
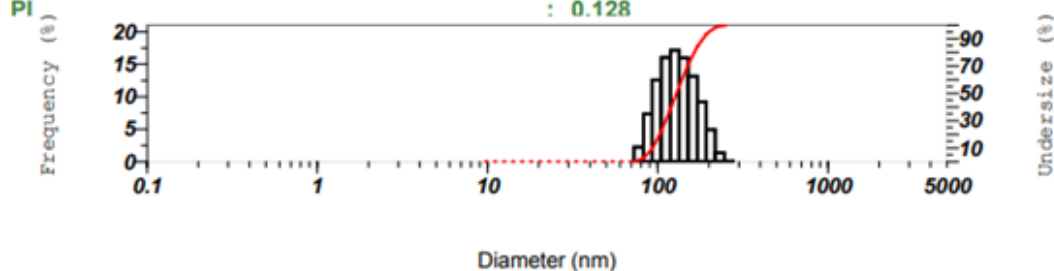
Date : Tuesday, September 27, 2022 14:56:24 PM
 Measurement Type : Particle Size
 Sample Name : HMSN-L64
 Scattering Angle : 90
 Temperature of the Holder : 25.0 °C
 Dispersion Medium Viscosity : 0.694 mPa·s
 Transmission Intensity before Meas. : 29475
 Distribution Form : Standard
 Distribution Form(Dispersity) : Monodisperse
 Representation of Result : Scattering Light Intensity
 Count Rate : 988 kCPS

Calculation Results

Peak No.	S.P.Area Ratio	Mean	S. D.	Mode
1	1.00	134.3 nm	34.5 nm	126.2 nm
2	---	--- nm	--- nm	--- nm
3	---	--- nm	--- nm	--- nm
Total	1.00	134.3 nm	34.5 nm	126.2 nm

Cumulant Operations

Z-Average : 124.5 nm
 PI : 0.128



DLS size of HMSN-F68

2022.09.27 15:40:14



HORIBA SZ-100 for Windows [Z Type] Ver2.20

SZ-100

HMSN-F68_14.nsz Measurement Results

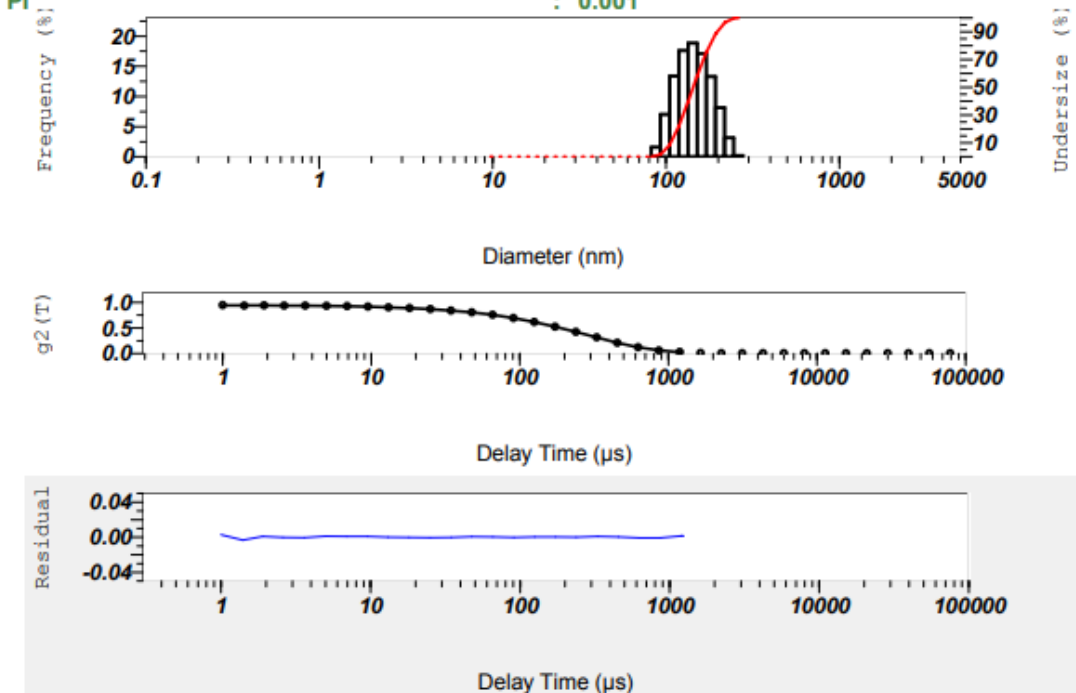
Date : Tuesday, September 27, 2022 15:33:57 PM
 Measurement Type : Particle Size
 Sample Name : HMSN-F68
 Scattering Angle : 90
 Temperature of the Holder : 25.0 °C
 Dispersion Medium Viscosity : 0.692 mPa·s
 Transmission Intensity before Meas. : 25654
 Distribution Form : Standard
 Distribution Form(Dispersity) : Monodisperse
 Representation of Result : Scattering Light Intensity
 Count Rate : 1458 KCPS

Calculation Results

Peak No.	S.P.Area Ratio	Mean	S. D.	Mode
1	1.00	148.2 nm	34.5 nm	142.4 nm
2	--	-- nm	-- nm	-- nm
3	--	-- nm	-- nm	-- nm
Total	1.00	148.2 nm	34.5 nm	142.4 nm

Cumulant Operations

Z-Average : 142.1 nm
 PI : 0.001



DLS size of HMSN-F127

2022.09.27 15:40:00



HORIBA SZ-100 for Windows [Z Type] Ver2.20

SZ-100

HMSN-F127_3.nsz

Measurement Results

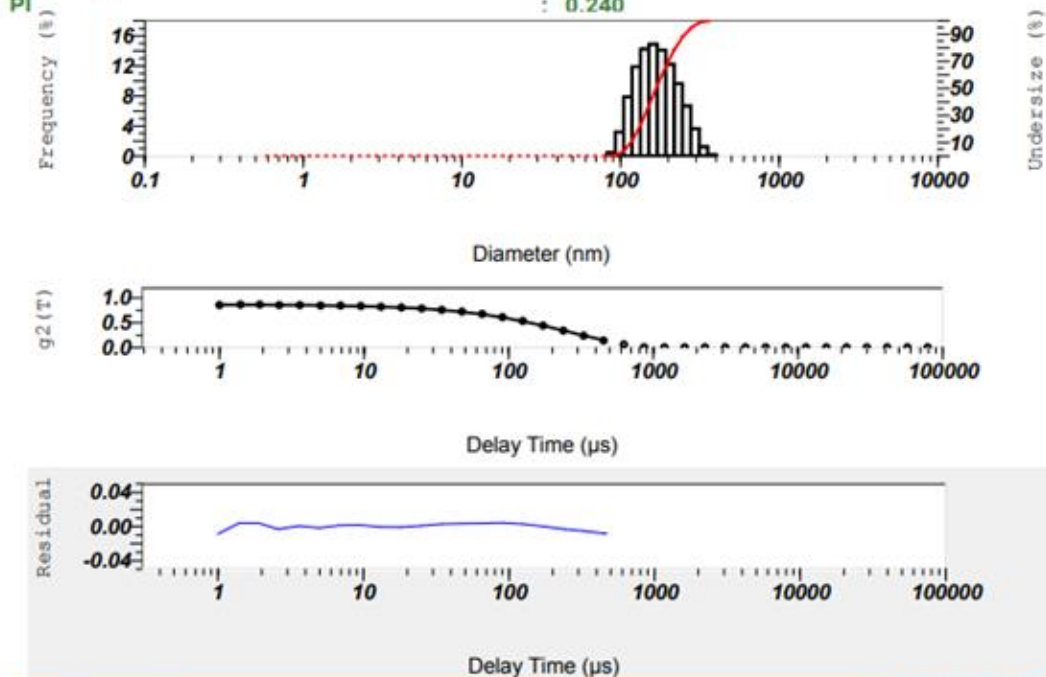
Date : Tuesday, September 27, 2022 15:08:52 PM
 Measurement Type : Particle Size
 Sample Name : HMSN-F127
 Scattering Angle : 90
 Temperature of the Holder : 25.0 °C
 Dispersion Medium Viscosity : 0.894 mPa·s
 Transmission Intensity before Meas. : 21051
 Distribution Form : Standard
 Distribution Form(Dispersity) : Monodisperse
 Representation of Result : Scattering Light Intensity
 Count Rate : 1284 kCPS

Calculation Results

Peak No.	S.P.Area Ratio	Mean	S. D.	Mode
1	1.00	177.5 nm	53.4 nm	161.0 nm
2	---	--- nm	--- nm	--- nm
3	---	--- nm	--- nm	--- nm
Total	1.00	177.5 nm	53.4 nm	161.0 nm

Cumulant Operations

Z-Average : 172.7 nm
 PI : 0.240



Zeta potential of dSiO₂

2021.11.02 13:04:01



HORIBA SZ-100 for Windows [Z Type] Ver2.20

SZ-100

Measurement Results

dSiO₂_003.nzt

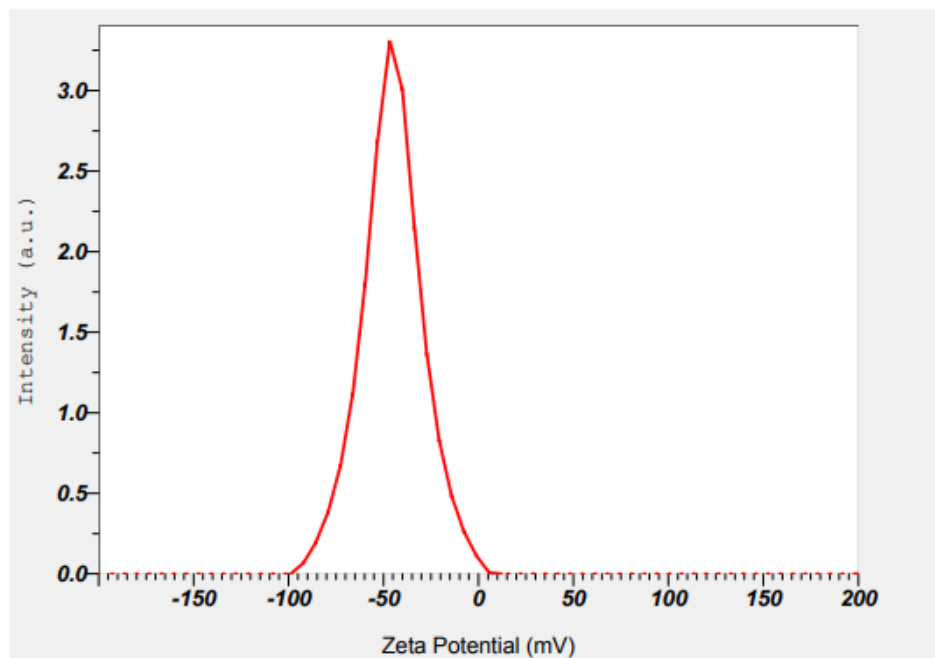
Measurement Results

Date : Tuesday, November 2, 2021 12:59:07 PM
Measurement Type : Zeta Potential
Sample Name : dSiO₂
Temperature of the Holder : 25.0 °C
Dispersion Medium Viscosity : 0.895 mPa·s
Conductivity : 0.068 mS/cm
Electrode Voltage : 3.8 V

Calculation Results

Peak No.	Zeta Potential	Electrophoretic Mobility
1	-45.3 mV	-0.000351 cm ² /Vs
2	--- mV	--- cm ² /Vs
3	--- mV	--- cm ² /Vs

Zeta Potential (Mean) : -45.3 mV
Electrophoretic Mobility Mean : -0.000351 cm²/Vs



Zeta potential of HMSN

2022.03.02 16:45:37

HORIBA
Scientific

HORIBA SZ-100 for Windows [Z Type] Ver2.20

SZ-100

Measurement Results

HMSN_0003.nzt

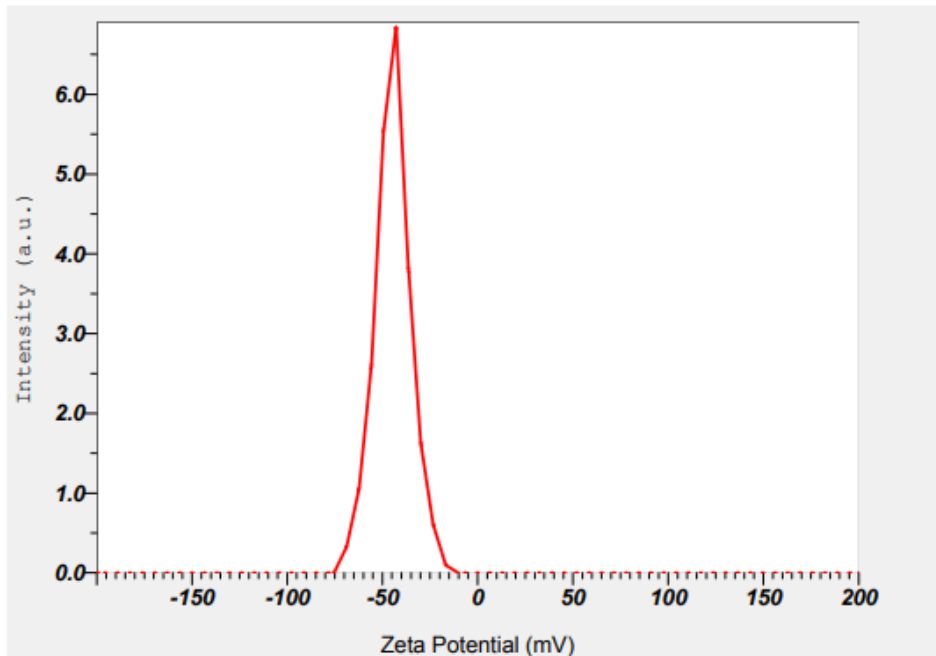
Measurement Results

Date : Tuesday, February 15, 2022 17:10:57 PM
Measurement Type : Zeta Potential
Sample Name : HMSN
Temperature of the Holder : 25.0 °C
Dispersion Medium Viscosity : 0.895 mPa·s
Conductivity : 0.065 mS/cm
Electrode Voltage : 3.8 V

Calculation Results

Peak No.	Zeta Potential	Electrophoretic Mobility
1	-44.5 mV	-0.000345 cm ² /Vs
2	-- mV	-- cm ² /Vs
3	-- mV	-- cm ² /Vs

Zeta Potential (Mean) : -44.5 mV
Electrophoretic Mobility Mean : -0.000345 cm²/Vs



Zeta potential of HMSN-NH₂

2022.09.15 16:20:32



HORIBA SZ-100 for Windows [Z Type] Ver2. 20

SZ-100

Measurement Results

HMSN-NH₂_1.nzt

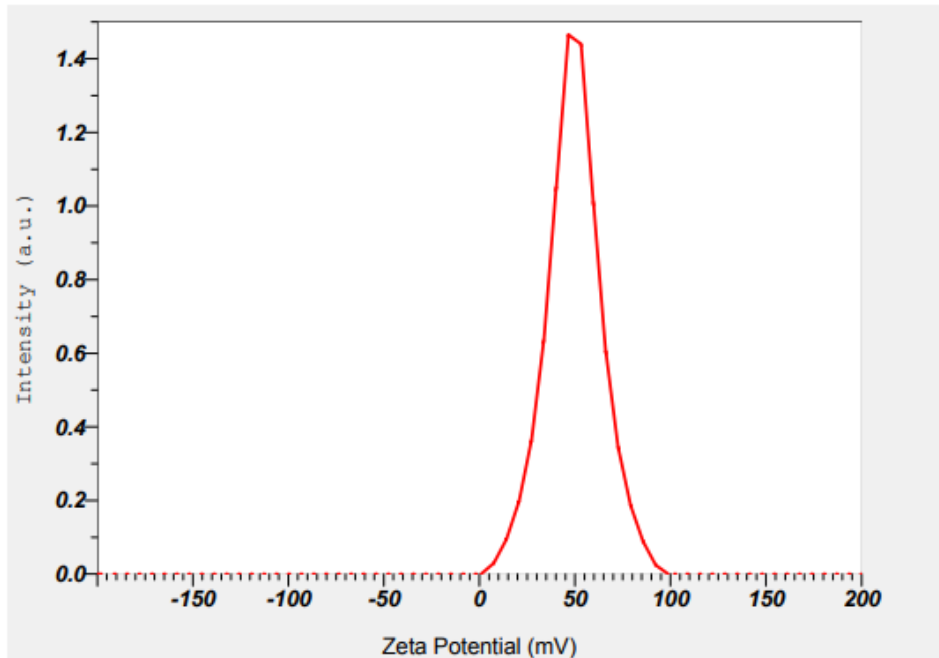
Measurement Results

Date : Thursday, September 15, 2022 16:03:11 PM
Measurement Type : Zeta Potential
Sample Name : HMSN-NH₂
Temperature of the Holder : 25.0 °C
Dispersion Medium Viscosity : 0.896 mPa·s
Conductivity : 0.058 mS/cm
Electrode Voltage : 3.8 V

Calculation Results

Peak No.	Zeta Potential	Electrophoretic Mobility
1	49.6 mV	0.000384 cm ² /Vs
2	--- mV	--- cm ² /Vs
3	--- mV	--- cm ² /Vs

Zeta Potential (Mean) : 49.6 mV
Electrophoretic Mobility Mean : 0.000384 cm²/Vs



Zeta potential of HMSN-L64

2022.09.15 16:20:30



HORIBA SZ-100 for Windows [Z Type] Ver2.20

SZ-100

Measurement Results

HMSN-L64_2.nzt

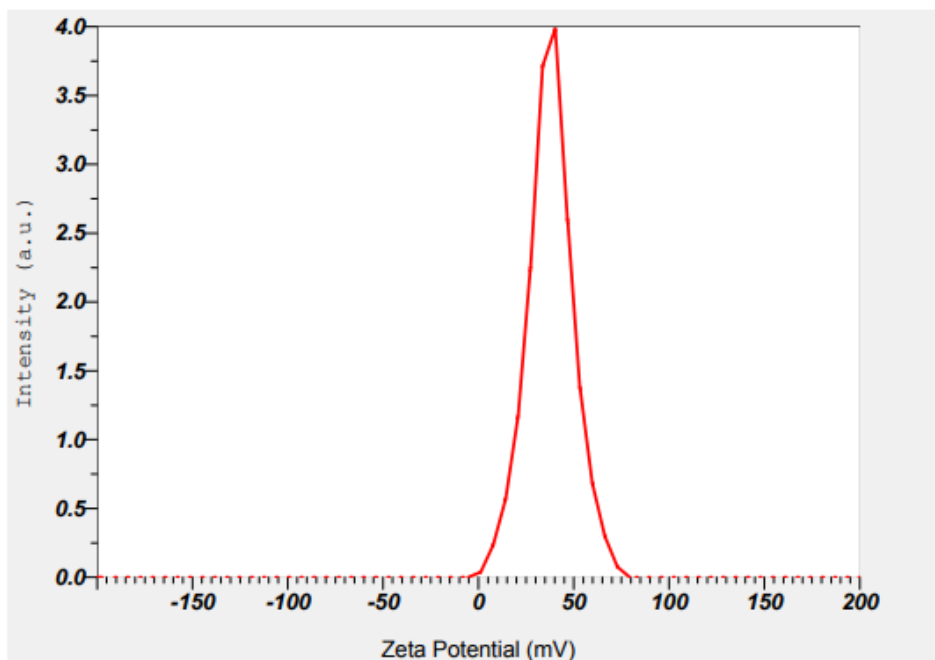
Measurement Results

Date : Thursday, September 15, 2022 15:58:46 PM
Measurement Type : Zeta Potential
Sample Name : HMSN-L64
Temperature of the Holder : 25.0 °C
Dispersion Medium Viscosity : 0.894 mPa·s
Conductivity : 0.059 mS/cm
Electrode Voltage : 3.8 V

Calculation Results

Peak No.	Zeta Potential	Electrophoretic Mobility
1	37.8 mV	0.000293 cm ² /Vs
2	-- mV	-- cm ² /Vs
3	-- mV	-- cm ² /Vs

Zeta Potential (Mean) : 37.8 mV
Electrophoretic Mobility Mean : 0.000293 cm²/Vs



Zeta potential of HMSN-F68

2022.09.12 09:57:01



HORIBA SZ-100 for Windows [Z Type] Ver2.20

SZ-100

Measurement Results

HMSN-F68_3.nzt

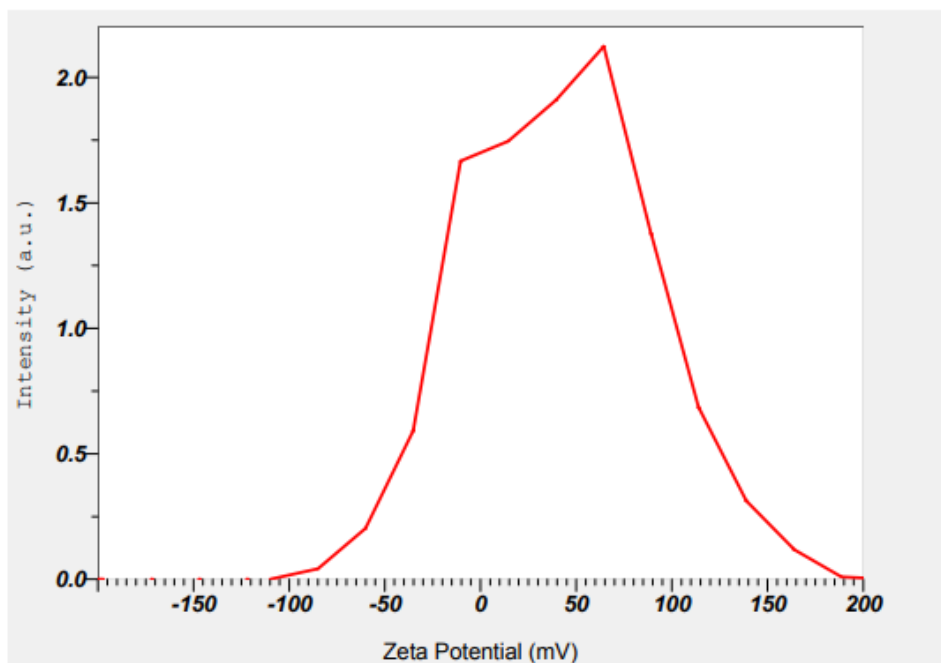
Measurement Results

Date : Monday, September 12, 2022 9:46:06 AM
Measurement Type : Zeta Potential
Sample Name : HMSN-F68
Temperature of the Holder : 25.0 °C
Dispersion Medium Viscosity : 1.084 mPa·s
Conductivity : 0.081 mS/cm
Electrode Voltage : 3.8 V

Calculation Results

Peak No.	Zeta Potential	Electrophoretic Mobility
1	-2.3 mV	-0.000005 cm ² /Vs
2	59.8 mV	0.000121 cm ² /Vs
3	-- mV	-- cm ² /Vs

Zeta Potential (Mean) : 30.2 mV
Electrophoretic Mobility Mean : 0.000061 cm²/Vs



Zeta potential of HMSN-F127

2022.09.15 16:20:29



HORIBA SZ-100 for Windows [Z Type] Ver2.20

SZ-100

Measurement Results

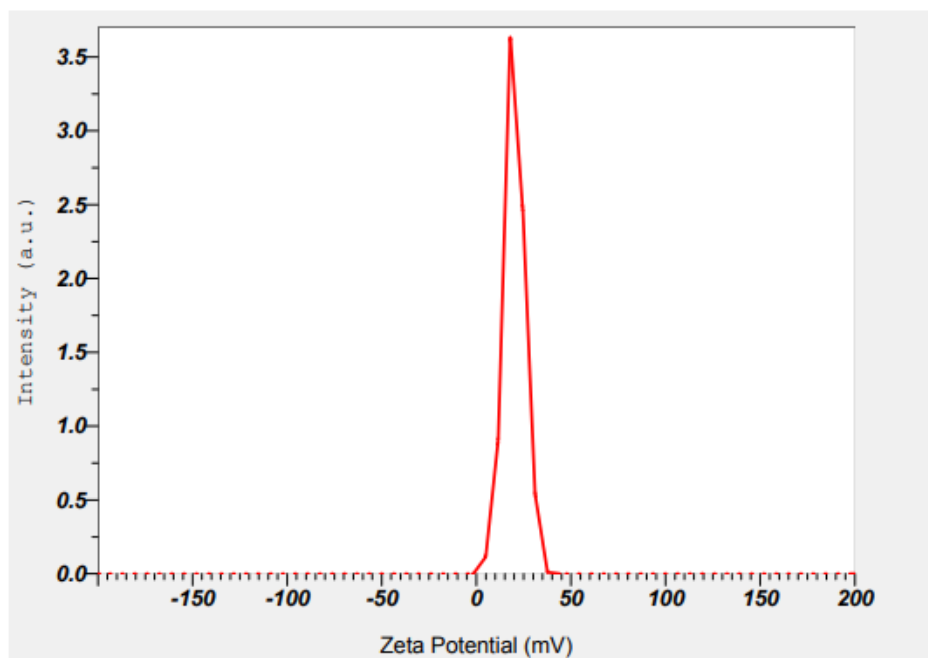
HMSN-F127_1.nzt Measurement Results

Date : Thursday, September 15, 2022 15:54:54 PM
Measurement Type : Zeta Potential
Sample Name : HMSN-F127
Temperature of the Holder : 25.0 °C
Dispersion Medium Viscosity : 0.896 mPa·s
Conductivity : 0.059 mS/cm
Electrode Voltage : 3.8 V

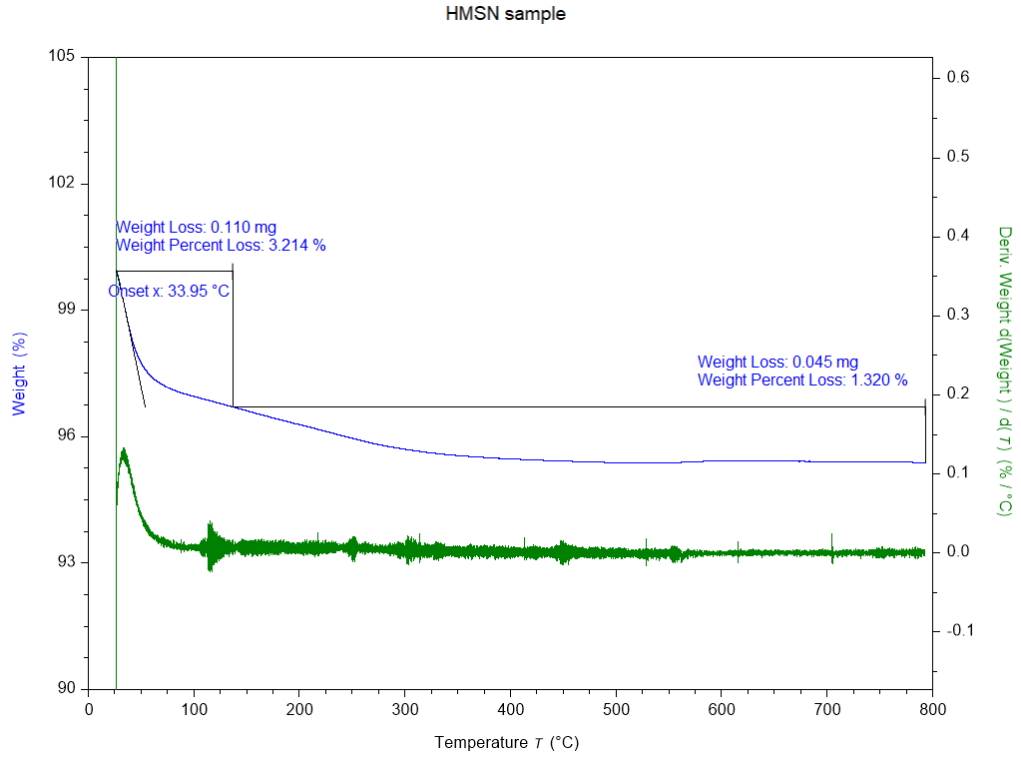
Calculation Results

Peak No.	Zeta Potential	Electrophoretic Mobility
1	20.2 mV	0.000157 cm ² /Vs
2	--- mV	--- cm ² /Vs
3	--- mV	--- cm ² /Vs

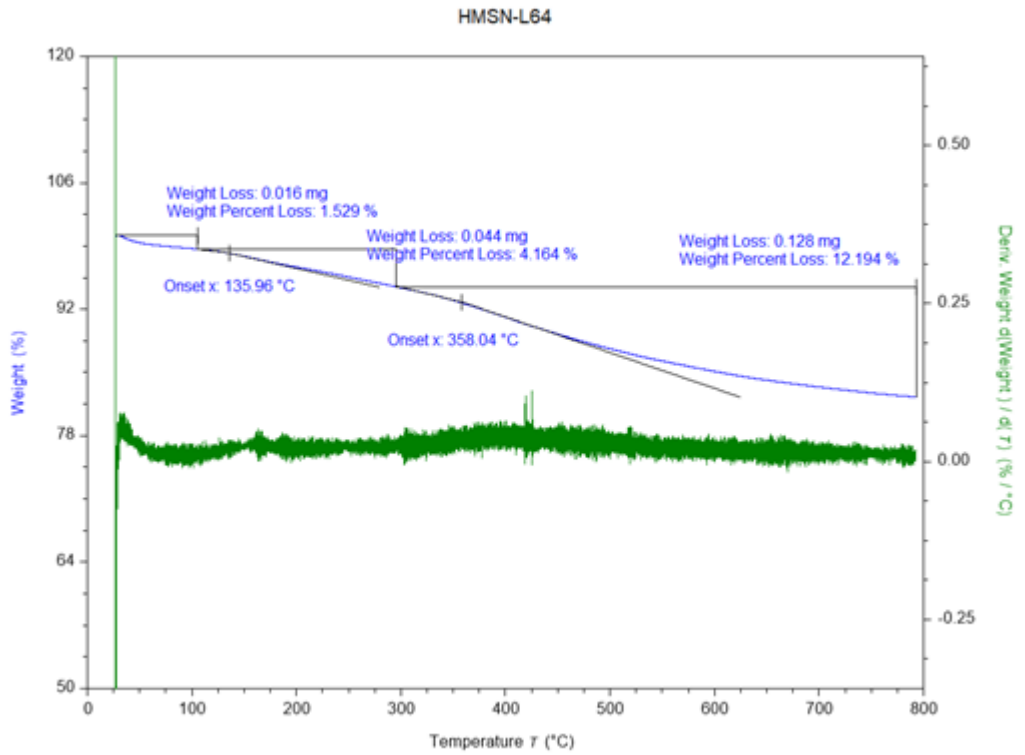
Zeta Potential (Mean) : 20.2 mV
Electrophoretic Mobility Mean : 0.000157 cm²/Vs



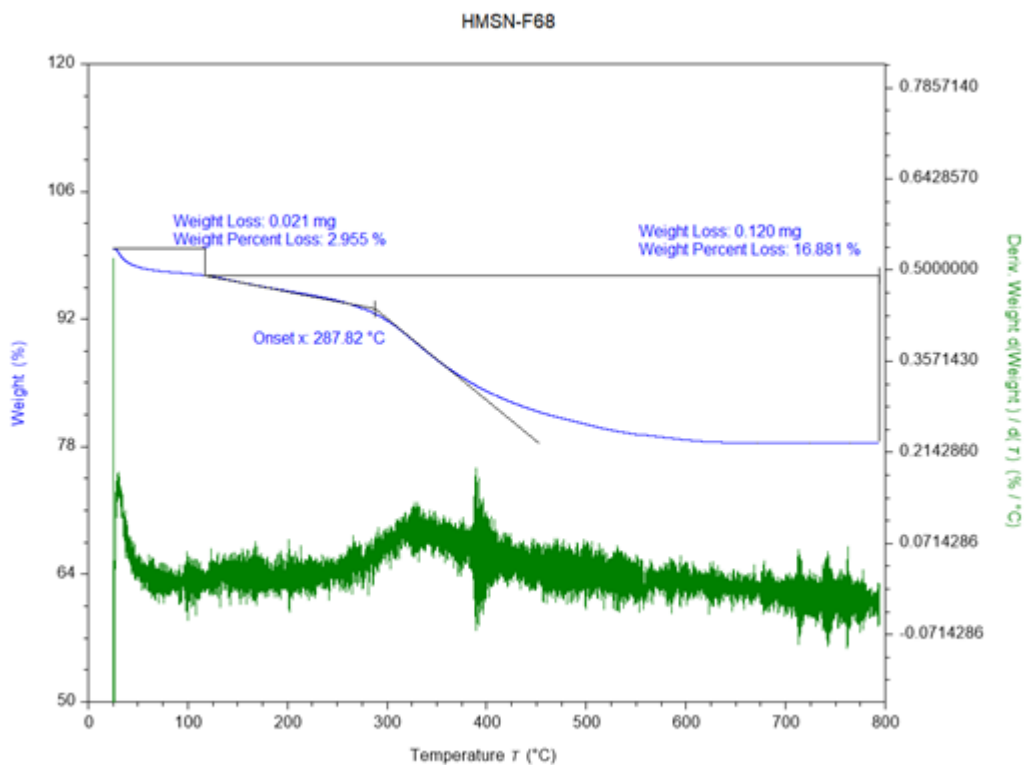
TGA graph of HMSN



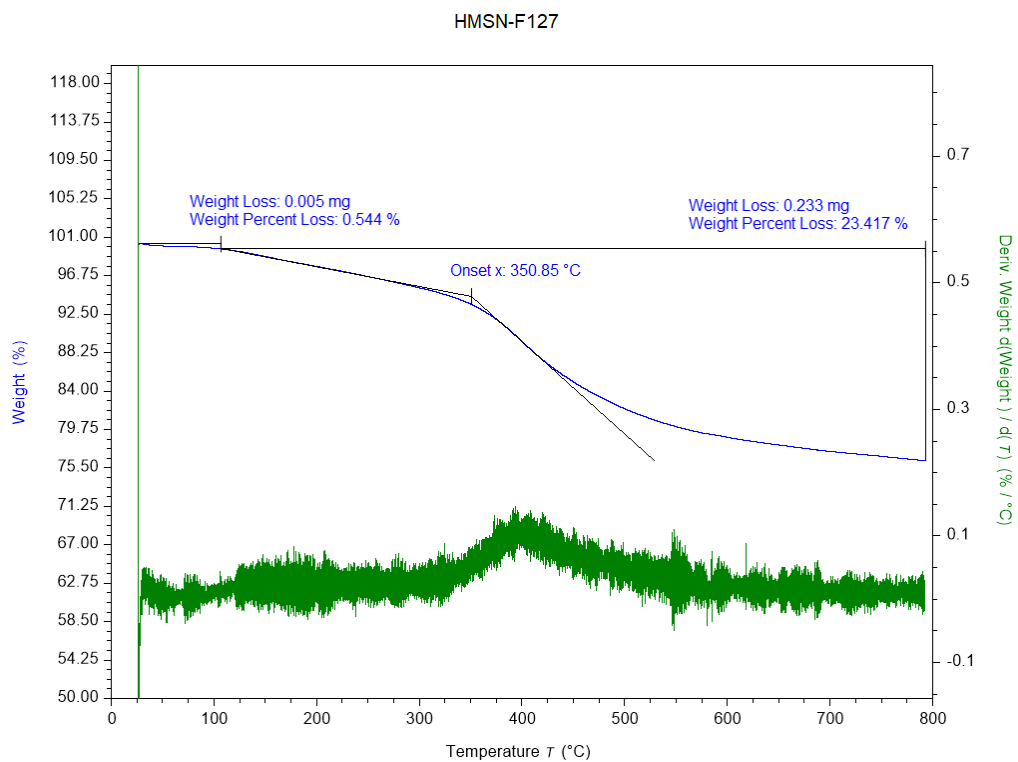
TGA graph of HMSN-L64



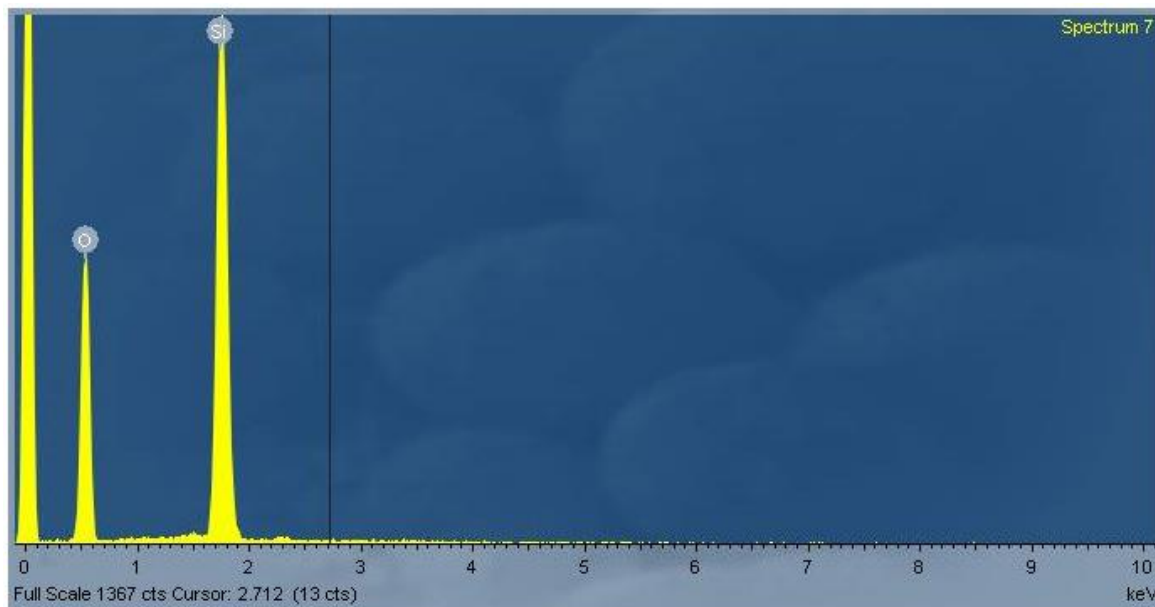
TGA graph of HMSN-F68



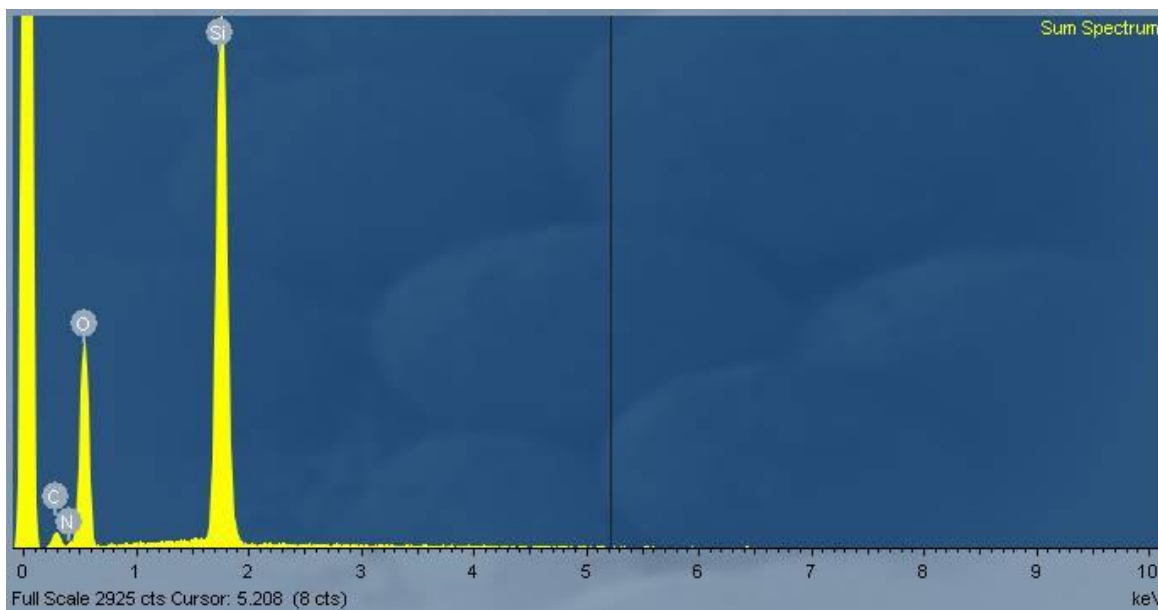
TGA graph of HMSN-F127



EDX pattern of HMSN



EDX pattern of HNSM-NH₂



Isotherm Linear Plot of HMSN



TriStar II Plus 3.03

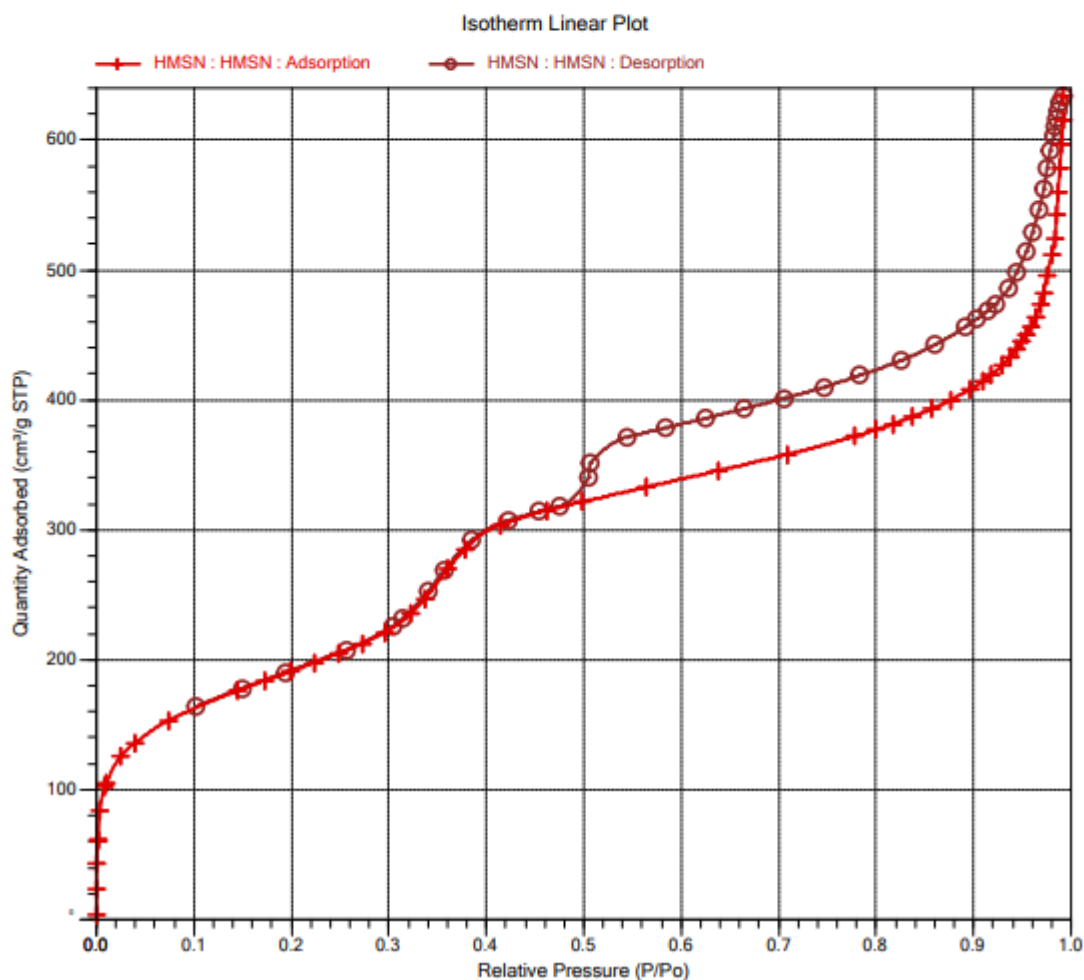
TriStar II Plus Version 3.03
Serial # 2090 Unit 1 Port 1

Page 7 of 55

Sample: HMSN
Operator: Mr. Mouse
Submitter:
File: C:\TriStar II Plus\data\Mr Ty\Nguyen Thi Ho\HMSN.SMP

Started:	9/13/2022 5:16:40 PM	Analysis adsorptive:	N2
Completed:	9/14/2022 9:36:47 AM	Analysis bath temp.:	77.350 K
Report time:	9/14/2022 10:58:35 AM	Thermal correction:	No
Sample mass:	0.1116 g	Ambient free space:	11.9593 cm ³ Measured
Analysis free space:	31.1547 cm ³	Equilibration interval:	10 s
Low pressure dose:	None	Sample density:	1.000 g/cm ³
Automatic degas:	No		

Comments: Degas: at 105C, by N2 gas, in 2h



BJH Adsorption dV/dD Pore Volume of HMSN



TriStar II Plus 3.03

TriStar II Plus Version 3.03
Serial # 2090 Unit 1 Port 1

Page 24 of 55

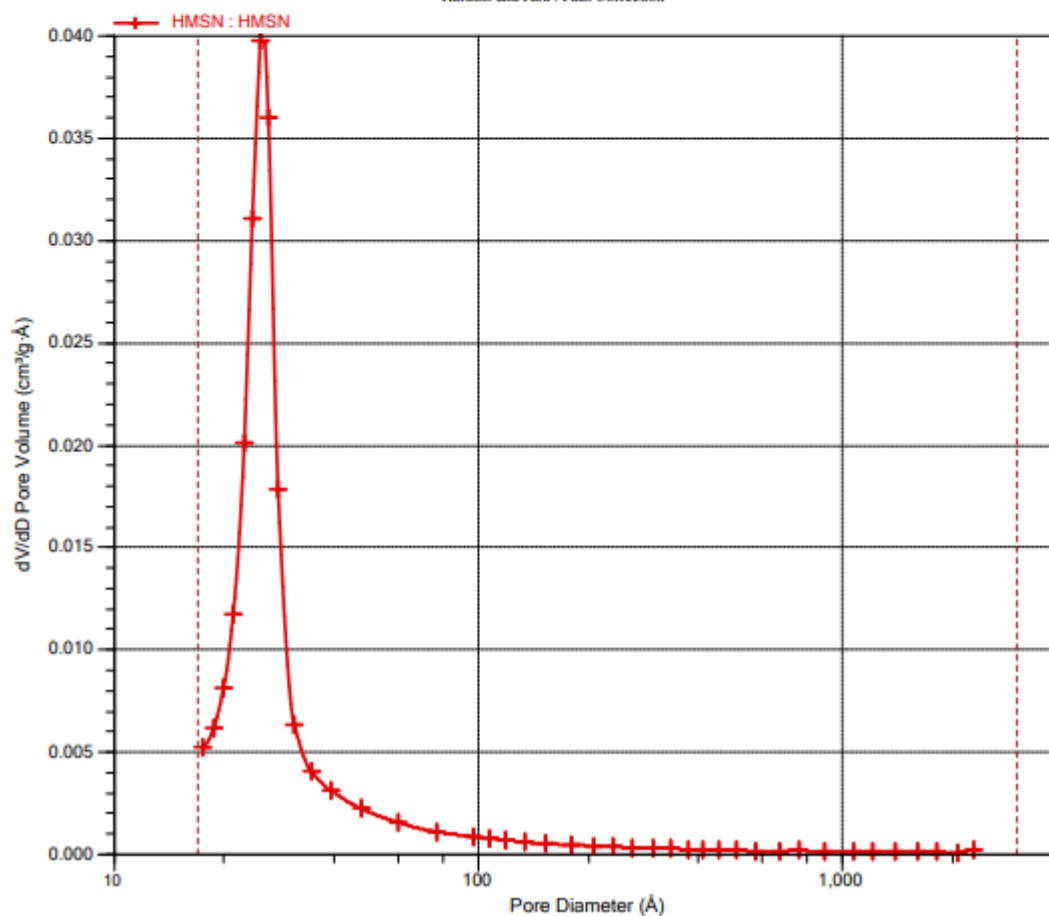
Sample: HMSN
Operator: Mr. Mouse
Submitter:
File: C:\TriStar II Plus\data\Mr Ty\Nguyen Thi Ho\HMSN.SMP

Started:	9/13/2022 5:16:40 PM	Analysis adsorptive:	N2
Completed:	9/14/2022 9:36:47 AM	Analysis bath temp.:	77.350 K
Report time:	9/14/2022 10:58:35 AM	Thermal correction:	No
Sample mass:	0.1116 g	Ambient free space:	11.9593 cm ³ Measured
Analysis free space:	31.1547 cm ³	Equilibration interval:	10 s
Low pressure dose:	None	Sample density:	1.000 g/cm ³
Automatic degas:	No		

Comments: Degas: at 105C, by N2 gas, in 2h

BJH Adsorption dV/dD Pore Volume

Harkins and Jura : Faas Correction



Isotherm Linear Plot of HMSN-NH₂



TriStar II Plus 3.03

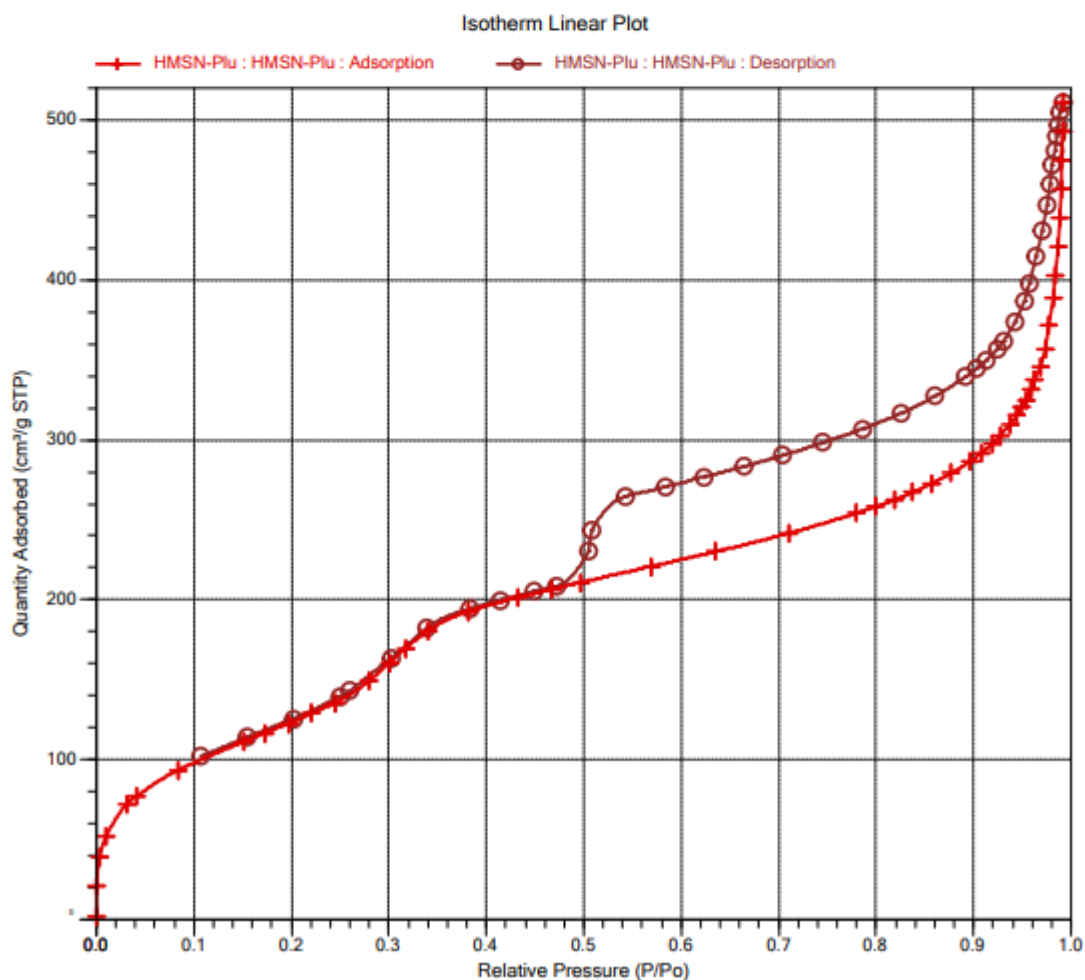
TriStar II Plus Version 3.03
Serial # 2090 Unit 1 Port 2

Page 7 of 52

Sample: HMSN-Plu
Operator: Mr. Mouse
Submitter:
File: C:\TriStar II Plus\data\Mr Ty\Nguyen Thi Ho\HMSN-Plu.SMP

Started: 9/13/2022 5:16:40 PM	Analysis adsorptive: N2
Completed: 9/14/2022 9:36:47 AM	Analysis bath temp.: 77.350 K
Report time: 9/14/2022 10:59:08 AM	Thermal correction: No
Sample mass: 0.0864 g	Ambient free space: 11.7803 cm ³ Measured
Analysis free space: 30.4813 cm ³	Equilibration interval: 10 s
Low pressure dose: None	Sample density: 1.000 g/cm ³
Automatic degas: No	

Comments: Degas: at 105C, by N2 gas, in 2h



BJH Adsorption dV/dD Pore Volume of HMSN-NH₂



TriStar II Plus 3.03

TriStar II Plus Version 3.03
Serial # 2090 Unit 1 Port 2

Page 21 of 52

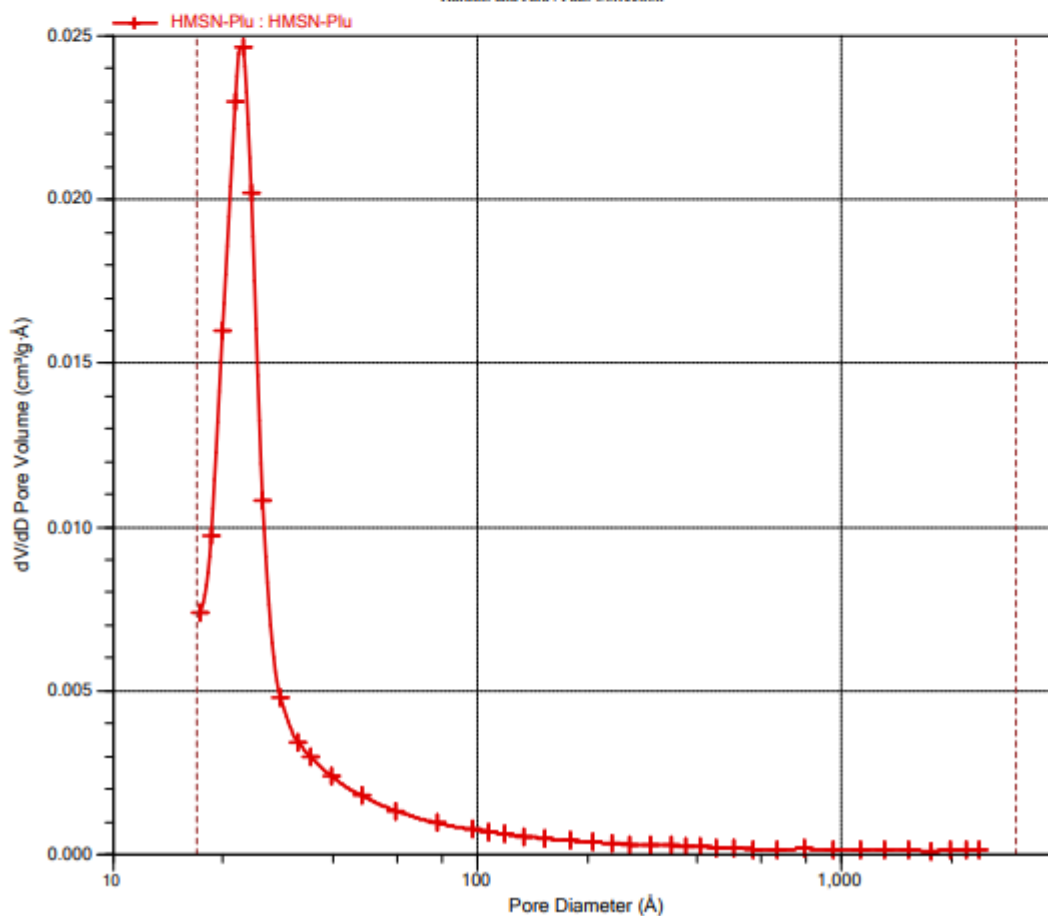
Sample: HMSN-Plu
Operator: Mr. Mouse
Submitter:
File: C:\TriStar II Plus\data\Mr Ty\Nguyen Thi Ho\HMSN-Plu.SMP

Started:	9/13/2022 5:16:40 PM	Analysis adsorptive:	N2
Completed:	9/14/2022 9:36:47 AM	Analysis bath temp.:	77.350 K
Report time:	9/14/2022 10:59:08 AM	Thermal correction:	No
Sample mass:	0.0864 g	Ambient free space:	11.7803 cm ³ Measured
Analysis free space:	30.4813 cm ³	Equilibration interval:	10 s
Low pressure dose:	None	Sample density:	1.000 g/cm ³
Automatic degas:	No		

Comments: Degas: at 105C, by N2 gas, in 2h

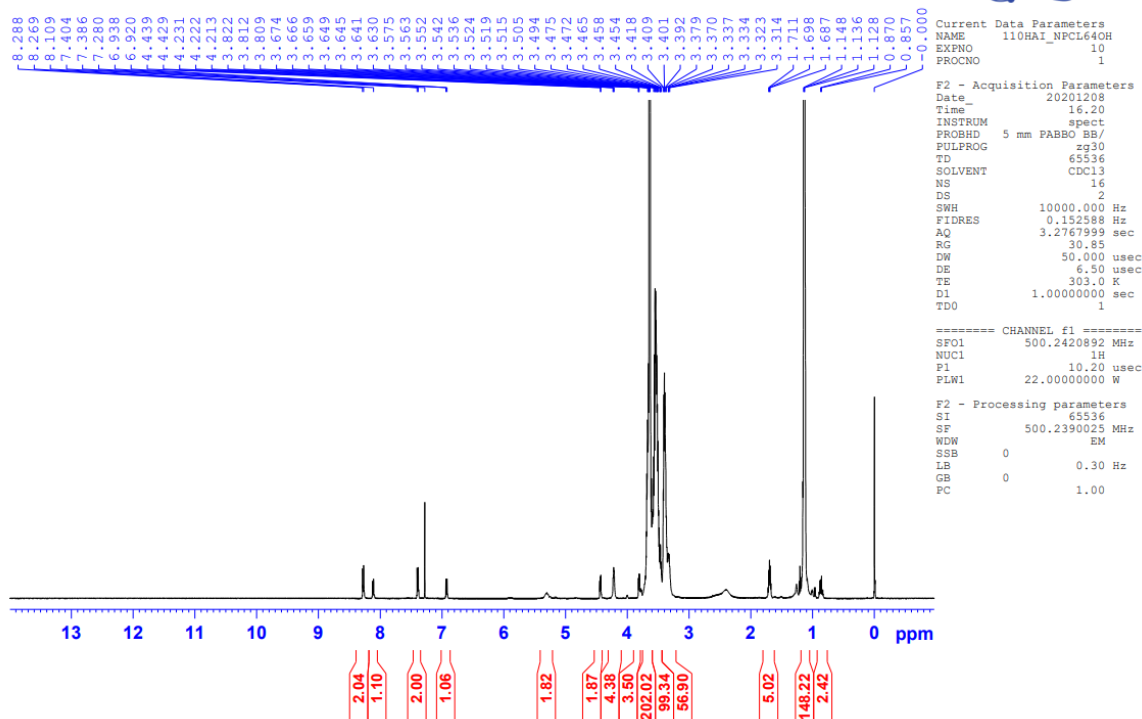
BJH Adsorption dV/dD Pore Volume

Harkins and Jura : Faas Correction



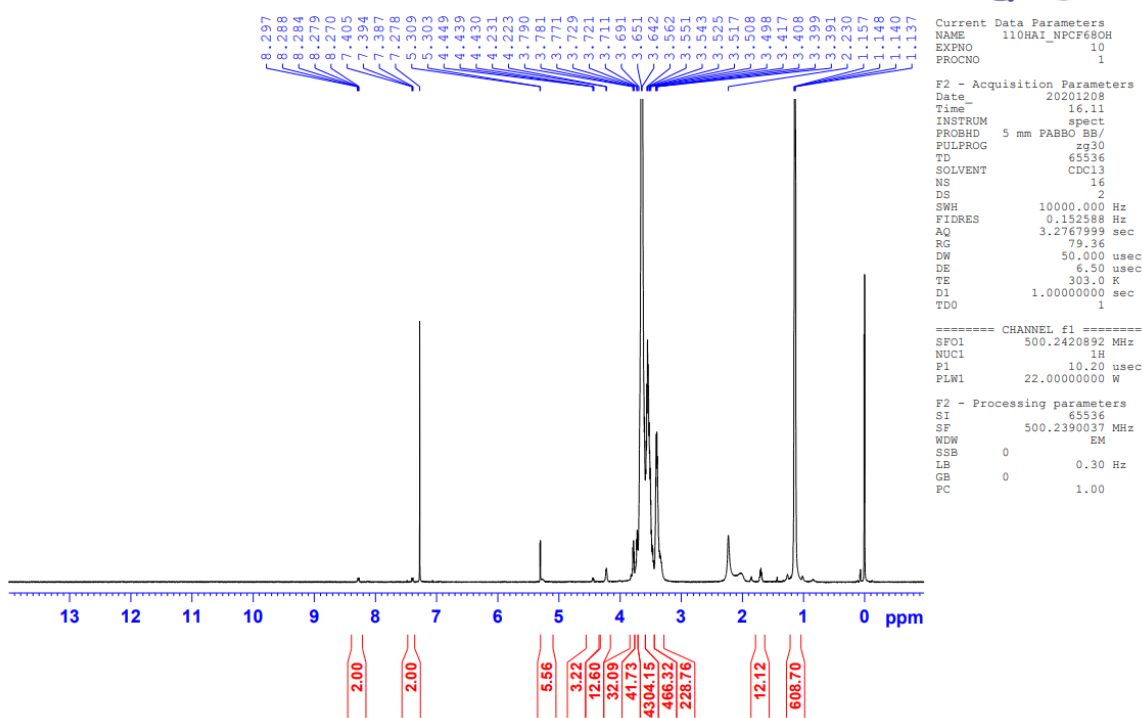
¹H-NMR spectrum of NPC-L64-OH

NPCL64OH-CDCl3-1H



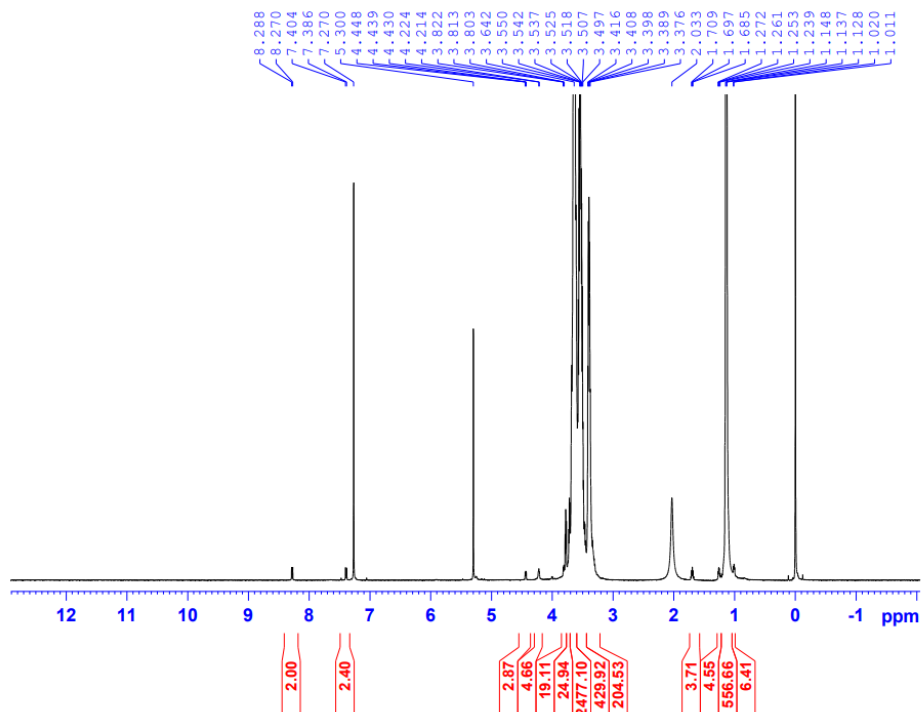
¹H-NMR spectrum of NPC-F68-OH

NPCF68OH-CDCl3-1H



¹H-NMR spectrum of NPC-F127-OH

NPCF127OH-CDC13-1H



```
Current Data Parameters
NAME      110HA1_NPCF127OH
EXPNO     10
PROCNO    1

F2 - Acquisition Parameters
Date_     20201208
Time      16.07
INSTRUM   spect
PROBHD    5 mm PABBO BB/
PULPROG   zg30
TD         65536
SOLVENT   CDCl3
NS         16
DS         2
SWH        10000.000 Hz
FIDRES     0.152588 Hz
AQ         3.2767999 sec
RG         89.63
DW         50.000 usec
DE         6.50 usec
TE         303.0 K
D1         1.00000000 sec
TDO        1

===== CHANNEL f1 =====
SFO1      500.2420892 MHz
NUC1       1H
P1         10.20 usec
PLW1       22.00000000 W

F2 - Processing parameters
SI         65536
SF         500.2390076 MHz
WDW        EM
SSB        0
LB         0.30 Hz
GB         0
PC         1.00
```